FACULTY OF SCIENCE
UNIVERSITY OF COPENHAGEN

PhD Thesis

by Karsten Bjerrum Dideriksen

A room-temperature single-photon source with built-in memory

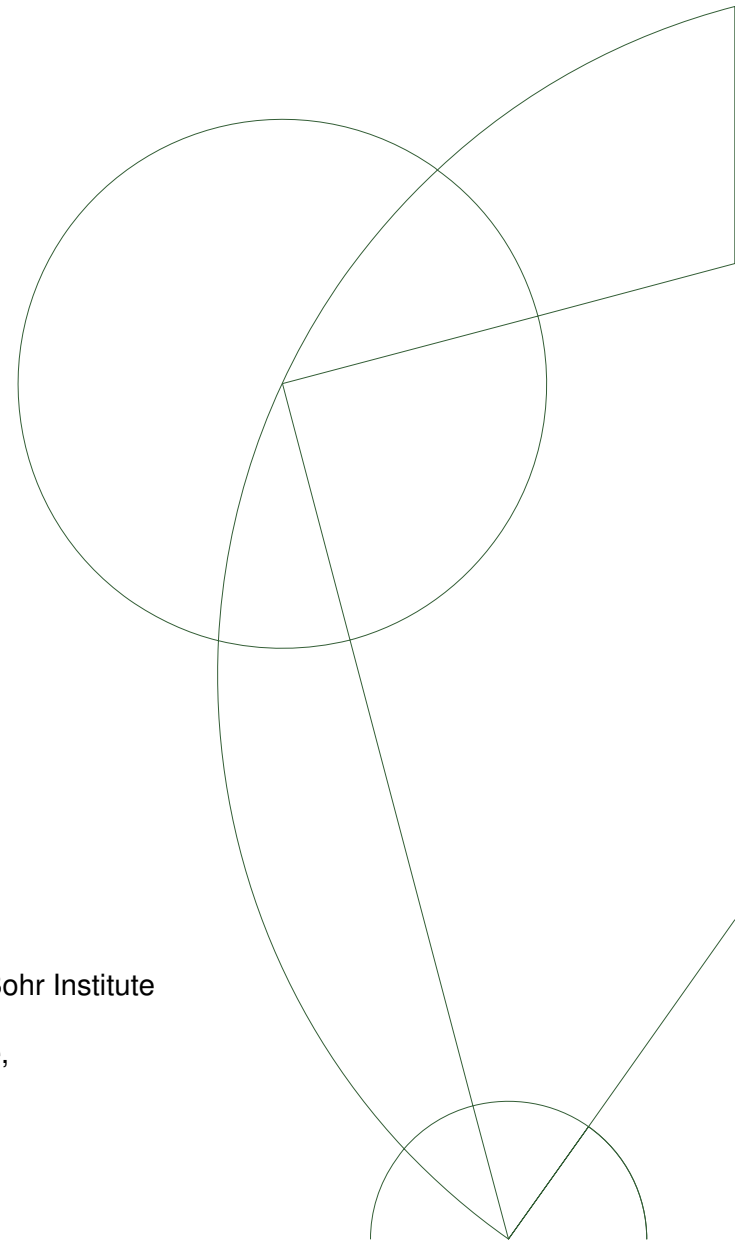

Supervisor: Prof. Eugene S. Polzik, QUANTOP, Niels Bohr Institute

Submitted to the PhD School of The Faculty of Science,
University of Copenhagen, on February 28, 2021.

Abstract

Coherent light-matter interfaces in atomic ensembles at room-temperature have been studied for decades and have been found to be suitable systems for applications such as magnetometry and frequency references. In particular, warm atomic ensembles are favoured due to their experimental simplicity over cold quantum platforms. At the onset of the second quantum revolution these systems are also receiving much attention as a platform for non-classical light generation and quantum memory for light. Studies are often focused on either probabilistic single-photon generation or fast, high-bandwidth memories with short memory time for external photon sources.

This thesis presents an investigation of on-demand single-photon generation following the DLCZ scheme in a warm caesium vapour. As a novel approach we employ the long-lived collective spin mode in an anti-relaxation-coated cell to extend the memory time by orders of magnitude beyond previous demonstrations.

Initially attempting on the D_2 spectral line we show that single-photon readout in this configuration is prohibited by four-wave mixing. When changing to the D_1 line, the interaction is performed at the magic detuning where four-wave mixing is strongly suppressed. In this configuration we are able to achieve single-photon generation and retrieval with a conditional anti-bunching of 0.20 ± 0.07 for the readout field. The cross correlation between heralding and readout fields reaches 10 ± 1 which is highly non-classical and sufficient for quantum entanglement generation. The correlation remains non-classical for a memory storage time up to 0.68 ± 0.08 ms. The performance of the source-memory system is limited by a combination of imperfect initial state preparation and readout noise induced by atomic decay.

This work shows that the long-lived collective spin mode of room-temperature atomic vapours can be utilized as a narrowband single-photon source with built-in memory. Such devices could find application in quantum information and communication based on single photon interference where the memory capability can enhance photon coincidence rates or long-distance entanglement generation probability.

Resumé

Kohærent vekselvirkning mellem lys og stof i atomare ensembler ved stuetemperatur har været undersøgt gennem årtier og er fundet egnede fysiske systemer til anvendelser såsom magnetometri og frekvensreferencer. Særligt er varme atomare gasser at foretrække frem for kolde kvanteplatforme pga. deres eksperimentelle enkelhed. Her ved begyndelsen af den anden kvanterevolution vokser interessen for disse systemer som en platform til generering af ikke-klassisk lys og til kvantehukommelse for lys. Studier fokuserer ofte på enten probabilistisk generering af enkeltstående fotoner eller hurtige, bredbåndede hukommelser med kort hukommelsestid i sammenhæng med eksterne fotonkilder.

I denne afhandling præsenteres et studie af *on-demand* generering af enkeltstående fotoner i en varm cæsium gas efter DLCZ-fremgangsmåden. I en ny tilgang anvender vi det kollektive spinmodus med lang levetid i en beholder med anti-relaksationsbeklædning til at forlænge hukommelsestiden med flere størrelsesordner over tidligere demonstrationer.

Efter forsøg på D_2-spektrallinjen påviser vi, at enkeltfoton-udlæsning i denne konfiguration er udelukket pga. firbølgeblanding. Ved at skifte til D_1-linjen formår vi at opnå enkeltfotongenerering og -tilbagekaldelse med en betinget anti-sammenklumpning på 0.20 ± 0.07 for udlæsninglyset. Tværkorrelationerne mellem signalerings- og udlæsningslyset når værdien 10 ± 1 hvilket er en stærkt ikke-klassisk værdi og tilstrækkeligt til at generere kvantemekanisk sammenfiltring. Tværkorrelationen forbliver ikke-klassisk inden for en opbevaringstid på $0.68 \pm 0.08\,\mathrm{ms}$. Ydeevnen for dette kilde/hukommelses-system er begrænset af en kombination af ufuldstændig initiering af ensembletilstanden og udlæsningsstøj forårsaget af atomart henfald.

Dette arbejde påviser, at det langtidslevende kollektive spinmodus i en atomar gas ved stuetemperatur kan benyttes som en smalbåndet enkeltfotonkilde med indbygget hukommelse. En sådan enhed kan finde anvendelse inden for kvanteinformation og -kommunikation baseret på enkeltfotoninterferens, hvor hukommelsesevnen kan forbedre hyppigheden af fotonsammenfald eller sandsynligheden for sammenfiltringsgenerering over store afstande.

Publications related to the thesis

Dideriksen, K.B.*, Schmieg, R.*, Zugenmaier, M.*, and Polzik, E.S. (2020). *Room-temperature single-photon source with near-millisecond built-in memory.* Under review. Preprint at arxiv:2010.06875.

Zugenmaier, M.*, Dideriksen, K.B.*, Sørensen, A.S., Albrecht, B.*, and Polzik, E.S. (2018). Long-lived non-classical correlations towards quantum communication at room temperature. *Communications Physics*, **1**(1):76.

* These authors contributed equally.

Conference presentations

Dideriksen, K.B., Schmieg, R., Zugenmaier, M., and Polzik, E.S. *Room-temperature single-photon source with near-millisecond built-in memory.* Scheduled for APS March Meeting 2021. (Contributed talk)

Dideriksen, K.B., Zugenmaier, M., Sørensen, A.S., Albrecht, B., and Polzik, E.S. *Towards an on-demand single-photon source based on room-temperature atomic vapours.* At 2nd International Symposium on Single Photon based Quantum Technologies, Berlin, 2019. (Contributed talk)

Dideriksen, K.B., Zugenmaier, M., Sørensen, A.S., Albrecht, B., and Polzik, E.S. *Towards a on-demand single-photon source for quantum repeater application at room temperature.* At Danish Optical Society Annual Conference 2018, Copenhagen. (Contributed talk)

Public outreach

Dideriksen, K.B. *Hvordan ser fremtidens kvante-internet ud?* Kulturnatten, Copenhagen, 2017. (Invited talk)

Fjeldberg, Anders. Speed til kvantecomputeren. *Uniavisen*, 2019. (Interview article)

Preface

The work presented in this thesis is the outcome of my research at QUANTOP, The Danish Center for Quantum Optics, over the past many years. My involvement with QUANTOP started in spring 2014 where I joined the group as a Bachelor student. The group environment and research activities appealed to me strongly and sparked a curiosity to continue research within quantum optics. In 2015 I embarked on an integrated Master and PhD scheme in a project to demonstrate single-photon generation in warm caesium vapour. Due to two parental leaves along the way my time at QUANTOP extended beyond the initial anticipation. I am grateful for the many years in the group that enabled the completion of the single-photon experiment.

Here, I would like to express my gratitude towards Prof. Eugene S. Polzik who saw competence in me during my Bachelor thesis work and suggested that I stayed around for PhD studies. The PhD studies have been a journey of ups and downs, seemingly endless frustration and mind-boggling experimental physics. It has required a, for me, unprecedented level of hard work and dedication to complete the work and I would like to thank everyone involved in making it happen. As a supervisor Eugene has managed to keep me and the experiment on track, often repeating the mantra that everything that is easy has already been done.

The experimental progress has been very much a collective effort with close collaboration on all aspects of the work. All the way since the very beginning Michael Zugenmaier has been my closest colleague. I owe Michael great thanks for many things that cannot all be written here but it includes initiating the experiment and accepting me on the team, introducing me to a lot of basic stuff about optics, and many, many hours of fruitful discussions and help in the lab. I also thank Boris Albrecht who played a major part in the advancement of the experiment in its early phase. In particular for his insistence on and implementation of setup automatization requiring extensive coding. We are often reminded of Boris' effort when we stumble upon the quirky comments, he has left in the code. After Boris left, Rebecca Schmieg joined the single-photon experiment team. I am thankful to Rebecca for all her hard work that has helped push the experiment to the final level. Especially, I want to thank her and Michael for good company during many long overnight hours in the lab monitoring the setup while acquiring large amounts of data. And thanks to both of you for the help in proof reading and commenting on the thesis manuscript.

I am grateful for the invaluable help I have had from my senior colleagues Jörg Helge Müller and Jürgen Appel whom I have always been able to count on for an answer to experimental challenges. And to all of the QUANTOP colleagues over the years: Thank you for creating such a stimulating and exciting lab environment!

To my family: Thank you for love, support and understanding. Especially, when presence in the lab was required at odd hours.

Finally, I am grateful for the funding that has enabled my research. The support has come from grants to my supervisor Eugene S. Polzik from the ERC AdG Interface, ERC AdG Quantum-N, ERC consolidator QIOS, ARO grant W911NF, the John Templeton Foundation, the Innovation Fund (project Q-GWD), and The Villum Foundation (grant no. 25880).

Karsten Bjerrum Dideriksen, February 2021.

Thesis outline

The thesis is divided into seven chapters. The first two chapters are intended as an introduction to the context of which the experimental work has been carried out. **Chapter 1** outlines the motivation for investigating on-demand single-photon generation in a warm atomic vapour. In **chapter 2** we will dive into the details and discuss how quantum mechanics apply to atomic ensembles and introduce the theoretical aspects of single-photon generation and memory. The chapter is intended to gradually build up the theoretical framework under which we understand the light-matter interaction in vapour cells.

The following three chapters present the experimental work behind the thesis. **Chapter 3** describes the experimental setup and how the different critical parameters are characterised. In **chapter 4** the results from the early stages of the experiment are presented and discussed. This was the first attempt to demonstrate the single-photon scheme and we show that high-fidelity readout is prohibited by noise intrinsic to the specific atomic spectral line. The main results of the thesis are presented in **chapter 5** where the insights from the first attempt are used to demonstrate an operational single-photon source.

The last two chapters round off the thesis by discussing limitations of the scheme, benchmarking against other works, and presenting future prospects in **chapter 6** and giving concluding statements in **chapter 7**.

Contents

Preface **ii**

1 Introduction **1**
1.1 Long-distance quantum communication . . . 2
1.2 Optical quantum computation . . . 5
1.3 Single-photon sources . . . 7
1.4 Optical quantum memories . . . 8
1.5 Atomic vapour cells . . . 9

2 Single-photon interface in atomic ensembles **11**
2.1 Generic single-photon herald-retrieve scheme . . . 11
2.2 The caesium atom . . . 14
2.3 Ensemble interaction . . . 16
2.3.1 Parametric-gain interaction . . . 18
2.3.2 Beam-splitter interaction . . . 21
2.4 Spin wave . . . 22
2.5 Cavity Enhancement . . . 24
2.6 Interaction with moving atoms . . . 27
2.7 Non-classical correlations . . . 35
2.7.1 Relation to entanglement . . . 37

3 Experimental Set-Up **39**
3.1 Vapour cells . . . 39
3.1.1 Magnetic shielding and bias field coil . . . 41
3.1.2 Optical pumping . . . 42
3.2 Optics and electronics . . . 43
3.2.1 Filtering . . . 43
3.2.2 Excitation Laser . . . 47
3.2.3 Single-photon detection . . . 48
3.2.4 FPGA sequence control . . . 49

3.3 Characterization . . . 49
3.3.1 Optical depth . . . 49
3.3.2 Magneto-optical resonance spectroscopy . . . 51
3.3.3 Pumping Optimization . . . 60
3.3.4 Population decay in the dark . . . 63
3.3.5 Cell Cavity . . . 65

4 Four-Wave-Mixing-limited DLCZ scheme on the D_2 line 74
4.1 Experimental realization . . . 75
4.2 Performance . . . 78
4.2.1 Noise sources . . . 81
4.2.2 Four-Wave-Mixing Suppression . . . 87

5 Single-photon source on the D_1 line 90
5.1 Experimental realization . . . 90
5.1.1 Optimization of parameters . . . 94
5.2 Source-Memory Performance . . . 98
5.2.1 Excitation probability influence . . . 99
5.2.2 Memory performance . . . 103
5.2.3 Noise Sources . . . 106
5.2.4 Modelling correlations in the presence of noise . . . 112

6 Discussion and future outlook 117
6.1 Limiting noise processes . . . 117
6.2 Verification of FWM suppression . . . 118
6.3 Efficient motional averaging . . . 119
6.4 Benchmarking . . . 120
6.5 Possible improvements . . . 126

7 Conclusion 129

Appendices 131

A Correlation model 132

Bibliography 138

Chapter 1

Introduction

In current years a lot of attention has been directed at the development of so-called quantum technologies – from basic research communities as well as industrial companies and political institutions. In a broad sense this category covers technology which brings solutions to practical problems by employing quantum systems. Often this is taken to mean systems prepared in a state that cannot be described by classical physics. Potential quantum technologies fall in the three domains: sensing/metrology, communication and simulation/computation. Because of the prospective improvements that quantum technologies can bring, present time is sometimes referred to as the second quantum revolution. Here our current development is seen as a sequel to a quantum revolution in the mid-20th century where development of new technologies – such as semi-conductors and lasers – were driven by an understanding of the systems on a quantum mechanical level but without direct manipulation of the quantum states.

The field of quantum optics has been a main driver of fundamental research that has enabled quantum technologies. When quantum optics has this role, it is because a high degree of control at the quantum level has been developed over several decades. In the same period strange quantum effects such as superposition and entanglement have been immensely studied within quantum optics. Many proposals for quantum technologies within all the domains mentioned above are therefore based on light-matter interaction, the pivot point of quantum optics.

A core resource for many of these proposals is the ability to generate pulses of light that contain exactly one quantum of energy – the single-photon pulse. A plethora of systems and schemes has been demonstrated to enable single-photon generation (for a recent review see Meyer-Scott *et al.*, 2020). However, performances that allow these sources to be scaled up to sizes where practical computational problems can be solved are only just emerging (Zhong *et al.*, 2020; Uppu *et al.*, 2020).

In this introduction we shall focus on long-distance quantum communication and quantum computation as specific domains where single-photon sources are prospect to play a central

role and where the combination with quantum memories for single photons will enhance performance.

1.1 Long-distance quantum communication

Quantum communication can be useful for secret-message sharing, e.g. based on quantum key distribution (Bennett and Brassard, 1984) and for transferring quantum information for the use of a variety of computation protocols (Simon, 2017). In the simplest scheme, quantum communication can be realized by encoding information in a single photon, e.g. in the polarization basis, and transmitting it directly (free-space or guided in an optical fibre). As an example, the generic polarization qubit encoding can be written as the superposition

$$|\psi\rangle = \alpha\,|\mathrm{H}\rangle + \beta\,|\mathrm{V}\rangle \;\text{ with }\; |\mathrm{H}\rangle = |1\rangle_\mathrm{H}\,|0\rangle_\mathrm{V}\,,\; |\mathrm{V}\rangle = |0\rangle_\mathrm{H}\,|1\rangle_\mathrm{V}\,, \tag{1.1}$$

where we explicitly define the polarization states in the two-mode photon-number basis. This is sometimes referred to as "dual-rail" encoding because the single photon exists in either of the two polarization modes (horizontal or vertical). In contrast, "single-rail" encoding uses a single mode only where the basis states can be e.g. the photon-number states $|0\rangle$ and $|1\rangle$. The dual-rail encoding has the advantage that the state always contains a photon which can be detected. This makes dual-rail encoding more resilient to photon loss because post-selection on measurement outcomes is possible. I.e. if the measurement outcome is "zero" (no photon detected), the measurement is false.

Alternatively to direct transmission, a resource of entanglement such as an Einstein-Podolsky-Rosen (EPR) pair, e.g. the singlet state

$$|\mathrm{EPR}\rangle_\mathrm{AB} = \frac{|1\rangle_\mathrm{A}\,|0\rangle_\mathrm{B} - |0\rangle_\mathrm{A}\,|1\rangle_\mathrm{B}}{\sqrt{2}}, \tag{1.2}$$

is shared between the communicating parties A and B. The distribution of the entanglement could happen by means of an entangled photon travelling from A to B or a central station transmitting pairs of entangled photons to A and B. This resource can then be used to communicate an arbitrary qubit state via teleportation (Bennett *et al.*, 1993) or establish a secret encryption key from the non-classical correlation (Ekert, 1991).

In both cases the communication rate will suffer from finite propagation losses when the distance becomes large enough. The typical propagation loss for light at telecom wavelengths in optical fibres is 0.2 dB/km. Hence, after 100 km the photon arrival probability is reduced to 1% which heavily reduces the achievable communication rate. Furthermore, for direct transfer of a quantum state, the probabilistic communication channel requires many copies of the state to be sent before successful transmission. Since arbitrary quantum states cannot be cloned, sending multiple copies of the same state until success is prohibited – unless the generation process can be repeated. In classical communication, the process of amplification

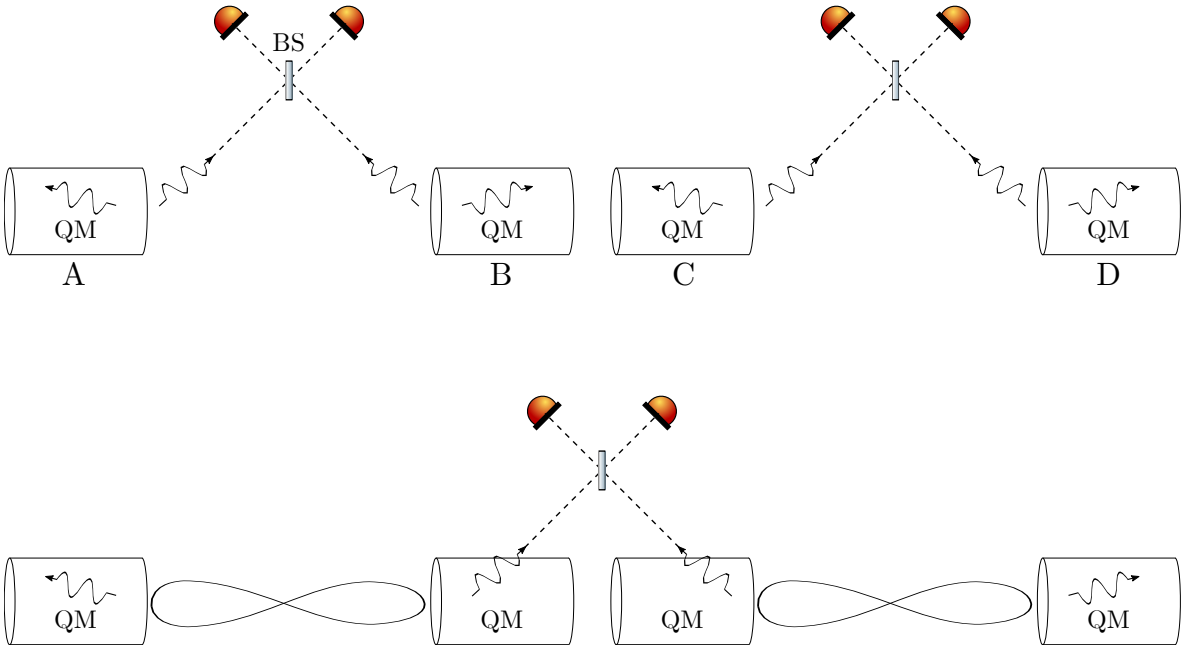

Figure 1.1: **DLCZ quantum-repeater protocol. Top:** Entanglement distribution in the elementary link. Probabilistic photon-pair generation in nodes A and B where one photon is held in an atomic ensemble and one propagates to joint detection with the field from the other node. Upon detection of a photon, the two atomic ensembles are entangled, sharing one excitation. **Bottom:** Entanglement swapping between links. After successful entanglement generation in two neighbouring links, entanglement swapping is performed at the central nodes B and C. The atomic ensemble state is converted into light and joint detection of the fields from B and C is performed. If successful, the entanglement is swapped such that nodes A and D now share one excitation.

(making copies) is used to enhance communication rates over large distances in a device called a repeater. To achieve practical quantum communication rates over long distances the propagation loss of photons will need to be remedied. This has sparked the interest in quantum-repeater (QR) technology. Existing proposals are based on quantum memory buffers (Sangouard *et al.*, 2011) or error correction (e.g. Azuma *et al.*, 2015).

One specific quantum-repeater protocol is the DLCZ scheme (Duan, Lukin, Cirac, and Zoller, 2001) based on atomic ensembles. The protocol aims to distribute entanglement between end nodes by dividing the communication channel into segments containing quantum memories, see Fig. 1.1. With low probability p, a laser pulse in the ensemble A generates a photon pair where one is stored inside the ensemble (acting as a memory) while the other travels to an intermediate detection station between nodes A and B. Simultaneously, the same process

happens in ensemble B. The full-system state can then be written as

$$|\psi\rangle_{AB} \propto (|00\rangle_A + \sqrt{p}\,|11\rangle_A) \otimes (|00\rangle_B + \sqrt{p}\,|11\rangle_B), \tag{1.3}$$

where both A and B are in a superposition of having and not having generated a photon pair. Light from the two ensembles is combined on a beam-splitter (BS) and detectors are placed at both output ports. This performs a joint measurement on the two light paths. When light from the two ensembles is indistinguishable, the detection has no "which-path" information. After a single photon is detected, the atomic ensembles are thus projected into the entangled state

$$\left|\Phi^{\pm}\right\rangle_{AB} = \frac{|1\rangle_{\mathrm{A}}\,|0\rangle_{\mathrm{B}} \pm |0\rangle_{\mathrm{A}}\,|1\rangle_{\mathrm{B}}}{\sqrt{2}}, \tag{1.4}$$

with one excitation shared between A and B. The sign depends on which of the detectors in the joint measurement clicks. When entanglement is heralded in two neighbouring links, the entanglement is swapped by performing a joint measurement on the two central ensembles B and C (Fig. 1.1, bottom panel). The joint measurement is realized by converting the atomic state into light (memory readout) and performing a joint measurement of the light from B and C. If the joint measurement is successful (i.e. exactly one photon is detected), the entangled state in eq. (1.4) is swapped and now shared between A and D. Swapping the entanglement between neighbouring segments can continue until the end nodes of the channel are entangled. Both entanglement generation and swapping rely on photon indistinguishability.

The incorporation of quantum-memory nodes enables synchronization of link entanglement prior to swapping. I.e., the heralded entanglement can be kept in memory until successful entanglement is present in the neighbouring link. This drastically improves the entanglement distribution probability. It has been shown that the average time for distributing entanglement over a channel scales polynomially in the channel length for quantum-repeater schemes whereas the scaling is exponential for direct photon transmission due to propagation loss (Duan *et al.*, 2001; Sangouard *et al.*, 2011).

In the context of QR application, the main figures of merit for a quantum memory are: 1) the readout efficiency (the atomic state conversion probability) which can be close to unity when using atomic ensembles. 2) the memory time (the duration a photon can be faithfully kept in the memory). Since the entanglement generation and swapping is probabilistic, many trials will have to be performed before entanglement at the end nodes is heralded. Collins *et al.* (2007) performed an analysis of the QR performance where they show that in order not to be limited by memory time, the QR memory time would have to be orders of magnitude longer than the time-of-flight between nodes. This means that the relevant time scale becomes the time-of-flight between *end nodes*. For this reason many studies have focussed on extending the memory time of quantum memories. In the same work the authors also show that spatial multiplexing can dramatically reduce the necessary memory time – down to only one order of magnitude longer than the inter-station time.

For QRs to become interesting as an alternative to direct photon transmission the distances involved are above 100 km. Therefore quantum memories for QR application need memory times at least on the order of milliseconds and practically significantly more to compensate for inefficiencies in both memories and detection (Sangouard *et al.*, 2011).

Long-distance quantum communication with quantum repeaters has not yet been demonstrated and it is considered the outstanding challenge for establishing the Quantum Internet (Wehner *et al.*, 2018). However, (low-rate) long-distance entanglement distribution *without* quantum repeaters has been shown. By using a space satellite, Yin *et al.* (2017) were able to distribute entangled photon pairs over a 1200 km ground distance at 1 Hz rate, limited by >64 dB loss from beam divergence, atmospheric absorption and optics. Scaling up the the rate over this distance will likely require implementation of QRs.

1.2 Optical quantum computation

Classical computation is often comprised of gate operations on two input states. However, light only interacts very weakly with light, hence such two-photon gates would require a medium of strong optical non-linearity. While the realization of such gates is being pursued, e.g. in single atoms (Hacker *et al.*, 2016) or ultracold as well as room-temperature Rydberg atoms (Tiarks *et al.*, 2019; Kübler *et al.*, 2010), another option was proposed in the seminal paper by Knill *et al.* (2001). Knill *et al.* show that universal quantum computation can be achieved in a network of single-photon sources, linear optics and single-photon detectors (Fig. 1.2). The operation principle for linear-optics quantum computation is multi-photon interference such as Hong-Ou-Mandel interference (Hong *et al.*, 1987). This type of interference relies on photon indistinguishability and overlapping wavepackets. From this we get a set of figures of merit for application of single-photon sources in quantum computing. A scalable source must produce single photons of high purity (i.e. vanishing two-photon component), and indinstinguishable photons. On top of that, a high brightness (i.e. high photon flux) is desirable for fast operation. For a linear computation network it is important that input photons are synchronized to observe the interference. For sources with a non-unity generation probability p this can be ensured by post-selection. I.e., the computation network output data is post-selected to cases where the correct number of output photons were detected. While this works and has been demonstrated (Carolan *et al.*, 2015), the photon coincidence rate will be extremely low for realistic sources and networks that require more than just a few input modes. Unfortunately, this linear-optics quantum computation has a huge overhead in terms of the resources (number of sources/detectors) needed. A way to reduce the overhead is by using large entangled photon states, so-called cluster states that enable error correction schemes. One primer for building cluster states is the entangled, three-photon GHZ states

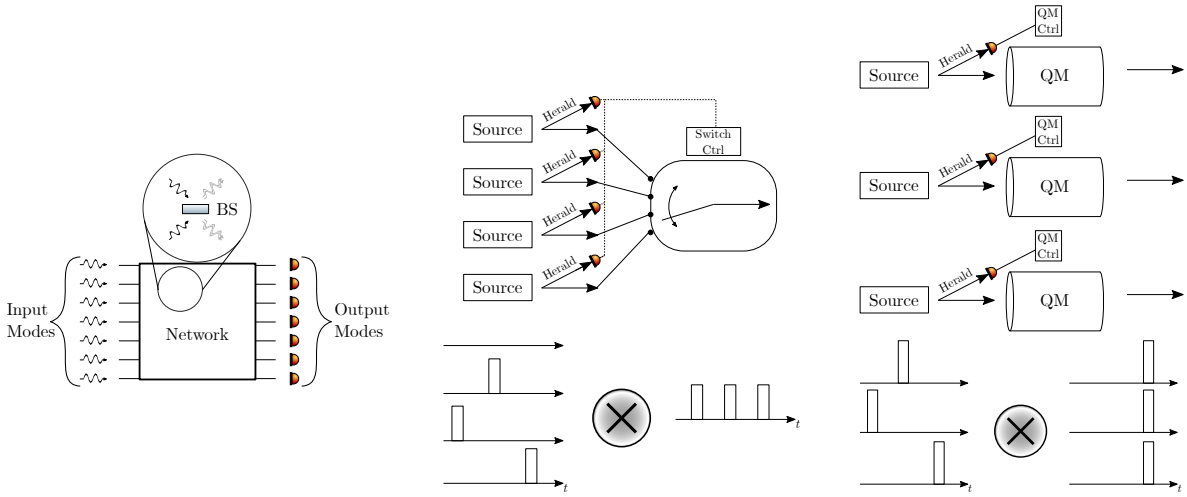

Figure 1.2: **Optical quantum computation and single-photon source multiplexing.** **Left:** Quantum computation network. Synchronous single-photon pulses are input on the network which is based on photon interference on beam-splitter (BS) interfaces. The network output is detected by single-photon detectors.
Centre: Spatial multiplexing. Several sources can be combined into one high-efficiency source by a switch that routes heralded photons to one joint output mode.
Right: Temporal multiplexing. Heralded photons from parallel sources can be delayed by quantum memories (QM) and released synchronously as input to a quantum network.

(Greenberger, Horne, and Zeilinger, 1989)

$$|\mathrm{GHZ}\rangle = \frac{|000\rangle + |111\rangle}{\sqrt{2}}. \tag{1.5}$$

The GHZ state can be generated and heralded in a linear-optics network which requires six synchronized input photons (Nunn, 2019). The probability of n-photon coincidences for probabilistic sources is given by $P = p^n$ which even for $p = 50\%$ yields $P = 1.6\%$ for six-photon coincidence. We note that here p is the heralding probability, i.e. the probability that a photon is generated *and* heralded. For this reason, ways of source multiplexing are increasingly pursued. The idea is to enhance the effective photon probability by combining the output of many identical sources or many output modes of one source. The principle is illustrated in Fig. 1.2. This can drastically increase the multi-photon coincidence rates. Among several types of multiplexing, one is *spatial* multiplexing where many heralded sources are operated in parallel. In this case feedforward from the heralding detector to optical switches enables routing of the heralded source outputs to the relevant network inputs. The challenge here is to reach fast, low-loss switching and indistinguishability between sources. Another option is *temporal* multiplexing where the output of a heralded source at different times can be individually delayed and combined for simultaneous input to the network. This requires the implementation of on-demand variable-delay lines which can in general be considered quantum

memories. For this application the figures of merit for the quantum memory becomes input (write) and output (read) efficiencies, η, as well as the memory time-bandwidth product, B, i.e. the number of temporal storage modes covered by the available storage time. Nunn *et al.* (2013) show that in the limit of low photon rates, the n-photon coincidence rate for n parallel source-memory systems is

$$P = (pB\eta)^n, \tag{1.6}$$

enhancing the heralding probability of each source by the time-bandwidth-efficiency product. This exponential scaling highlights the practical implication of high-performance quantum memories. In practise the different types of multiplexing can also be combined for further enhancement.

1.3 Single-photon sources

Over decades the laser community has managed to achieve a remarkable control over monochromatic light generated from laser system. The main challenge for single-photon generation is that it cannot be generated by simply attenuating a laser pulse. The ideal laser generates a sinusoidal wave of light. In quantum optics the equivalent is the coherent state (Gerry and Knight, 2004)

$$|\alpha\rangle = e^{-\frac{|\alpha|^2}{2}} \sum_{n=0}^{\infty} \frac{\alpha^n}{\sqrt{n!}} |n\rangle \,, \tag{1.7}$$

where $|n\rangle$ is the photon-number basis states and α is related to the wave amplitude and phase. Evidently, the coherent state has Poissonian photon statistics with n-photon probability

$$P(n) = |\langle n|\alpha\rangle|^2 = e^{-|\alpha|^2} \frac{|\alpha|^{2n}}{n!}. \tag{1.8}$$

Under attenuation, photons are randomly removed such that $|\alpha|^2$ reduces but the distribution of photons remains Poissonian. Thus, even for a very faint source, $|\alpha|^2 \ll 1$, with one-photon probability $p \approx |\alpha|^2$, the two-photon probability remains $p^2/2$. One strategy would be to measure the photon number but photon-number detection is performed by absorption and thus demolishes the state. Another strategy is therefore required.

In general, single-photon sources operate in distinct regimes: probabilistic or deterministic. A probabilistic source (Fig. 1.3, left) is typically based on parametric scattering (spontaneous parametric down conversion or spontaneous four-wave mixing) where the excitation probability p has to be kept very low (few percent) to keep the double excitation with probability p^2 low. Clearly, this has an even worse two-photon probability than the attenuated laser but the strong advantage is that photons are generated in pairs in different modes. The detection of one photon in one mode can be used to herald one photon in the other mode without disturbing

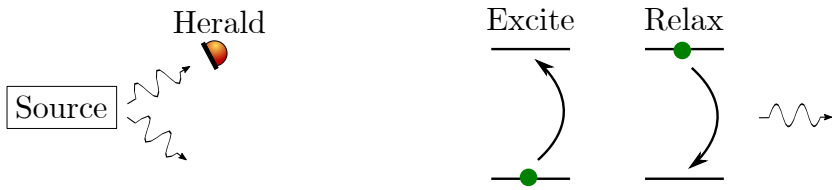

Figure 1.3: **Types of single-photon sources. Left:** Probabilistic heralded photon source. Photons are probabilistically generated in pairs in two modes. The detection in one mode heralds the single-photon state in the other mode. **Right:** Deterministic single-emitter source. The system is excited by an external pulse (e.g. laser pulse) and afterwards relaxes by emitting a photon. The single emitter can only contain one excitation hence photons are released one at a time.

the heralded photon. Because reliable photon-number detection is extremely difficult, these schemes are required to operate probabilistically with $p \ll 1$ and the way to enhance effective generation probability is through multiplexing to reach (quasi-)deterministic operation.

On the other hand, a deterministic source is based on a single emitter (Fig. 1.3, right). The single-emitter system can only accommodate one excitation and this excitation is released through radiative decay. High-performance single-emitter sources can reach almost unity intrinsic efficiency (Uppu *et al.*, 2020) such that only collection efficiency and outcoupling losses prevent truly deterministic generation. Very high source efficiency is necessary because deterministic single-photon sources are not heralded and thus incompatible with the multiplexing schemes mentioned above. It is also worth mentioning that demonstrations of high-performance, deterministic single-photon sources are so far in either cryogenic solid-state systems or ultracold atomic systems. While this is not a principle challenge, the setup complexity and need for helium cooling reduces the practical scalability of such sources.

1.4 Optical quantum memories

If we consider a broad definition of quantum memory as a device that can take a weak (single-photon level) input pulse and release it on demand after some time, many schemes and protocols exist in a variety of systems. This definition does not restrict memories to those that can store qubits states where the encoding is dual rail as in eq. (1.1). Quantum memories for dual-rail qubits require two storage modes. However, for single-photon synchronization as discussed above, a single-mode memory suffices.

In the context of single-photon synchronization we can broaden the quantum memory definition even further by including so-called ”read-only” or ”emissive” memories (as opposed to ”absorptive”/”write-read” memories described above). This is a type of memory where the memory is loaded with a single photon by spontaneous scattering which later can be retrieved on-demand (see Fig. 1.4). Thus, this type of memory combines source and memory in one

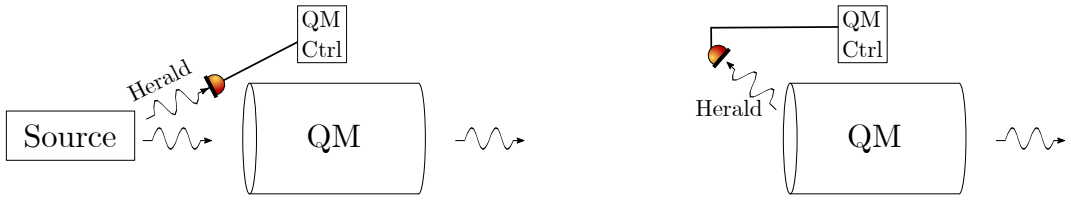

Figure 1.4: **Types of single-photon quantum memories. Left:** Absorptive memory. This type of memory absorbs a heralded photon from an external source and releases it on demand. **Right:** Emissive memory. This system combines source and memory. The memory is loaded by detection of a heralding photon and releases the stored photon on demand.

system. The source-memory system investigated in the present thesis is based on the DLCZ protocol described above and falls into the category of emissive memories.

Optical quantum memory systems range from all-optical systems like optical cavities (Makino *et al.*, 2016) and switchable free-space loops (Bouillard *et al.*, 2019; Kaneda and Kwiat, 2019; Pang *et al.*, 2020) to matter systems like single atoms (Specht *et al.*, 2011) or ions (Wang *et al.*, 2017), solid-state single spins (Kalb *et al.*, 2017) or spin ensembles (Saglamyurek *et al.*, 2011; Zhong *et al.*, 2017; Kutluer *et al.*, 2017; Laplane *et al.*, 2017), phononic modes (England *et al.*, 2015; Riedinger *et al.*, 2016; Wallucks *et al.*, 2020) and atomic ensembles (Duan *et al.*, 2001).

1.5 Atomic vapour cells

Vapour cells are an attractive platform for many sensing technologies – such as clocks (Knappkiewicz, 2018), magnetometers (Jensen *et al.*, 2018; Boto *et al.*, 2018), electrometers (Sedlacek *et al.*, 2012) and gyroscopes (Fang and Qin, 2012) – because of their high precision and sensitivity. More specifically, the vapour cell platform has shown high performance while still being a relatively simple system in terms of fabrication and miniaturization.

When it comes to quantum information, vapour cells have already been shown to have potential as a number of core building blocks such as non-classical light sources. Examples are spontaneous four-wave mixing (Jeong *et al.*, 2017; Mika and Slodička, 2020; Wasilewski *et al.*, 2009), Rydberg-blocked four-wave mixing (Ripka *et al.*, 2018), and spontaneous Raman scattering (Eisaman *et al.*, 2005). Also single-photon detector application has been proposed (Matekole *et al.*, 2018).

The use of atomic vapours for quantum memories have been immensely studied since the first demonstrations for continuous-variable states (van der Wal *et al.*, 2003; Julsgaard *et al.*, 2004a). Single-photon memory protocols include photon echo (Hosseini *et al.*, 2011), electromagnetically induced transparency (EIT, Katz and Firstenberg, 2018), Rydberg polaritons

(Ripka *et al.*, 2016), and far-off Raman scattering (Reim *et al.*, 2011). Particularly, far-off Raman memories in a ladder configuration (Finkelstein *et al.*, 2018; Kaczmarek *et al.*, 2018) have shown promising performance in terms of readout noise, speed and time-bandwidth product. In these low-noise schemes a time-bandwidth-efficiency product of more than 12 was reported (Finkelstein *et al.*, 2018).

The far-off Raman memory is attractive because of its GHz bandwidth capability. However, the memory time is limited by atomic motion that move atoms out of the interaction region. Successful mitigation of motional decay has been achieved by the use of buffer gas which renders the atomic motion diffusive and slow due to collisions with the buffer gas. With buffer gas, memory times up to 20 µs have been demonstrated (Namazi *et al.*, 2017) for laser pulses at the few-photon level and up to a few microsecond for non-classical light storage Dou *et al.* (2018).

An alternative to buffer gas is to apply spin-preserving coating on the vapour cell walls. In such cells, the atomic spin state is preserved for thousands of walls collisions. This enables atoms that leave the interaction region to collide with the wall and return to the interaction region and this way the coherent spin interaction time is extended. A spin coherence time in coated cells on the minute timescale has been demonstrated (Balabas *et al.*, 2010). Storage of classical light pulses in coated cells can reach one second (Katz and Firstenberg, 2018) but it remains to be seen if this EIT scheme can operate at sufficiently low readout noise levels to allow high-fidelity single-photon storage. Non-classical light storage on the time scale of millisecond has been demonstrated for continuous-variable states (Jensen *et al.*, 2011).

Furthermore, atomic vapour memories have been used to demonstrate entanglement of atomic ensembles (Julsgaard *et al.*, 2001; Li *et al.*, 2020) and teleportation of continuous-variable states (Sherson *et al.*, 2006; Krauter *et al.*, 2013).

In this thesis we pose the question: Can the long-lived collective spin of coated vapour cells at room-temperature be utilized as a heralded single-photon source with on-demand retrieval? We give a positive answer to the question by experimentally demonstrating a scheme where this is possible and investigate the limitations of the scheme from intrinsic atomic noise.

This result prolongs the achievable single-photon storage time in room-temperature atomic vapours and room-temperature systems in general by two orders of magnitude over previous demonstrations. While our work show that there are still challenges to overcome for our source-memory system, there is potential that the scheme can find application in QR networks where the long storage time is a requirement.

Chapter 2

Single-photon interface in atomic ensembles

This chapter introduces the relevant theoretical framework that describes systems where the DLCZ protocol can be realized. The purpose of the chapter is to equip the reader with an understanding of the dynamics – and the theoretical description of said dynamics – involved in single-photon generation in warm atomic ensembles. The focus of the thesis is the experimental results and we shall therefore not reprint involved derivations which have already been given elsewhere.

The structure of the chapter follows a thread where general results will be introduced and gradually specialized to the present implementation. We will start from the general Hamiltonians for single-excitation generation and retrieval, introduce the caesium atom and the interaction with an ensemble of caesium. We will then discuss how the interaction is enhanced by an optical cavity and introduce the specific implementation of the thesis. The chapter concludes with an introduction to non-classicality measures that will be the fulcrum of the experimental results.

2.1 Generic single-photon herald-retrieve scheme

The DLCZ protocol relies on two processes which can be described in generic terms. The first step in the protocol is the write process which entangles an atomic spin mode with an optical mode. Upon detection of a photon, a single spin excitation is heralded. The second step is the read process. Here the state of the atomic spin mode is mapped onto a light mode. We shall here discuss the basic properties of the generic processes before proceeding to discuss how it is realized in atomic systems.

The generic process for generating single-photons in the DLCZ protocol is known as two-mode squeezing. It is the basis for many types of probabilistic single-photon generation schemes, e.g. spontaneous parametric downconversion. The process is described by the

Figure 2.1: **Generic interaction types involved in the DLCZ scheme. Left:** The parametric gain interaction generates excitation pairs in the modes $\hat{a}$ and $\hat{b}$. The output state is the two-mode squeezed state. **Right:** The beam splitter interaction maps the input state in $\hat{a}$ to the output state in $\hat{b}$ and vice versa.

parametric-gain Hamiltonian

$$\hat{H}_{\mathrm{PG}} = \hbar\xi\hat{a}^\dagger\hat{b}^\dagger + \mathrm{h.c.} \tag{2.1}$$

Assuming both modes $\hat{a}, \hat{b}$ to be empty at $t = 0$, the interaction produces the state (Sangouard *et al.*, 2011)

$$|\psi_{\mathrm{TMSS}}\rangle = \sqrt{1-p_0}\sum_n (-i)^n p_0^{n/2} \,|n\rangle_a \,|n\rangle_b \,, \tag{2.2}$$

$$p_0 = \tanh^2 \xi t. \tag{2.3}$$

This is a two-mode squeezed state where the photon number in the two modes is correlated. The interaction is illustrated in Fig. 2.1. Therefore the common strategy is to use detection of one mode to herald the state in the other mode. For the state in eq. (2.2) the probability to find n excitations is simply

$$p_n = (1-p_0)p_0^n. \tag{2.4}$$

This is often referred to as the geometric distribution or in the context of quantum mechanics as the thermal distribution because it describes the bosonic statistics for a thermal state with $p_0 = e^{-\hbar\omega/k_BT}$ where ω is the mode frequency, k_B is the Boltzmann constant and T is temperature. The mean excitation is $\mu = p_0/(1-p_0)$.

Photon detection schemes are (so far) always limited in number precision either because of limited detection efficiency or the nature of detection. The latter because most single-photon detectors operate in a sense of Geiger mode where one event renders the detector blind to sequential photons. That prohibits efficient distinction between one-photon states and multi-photon states. Therefore p_0 is always kept very low, $\sim 1\%$, to avoid heralding multiple excitations. The dependency on p_0 will be discussed in more detail in section 2.7. In the DLCZ scheme $\hat{a}$ describes a scattering light field while $\hat{b}$ describes an atomic spin mode.

The generic process for retrieving the spin mode state is the beam splitter interaction. The process is described by the Hamiltonian

$$\hat{H}_{\mathrm{BS}} = \hbar\chi\hat{a}^\dagger\hat{b} + \mathrm{h.c.} \tag{2.5}$$

The beam-splitter Hamiltonian leads to coherent mapping between the two modes with the Heisenberg equations of motion

$$\begin{aligned}\frac{\partial}{\partial t}\hat{a} &= -i[\hat{a}, \hat{H}/\hbar] = -i\chi b(t),\\ \frac{\partial}{\partial t}\hat{b} &= -i[\hat{b}, \hat{H}/\hbar] = -i\chi a(t),\end{aligned} \tag{2.6}$$

and the solution (for χ real)

$$\begin{pmatrix}\hat{a}(t)\\ \hat{b}(t)\end{pmatrix} = \begin{pmatrix}\cos(\chi t) & -i\sin(\chi t)\\ -i\sin(\chi t) & \cos(\chi t)\end{pmatrix}\begin{pmatrix}\hat{a}(0)\\ \hat{b}(0)\end{pmatrix}. \tag{2.7}$$

In principle the beam splitter interaction can lead to direct exchange of the of the two states, $\hat{a} \to -i\hat{b}$, $\hat{b} \to -i\hat{a}$ as illustrated in Fig. 2.1. For strong coupling between the two modes mode, the coupling χt will have to be calibrated to achieve complete exchange.

Often, the exchanged energy leaves the interaction region faster than the exchange rate. This means that the exchange energy does not transfer back to the occupied mode $\hat{b}$. To capture these dynamics we will have to treat the interaction in an open system where energy is exchanged with the surroundings. We introduce the open system by adding decay to the equation of motion in eq. (2.6)

$$\frac{\partial}{\partial t}\hat{a} = -\frac{\kappa}{2}\hat{a}(t) + \hat{F}(t) - i\chi\hat{b}(t). \tag{2.8}$$

Together with the energy decay rate κ we have introduced the Langevin noise operator $\hat{F}(t)$. Eq. (2.8) has the solution

$$\hat{a}(t) = e^{-\kappa t/2}\hat{a}(0) + \int_0^t dt' e^{-\kappa(t-t')/2}\left[\hat{F}(t') - i\chi\hat{b}(t')\right]. \tag{2.9}$$

Assuming that the decay is faster than the internal dynamics this reduces to

$$\hat{a}(t) = e^{-\kappa t/2}\hat{a}(0) + \frac{2}{\kappa}\left[\hat{F}(t) - i\chi\hat{b}(t)\right]. \tag{2.10}$$

From eq. (2.6) we still have $\dfrac{\partial}{\partial t}\hat{b} = -i\chi^*\hat{a}(t)$, thus

$$\frac{i}{\chi^*}\frac{\partial}{\partial t}\hat{b} = e^{-\kappa t/2}\hat{a}(0) + \frac{2}{\kappa}\left[F(t) - i\chi\hat{b}(t)\right]. \tag{2.11}$$

Assuming the optical mode to be initially empty $\left\langle a^\dagger a\right\rangle(t=0) = 0$ and the Langevin noise to be vacuum noise $\left\langle F^\dagger F\right\rangle(t) = 0$, we get

$$\left\langle \hat{b}^\dagger\hat{b}\right\rangle(t) = \left\langle \hat{b}^\dagger\hat{b}\right\rangle(t=0)e^{-\frac{4|\chi|^2}{\kappa}t}. \tag{2.12}$$

If the decay of the optical mode is collected into a single detection mode (e.g. a cavity output mode), it is beneficial to introduce the output flux operator

$$\hat{a}_{\mathrm{out}}(t) = \sqrt{\kappa}\ \hat{a}(t), \tag{2.13}$$

such that $\left\langle \hat{a}^\dagger_{\mathrm{out}}\hat{a}_{\mathrm{out}} \right\rangle (t)$ describes the photon flux in the output mode (e.g. in front of a detector). Combining eqs. (2.10), (2.12) and (2.13), we find the outgoing flux

$$\left\langle \hat{a}^\dagger_{\mathrm{out}}\hat{a}_{\mathrm{out}} \right\rangle (t) = \kappa \left\langle \hat{a}^\dagger\hat{a} \right\rangle (t) = \frac{4|\chi|^2}{\kappa} \left\langle \hat{b}^\dagger\hat{b} \right\rangle (t). \tag{2.14}$$

For verification we see that $\left\langle \hat{a}^\dagger_{\mathrm{out}}\hat{a}_{\mathrm{out}} \right\rangle (t) = -\partial/\partial t \left\langle \hat{b}^\dagger\hat{b} \right\rangle$. Evidently, the energy in $\hat{b}$ will transfer slowly to $\hat{a}_{\mathrm{out}}$ with the exponential readout shape that is often observed in atomic memories.

We note that the beam-splitter interaction can also be used to map an input light state onto an initially empty atomic mode. In this example the input state would enter through the input operator $\hat{F}(t) = \sqrt{\kappa}/2\ \hat{a}_{\mathrm{in}}(t)$. The beam-splitter interaction is therefore the generic interaction describing a quantum memory. We shall now proceed to review how the parametric-gain and beam-splitter Hamiltonians can be realized in the interaction of light and atomic ensembles.

2.2 The caesium atom

The present study investigates how to generate and store single photons using the light-matter interaction in an atomic caesium vapour. In this section we shall introduce the caesium atom and the dipole interaction with light.

More specifically, the vapour consists of ^{133}Cs, the only stable isotope. The caesium atom has a single valence electron which in the ground state occupies the $6S_{1/2}$ orbital. With electron spin $S = 1/2$ and nuclear spin $I = 7/2$, the ground state is split into two hyperfine manifolds with spin numbers $F = I \pm S = \{3, 4\}$.

In this study we shall only concern ourselves with the excitation to the first excited states, i.e. the $6P$ orbital with orbital angular momentum $L = 1$. Due to spin-orbit coupling the $6P$ orbital is split into two levels with electron angular momentum $J = L \pm S = \{1/2, 3/2\}$. The transition $6S_{1/2} \rightarrow 6P_{1/2}$ at wavelength $\lambda = 894.6\,\mathrm{nm}$ is referred to as the D_1 line while the transition $6S_{1/2} \rightarrow 6P_{3/2}$ at wavelength $\lambda = 852.3\,\mathrm{nm}$ is referred to as the D_2 line. Fig. 2.2 illustrates the caesium level structure including the hyperfine splitting of the excited states.

When applying an external DC magnetic field, the hyperfine manifolds split into $2F + 1$ magnetic sublevels. To first order the energy shift is given by the Zeeman effect as

$$\Delta E_{\mathrm{B}} = \mu_{\mathrm{B}} g_F m_F B, \tag{2.15}$$

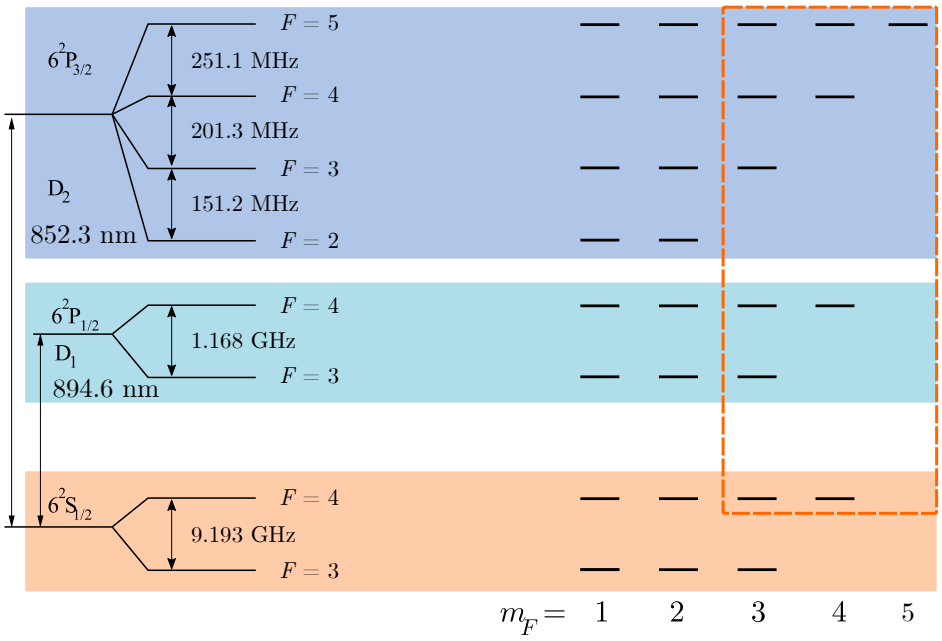

Figure 2.2: **Caesium level structure.** The transition $6S_{1/2} \rightarrow 6P_{1/2}$ is referred to as the D_1 line while the transition $6S_{1/2} \rightarrow 6P_{3/2}$ is referred to as the D_2 line. On the left the hyperfine splitting is illustrated. On the right a subset of the level degeneracy with spin projection m_F is illustrated. The degeneracy can be lifted by applying a magnetic field. The orange box highlights the atomic states that will be considered in the thesis. Figure adapted from Julsgaard (2003).

where μ_B is the Bohr magneton and g_F is the Landé g-factor for the F manifold. The quantum number m_F describes the spin projection onto the orientation of the magnetic field with magnitude B. The external magnetic field thus splits the hyperfine manifolds into equidistant magnetic sublevels. The splitting is often described in terms of the Larmor precession frequency $\nu_L = \mu_B g_F B/h$. For the caesium ground state $F = 4$ manifold the Larmor frequency is 0.35 MHz/G. In section 3.3.2 we shall discuss the quadratic correction to eq. (2.15).

Dipole interaction

The entry point for light-atom interaction is the dipole interaction. It describes the coupling of an AC electric field and atomic dipole formed by the valence electron and the (screened) nucleus. The dipole interaction is described by the Hamiltonian

$$\hat{H}_{\text{int}} = -\hat{\vec{D}} \cdot \vec{E} = -e\hat{\vec{r}} \cdot \vec{\epsilon} E, \tag{2.16}$$

with $\hat{\vec{r}}$ being the position operator, $\vec{\epsilon}$ being the unit vector of the field polarization and the dipole operator described in terms of the atomic states

$$\hat{\vec{D}} = \sum_{\substack{F,m_F \\ F',m'_F}} D_{F,m_F}^{F',m'_F} \vec{\epsilon}_{\Delta m_F} \left|F', m'_F\right\rangle \left\langle F, m_F\right|, \tag{2.17}$$

such that the interaction can be described by transition matrix elements

$$D_{F,m_F}^{F',m'_F} = e \left\langle F', m'_F\right| \vec{\epsilon}_{\Delta m_F} \cdot \hat{\vec{r}} |F, m_F\rangle, \tag{2.18}$$

between ground states $|F, m_F\rangle$ and excited states $|F', m'_F\rangle$. The non-zero matrix elements have specific electric field polarization $\vec{\epsilon}_{\Delta m_F}$. For $\Delta m_F = m'_F - m_F = 0$ the coupling polarization is π (i.e. linearly polarized along the quantization axis). For $\Delta m_F = +1$ (-1) the coupling polarization is σ_+ (σ_-), i.e. right-hand (left-hand) circularly polarized in the plane perpendicular to the quantization axis.

The electric field can be written as a sum of positive and negative frequency components

$$E(t) = \frac{1}{2}\mathcal{E}e^{-i\omega t} + \text{h.c.} \tag{2.19}$$

Inserting eq. (2.19) into eq. (2.16) and assuming the electric field to be in the transition polarization, we reach the usual interaction Hamiltonian for a two-level system in the rotating-wave approximation

$$\hat{H}_{\text{int}} = -\frac{\hbar\Omega}{2}\hat{\sigma}_{e,g}e^{-i\omega t} + \text{h.c.} \tag{2.20}$$

expressed in terms of the Rabi frequency $\Omega = \mathcal{E}D_{ge}/\hbar$ and the density matrix element $\hat{\sigma}_{e,g} = |g\rangle\langle e|$. Note that D_{ge} is short-hand notation for the dipole matrix element connecting the ground state $|g\rangle$ and excited state $|e\rangle$.

2.3 Ensemble interaction

In the caesium vapour the light interacts with the whole ensemble of caesium atoms. We shall therefore describe a framework for treating the ensemble interaction. The first step is to introduce collective operators to replace the single atom counterparts. We follow the derivation given in Hammerer *et al.* (2010). For simplicity we consider atoms with only two ground states, $|g\rangle$ and $|s\rangle$. The single atom density matrix operators of interest are

$$\text{Spin projection operator: } \hat{j}_x = \frac{1}{2}(|g\rangle\langle g| - |s\rangle\langle s|). \tag{2.21}$$

$$\text{Spin raising operator: } \hat{j}_+ = |g\rangle\langle s|. \tag{2.22}$$

Note that $\hat{j}_+$ raises the spin because we use the convention where $|g\rangle$ is the positive projection onto $\hat{j}_x$ (see Fig. 2.3). For the caesium experiments in this thesis, we will use $|g\rangle = |F = 4, m_F = 4\rangle$ and $|s\rangle = |F = 4, m_F = 3\rangle$ such that the energy splitting is $h\nu_{\text{L}}$.

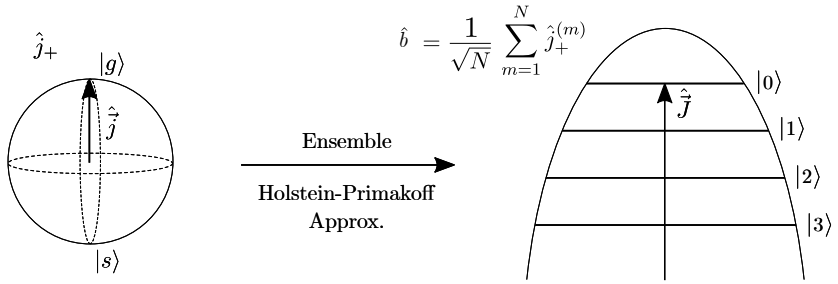

Figure 2.3: **Spin-ensemble modes.** When interacting with an ensemble of spins, the single atom spin – here modelled as a spin 1/2 atom – is replaced by a set of harmonic macroscopic-spin oscillator modes in the Holstein-Primakoff approximation.

We introduce the ensemble spin operators as the sum over individual atom operators:

$$\text{Macroscopic spin projection operator: } \hat{J}_x = \sum_{m=1}^{N} \hat{j}_x^{(m)}. \tag{2.23}$$

$$\text{Macroscopic spin raising operator: } \hat{J}_+ = \sum_{m=1}^{N} \hat{j}_+^{(m)}. \tag{2.24}$$

We are interested in the situation where all atoms are initialized in the state $|g\rangle$ and study weak perturbations (single excitations). For this reason we apply the Holstein-Primakoff approximation such that the spin ensemble becomes an effective harmonic oscillator (Hammerer *et al.*, 2010) where the oscillator frequency is given by the Larmor frequency. We approximate $\hat{J}_x \approx \langle J_x \rangle = N/2$ with its expectation value. Under this approximation the collective canonical annihilation operator then becomes

$$\hat{b} = \frac{\hat{J}_+}{\sqrt{2\langle J_x \rangle}} = \frac{\hat{J}_+}{\sqrt{N}}. \tag{2.25}$$

In the case where the macroscopic spin is initialized parallel to the magnetic field, the macroscopic-spin oscillator becomes a 'negative-mass' oscillator because excitations remove energy from the system, see Fig. 2.3.

Atomic modes

In the definitions above we have only used symmetric collective operators where all atoms contribute identically. Such operators can only describe symmetric superposition states like the single-excitation state

$$\hat{b}^\dagger |gg...g\rangle = \frac{1}{\sqrt{N}} \sum_{m=1}^{N} |gg...s_m...g\rangle . \tag{2.26}$$

However, we can also imagine localized (asymmetric) excitations where some atoms, or more conveniently, some volume of the ensemble is excited. To include asymmetric modes we introduce a normalized set of spatial mode functions $u_n(\vec{r})$ and construct mode-specific annihilation operators

$$\hat{b}_n = \int \mathrm{d}^3\vec{r}\; u_n^*(\vec{r})\hat{b}(\vec{r}), \tag{2.27}$$

$$\hat{b}(\vec{r}) = \frac{\hat{j}_+(\vec{r})}{\sqrt{2\left\langle \hat{j}_x(\vec{r})\right\rangle}}, \tag{2.28}$$

with the commutator relation $[\hat{b}(\vec{r}), \hat{b}^\dagger(\vec{r}')] \approx \delta(\vec{r}-\vec{r}')$ (Hammerer *et al.*, 2010). The last line introduces the position dependent atomic annihilation operator $\hat{j}_+(\vec{r}) = \sum_m \delta(\vec{r}-\vec{r_m})\hat{j}_+^{(m)}$. Using the mode-specific operators we can describe asymmetric modes of the form

$$\hat{b}_n^\dagger \left|gg...g\right\rangle = \sum_{m=1}^{N} c_n(\vec{r}_m)\left|gg...s_m...g\right\rangle. \tag{2.29}$$

In a thermal vapour, atoms will quickly redistribute inside the ensemble volume due to their thermal motion. This means that the spin decay in a specific spatial mode will not only depend on the single atom decay mechanisms (e.g. wall collisions) but also on thermal diffusion. The dynamics of collective spin states were studied theoretically by Shaham *et al.* (2020). The authors find that the spin decay can be described in a basis of spatial diffusion eigenmodes with mode-specific decay rates. For anti-relaxation-coated cells where atoms can undergo a high number of wall collisions before depolarising, the slowest decay rate is specific to the symmetric mode in eq. (2.25). For this mode there is no decay associated with diffusion whereas the decay rate for higher-order modes will be dominated by diffusion and thus much faster as we shall treat in section 2.6.

2.3.1 Parametric-gain interaction

We now consider the dipole interaction with a classical laser field Ω and quantized field $\hat{a}$ with single-photon Rabi frequency g in a Λ configuration as depicted in Fig. 2.4 (left). For far-detuned light, i.e. $\Omega \ll \Delta$, the interaction leads to spontaneous Raman scattering where the two ground states are coherently coupled via the dipole coupling to a virtual excited state level. In this case the excited state can be adiabatically eliminated and the effective ground state coupling is described by the single-atom Hamiltonian (Hammerer *et al.*, 2010)

$$\hat{H}'_{\mathrm{int}} = -\frac{\hbar|\Omega(t)|^2}{4\Delta}\left|g\right\rangle\!\left\langle g\right| - \frac{\hbar|g|^2}{\Delta}\hat{a}^\dagger\hat{a}\left|s\right\rangle\!\left\langle s\right| - \left(\frac{\hbar\Omega(t)g^*}{2\Delta}\hat{a}^\dagger\hat{j}_- + \mathrm{h.c.}\right) \tag{2.30}$$

Note that when multiple excited states are present, the parameters including dipole matrix elements (g, Ω) should be summed over the excited states, e.g. $|g|^2/\Delta \to \sum_{F'}|g|^2_{F'}/\Delta_{F'}$.

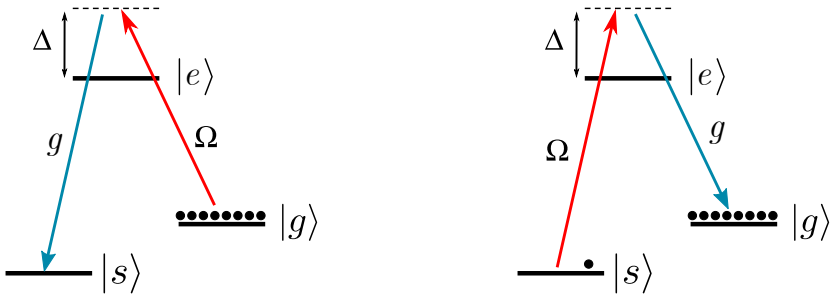

Figure 2.4: **Λ configurations for the ensemble interaction schemes. Left:** Parametric-gain configuration. The laser field Ω couples the populated $|g\rangle$ state to $|e\rangle$ which is coupled to $|s\rangle$ with the coupling rate g. **Right:** Beam-splitter configuration. The laser field Ω couples the storage state $|s\rangle$ to the excited state $|e\rangle$ which is coupled to the populated ground state $|g\rangle$ with the coupling rate g.

We now change the mode functions in eq. (2.27) to only describe transverse modes in order to make the ensemble Hamiltonian 1-dimensional.

$$\hat{b}_n(z) = \int \mathrm{d}^2\vec{r}_\perp \; u_n^*(\vec{r})\hat{b}(\vec{r}). \tag{2.31}$$

For the ensemble interaction we consider light modes $\hat{a}_m$ defined similar to eq. (2.27). Hammerer *et al.* (2010) reaches the following ensemble interaction Hamiltonian for the write step Λ configuration

$$\begin{aligned}\hat{H}_\mathrm{W} =& \hbar \int_0^L \mathrm{d}z \left[\frac{|\Omega(z,t)|^2}{4\Delta} \sum_m \hat{b}_m^\dagger(z)\hat{b}_m(z) \right. \\ & \left. - \left(\frac{g^*(z)\Omega(z,t)}{2\Delta} e^{i\Delta k z} \sum_m \hat{a}_m^\dagger(z)\hat{b}_m^\dagger(z) + \mathrm{h.c.} \right) \right].\end{aligned} \tag{2.32}$$

Note that here z is the propagation direction of light and Ω is assumed to have a transverse flat profile. The first term is the AC Stark shift that shifts the energy of the atomic modes and the second term describes the parametric-gain interaction that we recognize from eq. (2.1). In eq. (2.32), g is no longer the single-photon Rabi frequency but the coupling constant between the bosonic modes $\hat{a}_m$ and $\hat{b}_m$ and will be discussed below. The phase $e^{i\Delta k z}$ in the last term describes the spin wave arising from an energy difference between $|g\rangle$ and $|s\rangle$. The effect of this spin wave will be discussed in section 2.4.

Atomic mode selection

According to eq. (2.32) the light mode $\hat{a}_m$ couples to the atomic mode $\hat{b}_m$ only. Hence, if the detection happens in light mode m, the heralded atomic state will be in atomic mode m. In the limit of very low excitation probability, the write process becomes a small perturbation to the light and atomic modes. Hence, the variation along z is negligible and we can remove

the dependency. Probabilistic generation of a single collective excitation therefore happens in the atomic mode which is flat along z (Gorshkov *et al.*, 2007b; Hammerer *et al.*, 2010). Since laser light profiles are typically Gaussian and atomic diffusion eigenmodes depend on the cell geometry but are generally not Gaussian (Shaham *et al.*, 2020), the light will couple to different diffusion eigenmodes. If the laser pulse is sufficiently weak and have long duration, only atomic modes with slow decay rates will interact coherently. For higher-order modes the diffusion-dominated decoherence rate will be faster than the coupling rate. This opens a path for efficient interaction with the symmetric mode. We refer to this mechanism as *motional averaging*. It is enabled by light pulses that are long enough that the atoms will pass through the beam many times. We shall return to this for a quantitative description in section 2.6.

For experiments with continuous-variable quantum states the long optical mode can be selected through homodyne detection by having the quantum signal at a specific sideband frequency. In our group we have extensive experience in this (Julsgaard *et al.*, 2001, 2004b; Sherson *et al.*, 2006; Wasilewski *et al.*, 2009; Jensen *et al.*, 2011; Krauter *et al.*, 2011; Vasilakis *et al.*, 2015). However, discrete-variable quantum states are measured through photon counting. Photon-counting detectors are in their nature extremely broadband, selecting an (almost) instantaneous mode. This establishes a one-to-one correspondence between the atoms inside the beam and the light at the detector when it clicks. As such the detection event becomes a snap shot of the atomic positions and carries "which-atom" information. A single-photon detection event thus collapses the collective state into an asymmetric atomic mode thereby cancelling the motional averaging. In section 2.6 we will discuss the remedy to sustain motional averaging in photon detection which is the experimental novelty of the thesis.

Another difference between homodyne and photon detection is that the former establishes a deterministic interface because the measurement outcome is always valid. Protocols relying on homodyne detection do not need to condition on a specific measurement outcome for the protocol to be successful. This is for instance the case in continuous-variable teleportation (Krauter *et al.*, 2013) where any measurement outcome can be used to generate the feedback signal that completes the teleportation protocol. In photon detection, on the other hand, if the measurement outcome is 'vacuum' (no click), the protocol fails. This also means that photon detection is not as sensitive to photon loss because the vacuum outcome can be sorted out. Hence photon detection has built-in purification. E.g. in the DLCZ scheme, the photon detection heralds and purifies the single excitation state and is (ideally) independent of photon loss. Photon loss only decreases success rate. Similarly, for entanglement generation between two ensembles in the DLCZ quantum-repeater protocol, the photon detection purifies the entanglement.

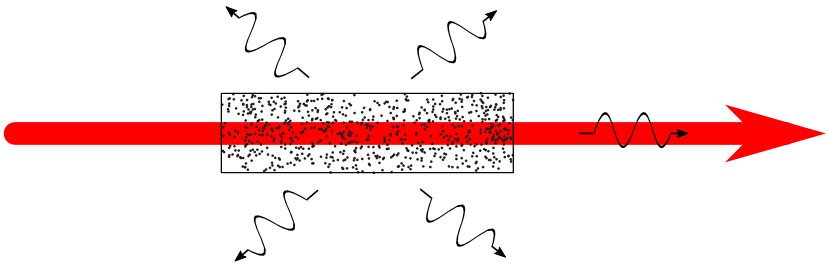

Figure 2.5: **Collective enhancement.** The spontaneous Raman scattering into the target mode – here taken as the forward-propagating mode – is coupled to the excitation of the atomic storage mode (e.g. the symmetric mode). The scattering rate is collectively enhanced and scales with number of atoms N. Undetected spontaneous emission in other directions also scale with N but spreads excitation over all N atomic modes. Hence the excitation of the target mode from spontaneous emission is independent of N.

Collective Enhancement

Another aspect of ensemble interaction is the phenomenon known as collective enhancement. The atom-light coupling constant in eq. (2.32) is $g(z) = D_{se}\sqrt{2\pi\omega\rho(z)/c}$ where c is the speed of light, ω is the frequency of the transition $|s\rangle \rightarrow |e\rangle$ and $\rho(z)$ is the atomic density at position z (Hammerer *et al.*, 2010). In a vapour cell we can assume the density to be uniform, i.e. $\rho = N/V$. From this it is evident that the scaling with the number of atoms in the ensemble is then $g \propto \sqrt{N}$. Thus, the scattering rate is proportional to N. This feature originates from the result that all atoms interact coherently with the same light mode and highlights the strength over single-atom schemes. Similar enhancement can be achieved in the single atom case through the Purcell enhancement in a small-volume, high-finesse cavity. The downside is that it requires a sophisticated setup for creating the cavity and keeping the atom in the cavity mode. It also highlights why a large optical depth (many atoms) is preferable.

Besides the coherent interaction described by the Hamiltonian in eq. (2.32), the atoms will spontaneously emit into other directions. This process will also transfer atoms to $|s\rangle$. The spontaneous emission rate is proportional to the number of atoms N of the ensemble but the atomic excitation from the spontaneous emission will distribute evenly over all N atomic modes. Hence, the incoherent excitation of the symmetric mode of interest does not scale with N (Duan *et al.*, 2001). It is therefore only the coherent interaction that is collectively enhanced. See Fig. 2.5 for an illustration.

2.3.2 Beam-splitter interaction

A change in the Λ configuration (see Fig. 2.4, right) realises the beam-splitter interaction. Now the laser light couples to the weakly occupied storage state which causes a Raman transition to the ground state by releasing a photon on the $|e\rangle \rightarrow |g\rangle$ transition.

Because the photon scattering in this configuration is associated with an atomic transition in the opposite direction compared to the parametric-gain interaction, the Hamiltonian can be obtained through replacement $\hat{b}_m \leftrightarrow \hat{b}_m^\dagger$ in the light-atom coupling term (Hammerer *et al.*, 2010). Tn this configuration the AC Stark effect shifts $|s\rangle$ and not $|g\rangle$, thus we also have to change the sign of the first term. This yields

$$\begin{aligned}\hat{H}_{\mathrm{R}} =&\hbar \int_0^L \mathrm{d}z \left[\frac{-|\Omega(z,t)|^2}{4\Delta} \sum_m \hat{b}_m^\dagger(z)\hat{b}_m(z) \right. \\ &\left. - \left(\frac{g^*(z)\Omega(z,t)}{2\Delta} e^{i\Delta kz} \sum_m \hat{a}_m^\dagger(z)\hat{b}_m(z) + \mathrm{h.c.} \right) \right], \end{aligned} \tag{2.33}$$

where we have omitted a refractive index term on the quantized transition $\hat{a}_m$. We recognize the last term in eq. (2.33) as the beam-splitter type in eq. (2.5) that exchanges states between atomic and light modes of same mode number m. We note that this type of interaction can be realized both off resonance as described by eq. (2.33) as well as on resonance. The latter is achieved by employing electromagnetically-induced transparency (EIT). Though the two types of interaction are different in their nature, the storage performance is characterized by the same limits (Gorshkov *et al.*, 2007a).

2.4 Spin wave

The atomic spin modes are often referred to as spin waves (or spin gradients) because the spin mode is excited with a wave-like pattern $e^{i\Delta kz}$ in front of the interaction term in eq. (2.32) and eq. (2.33). During the write step, the pattern is generated from the frequency difference between the laser light and the scattered field. Experimentally, we set the frequency by applying a bias magnetic field transverse to the light propagation direction. Since scattering can happen into any direction, the difference in wave vector is imprinted on the spin phase $e^{i\Delta\vec{k}\cdot\vec{r}}$. However, since only the *difference* is imprinted, one can choose to use a different laser mode when reading out, e.g. backwards propagation. This leads to the phase-matching condition

$$\Delta\vec{k} = \vec{k}_{W,\Omega} - \vec{k}_{W,\hat{a}} = \vec{k}_{R,\hat{a}} - \vec{k}_{R,\Omega}, \tag{2.34}$$

where subscripts W, R refer to the write and read steps, respectively, and $\hat{a}, \Omega$ to quantum and laser fields, respectively. The reversed order between laser and quantum field in the two cases is because of the $\hat{b}_m \leftrightarrow \hat{b}_m^\dagger$ transformation.

The phase-matching condition becomes particularly important when not employing a collinear configuration where the laser and quantum field propagation directions overlap. In this case the phase-matching condition determines the wavevector for the readout quantum field. For cold atoms, a non-collinear configuration is often applied because the spatial separation of laser and quantum fields relaxes the need for filtering. In warm vapours a non-collinear

configuration is problematic. It only takes a very small angle to make the spin-wave wavevector $\Delta\vec{k}$ much longer (the typical frequency difference is of order GHz). A long wavevector means that the atomic motion in warm vapours quickly dephases the spin wave which reduces the retrieval efficiency. Even for cold atomic ensembles, spin wave dephasing sets the limit on storage time when not employing the collinear configuration. In the collinear configuration Zhao *et al.* (2009) demonstrated 1 ms storage time and claimed that the upper limit is 3 ms, set by the free fall of atoms. The same group later demonstrated free-fall-limited storage time (Bao *et al.*, 2012). By using optical lattices it was later demonstrated that the memory time can be extended to near second (Radnaev *et al.*, 2010; Li *et al.*, 2013; Yang *et al.*, 2016).

If one aims to achieve long time storage in warm vapours, one is restricted to the collinear configuration. Furthermore, using hyperfine storage can be problematic. Borregaard *et al.* (2016) show from simulations that for hyperfine storage in room-temperature caesium (9.2 GHz splitting), the spin-wave wavelength (~ 3 cm) starts to limit efficiency if the cell length is more than 1 cm in a cell without buffer gas.

Another property of the collective atomic modes is that they are excited by atoms incoherently occupying the storage state $|s\rangle$. These excitations then cause uncorrelated readout noise. Mewes and Fleischhauer (2005) treat the case where some atoms occupy the storage state due to a coupling to a thermal reservoir (e.g. imperfect initialization or atomic decay due to cell wall collisions). They find the excitation of a specific atomic mode (e.g. the symmetric mode) to be

$$\left\langle \hat{b}^\dagger \hat{b} \right\rangle = \frac{1}{N} \sum_{m=1}^{N} \left\langle \sigma_{ss}^{(m)} \right\rangle , \tag{2.35}$$

where $\langle \sigma_{ss} \rangle = M/N$ is the fractional occupation of $|s\rangle$ for the individual atom (set by the reservoir temperature). From eq. (2.35) it is evident that the collective mode excitation is $\left\langle \hat{b}^\dagger \hat{b} \right\rangle = M/N$. In other words, the distribution of incoherent atoms in $|s\rangle$ with maximal entropy is the one where excitation is spread uniformly over all atomic modes. The small overlap with the symmetric mode demonstrates that the initial preparation requirement is not the absolute occupation $M \ll 1$ but instead fractional occupation $M/N \ll 1$ which is a much more relaxed requirement.

During the storage time, incoherent transfer between $|g\rangle$ and $|s\rangle$ as well as loss of atoms into other states (e.g. into the other hyperfine manifold) dephases the spin wave. Mewes and Fleischhauer (2005) have shown that even though the collective state is an entangled state of atoms, it is robust to both incoherent transfer (spin flips) and loss of atoms. The loss of fidelity scales as $1/N$ per atom transferred or lost whereas the transfer or loss processes are individual to the atom. Thus the rate of atoms transferred or lost scales as N. This makes the spin wave decay rate independent on the number of atoms. This is in strong contrast to the GHZ state in eq. (1.5) where the decoherence of one particle destroys all entanglement.

On top of this, pure dephasing mechanisms, e.g. magnetic inhomogeneity, also contribute to the spin-wave dephasing.

The spin-wave dephasing will reduce the efficiency of readout as a function of storage time. For the symmetric mode, the dephasing follows the decay of the transverse macroscopic spin component which we shall assume to follow a single exponential decay $\langle J_{yz}(t)\rangle = \langle J_{yz}(0)\rangle\, e^{-t/T_2}$. As we shall see in chapter 3, this assumption agrees well with experimental observation. In terms of energy (number of photons retrieved) the retrieval efficiency will drop at twice the rate since $\left\langle \hat{b}^\dagger \hat{b} \right\rangle \propto \left\langle \hat{J}_- \hat{J}_+ \right\rangle$.

2.5 Cavity Enhancement

There exist several schemes for storing and retrieving light from atomic ensembles as we pointed out in chapter 1. However, it has been shown that despite their seemingly strong differences, the limits to performance are exactly the same. In a series of papers Gorshkov *et al.* (2007a,b,c) presented a general theoretical treatment of the light-atom interaction and demonstrated that the variety of schemes share the same figure of merit which is optical depth d. Mainly the storage and retrieval inefficiencies are governed by d and scale as either $1/\sqrt{d}$ or $1/d$ – dependent on the longitudinal atomic mode (Gorshkov *et al.*, 2007b). The inefficiency is $\bar{\eta} = 1 - \eta$ where the efficiency η is the probability that a photon is converted.

Throughout this thesis we shall define the optical depth as the on-resonance optical *intensity* attenuation such that

$$I_{\text{out}} = I_{\text{in}} e^{-d}. \tag{2.36}$$

Furthermore, since we are considering far-off resonance schemes, the effects of Doppler broadening are negligible and the proper optical depth to consider is the hypothetical intensity attenuation on atomic resonance *in the absence* of Doppler broadening (Gorshkov *et al.*, 2007c). The optical depth is specific to an atomic transition and can be expressed in terms of the absorption cross section σ as (Borregaard *et al.*, 2016)

$$d_i = \sigma_i \rho L_z = 3\beta_i \frac{\lambda^2}{2\pi} \rho L_z, \tag{2.37}$$

where ρ is the atomic density, L_z is the sample depth, and $\beta_i \leq 1$ is the branching ratio (Clebsch-Gordan coefficient) from the specific excited state to the specific ground state. An experimental estimation of d is given in chapter 3.

In the current context it is important to note that our experiment aims to interact with the so-called "flat" spin-wave mode where the atomic mode is uniform along z. This is the interaction mode, when the write process is spontaneous Raman scattering. In Gorshkov *et al.* (2007b) it is explicitly found that the retrieval inefficiency from the flat spin-wave mode follows the unfavourable $1/\sqrt{d}$ scaling.

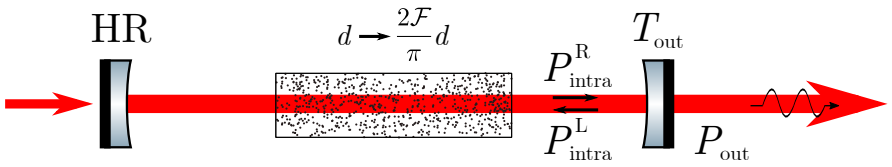

Figure 2.6: **Cavity enhancement.** We place the cell inside a single-sided cavity where the laser input is through the high-reflector mirror (HR) whereas no intracavity light escapes through the HR but through the outcoupling mirror with transmissivity T_{out}. The cavity enhancement is threefold: 1) it enhances the effective optical depth d by the average number of photon round trips. 2) it enables efficient coupling to the flat atomic mode. 3) it enhances the ratio of intracavity laser power to outcoupled laser power, thus reducing the filter requirement.

In the same papers, the authors demonstrate that the atomic interaction is enhanced when placing the atomic ensemble inside an optical cavity. It is found that that the optical depth is enhanced by a factor $\mathcal{F}/\pi$, i.e. the average number of photon round trips in the cavity. Gorshkov *et al.* define the cooperativity $C = d\mathcal{F}/(2\pi)$ where $\mathcal{F}$ is the cavity finesse[1] and find that the inefficiency is given as $1/(1+C)$ for the flat mode being the only cavity interaction mode (Gorshkov *et al.*, 2007a). The enhancement factor was found for a travelling-wave cavity where the light passes the ensemble once per round trip.

In the work of this thesis, we make use of a standing-wave cavity. Tanji-Suzuki *et al.* (2011) treats the case of a standing-wave cavity and finds that the free-space cooperativity $\eta_{\text{fs}} = d/2$ is enhanced by a factor $2\mathcal{F}/\pi$ in a gaseous ensemble. If instead the ensemble is structured to overlap with the antinodes of the cavity mode, the enhancement is $4\mathcal{F}/\pi$. In the case of a gaseous ensemble in a standing-wave cavity the cooperativity is thus

$$C = \frac{d\mathcal{F}}{\pi} \,. \tag{2.38}$$

This matches an intuitive enhancement from passing the cell twice per round trip compared to the travelling-wave cavity.

In terms of retrieval efficiency the cavity thus grants two enhancements: 1) It increases the effective optical depth (the figure of merit for efficiency). 2) It gives a favourable scaling of the inefficiency for the flat mode $\approx 1/C$ instead of $1/\sqrt{d}$. This is the case for both travelling-wave and standing-wave cavities.

Moreover, the cavity grants a third enhancement which is a substantial reduction in the laser power *after* the atomic interaction. Since we will be considering a cavity scheme where both scattered photons and the laser pulse are in the cavity mode, a reduction in the laser power relaxes the required extinction from filters in front of the single-photon detector. We

[1]Please note that Gorshkov *et al.* use a different convention for optical depth. Here the result is written in the convention of the thesis.

can quantify the reduction by considering the ratio of scattered photons to laser photons towards the filter and detector

$$\zeta = \frac{P_{\text{scatt}}\eta_{\text{esc}}}{P_{\text{out}}}, \tag{2.39}$$

where $P_{\text{scatt}} \propto \langle \hat{a}^\dagger \hat{a} \rangle$ is the photon scattering rate and P_{out} is the rate of laser photons at the cavity output. The cavity escape efficiency η_{esc} is the probability that a photon scattered into the cavity mode escapes into the detection mode through the outcoupling mirror. η_{esc} is a function of intracavity losses and will be discussed and estimated in chapter 3. To optimize the escape efficiency we employ a single-sided cavity between two mirrors where the incoupling mirror is highly reflective and the outcoupling mirror is partially reflecting, see Fig. 2.6. In this configuration negligible intracavity light is lost through the incoupling mirror.

We see from eq. (2.32) that the scattering rate depends on g and Ω such that

$$P_{\text{scatt}} \propto |g|^2|\Omega|^2 \propto dP_{\text{intra}}, \tag{2.40}$$

where $P_{\text{intra}} \propto |\Omega|^2$ is the laser power at the atoms (intracavity power). As discussed above, the optical depth is enhanced by $2\mathcal{F}/\pi$ by the cavity.

We can relate the intracavity laser power to the output power by considering the outcoupling mirror transmissivity T_{out} (see Fig. 2.6). In a standing-wave cavity the intracavity power is the sum of the power propagating in the two directions (which we shall here take to be right and left). The two are given by

$$P^{\text{R}}_{\text{intra}} = \frac{P_{\text{out}}}{T_{\text{out}}}, \tag{2.41}$$

$$P^{\text{L}}_{\text{intra}} = (1 - T_{\text{out}})P^{\text{R}}_{\text{intra}}, \tag{2.42}$$

with superscripts R and L referring to right and left propagation. The sum is thus given as

$$P_{\text{intra}} = P^{\text{R}}_{\text{intra}} + P^{\text{L}}_{\text{intra}} = \left(\frac{2}{T_{\text{out}}} - 1\right) P_{\text{out}}. \tag{2.43}$$

In the free-space alternative, $P^{\text{fs}}_{\text{intra}} = P^{\text{fs}}_{\text{out}}/\eta_{\text{win}}$ where η_{win} describe the losses on the cell output window. At the same time the scattered photons are subject to the same losses thus η_{win} drops out. Inserting the cavity enhancement of d and $P_{\text{intra}}/P_{\text{out}}$, we find that the filter ratio improves over the free-space situation by a factor

$$\frac{\zeta_{\text{cav}}}{\zeta_{\text{fs}}} = \frac{2\mathcal{F}}{\pi}\eta_{\text{esc}}\left(\frac{2}{T_{\text{out}}} - 1\right). \tag{2.44}$$

Here the enhancement is given in the three cavity parameters $\mathcal{F}, T_{\text{out}}$ and η_{esc} which we shall characterise in chapter 3. In that chapter we also show how the enhancement can be approximated by the finesse as the only cavity parameter when assuming low intracavity loss.

As a last remark on cavity enhancement we highlight another result from Gorshkov *et al.* The authors find that there is one noticeable difference between quantum memory schemes in whether they are performed close to resonance or far detuned. When considering the readout process, Gorshkov *et al.* (2007a) reach the expression for the readout time

$$T_{\mathrm{RO}} \sim \frac{\gamma^2 C^2 + \Delta^2}{\gamma C |\Omega|^2}, \tag{2.45}$$

where 2γ the excited state decay rate. Eq. (2.45) has two regimes: the resonance limit, $|\Delta| \ll C\gamma$, and the Raman limit, $|\Delta| \gg C\gamma$, with

$$T_{\mathrm{RO}}^{\mathrm{res}} \sim \frac{\gamma C}{|\Omega|^2}, \qquad |\Delta| \ll C\gamma, \tag{2.46}$$

$$T_{\mathrm{RO}}^{\mathrm{Raman}} \sim \frac{\Delta^2}{\gamma C |\Omega|^2}, \qquad |\Delta| \gg C\gamma. \tag{2.47}$$

The two regimes have very different dependency of C. Strikingly, in the resonance limit, the retrieval becomes slower when the cooperativity is increased. We see from eq. 2.47 that in the Raman limit, the readout rate $\Gamma_{\mathrm{RO}} = T_{\mathrm{RO}}^{-1}$ has the same dependency on the cavity-enhanced parameters C and $|\Omega|^2$ as P_{scatt}. We can use this to determine the cavity enhancement of ζ in the read process. If we want to fix Γ_{RO}, we require

$$C P_{\mathrm{intra}}^{\mathrm{cav}} = d P_{\mathrm{intra}}^{\mathrm{fs}} \iff \frac{P_{\mathrm{out}}^{\mathrm{fs}}}{P_{\mathrm{out}}^{\mathrm{cav}}} = \eta_{\mathrm{win}} \frac{2\mathcal{F}}{\pi} \left(\frac{2}{T_{\mathrm{out}}} - 1 \right). \tag{2.48}$$

When accounting for the difference in readout efficiency, η_{R}, and loss of scattered photons in the cavity and free space situations, we thus have

$$\frac{\zeta_{\mathrm{cav}}^{\mathrm{RO}}}{\zeta_{\mathrm{fs}}^{\mathrm{RO}}} = \frac{\eta_{\mathrm{R}}^{\mathrm{cav}} \eta_{\mathrm{esc}}}{\eta_{\mathrm{R}}^{\mathrm{fs}} \eta_{\mathrm{win}}} \frac{P_{\mathrm{out}}^{\mathrm{fs}}}{P_{\mathrm{out}}^{\mathrm{cav}}} = \frac{\eta_{\mathrm{R}}^{\mathrm{cav}}}{\eta_{\mathrm{R}}^{\mathrm{fs}}} \frac{\zeta_{\mathrm{cav}}}{\zeta_{\mathrm{fs}}}. \tag{2.49}$$

where $\eta_{\mathrm{R}}^{\mathrm{cav}} / \eta_{\mathrm{R}}^{\mathrm{fs}}$ is of order unity. The cavity thus grants approx. the same filter ratio enhancement is readout as for write.

2.6 Interaction with moving atoms

In the theoretical treatment above no atomic motion has been included. When working with warm vapours, this is naturally an important aspect of the dynamics. As already mentioned, in the diffusion model of Shaham *et al.* (2020) the excitation in the different atomic modes decay into the other modes because of the atomic motion. The only exception is the symmetric mode in an anti-relaxation-coated cell where the decay is not caused by spin diffusion but only non-collective effects like wall collisions and atom-atom collisions.

In the theoretical proposal by Borregaard *et al.* (2016), atomic motion in the DLCZ scheme was treated in the specific cell dimensions that are used in this thesis. The main

difference is that Borregaard *et al.* considered hyperfine storage $|s\rangle = |F = 3, m_F = 3\rangle$. In the experimental realization we chose to store in the Zeeman coherence $|s\rangle = |F = 4, m_F = 3\rangle$ for reasons that will be discussed later. The main difference between the two configurations is the frequency difference between $|g\rangle$ and $|s\rangle$, and hence the spin-wave wavelength, and the dipole moments involved. A more subtle difference is that the Zeeman-storage configuration enables four-wave mixing. The parasitic dynamics from FWM will be discussed in detail in chapter 4.

The experimental realization proposed by Borregaard *et al.* employs a cubic, warm vapour "microcell" with dimensions $2L$ x $2L$ x L_z with $2L = 300\,\mu\text{m}$ and $L_z = 10\,\text{mm}$. For vapour cells this is an unusually small cross-section. The unusual choice is motivated by the need for motional averaging. When the transverse dimension is small the atoms will quickly come back and cross the beam several times. The secondary motivation is the higher laser intensity when focussing on a small cell. This relaxes the filtering requirement as we shall show at the end of this section.

The storage state is chosen such that the laser light can also be filtered by means of a polarizer. The laser mode Ω is π-polarized, while the scattering mode $\hat{a}_{\text{cell}}$ is σ-polarized, see Fig. 2.7. For the same reason the magnetic field axis points perpendicular to the light propagation. This enables the π polarization and invokes that scattering into σ polarization is *linearly* polarized orthogonal to π. Moreover, the proposal includes a low-finesse cavity around the vapour cell ("cell cavity") to exploit the advantages of enhanced interaction as described in the previous section. The components of the proposal are illustrated in Fig. 2.7.

The motional-averaging technique proposed by Borregaard *et al.* is double-sided. On one hand, the interaction with the laser light has to be averaged by the atomic motion to enhance the interaction with the symmetric mode. Since the cell cavity mode is Gaussian, the coupling to the laser light is spatially inhomogeneous. The experimental requirement to achieve the motional averaging is rather simple since a long laser pulse enables the averaging.

On the other hand, the DLCZ scheme relies on heralding a single collective excitation by detection of a single photon. This therefore requires that the interaction with the detection mode is also motionally averaged. A single-photon detector detects the field intensity in a near-instantaneous mode. (In fact a lot of work has been put into minimizing the temporal jitter of single-photon detectors). The single-photon detection thus corresponds to a snap-shot measurement of the atoms in the cavity mode. To enable motional averaging this "which-atom" information has to be erased. Borregaard *et al.* propose to achieve this by the use of a narrowband filter cavity between the cell cavity and the detector, see Fig. 2.7. The narrowband transmission window of the filter cavity effectively erases the correspondence between time of detection and photon release in the cell cavity. Hence, atoms have traversed the beam several times in the corresponding release window and the which-atom information is lost.

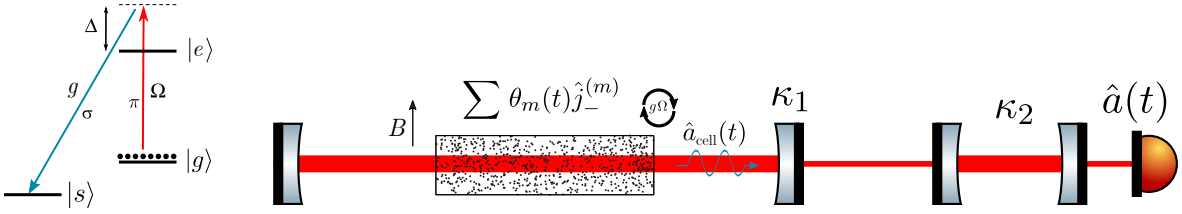

Figure 2.7: **Illustration of the proposal by Borregaard *et al.* (2016).** The vapour cell is placed inside a single-sided, low-finesse "cell cavity" with outcoupling rate κ_1. The cavity field $\hat{a}_{\text{cell}}$ couples to the atomic coherences $\hat{j}_-$ via spontaneous Raman scattering. A high-finesse "filter" cavity with decay rate κ_2 erases the "which-atom" information by altering the temporal correlation between detector click and light release in the cavity mode. The atomic motion averages the individual atom amplitude θ_m in the collective state during the effective interaction time.

To aid the reader's intuition for this detection strategy, it is to some extent the single-photon equivalent of photography with long shutter time.

Borregaard *et al.* treats the motional averaging in the write process by solving Heisenberg's equations of motion of an ensemble of three-level atoms like the one in Fig. 2.4. The main difference to the Hamiltonian in eq. (2.32) is that temporal variation of $\Omega_m(t)$ and $g_m(t)$ is linked with the individual atomic motion as it moves through the spatially inhomogeneous cavity mode. The intensity profile of both $\Omega_m(t)$ and $g_m(t)$ is given by the standing-wave cavity mode

$$\Omega_m(t) = \Omega \sin(k_{W,\Omega} z_m(t)) e^{\frac{-x_m^2(t)-y_m^2(t)}{w^2}}, \tag{2.50}$$

$$g_m(t) = g \sin(k_{W,\hat{a}} z_m(t)) e^{\frac{-x_m^2(t)-y_m^2(t)}{w^2}}, \tag{2.51}$$

with the single-photon Rabi frequency $g = D_{se}\sqrt{\omega/(2\hbar\epsilon_0 V)}$ where $V = \pi w^2 L_{\text{cav}}/4$ is the mode volume of the standing-wave cavity (Tanji-Suzuki *et al.*, 2011). The excited state is adiabatically eliminated similar to eq. (2.32). The outcoupled cell cavity field is propagated through the filter cavity to yield the flux at the detector

$$\hat{a}(t) = -\frac{\kappa_2\sqrt{\kappa_1}}{4} \sum_{m=1}^{N} \theta_m(t)\hat{j}_-^{(m)}, \tag{2.52}$$

where $\theta_m(t)$ describes the individual atomic coupling along its trajectory in the cell. It can be written as

$$\theta_m(t) = \int_0^t \mathrm{d}t'\, e^{-\kappa_2(t-t')/2} \int_0^{t'} \mathrm{d}t''\, e^{-\kappa_1(t'-t'')/2} \int_0^{t''} \mathrm{d}t'''\, e^{-(\gamma/2-i\Delta)(t''-t''')} g_m^*(t'')\Omega_m(t'''), \tag{2.53}$$

where the spontaneous emission rate γ is included. From eq. (2.53) we see the averaging effect of the filter cavity with energy decay rate κ_2. The field from the cell is propagated through the filter cavity kernel $e^{-\kappa_2(t-t')/2}$ which alters the temporal correspondence between atomic position and time of detection.

To calculate the ensemble mean, $\langle\theta(t)\rangle_e$, the inhomogeneous detuning due to Doppler shift has to be considered. In the long time limit, i.e. $e^{-\kappa_2 t/2} \approx e^{-\kappa_1 t/2} \approx 0$, Borregaard *et al.* reaches the expression

$$\langle\theta(t)\rangle_e = \frac{\pi^{3/2} g\Omega}{4\Gamma_\mathrm{D}} \mathrm{w}\left[\frac{\Delta + i\gamma/2}{\Gamma_\mathrm{D}}\right] \frac{w^2}{L^2} \frac{1}{\kappa_1\kappa_2}, \tag{2.54}$$

where Γ_D is the Doppler width (angular frequency) and $\mathrm{w}(z) = e^{-z^2}(1 - \mathrm{erf}(-iz))$ is the Faddeeva function that describes the complex refractive index of the ensemble. For room-temperature $\Gamma_\mathrm{D} \sim 2\pi \cdot 225\,\mathrm{MHz}$.

When a single photon reaches the detector, the atomic state will be projected into the single excitation state. But in what mode will this single excitation be? We can answer this question by calculating the overlap with the symmetric mode after detecting a photon within an integration time t_int. Using the definition of the symmetric mode in eq. (2.25), the overlap with the single symmetric excitation state $|1\rangle$ becomes

$$\int_0^{t_{int}} \mathrm{d}t\, |\langle 1|\, \hat{a}(t)\, |gg...g\rangle|^2 = \int_0^{t_{int}} \mathrm{d}t\, \frac{1}{N} \left|\left\langle \sum_{n=1}^{N} \hat{j}_+^{(m)} \hat{a}(t) \right\rangle\right|^2 = \frac{\kappa_2^2\kappa_1}{16} \int_0^{t_{int}} \mathrm{d}t\, N\, |\langle\theta(t)\rangle_e|^2\,, \tag{2.55}$$

where the subscript e refers to the ensemble average. Here we used the non-normalized ensemble state $\hat{a}(t)\,|gg...g\rangle$. To get the normalization right, we need to divide with the probability to detect a photon, given as

$$\int_0^{t_{int}} \mathrm{d}t \left\langle \hat{a}^\dagger \hat{a}(t) \right\rangle = \frac{\kappa_2^2\kappa_1}{16} \int_0^{t_{int}} \mathrm{d}t\, N \left\langle |\theta(t)|^2 \right\rangle_e. \tag{2.56}$$

We refer to the conditional overlap as the *write efficiency*, η_W, and dividing eq. (2.55) by eq. (2.56) we reach

$$\eta_\mathrm{W} = \frac{\int_0^{t_\mathrm{int}} |\langle\theta(t)\rangle_e|^2\, \mathrm{d}t}{\int_0^{t_\mathrm{int}} \left\langle |\theta(t)|^2 \right\rangle_e \mathrm{d}t}. \tag{2.57}$$

The write efficiency thus becomes a measure for how well the heralding to asymmetric modes has been averaged away by atomic motion during the effective integration time. We see from eq. (2.54), that $\left\langle |\theta(t)|^2 \right\rangle_e$ depends on the temporal correlation in the individual atom-light coupling $\langle g^*(t_1)\Omega(t_1)g(t_2)\Omega^*(t_2)\rangle_e$ (assuming g, Ω constant over the fast dynamics in the integral over t'''). Borregaard *et al.* assumes that the correlations are exponentially decaying such that

$$\langle g(0)g(t)\rangle_e = \left\langle g(0)^2 \right\rangle_e e^{-\Gamma t} + \langle g(0)\rangle_e^2 (1 - e^{-\Gamma t}), \tag{2.58}$$

and similar for Ω. The assumption is verified from simulation. In the realistic limit where the write pulse is long enough that the effective interaction time is set by the filter cavity ($t_{int} \gg 1/\kappa_2$) and the cell cavity can be ignored ($\kappa_1 \gg \Gamma, \kappa_2$), the authors find

$$\eta_W \approx \left(1 + \frac{\kappa_2}{2\Gamma + \kappa_2}\left(\frac{4L^2}{\pi w^2} - 1\right)\right)^{-1} \approx 1 - N_{\text{pass}}^{-1}. \tag{2.59}$$

If the filter cavity is sufficiently narrow ($\Gamma \gg \kappa_2$), the write efficiency can be approximated with the number of passes an atom makes through the beam during the filter cavity decay time, $N_{\text{pass}} \approx \Gamma w^2/(\kappa_2 L^2)$. We see that there is both a spatial and a spectral component determining the write efficiency. The spatial "filter" is given by the filling factor w^2/L^2 that should be increased in order to spatially select the symmetric mode. The spectral selection described by Γ/κ_2 rejects the short-lived correlations of the asymmetric modes. In fact the spectral selection also depends on the cell cavity mode. Borregaard *et al.* find from simulation that $\Gamma \sim 1.3v/w$ where v is the average thermal velocity, thus Γ is related to the transit time through the beam. For the microcell at room temperature and a beam radius $w = 55\,\mu\text{m}$ the spatial decorrelation rate is $\Gamma = 2\pi \cdot 0.75\,\text{MHz}$.

It is instructive to consider the motional averaging in the spectral domain. The temporal correlation of the atom-light coupling $\langle g(0)g(t)\rangle_e$ gives rise to two distinct spectral components, see Fig. 2.8: 1) a broad component with HWHM of $\Gamma/(2\pi)$. This is the noise coming

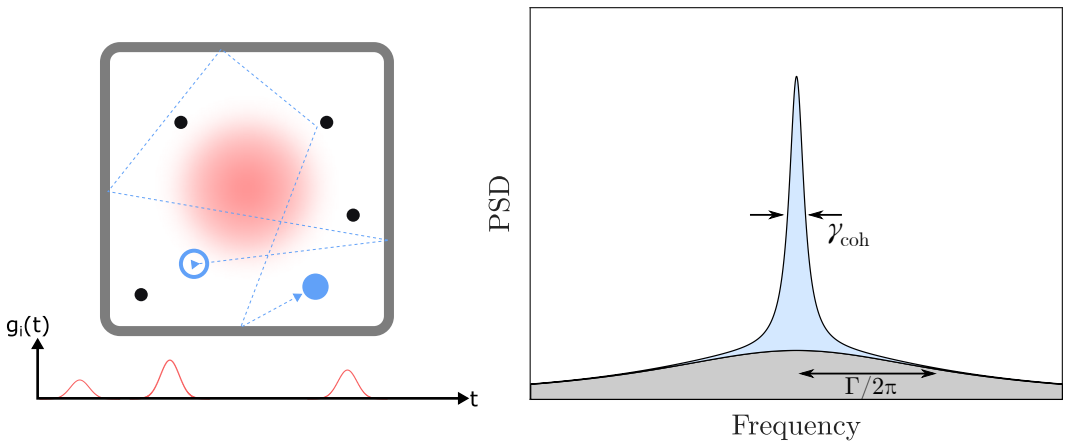

Figure 2.8: **Left: Time-dependent coupling.** The cell is illuminated by a laser with a transverse Gaussian beam profile (red). Atoms move across the cell, bouncing off the cell walls and other atoms (black dots), thus experiencing a time dependent light coupling. The coupling experienced by the atom over time is given by $g_i(t)$. Figure from Thomas (2020). **Right: Spectrum of scattered light.** The spectrum consists of a narrowband component associated with the long-time correlation of atoms moving in and out of the beam and a broadband component from short-time correlations related to the transit time through the beam for an atom. Figure from Dideriksen (2017).

from the transit time of an atom through the beam. 2) a narrow component from the long coherent interaction with the atom over many wall bounces. The linewidth of this component (γ_{coh}) is set by decoherence independent of atomic diffusion and is the spectral manifestation of the macroscopic transverse spin coherence time T_2. The scattering spectrum is often referred to as the spin-noise spectrum. In the spectral domain, the write efficiency is the ratio of the energy in the narrow component to the total energy in the filter cavity bandwidth. This makes for an experimental procedure for estimating the write efficiency by measuring the energy in and out of resonance with the narrow component. This tool is used for characterizing the motional averaging as we shall discuss in chapter 4.

We shall also note here that Shaham *et al.* (2020) treats the spin-noise spectrum in a general setting. In that work the authors find that in general the lineshape of the broad pedestal depends both on the beam profile and the cell dimensions. The eigenmodes of diffusion depend solely on the cell dimension while the amplitude of each mode depends on the overlap of the laser mode with the atomic mode. For a high filling factor the coupling is strong to the lowest-order modes. Because the spin-noise spectrum becomes a sum over modes with different Lorentzian linewidths, the broad pedestal is in general not a Lorentzian lineshape. However, when the filling factor is high, the broad pedestal is dominated by a single mode and approaches a Lorentzian lineshape.

Since the purpose of the filter cavity also is to reject the laser photons escaping the cavity together with the scattered photon, we shall here consider why a small transverse cell cross-section limits the necessary laser power. We see from eq. (2.55) that the rate of scattering (R_{symm}) associated with the symmetric mode is proportional to $N\left|\langle\theta(t)\rangle_e\right|^2$. From eq. (2.54) we find the mean coupling proportionality $\langle\theta(t)\rangle_e \propto g\Omega w^2/L^2$. For the laser field amplitude at beam centre we have $\Omega \propto \sqrt{P}w^{-1}$ with P as the laser power while also the coupling of scattering to the cavity mode depends on the mode size with $g \propto w^{-1}$. Hence, symmetric-mode scattering rate has proportionality

$$R_{\mathrm{symm}} \propto NP/L^4 \propto \rho L_z P/L^2. \tag{2.60}$$

We see that R_{symm} is proportional to the mean laser intensity over the whole *cell* cross-section area. Thus, it is advantageous to choose a small cell cross-section to limit the filter requirements. This is in contrasts to experiments that do not address the symmetric mode and thus do not rely on atoms returning to the interaction region. There the scattering rate depends on the *beam* cross-section area.

Readout

At the time of readout, any written excitations into the short-lived asymmetric modes will have decayed. Ideally, the motional averaging during readout therefore does not impose any

requirements on the filtering – only that a long pulse is required. However, the filter cavity is still beneficial because it extinguishes the detuned laser light.

The readout becomes a competition of two processes. 1) The coherent readout into the cell cavity mode and 2) loss due to spontaneous emission. In the limit of weak and long readout pulse, Borregaard *et al.* find the readout efficiency, i.e. the number of retrieved photons per excitation in the symmetric mode, to be

$$\eta_{\mathrm{RO}} \approx \left(1 + \frac{\pi}{d\mathcal{F}}\right)^{-1}. \tag{2.61}$$

This is the same fundamental limit described by the cooperativity as discussed in the previous section. Furthermore, Borregaard *et al.* (2016) derives an expression for the readout rate which scales the same way as the general result in eq. (2.45).

The readout rate can be increased through higher read pulse power but when the readout rate becomes high, the level of motional averaging and thus retrieval efficiency decreases. From simulation Borregaard *et al.* find the dependency on readout time as given in Fig. 2.9, left. This clearly shows that a long readout time is required for the motional averaging. As with the other effects of motional averaging, an improved filling factor is beneficial.

Borregaard *et al.* also considers readout noise from atoms incoherently transferred into the storage state, e.g. from imperfect initialization or atomic decay. As discussed in section 2.4, part of the incoherent population will overlap with the symmetric mode and thus be readout in the same narrowband optical mode. The remaining overlap with asymmetric modes causes readout of "incoherent" photons. Since these are much broader both spectrally and temporally than the coherent photons, they can be filtered out by the filter cavity and a short read time. The authors simulate readout probability of incoherent photons and find the dependency on filter cavity linewidth as given in Fig. 2.9, right.

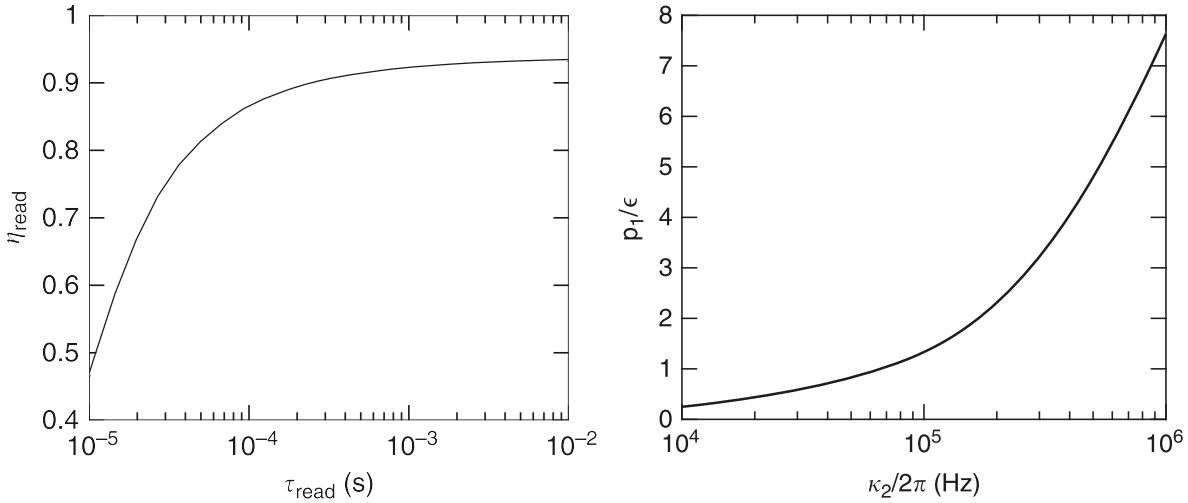

Figure 2.9: **Read efficiency and readout noise. Left:** "Optimal readout efficiency as a function of the readout time t_{read} without the filter cavity (corresponding to $\kappa_2 \to \infty$). [...] we have assumed that $t_{\text{read}}/3 = \Gamma_{\text{read}}$ where Γ_{read} is the readout rate, which is proportional to the classical drive intensity. The optical depth was assumed to be 168 as measured in the experiment. The finesse of the [cell] cavity was varied between 20 and 100 to get the optimal readout efficiency." **Right:** "The probability to read out incoherent photons (p_1) normalized by the fraction of atoms (ϵ) that have been incoherently transferred to the readout state as a function of the linewidth, κ_2 of the filter cavity. [...] we have assumed that $t_{\text{read}}\Gamma_{\text{read}} = 3$, which ensures a temporal filtering of the incoherent photons while keeping a high readout efficiency of the coherent photons." Figures and captions adapted from Borregaard *et al.* (2016), licensed under CC BY.

2.7 Non-classical correlations

It is customary to verify non-classicality of optical fields by means of intensity correlation. In this section we shall introduce and discuss relevant measures of intensity correlation and their feasibility as figures of merit for applications of non-classical light.

Second-order correlation function

Classically, the second-order correlation function is defined as the two-point (time-averaged) intensity correlation

$$\gamma^{(2)}(\vec{r}_1, t_1; \vec{r}_2, t_2) = \langle I(\vec{r}_1, t_1) I(\vec{r}_2, t_2) \rangle \,. \tag{2.62}$$

The quantum counterpart can be derived from the quantized electric field described by $\hat{a}_i(t)$ and the quantum counterpart of eq. (2.62) becomes (Gerry and Knight, 2004)

$$G^{(2)}(\vec{r}_1, t_1; \vec{r}_2, t_2) = \left\langle \hat{a}_1^\dagger \hat{a}_2^\dagger \hat{a}_1 \hat{a}_2 \right\rangle . \tag{2.63}$$

From here on, we shall only work with *normalized* correlation functions, i.e.

$$g^{(2)}(\vec{r}_1, t_1; \vec{r}_2, t_2) = \frac{\left\langle \hat{a}_1^\dagger \hat{a}_2^\dagger \hat{a}_1 \hat{a}_2 \right\rangle}{\left\langle \hat{a}_1^\dagger \hat{a}_1 \right\rangle \left\langle \hat{a}_2^\dagger \hat{a}_2 \right\rangle} \,. \tag{2.64}$$

From the general definition in eq. (2.64) we can define the second-order cross-correlation of fields described by commuting operators $\hat{a}_1, \hat{a}_2$ (e.g. the write and read fields of the DLCZ scheme)

$$g^{(2)}_{WR} = \frac{\langle \hat{n}_W \hat{n}_R \rangle}{\langle \hat{n}_W \rangle \langle \hat{n}_R \rangle} \,. \tag{2.65}$$

And the second-order auto-correlation

$$g^{(2)}_{ii} = \frac{\langle \hat{n}_i (\hat{n}_i - 1) \rangle}{\langle \hat{n}_i \rangle^2} \,, \tag{2.66}$$

which takes a slightly different form because of the normal ordering of operators in eq. (2.63). We have omitted the time dependency of the number operator $\hat{n}_i$ because, in this work, we shall only consider correlation functions of fields defined in a specific time window. The detector will not be limited to measure the number operator of a single quantized spatio-temporal optical mode because of its operation principle. Instead it will measure a large range of modes – both spectrally but also temporally as set in post-processing by our detection time window. The measurement operator then becomes a sum over modes, $\hat{D} = \sum_i \hat{n}_i$. However, classical bounds of correlation functions are still the same (see Sekatski *et al.*, 2012). Pollution from excitations in other modes will be discussed more in section 5.2.4.

For verifying single-photon generation, we shall also concern ourselves with the conditional read field, i.e. the read field conditioned on a single detection event during the preceding write pulse. The conditional auto-correlation function is given as

$$g^{(2)}_{\mathrm{RR|W=1}} = \frac{\langle \hat{n}_R(\hat{n}_R - 1)\rangle_{W=1}}{\langle \hat{n}_R\rangle^2_{W=1}} \ , \tag{2.67}$$

where $\langle ..\rangle_{W=1}$ indicates the expectation value over the conditional state.

Cauchy-Schwarz inequality

The Cauchy-Schwarz inequality $2I_1I_2 \leq I_1^2 + I_2^2$ leads to classical bounds on the correlation functions (Gerry and Knight, 2004; Clauser, 1974):

$$\begin{aligned} 1 &\leq g^{(2)}_{ii} && \text{(classical)}, \\ \left(g^{(2)}_{WR}\right)^2 &\leq g^{(2)}_{WW} g^{(2)}_{RR} && \text{(classical)}. \end{aligned} \tag{2.68}$$

The latter is often quantified by the Cauchy-Schwarz parameter

$$R = \frac{\left(g^{(2)}_{WR}\right)^2}{g^{(2)}_{WW} g^{(2)}_{RR}} \ , \tag{2.69}$$

with the classical bound $R \leq 1$.

We shall also add that for two-mode squeezed states $g^{(2)}_{\mathrm{WR}} > 2$ is often taken as signature of non-classicality because the ideal squeezed state has $g^{(2)}_{WW} = g^{(2)}_{RR} = 2$.

For photon-number states $|n\rangle$ we have the auto-correlation function

$$g^{(2)}_{nn} = 1 - \frac{1}{n}, \ n > 0. \tag{2.70}$$

Based on this $g^{(2)}_{ii} < 1/2$ indicates a high contribution from the single-photon state. Thus, crossing this threshold is a milestone for any single-photon source.

For the ideal two-mode squeezed state, the cross-correlation is limited by excitation probability since

$$g^{(2)}_{WR} = \frac{\sum_{n=0}^{\infty} n^2 p_0^n}{(1-p_0)\left(\sum_{n=0}^{\infty} n p_0^n\right)^2} = 1 + \frac{1}{p_0} \ , \tag{2.71}$$

where we have used the pair probability distribution in eq. (2.4). Please note that in the absence of number-resolving detection (which is often the case in similar experiments), the factors in the sums reduce to $n = n^2 = 1$, hence the ideal cross-correlation reduces to $g^{(2)}_{\mathrm{WR}}$

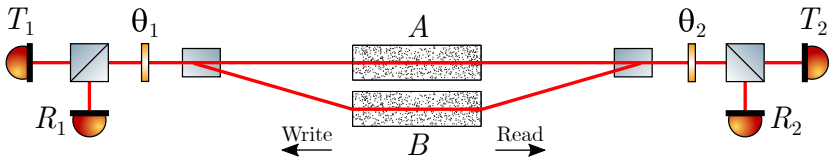

Figure 2.10: **Setup for Bell-inequality violation.** Entanglement generation and verification between two sources, A and B, can be achieved by polarimetric measurements in the write path and read path. The light from the two sources is orthogonally polarized and combined into one path. A half-wave plate rotates the measurement basis. For verification, the measurement is repeated in four different measurement bases with wave-plate angles $\{\theta_1, \theta_2\}$. The setup is equivalent to a polarization-entangled photon-pair source.

$= 1/p_0$. Similarly, the conditional read auto-correlation is also limited by the excitation probability. The dependency can be approximated to

$$g^{(2)}_{\mathrm{RR|W=1}} \approx 4p_0 \ , \tag{2.72}$$

for small p_0 and in the case of non-number-resolving detection (Chou *et al.*, 2004). As we shall see in section 5.2.4, low detection efficiency will produce the same approximate relation in the case of number-resolved detection.

2.7.1 Relation to entanglement

An interesting property of the cross-correlation is that it can be related to the achievable entanglement strength and thus the requirements for quantum network application (de Riedmatten *et al.*, 2006). If one assumes access to two identical two-mode-squeezed systems, entanglement can be generated by erasing the which-path information of the heralding photon (e.g. as the entanglement-generation step of the DLCZ protocol). The correlation between the retrieved fields can be quantified by performing joint measurements on the output modes on two detectors.

The procedure for entanglement verification is to choose four sets of joint measurement bases. This is often done by rotation of polarization as illustrated in Fig. 2.10. Here θ_1, θ_2 designates the half-wave plate angles with respect to a reference axis. In this configuration, the system of two DLCZ sources is analogous to a single source emitting polarization-entangled particles. The correlation function is calculated from detector coincidences according to (Clauser and Shimony, 1978)

$$E(\theta_1, \theta_2) = \frac{C_{T_1T_2} + C_{R_1R_2} - C_{T_1R_2} - C_{R_1T_2}}{C_{T_1T_2} + C_{R_1R_2} + C_{T_1R_2} + C_{R_1T_2}} \ . \tag{2.73}$$

For fixed θ_1, the correlation function will follow a sinusoidal oscillation with θ_2, thus producing and interference pattern. If two modes are indeed entangled, a rotation of θ_1 will shift the

interference pattern. In that case, the visibility of the interference pattern quantifies the indistinguishability of the two systems.

For any choice of joint measurement bases using a set $\{\theta_1, \theta_1'\}, \{\theta_2, \theta_2'\}$, the Bell parameter can be calculated as

$$S = E(\theta_1, \theta_2) + E(\theta_1', \theta_2) + E(\theta_1, \theta_2') - E(\theta_1', \theta_2') \leq 2\sqrt{2}. \tag{2.74}$$

The canonical choice $\theta_1 = \{22.5°, -22.5°\}, \theta_2 = \{0°, 45°\}$ maximises the Bell parameter (Matsukevich *et al.*, 2005; de Riedmatten *et al.*, 2006). This Clauser-Horne-Shimony-Holt (CHSH) variant of the Bell inequality bounds classical correlations (explainable by local-hidden-variable theory) to $|S| \leq 2$ (Clauser *et al.*, 1969).

Next, if one assumes the photons scattered from the two systems, A and B, to be indistinguishable and scattered with same probability, the only mechanism that can reduce the visibility is uncorrelated background noise on the detector. Hence, the visibility can be related to the cross-correlation (de Riedmatten *et al.*, 2006). This can be seen from Fig. 2.10. Consider the configuration where there is no mixing between the sources ($\theta_1 = \theta_2 = 0$) such that write (read) photons from source A goes to T_1 (T_2) and photons from source B goes to detector R_1, R_2. Then the positive coincidences in the numerator in eq. (2.73), $C_{T_1T_2}, C_{R_1R_2}$, are exactly the single system coincidences while the negative coincidences, $C_{T_1R_2}, C_{R_1T_2}$, are uncorrelated write and read across the two systems. For two identical systems this can be written as

$$\begin{aligned} V = E_{max} &= \frac{\langle WR\rangle_A + \langle WR\rangle_B - \langle W\rangle_A \langle R\rangle_B - \langle W\rangle_B \langle R\rangle_A}{\langle WR\rangle_A + \langle WR\rangle_B + \langle W\rangle_A \langle R\rangle_B + \langle W\rangle_B \langle R\rangle_A} \\ &= \frac{\langle WR\rangle - \langle W\rangle \langle R\rangle}{\langle WR\rangle + \langle W\rangle \langle R\rangle} = \frac{g^{(2)}_{\mathrm{WR}} - 1}{g^{(2)}_{\mathrm{WR}} + 1}\ . \end{aligned} \tag{2.75}$$

The visibility V is directly related to the Bell parameter since $S = 2\sqrt{2}V$ (Marcikic *et al.*, 2004). Thus, $V > 1/\sqrt{2}$ is required for Bell inequality violation. According to eq. (2.75) this requirement corresponds to $g^{(2)}_{\mathrm{WR}} \gtrsim 5.8$.

For cold atoms CHSH inequality violation was shown by de Riedmatten *et al.* (2006) using two spin-wave modes of the same ensemble. With $g^{(2)}_{\mathrm{WR}} = 57$ the authors were able to obtain $S = 2.7 \pm 0.1$ limited by a small imbalance in the excitation probability of the two modes. The same group later demonstrated entanglement of two independent atomic ensembles (Laurat *et al.*, 2007). More recently, Li *et al.* (2020) demonstrated entanglement of two independent, warm atomic ensembles in a similar way.

Chapter 3

Experimental Set-Up

In this chapter we shall describe and characterize the experimental setup that was build and used to demonstrate the DLCZ scheme. The demonstration is described in chapters 4 and 5 where the latter presents the latest results on the current experimental setup. The specificities of this chapter relate to the current setup but the concepts are the same for the early experimental setup.

3.1 Vapour cells

The caesium ensemble is contained in a glass cell where a caesium vapour fills the entire cell volume. The type of cell used in this work is referred to as a vacuum cell since it contains caesium evaporated into an evacuated chamber. This is opposed to buffer gas cells where the atomic vapour is mixed with a buffer gas at a desired pressure (typically tens of torr). Prior to caesium loading, the cell is coated with an anti-relaxation coating on the inside, covering ideally the whole internal surface. These coatings are typically formed by alkanes (paraffin) which is known to allow tens of thousands of wall collisions before depolarizing. The temperature is typically limited to 60-80 °C for paraffin coating before melting influences the anti-relaxation properties. On the other hand, alkene compounds have shown better anti-relaxation performance but are limited to temperatures only slightly above room temperature (Balabas *et al.*, 2010). When very high temperatures are needed, e.g. in spin-exchange-relaxation-free application, the coating material is often formed by organochlorosilanes (Chi *et al.*, 2020). The cell used for DLCZ demonstration has paraffin coating.

In general vapour cells are made with a main volume (typically cylindrical) where the vapour is supposed to interact with light. Attached to this main volume is a 'stem' containing a droplet of solid metal (in our case caesium). The presence of condensed caesium enables control of the vapour pressure and hence the atomic density by varying the cell temperature. However, the collision of evaporated atoms with the condensed caesium is highly depolarizing. So in order to maintain long spin coherence times, it is important that caesium only condenses

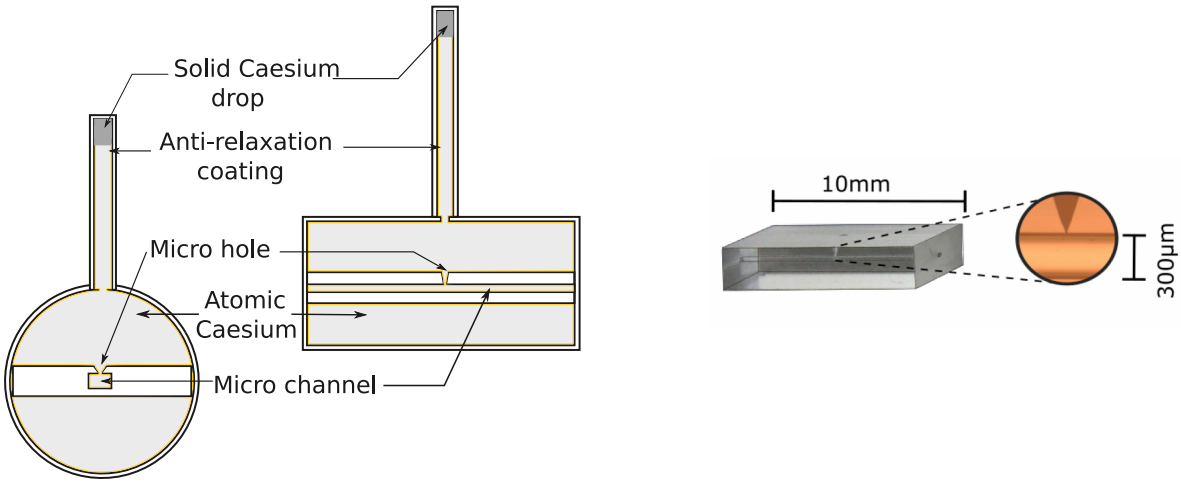

Figure 3.1: **Micro cell design.** A glass chip with a 300 µm x 300 µm x 10 mm channel is encapsulated in a cylindrical glass cell. The complete internal surface is anti-relaxation coated. From a droplet in the cell stem caesium evaporates into the cell volume. The micro-channel is connected to the encapsulating volume via a funnel-shaped micro hole. Drawings adapted from Enault-Dautheribes (2017) and Thomas (2020).

in the stem and that the stem is connected to the main volume through a small channel to lower the rate of atomic exchange between the coherent atoms leaving the main volume and incoherent atoms entering from the stem. A common technique for ensuring that the caesium condenses in the stem only is to keep the stem a few degrees colder than the main body. However, in the present work we have not found it necessary to cool the stem.

As discussed in section 2.6, for fast motional averaging and relaxed filtering requirements, we require a small cell cross-section for the DLCZ experiment. This has inspired a novel design of the vapour cell which is illustrated in Fig. 3.1. Because of the small geometry we refer to this design as 'micro cells'. An interaction volume of 300 µm x 300 µm x 10 mm is formed inside a glass chip by glass pulling. The square cross-section is chosen in order to enable good optical access from the side which is needed for optical pumping. For such a small cross-section the lensing effect for side illumination would be substantial had the channel been cylindrical. The glass chip is produced by VitroCom Inc.

To enable attachment of windows and stem by standard glass blowing, the chip is placed inside an encapsulating cylindrical glass cell. Glass blowing directly on the chip would deform the chip. The chip is clamped between two windows which are then glass blown onto a glass tube to form the encapsulating cylinder. The clamping is tight in order to avoid atomic exchange at the windows. Instead the chip channel is connected to the encapsulating cylinder through a small laser drilled hole at the channel centre. The hole diameter is typically 20-30 µm.

Because the cell is intended for application inside an optical cavity, the light transmission loss has to be minimized. To minimize reflection the windows are anti-reflection coated on both sides. The anti-reflection properties survive the cell fabrication.

After glass blowing the cell is cleaned internally using hydrochloric acid followed by evacuation. The anti-relaxation coating is applied by evaporating the coating into the cell through the stem at high temperature (280-380 °C). As a final step the caesium droplet is introduced in the stem and the stem is sealed off by glass blowing.

Over time it can happen that the cell properties change, e.g. spin coherence time decrease or atomic density decrease. We speculate that this behaviour is caused by atoms condensing inside the channel or the coating migrating potentially clogging the micro-hole. We have found that such changes can in many cases be remedied by 'recuring' the cell. The recurring process involves heating the cell to 70-90 °C for several hours and letting it slowly cool down while keeping the stem a few degrees colder than the main body.

We owe great gratitude to Assoc. Prof. Mikhail Balabas of Saint-Petersburg State University for fabricating our vapour cells using his expertise in anti-relaxation coating as well as glass blowing.

3.1.1 Magnetic shielding and bias field coil

For all experiments relying on spin coherence, the relaxation induced by magnetic field fluctuations has to be minimized. For this reason we employ a standard magnetic shield. The shield consists of several layers of iron, aluminium and μ-metal (a high-permeability alloy) which screens both power-line and high-frequency magnetic noise as well as the constant Earth field. In the DLCZ experiment the suppression does not have to be extremely high since we apply a strong bias field and the spin coherence time is already limited by the small cell cross-section. However, we do have to minimize spatial inhomogeneity in the strong bias field to limit inhomogeneous broadening of the spin-resonance line.

The bias field is produced by a current in a bias coil in a Lee-Whiting-type configuration with three coaxial pairs of equidiameter loops (see Fig. 3.2). The bias coil creates a field oriented transverse to cell channel with a good uniformity along the channel. To compensate for a small second-order inhomogeneity we add an extra coil in a double-saddle configuration which produces a field in the same direction as the bias coil but with opposite second-order inhomogeneity. By carefully optimizing the current ratio in the two coils, the field can become highly uniform along the 10 mm channel. This enables operation at the Larmor frequency 2.4 MHz, corresponding to 6.9 G, without strong line-broadening from inhomogeneity. Both coils are wound on the outside of an aluminium frame which screens RF field fluctuations.

Furthermore, we insert a small RF coil in a Helmholtz configuration inside the aluminium

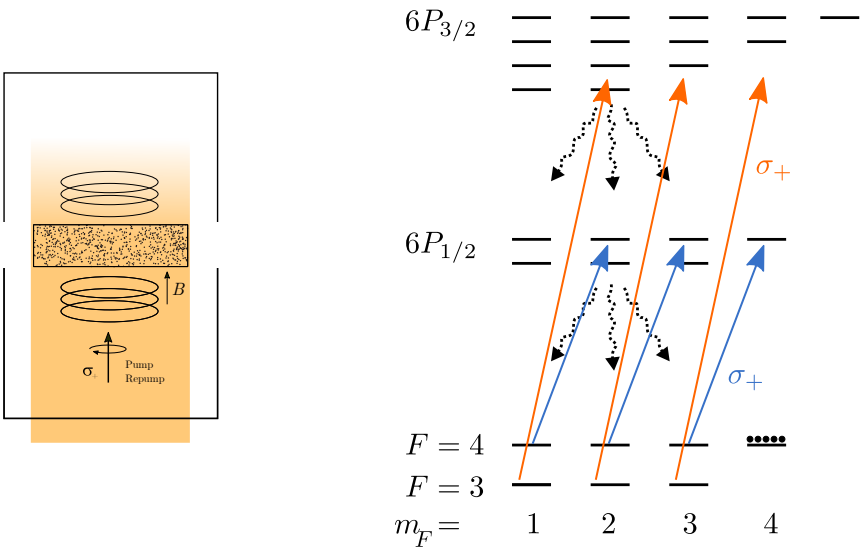

Figure 3.2: **Left: Cell setup.** The cell is held inside a magnetic shield where a coil set (not to scale) generates a bias magnetic field. Optical pumping comes from the side of the cell. **Right: Optical pumping scheme.** A σ_+-polarized 'pump' laser on the D_1 $4 \rightarrow 4'$ line (blue arrows) accumulates atoms in the dark $|4,4\rangle$ state after several absorption cycles. A σ_+-polarized 'repump' laser on the D_2 $F = 3$ line (orange arrows) recycles atoms into the $F = 4$ ground state manifold.

frame. The RF coil generates a field perpendicular to the bias field and is intended for RF spin excitation in characterization measurements. We emphasize that because the RF coil is inside the aluminium frame, it is very important that the coil connector is terminated during experiments where it is not in use. If the connector is left open, substantial magnetic noise will be coupled from the outside to the cell causing excess spin noise.

3.1.2 Optical pumping

In the DLCZ experiment we require all atoms to be initialized in $|F = 4, m_F = 4\rangle$ which is the maximal spin alignment along the magnetic field axis. The magnetic field points perpendicular to the microchannel. A way to achieve this is through optical pumping from the side. By applying resonant light carrying non-vanishing angular momentum, the angular momentum is transferred to the atoms through absorption. We use a σ_+-polarized 'pump' laser locked close to the $4 \rightarrow 4'$ transition on the D_1 line. Absorption transfers atoms to the excited state level with $\Delta m = +1$ as illustrated in Fig. 3.2. When atoms spontaneously decay, they will on average have gained angular momentum. This step-wise spin aligning continues until atoms have gathered in the dark state $|4,4\rangle$. Spontaneous decay will also happen into the $F = 3$ manifold hence we need a 'repump' laser to transfer atoms back to the $F = 4$ manifold. The repump laser is also σ_+-polarized to assist the spin alignment and it is locked near the $3 \rightarrow 2'$

transition on the D_1 line. More precisely it is locked on the 2',3'-crossover of a Doppler-free spectroscopy signal. The efficiency of this optical pumping scheme is investigated in detail in section 3.3.2.

A downside of the encapsulated micro-cell design is that the optical access to the micro-channel from the side is distorted by the encapsulating cylinder. The glass-blowing attachment of the windows leaves dents in the cylinder tube near the window interface. That means that the regions close to the windows are inaccessible from the side (typically 10-20% of the full channel length). To remedy this, we are investigating other techniques for bonding the windows such as laser welding (both CW and pulsed) and anodic bonding. This includes techniques for attaching the window directly onto the micro-chip.

3.2 Optics and electronics

3.2.1 Filtering

The price to pay for using a scheme with single-photon detection as opposed to homodyne detection is that the frequency selection happens for absolute frequency and not relative to a local oscillator. The light will have to pass an absolute frequency filter which means that the filter frequency has to be stabilized and that the signal bandwidth must be accommodated by the filter to avoid suppression.

In this work, we use optical cavities for spectral filtering. For all cavities one of the cavity mirrors is clamped with a piezo-electric transducer. Applying a voltage across the piezo translates the mirror on sub-wavelength scale whereby the cavity length, hence the resonance frequency, changes. Over the years the design of the cavities has been modified and improved. Here we shall only present the cavities used in the most recent D_1-line experiment described in chapter 5.

In the latest version, the experiment has two independent filtering setups - one for write and one for read. The purpose of the filters is both to reject the excitation laser light that comes out of the cell cavity together with the scattered signal, and to suppress the broadband scattering associated with asymmetric atomic modes.

To reject the excitation light, the first stage of the filtering is a Glan-Thompson polarizer immediately after the cell cavity to separate the two linear polarizations of excitation light and scattered light, see Fig. 3.3. The polarizer suppresses the excitation light by approx. 40 dB. In principle higher extinction with commercially available calcite polarizers is possible but the rejection is limited by polarization distortion from cell cavity birefringence. We place a quarter-wave and a half-wave plate before the polarizer to optimize the rejection.

During the write pulse, the scattered light in vertical polarization travels to the write fil-

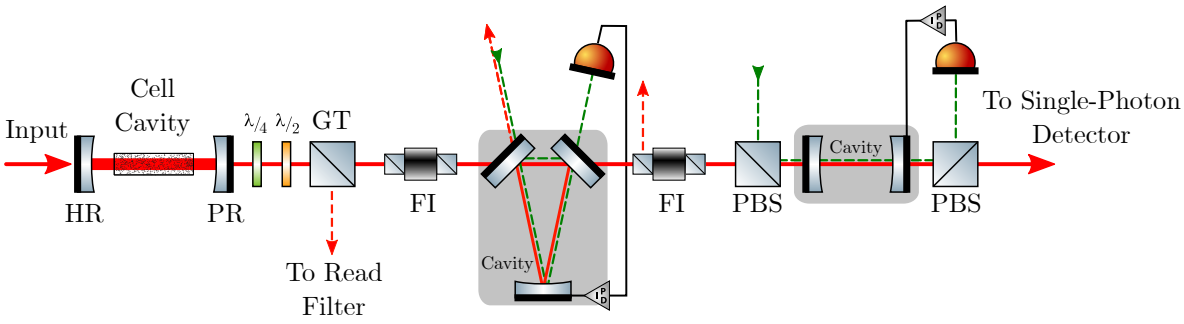

Figure 3.3: **Polarization filter and write filter stages.** After the cell cavity the light is polarization filtered on a Glan-Thompson polarizer (GT). The vertically-polarized (σ) write scattered light propagates to the write filter stage. The filter consists of two cavities: first a triangular cavity which reflects the detuned residual excitation light, second a Fabry-Perot cavity to reflect the last reminiscence of excitation light. A Faraday isolator rejects reflected light from the Fabry-Perot cavity as it travels backwards. The lock light paths for the two cavities are illustrated as green, dashed lines. For the triangular cavity we use the counter-propagating mode to lock. For the Fabry-Perot cavity we use the orthogonal polarization mode to lock by inserting polarizing beam splitters (PBS).

ter while the horizontally polarized laser light is rejected towards the off-resonant read filter. Conversely, during the read pulse the scattered light is horizontally polarized and travels to the read filter while the laser light is rejected towards the off-resonant write filter.

In the write setup, the spectral filter consists of two cascaded cavities. The first one is a triangular cavity. The advantage of a travelling wave cavity is that there are two fundamental modes (travelling in opposite directions). Hence the locking light and the signal can be in separate spatial modes. However, because of the very sensitive single-photon detection, we are still unable to lock the cavity continuously without excess noise on the detector.

To achieve high transmission we chose a design with identical in- and outcoupling mirrors with modest reflectivity of 99.91%. This limits the finesse to a few thousand but we achieve a FWHM linewidth of about 70 kHz by using a long round trip length of 1.49 m. The theoretically expected suppression of the excitation light is approx. 40 dB. We used this cavity for both D_2 and D_1 experiments and the more precise linewidth for the respective wavelengths is given in the respective chapters 4 and 5.

The second cavity is a Fabry-Perot cavity where the main purpose is to add suppression of the excitation light. Therefore the linewidth is designed to be significantly broader at 240 kHz. This still gives a suppression of almost 30 dB at the laser frequency while relaxing the sensitivity to frequency fluctuations.

The two mirrors of the cavity are mounted on a cylindrical Invar steel spacer. The spacer

is clamped at the centre in a ring mount fixed to the optical table.

The standing-wave cavity only has a single spatial, fundamental mode. Hence the lock light is separated by using orthogonal polarizations. The two linear polarizations are overlapped on a polarizing beam-splitter (PBS) in front of the cavity and separated on a PBS after the cavity such that the lock light transmission is sent to a photodetector.

We place Faraday isolators between the cavities to avoid any coupled cavity effects.

Both cavities are locked to a signal derived from the excitation laser. The lock pulses are generated with an acousto-optical modulator (AOM) which enables control of the locking frequency for the cavities by selecting the modulation frequency. We lock the cavities in a lock-in scheme where the lock light frequency is modulated at ± 3 kHz around the target frequency. The lock light transmission is recorded on a photodetector, demodulated and input to a PID controller which feeds back to the cavity piezo.

Because of the lock light pollution of the single-photon detection we cannot keep the lock light on continuously. Thus we implement sequential locking scheme where the cavities are actively locked in the first stage and frozen in the second stage where the lock light is off and the experimental pulse sequence is carried out. This heavily limits the lock bandwidth. During the freezing stage, the cavity frequency fluctuations rely on passive stability. Therefore the lock can only suppress slow drifts on the timescale of the freezing stage duration which is typically about 65 ms.

Read filter

Where the write filter setup is to a large extent a reuse of the filter used for the early experiments, the read filter was redesigned based on the experiences of the first experiment. Here we use two almost identical Fabry-Perot cavities, each mounted on a 30 cm spacer which is clamped at the centre point with a ring mount. The design is an early version of a high-stability design developed in parallel at QUANTOP by Galinskiy *et al.* (2020). The measured linewidths of the two cavities are 117 kHz and 128 kHz, respectively. Again the lock light is in a polarization orthogonal to the signal. We chose to use a combination of PBSs and quarter-wave plates such that the light reflected off the cavity would not return in the same path as it came. This way we suppress coupled cavity effects between the cavities in the path (cell and filter cavities).

We made the filter setup somewhat compact such that it fits on a 30 cm x 60 cm optical table. For that reason we chose to split the lock light for the two cavities on the same PBS where the overlapping with the scattered photons happens and input the lock light to the second cavity in the reverse direction. This turned out to be a design flaw. As indicated in Fig. 3.4 this opens a path for the quantum signal to bypass the cavities and still reach the detector. To remedy this flaw, we inserted a mechanical beam shutter in the bypass path to

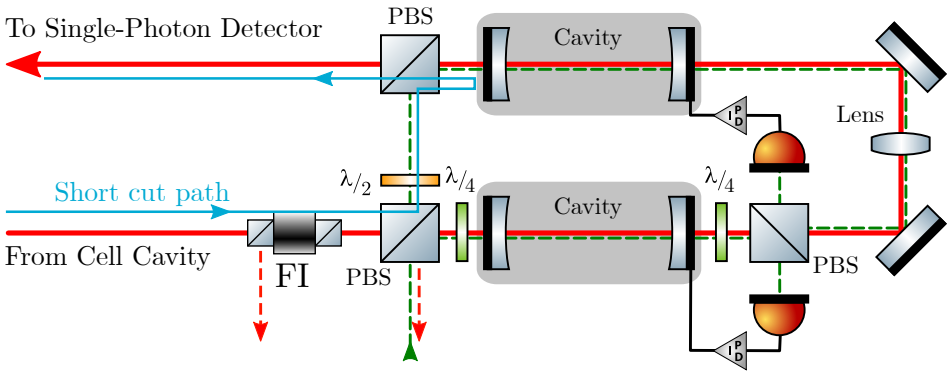

Figure 3.4: **Compact read filter setup.** Two sequential Fabry-Perot filters are locked with a beam (green, dashed line) split on the same PBS which combines with the light from the cell cavity. This enables an unintended short cut path for the cell cavity output light (blue line). A quarter-wave plate before the first cavity avoids that the cavity-reflected light returns to the cell cavity. However, reflection from the second cavity would still return if the Faraday isolator (FI) is removed.

block it during the freeze window.

The locking of the read setup is again done through lock-in detection. However, here the cavity resonance frequencies are modulated via the cavity piezos instead of the lock light frequency.

Where the write setup uses home-made analogue electronics for locking, the read locks were based on a more versatile digital platform. We use the cheap Red Pitaya field-programmable gate array (FPGA) board together with a modified version of the PyRPL software package (Neuhaus and Deléglise, 2017). Together with a PC-controlled relocking algorithm the modulation, demodulation and feedback happens on the FPGA board. This makes for an easily-deployable, fully-automatic lock.

To avoid limitations due to the finite bit resolution of the digital-to-analogue converter on the FPGA board, we use a two-channel lock routine. A coarse channel can scan more than a free-spectral range (FSR) of the cavity and is used to find the resonance. When close to resonance, the coarse channel freezes while the feedback is applied on a fine channel which also contains the modulation signal. The output of the two channels is combined on a summing amplifier that drives the cavity piezo.

In both write and read spectral filters we observe a suppression of about 60 dB of the excitation light over the transmission of the scattered light. Combined with the polarization filtering, the excitation light is suppressed to a degree where it is not limiting the experimental results.

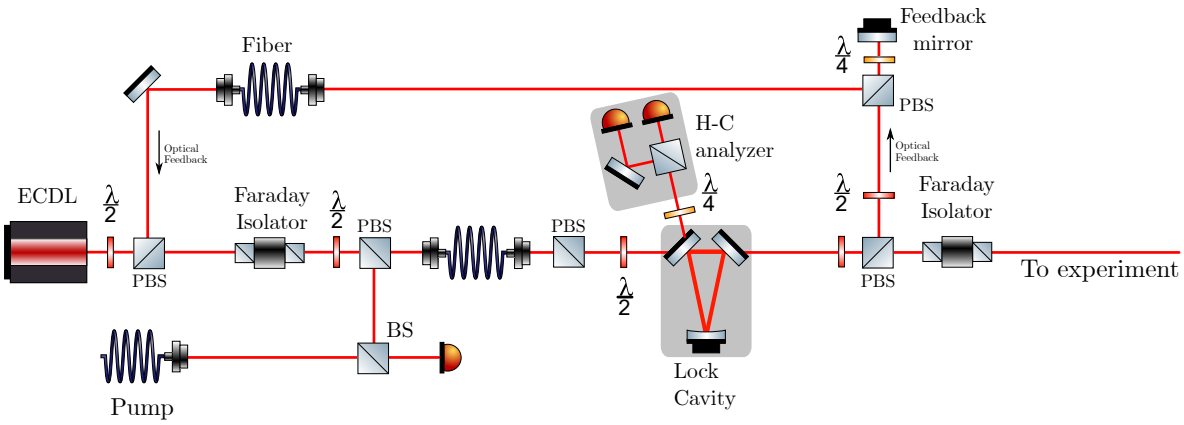

Figure 3.5: **Narrow-line laser setup.** An external-cavity diode laser (ECDL) is line-narrowed by optical feedback from a referenced 'lock' cavity. The details of the scheme are explained in the text. The figure is adapted from Zugenmaier (2018).

3.2.2 Excitation Laser

The spectral filters invoke a requirement on the excitation laser linewidth. In the DLCZ experiment, the scattering happens at a specific sideband frequency of the excitation laser. Therefore the laser linewidth must be narrower than the filter linewidth to avoid suppression due to spectral mismatch.

To meet the requirements we employ a custom-build laser source inspired by the optical-locking scheme by Hayasaka (2011). In the scheme, a home-build external-cavity diode laser (ECDL) is locked to a narrow-linewidth cavity via resonant optical feedback. The setup is illustrated in Fig. 3.5. The output of the ECDL is coupled to a triangular 'lock' cavity and the reflection is used to analyze the cavity detuning in the modulation-free Hänsch-Couillaud method (Hänsch and Couillaud, 1980). The transmission is split on a PBS such that a small fraction impinges on a phase-stabilizing feedback mirror that reflects the cavity-transmitted light back into the ECDL. The feedback mirror is attached to a piezo that controls the phase of the feedback light. A PID controller stabilizes the feedback phase in an electronic feedback loop using the Hänsch-Couillaud error signal.

In this setup the lock cavity acts both as a spectral filter of the ECDL light and as a reference cavity for optical feedback. Through a beat note measurement with a narrow line reference laser, the laser output linewidth was determined with an upper limit of 30 kHz (FWHM) in 200 µs (Dideriksen, 2014b).

We designed the lock cavity such that it is mounted on the same spacer as the triangular filter cavity described above - one above and one below a 0.75 m H-profile aluminium bar. The idea was to have suppression of common-mode noise from the mechanical modes of the spacer. While this is achieved to some extent, we still observe substantial noise from spacer

bending modes with anti-correlated path length excursion. More details on the laser system can be found in Zugenmaier (2018) and Dideriksen (2014a).

In order to lock the excitation laser with respect to the caesium line, we beat it against the pump laser (locked on the $4 \rightarrow 4'$ transition). The beating frequency is analyzed in an RF electronic interferometer in the scheme of Schünemann *et al.* (1999). Via a PID controller the error signal is fed back to the piezo of the lock cavity thereby stabilizing the laser frequency.

In the DLCZ experiment we need excitation light in well defined write and read pulses. We use the first-order diffraction of an AOM to control the pulses. The amplitude of the RF drive is used to shape the pulses.

3.2.3 Single-photon detection

At the output of the filter stages, the single-photon detectors are located. In the early D_2-line experiment we used a single-photon avalanche detector (LaserComponents Count-10) while for the D_1-line experiment we used super-conducting nanowire single-photon detectors (SNSPDs from Photon Spot). Though the operation principle of the two types of detectors is very different, the output signal is very similar. For each photon impinging on the detector a fast pulse is output with a finite probability, the quantum efficiency. A pulse is followed by a 'dead' time where new impinging photons cannot generate an output pulse. Because of this behaviour single-photon detectors are often referred to as "click" detectors. If there is light on the detector, it gives a click but it does not resolve the light power. However, if the photon flux is low, such that the mean time separation between clicks by far exceeds the dead time, the detector click rate is linear in the input power.

In the case of the present DLCZ experiment the pulses during which we aim to detect single photons are tens of microsecond long. This is significantly larger than the detector dead time which is less than 50 ns for both detector types. Therefore the single-photon detectors are effectively photon-number resolving within the long pulses for up to several photons per pulse without need for dead time correction. This feature enables the use of a single detector to measure the second-order auto-correlation whereas typical auto-correlation measurements of short pulses involve two detectors in a Hanbury-Brown-Twiss setup.

Electronic noise of the detectors causes 'dark' counts to appear even when the optical input is blocked. Because of the long pulses in the experiment, the obtained results are sensitive to the dark count rate. More precisely, the detector signal-to-noise ratio (SNR) for a single photon is given by $\eta_{\mathrm{qe}}/(t_{\mathrm{p}} r_{\mathrm{dark}})$ where η_{qe} is the quantum efficiency, t_{p} is the pulse duration and r_{dark} is the dark count rate. Here the SNSPDs excel over other detector types since $\eta_{\mathrm{qe}} > 90\%$ is available for near-infrared light and r_{dark} can be far below 1 Hz. Practically, the background count rate is limited by screening of stray light from the detector. In the experiment we operate far below a mean photon rate of one per pulse. Hence, the detector SNR must be much higher than one (rather in the thousands) to suppress dark

count pollution. For pulses of 50 µs, the intrinsic detector SNR is greater than 10^4 for our SNSPDs.

3.2.4 FPGA sequence control

At the heart of the experiment we employ a custom-configured FPGA board to control the experiment. We define the experimental sequence and evaluate it on the FPGA board from where triggers and pulse shapes are distributed to the individual experimental apparatus. As such, the FPGA operates as the experiment clock. The pulses from the single-photon detectors are input on the FPGA where they are time tagged with respect to the experimental cycle. All time tags are stored on a hard drive for later processing.

Due to the low excitation probability and long light pulses the experiment has to run for hours for each data point to have enough trials to estimate correlation values with satisfactory statistical uncertainty. On this timescale, the experiment is prone to slow drifts, particularly in propagation losses because of cavity misalignment. To mitigate the influence of drifts on results, we interleave trials for different sets of parameters. The FPGA randomly picks from a set of predefined experimental sequences with different parameters such that interleaving happens on the one second time scale.

3.3 Characterization

3.3.1 Optical depth

As discussed in section 2.5 the figure of merit for the performance capability of an ensemble-based quantum memory is the optical depth (OD). Here we present a characterization measurement to estimate the atomic density in the cell from which we can calculate the hypothetical OD.

The measurement is performed as illustrated in Fig. 3.6 by simply sending a weak probe beam through the ensemble and recording the transmission power on a photodetector behind the cell while scanning the probe frequency. The probe has to be kept sufficiently weak to avoid saturating the atomic transitions. For microcells this typically means $< 50\,\mathrm{nW}$.

We use probe light at the D_2 line and scan the probe light across both hyperfine ground-state transitions. The recorded signal displays the Doppler-broadened transitions separated by 9.2 GHz, see Fig. 3.6. For a sample of low optical depth (e.g. a microcell at room temperature), the atomic density can be well estimated by simply integrating over the absorption dips (see Fabricant, 2014, as an example). However, when the OD becomes appreciable, a more reliable estimate can be obtained from fitting. We fit an absorption model which accounts for the Voigt profile of the different transitions involved and their absolute strengths. The fitting algorithm was developed by Schmieg (2018).

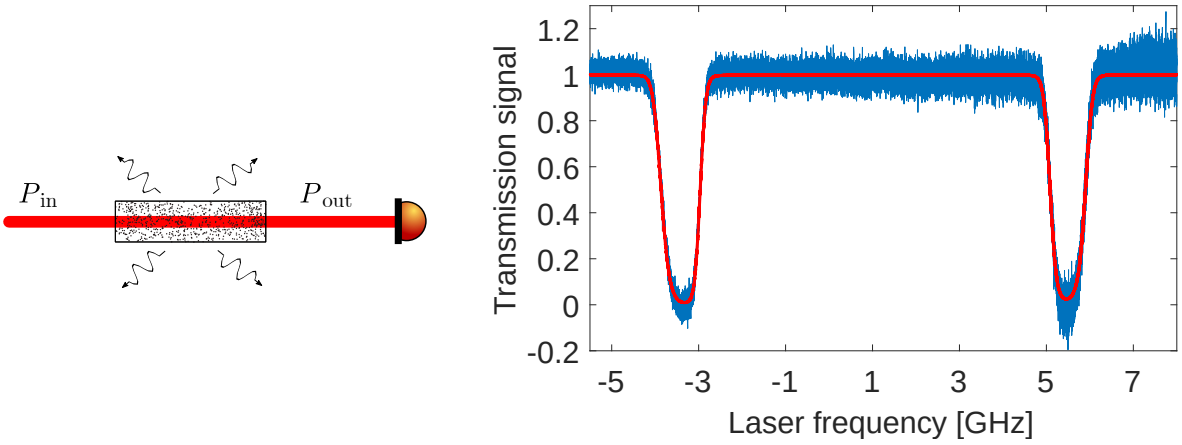

Figure 3.6: **Atomic density measurement on the D_2 line.** For the cell "G2" at 42.2 °C. We see the absorption lines for the two ground state hyperfine levels. The splitting of the excited states is smaller than the Doppler broadening and hence not resolved. The yellow line is a fit of the model in eq. (3.3).

The frequency-dependent attenuation of the probe light can be described by an absorption coefficient, $\alpha(\nu)$, from Beer-Lambert's law

$$\frac{P_{\text{out}}}{P_{\text{in}}} = e^{-\rho\sigma(\nu)L_z} = e^{-\alpha(\nu)L_z}, \tag{3.1}$$

where σ is the atomic density, $\sigma(\nu)$ is the absorption cross section and L_z is the sample depth. The absorption spectrum is given by the Voigt function

$$S_{FF'}(\nu) = \int_{-\infty}^{\infty} \mathrm{d}\nu' \, \frac{\frac{\gamma}{4\pi^2}}{(\nu - \nu_{FF'})^2 + \left(\frac{\gamma}{4\pi}\right)^2} \frac{e^{-\ln 2 \frac{(\nu-\nu')^2}{\Gamma_{\text{D}}^2}}}{\sqrt{\frac{\pi}{\ln 2}}\Gamma_{\text{D}}}, \tag{3.2}$$

i.e. the convolution of Doppler broadening with HWHM $\Gamma_{\text{D}} = 233\,\text{MHz}$ and the natural line centred at the transition frequency of $F \to F'$. The excited state decay rate is $\gamma = 2\pi \cdot 5.23\,\text{MHz}$. The Voigt function is then weighted according to the relative transition strength $A_{FF'm_F}$ given by Clebsch-Gordan coefficients (for a table of values see Steck, 2010). Thus,

$$\alpha(\nu) = k_1 \sum_{F,F',m_F} A_{FF'm_F} S_{FF'}(\nu) \ . \tag{3.3}$$

k_1 is a fit parameter which is proportional to the atomic density. Here we assume a uniform distribution of atoms between all ground state levels. Since the probe power is low, this is a good assumption.

By integrating over the data-fitted theoretical absorption spectrum and normalizing to the atomic absorption cross-section, σ, we find the atomic density

$$\rho = \frac{\int_0^\infty \alpha(\nu)\mathrm{d}\nu}{\int_0^\infty \sigma(\nu)\mathrm{d}\nu} = \frac{1}{\pi c r_e f} \int_0^\infty \alpha(\nu)\mathrm{d}\nu \ . \tag{3.4}$$

where $r_e = 2.8179 \times 10^{-15}\,\mathrm{m}$ is the electron radius and $f = 0.7164$ is the D_2-line absorption oscillator strength including the degeneracy of the level structure (Steck, 2010). Here we have used $\int_0^\infty \sigma(\nu)\mathrm{d}\nu = \pi c r_e f$ (Foot, 2005).

Because of the high OD in the centre of the absorption dip, where the beam is almost fully absorbed, the fit becomes mostly sensitive to the width of the dip rather than the actual level at the dip centre. The sensitivity to the width then calls for a careful calibration of the laser frequency scan. To that end the probe light is simultaneously sent to a Mach-Zehnder interferometer to correct for non-linearities in the frequency scan. The hyperfine splitting of the ground states can then serve as the absolute frequency reference.

One might notice in Fig. 3.6 that the signal-to-noise ratio decreases for increasing laser frequency. This is an artefact of the laser scan also changing the probe power. The transmission data is corrected for the input probe power dependency on frequency. The dominating noise source is the detector electronic noise.

For the cell used in the DLCZ experiments (internally labelled "G2"), we obtain an atomic density $\rho = (25 \pm 3) \times 10^{16}\,\mathrm{m}^{-3}$ at the operation temperature $T = 42.2\,^\circ\mathrm{C}$. The error is a conservative estimate from the fit residuals. Hence, the corresponding number of atoms inside the microchannel is $N = 300\,\mu\mathrm{m}^2 \cdot 10\,\mathrm{mm} \cdot \rho = (0.22 \pm 0.02) \times 10^9$. For a fully-polarized ensemble, the optical depth on the D_1, π-polarized, $|4,4\rangle \rightarrow |4',4'\rangle$ transition can then be calculated according to eq. (2.37)

$$d_\pi = 3\beta_{44}\frac{\lambda^2}{2\pi}\rho L_z = \frac{\lambda^2}{2\pi}\rho L_z = (0.32 \pm 0.03) \times 10^3 \tag{3.5}$$

where we have included the branching ratio $\beta_{44} = 1/3$ of spontaneous-emission decay from the excited state $|4',4'\rangle$ to $|4,4\rangle$ (Steck, 2010). $\lambda = 894.6\,\mathrm{nm}$ is the D_1-line wavelength and L_z is the cell length.

3.3.2 Magneto-optical resonance spectroscopy

One of the most important characterization techniques that we employ is magneto-optical resonance spectroscopy (MORS) – also sometimes referred to as RF spectroscopy. The concept is to record the atomic response to an external AC magnetic field by mapping the collective spin state onto light. The technique can be used for determining transverse spin coherence time T_2 as well as the atomic population distribution. The latter is especially of interest when optimizing optical pumping where typically the goal is to achieve the highest possible atomic spin orientation.

Here we will present an outline of the technique and show how the atomic population distribution is mapped to the recorded photo detector signal. We will discuss some recent refinements of the technique developed over the course of the PhD work and apply MORS to optimize

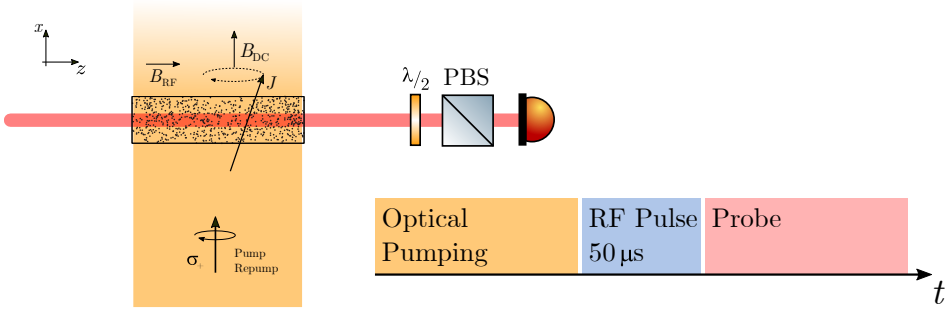

Figure 3.7: **Pulsed magneto-optical resonance spectroscopy.** Initially the atomic ensemble is optically pumped. Then an RF pulse generates an RF magnetic field perpendicular to the bias magnetic field. The pulse tilts the macroscopic atomic spin that precesses around the magnetic field. Linearly polarized probe light maps the spin component J_z onto the light Stokes component S_y which is recorded on a photodetector by measuring the light polarization at 45°.

and characterize the atomic system.

The idea was presented by Julsgaard *et al.* (2004b) who mainly focussed on continuous pumping and probing while sweeping the magnetic field RF frequency across the atomic resonance. Since the DLCZ scheme is a pulsed scheme where the optical pumping is turned off prior to experiments, we would rather like to probe the atomic state in a pulsed pumping scheme. The pulsed MORS scheme is depicted in Fig. 3.7. Initially the atomic ensemble is optically pumped using both pump laser and repump laser. Immediately after the pumping beams are turned off, a short pulse (typ. 50 µs) RF current is run through a Helmholtz coil pair inside the magnetic shield. This produces an RF magnetic field transverse to the bias magnetic field which will tilt the macroscopic atomic spin away from alignment with the bias field and it will start to precess.

Immediately after the RF pulse stops, off-resonant probe light is turned on and after interacting with the ensemble the probe polarization is analysed on a photo detector. The spin precession is mapped onto the probe light polarization.

A central difference to the method used by Julsgaard *et al.* (2004b), and later also by Chalupczak *et al.* (2018), is that the magnetic RF signal is not applied continuously (single frequency or sweep) but instead applied as a short pulse between pumping and probing. In this fashion the probe signal measures the kick response of the macroscopic atomic spin.

An example of the pulsed MORS signal is displayed in Fig. 3.8. The data in the figure was recorded with the bias magnetic field turned off leaving only the residual field that is not screened by the magnetic shield. We see clearly how the precession is excited by the RF pulse and decays while being probed. It is important that the probe intensity is low to avoid additional decay from light absorption.

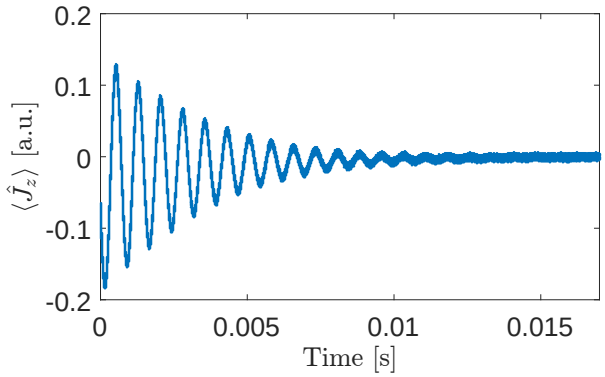

Figure 3.8: **Example of pulsed magneto-optical resonance spectroscopy signal.** With no bias magnetic field applied, the Larmor frequency is set by the residual field inside the magnetic shield. Here the Larmor frequency is 1.3 kHz.

Macroscopic spin

First we expand the macroscopic spin operators defined in section 2.3 to include the nuclear spin of caesium. Typically, the laser detuning is chosen such that interaction only happens with one of the hyperfine manifolds F. We will therefore describe the macroscopic spin within a single hyperfine manifold. The three macroscopic spin components can be written as

$$\hat{J}_x = \sum_{k=1}^{N} \sum_{m_F=-F}^{F} m_F \hat{\sigma}^{(k)}_{m_F m_F} \tag{3.6}$$

$$\begin{aligned} \hat{J}_y &= \frac{1}{2} \sum_{k=1}^{N} \sum_{m_F=-F}^{F-1} C(F, m_F) \left(\hat{\sigma}^{(k)}_{m_F+1, m_F} + \hat{\sigma}^{(k)}_{m_F, m_F+1} \right) \\ &= \sum_{k=1}^{N} \sum_{m_F=-F}^{F-1} C(F, m_F) \, \mathrm{Re} \left[\hat{\sigma}^{(k)}_{m_F+1, m_F} \right] \end{aligned} \tag{3.7}$$

$$\begin{aligned} \hat{J}_z &= \frac{1}{2i} \sum_{k=1}^{N} \sum_{m_F=-F}^{F-1} C(F, m_F) \left(\hat{\sigma}^{(k)}_{m_F+1, m_F} - \hat{\sigma}^{(k)}_{m_F, m_F+1} \right) \\ &= \sum_{k=1}^{N} \sum_{m_F=-F}^{F-1} C(F, m_F) \, \mathrm{Im} \left[\hat{\sigma}^{(k)}_{m_F+1, m_F} \right] \end{aligned} \tag{3.8}$$

with $C(F, m_F) = \sqrt{F(F+1) - m_F(m_F+1)}$ (Julsgaard *et al.*, 2004b). In this case we can also define a spin lowering operator as $\hat{J}_- = \hat{J}_y - i\hat{J}_z$. From the linear sums in the macroscopic operators we see that we can consider the individual spin operators by removing the sum over atoms. All experiments are performed with a high degree of atomic polarization which means that we can apply the Holstein-Primakoff approximation and replace the operator $\hat{J}_x$ with its expectation value J_x (see chapter 2). Furthermore, we will consider an open system where the longitudinal spin decay as $J_x(t) = J_x(0)e^{-t/T_1}$ and the transverse spin as $\langle J_{yz}(t) \rangle = \langle J_{yz}(0) \rangle \, e^{-t/T_2}$.

Macroscopic light

Similarly, it is beneficial to describe the polarization modes of light in terms of Stokes operators instead of annihilation operators $\hat{a}_i$. For light propagating along z-axis we have

$$\hat{S}_x = \frac{1}{2}(\hat{n}_x - \hat{n}_y), \tag{3.9}$$

$$\hat{S}_y = \frac{1}{2}(\hat{n}_D - \hat{n}_A), \tag{3.10}$$

$$\hat{S}_z = \frac{1}{2}(\hat{n}_+ - \hat{n}_-). \tag{3.11}$$

The three components of the Stokes vector $\hat{\vec{S}}$ are then the intensity difference between orthogonal polarization modes in three bases: horizontal/vertical, diagonal/anti-diagonal, and right/left-hand circular. In the following we will assume that the input light is horizontally polarized such that $\left\langle \hat{S}_y^{\text{in}} \right\rangle = \left\langle \hat{S}_z^{\text{in}} \right\rangle = 0$ and we can replace $\hat{S}_x$ with its expectation value S_x similar to the macroscopic spin operator.

Input-Output relations

The atom-light interaction has been treated by Julsgaard (2003) and Hammerer *et al.* (2010) who show that the input-output relations of light travelling through an ensemble of atoms is

$$\hat{S}_y^{\text{out}} = \hat{S}_y^{\text{in}} + aS_x\hat{J}_z. \tag{3.12}$$

I.e. the atomic spin component along the light propagation direction will rotate the linear input light polarization by an angle proportional to $a\left\langle \hat{J}_z \right\rangle$ where the vector polarizability a is a function of probe light detuning. This is known as the Faraday effect. As a result the atomic spin $\hat{J}_z$ is mapped onto the $\hat{S}_y$-component of light. All MORS measurements are performed far detuned (typically $\sim 2\,\text{GHz}$ blue of the D_2 line $4 \rightarrow 5'$ transition) to avoid absorption. Please note that we have omitted the back-action term $\frac{\partial}{\partial t}\hat{J}_y = aJ_x\hat{S}_z^{\text{in}}$ which couples light input noise to the macroscopic spin (Julsgaard, 2003). For a coherently driven spin oscillation the back-action will be insignificant.

We measure the output light polarization by first rotating the polarization by 45° through a half-wave plate and measuring the light intensity after a horizontal polarizer (see Fig. 3.7). This can be viewed as a self-homodyne measurement of the vertical polarization mode where the horizontal mode is used as a local oscillator (LO). Since the two are propagating together, the relative phase is passively stable. For small rotation angles, the detector photo current is proportional to the angle and we have $I(t) \propto \left\langle \hat{S}_y^{\text{out}}(t) \right\rangle = aS_x\left\langle \hat{J}_z(t) \right\rangle$ plus an uninteresting DC offset $I_{\text{DC}} \propto S_x$.

Response function

When the atomic ensemble is put in an external magnetic field, the spin interaction will give

rise to the Zeeman effect described by the Hamiltonian $\hat{H}_{\rm Z} = g_F \mu_{\rm B} \hat{\vec{j}} \cdot \vec{B}$. For now we ignore the higher order terms in $\vec{B}$.

For a bias DC magnetic field the atomic spin will be precessing around the magnetic field at the Larmor frequency $\nu_{\rm L} = g_F \mu_{\rm B} B_{DC}/h$ while an RF magnetic field, $B_{\rm RF}\sin(\omega t)$, transverse to the bias field excites coherence between the magnetic sublevels (see Julsgaard *et al.*, 2004b, for a detailed derivation). To understand the interaction it is sufficient to consider single atom interaction. The Zeeman Hamiltonian of a specific Hyperfine manifold F is then (in the rotating wave approximation)

$$\hat{H}_Z = h\nu_{\rm L}\hat{j}_x + \frac{g_F\mu_{\rm B}}{4}\left(\hat{j}_- B_{\rm RF} e^{i\omega t} + \text{h.c.}\right). \tag{3.13}$$

From the Hamiltonian we get the Heisenberg equation of motion

$$\frac{\partial\hat{\tilde{\sigma}}_{m_F,m_F+1}}{\partial t} = \left(i\Delta\omega_{m_F} - \Gamma/2\right)\hat{\tilde{\sigma}}_{m_F,m_F+1} + \frac{ig_F\mu_{\rm B}B_{\rm RF}}{4\hbar}C(F,m_F)(\hat{\sigma}_{m_F+1,m_F+1} - \hat{\sigma}_{m_F,m_F}) \tag{3.14}$$

with $\Delta\omega_{m_F} = \omega - \omega_{m_F+1,m_F}$. Here we have added the decoherence $\Gamma = 2/T_2$ but ignore the associated noise forces since the RF excitation is much stronger. The tilde indicates the rotating frame $\hat{\tilde{\sigma}}_{jk} = \hat{\sigma}_{jk}e^{i\omega t}$. Here we consider the coherences between neighbouring Zeeman levels instead of the spin projections because the aim is to operate at high enough magnetic field that the we can resolve the Zeeman resonances because of quadratic splitting. The resonance frequencies ω_{m_F+1,m_F} are different because of a quadratic term in $\hat{H}_{\rm Z}$ which give rise to a quadratic Zeeman splitting (Julsgaard, 2003)

$$\nu_{\rm QZ} = \frac{2\nu_{\rm L}^2}{\nu_{\rm HFS}} \tag{3.15}$$

where $\nu_{\rm HFS} = 9.1926\,\text{GHz}$ is the hyperfine splitting. This implies a second-order correction to the first term in eq. (3.13) such that

$$\frac{\omega_{m_F+1,m_F}}{2\pi} = \nu_{\rm L} - \nu_{\rm QZ}(m_F + 1/2). \tag{3.16}$$

At our operating Larmor frequency $\nu_{\rm L} = 2.4\,\text{MHz}$ we get a quadratic splitting of $\nu_{\rm QZ} = 1.25\,\text{kHz}$.

For a stationary RF field, the solution to eq. (3.14) is

$$\begin{aligned}\hat{\tilde{\sigma}}_{m_F,m_F+1}(t) = {}& \hat{\tilde{\sigma}}_{m_F,m_F+1}(0)e^{(i\Delta\omega_{m_F}-\Gamma/2)t} \\ & - \frac{ig_F\mu_{\rm B}B_{\rm RF}}{4\hbar}C(F,m_F)\frac{1-e^{(i\Delta\omega_{m_F}-\Gamma/2)t}}{i\Delta\omega_{m_F}-\Gamma/2}[\hat{\sigma}_{m_F+1,m_F+1}(0) - \hat{\sigma}_{m_F,m_F}(0)]\end{aligned} \tag{3.17}$$

where we assume that the population does not vary during the time t. In the continuous MORS the frequency scan is slow enough that the coherences $\hat{\tilde{\sigma}}_{m_F,m_F+1}$ follow adiabatically

and we reach the response function (Julsgaard, 2003)

$$\hat{\tilde{J}}_z(\omega) = \mathrm{Im}\left[\frac{ig_F\mu_B B_{RF}N}{4\hbar}\sum_{m_F=-F}^{F-1}\frac{F(F+1)-m(m+1)}{i(\omega_{m_F+1,m_F}-\omega)-\Gamma_{m_F+1,m_F}/2}(\hat{\sigma}_{m_F+1,m_F+1}-\hat{\sigma}_{m_F,m_F})\right] \tag{3.18}$$

This corresponds to the transfer function of $2F$ superposed harmonic oscillators (in the high-Q approximation). The relative amplitude of the oscillators in eq. (3.18) is given by the population difference between neighbouring Zeeman levels, $\langle\hat{\sigma}_{m_F+1,m_F+1}-\hat{\sigma}_{m_F,m_F}\rangle$. Hence, this signal can be used to measure the population distribution within the hyperfine manifolds. We also assume that all coherences are subject to the same broadening $\Gamma = \Gamma_{m_F+1,m_F}$.

Pulsed MORS

In our pulsed scheme, we apply an RF pulse which is much shorter than the coherence time, $t_{RF} \ll T_2$. The RF pulse consists of a single tone running for a fixed number of cycles where the number of cycles is low enough that spectral width of the RF pulse is much broader than the separation of resonance frequencies, i.e. $t_{RF} \ll 1/\nu_{QZ}$. In this regime, the RF pulse corresponds to a "kick" where all oscillators see the same driving amplitude. The coherences after the RF kick are described by eq. (3.17) where we can assume $\left\langle\hat{\tilde{\sigma}}_{m_F,m_F+1}\right\rangle(t=0) = 0$ after optical pumping. Because of the quadratic splitting, the different Zeeman resonances will acquire different phases from the RF excitation. The phase and amplitude of $\left\langle\hat{\tilde{\sigma}}_{m_F,m_F+1}(t_{RF})\right\rangle$ after the kick is calculated from eq. (3.17) and illustrated in Fig. 3.9 as a function of RF detuning $\Delta\omega_{m_F}$. After the pulse we observe the superposed damped harmonic oscillation which is described by the inverse Fourier transform of eq. (3.18) and exemplified in Fig. 3.8. Because of the RF kick, there will be a relative phase between the coherences $\hat{\tilde{\sigma}}_{m_F,m_F+1}$ that needs to be factored in for each term in eq. (3.18).

We record the time trace and average over many trials (~ 500) to suppress incoherent noise. The averaged time trace is then Fourier transformed (FFT) and the model in eq. (3.18) is fitted to the complex Fourier data.

Population models

In the original technique (Julsgaard *et al.*, 2004b), the authors reduced the number of fit parameters by assuming that the population distribution follows a thermal distribution. For a given atomic orientation p the population distribution would be the one that maximizes the entropy. They find that atoms are exponentially distributed according to $\langle\hat{\sigma}_{m_F,m_F}\rangle \propto \epsilon^{4-m_F}$. The population-difference terms in eq. (3.18) are then

$$\langle\hat{\sigma}_{m_F+1,m_F+1}-\hat{\sigma}_{m_F,m_F}\rangle \propto \epsilon^{4-m_F}(\epsilon^{-1}-1) \tag{3.19}$$

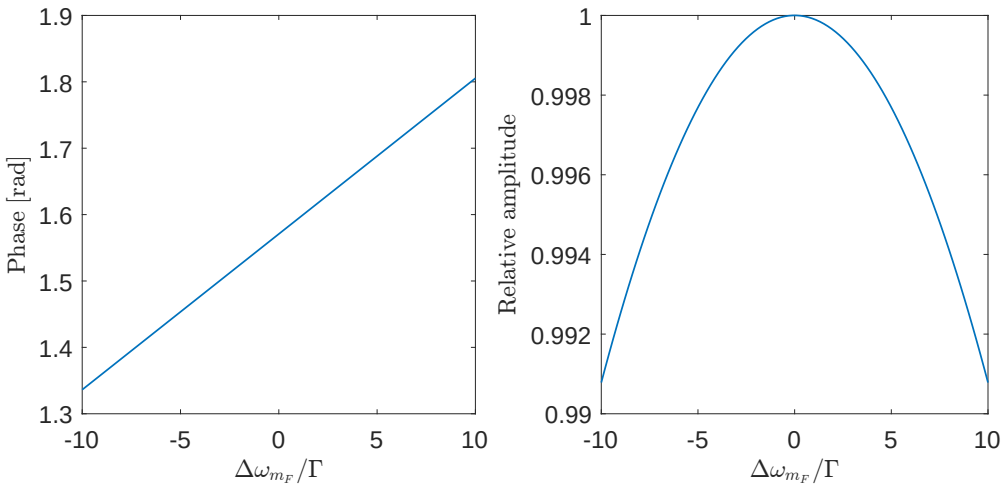

Figure 3.9: **RF pulse response of the Zeeman coherences $\hat{\tilde{\sigma}}_{m_F,m_F+1}$.** The phase and relative amplitude was calculated from eq. (3.17) with $t_{\mathrm{RF}}\Gamma = 0.0471$ which matches the typical values $t_{\mathrm{RF}} = 50\,\mu\mathrm{s}$ and $\Gamma = 2\pi \cdot 150\,\mathrm{Hz}$. A separation equal to the quadratic splitting at $\nu_{\mathrm{L}} = 2.4\,\mathrm{MHz}$ is then $\omega_{\mathrm{QZ}} = 8.3\Gamma$.

This assumption has worked very well in the group over the years for reproducing the MORS data. The reduction of fit parameters has been key to the successful fitting of the model to data. However, when we reach very high atomic polarization in the microcells, we observe a poor consistency between this model and the data.

In the very high atomic polarization limit, most of the $2F$ peaks vanish, simply because the corresponding atomic levels are empty. Usually, we are able to distinguish three peaks determined by atomic levels $m_F \in \{1, 2, 3, 4\}$. Therefore we restrict the MORS model to just three oscillators where the peak heights are independent fit parameters. The same model was explored by Schmieg (2019).

Furthermore, we observe that the ability for the fitted model to reproduce the data improves when including a relative phase between the peaks. This is specific to pulsed MORS experiments where the atomic response does not reach steady-state evolution, as opposed to continuous MORS. The phase will depend on the kick duration and the delay time after the kick before data is acquired, as expressed in eq. (3.17) and Fig. 3.9. The reason is the frequency difference between the peaks that leads to a relative displacement of the phases.

In this model the population-difference terms in eq. (3.18) are replaced by complex fit

parameters

$$\begin{aligned}\langle\hat{\sigma}_{4,4}-\hat{\sigma}_{3,3}\rangle &\to A_{4,3}\\ \langle\hat{\sigma}_{3,3}-\hat{\sigma}_{2,2}\rangle &\to A_{3,2}\\ \langle\hat{\sigma}_{2,2}\rangle &\to A_{2,1}\\ \langle\hat{\sigma}_{m_F,m_F}\rangle &= 0 \quad \text{for } m_F \in [-4,1]\ .\end{aligned} \tag{3.20}$$

A comparison of the fitted models is shown in Fig. 3.10. From eq. (3.17) the relative phase ϕ_{RF} of two coherences with 1.25 kHz splitting and $\Gamma = 2\pi \cdot 150\,\mathrm{Hz}$ after a 50 µs RF kick is $\phi_{\mathrm{RF}} = 0.20$. In our analysis we wait an extra 30 µs after the kick before the Fourier analysis starts. During this time, the relative phase will acquire an extra $\phi_{\mathrm{wait}} = 2\pi\nu_{\mathrm{QZ}}t_{\mathrm{wait}} = 0.24$ (cf. eq. 3.17 with $B_{\mathrm{RF}} = 0$). Hence we expect the total relative phase $\phi = 0.44$. When fitting to experimental data, we typically find a relative phase between the two dominating peaks in the range 0.25 to 0.35. Even though the fit phase does not match the expected value exactly, it does indicate that the interference dip between peaks can be explained by the phase induced from the RF kick and subsequent wait time.

Typically, the model has been fitted to the power spectral density $\left|\left\langle \hat{\tilde{J}}_z(\omega)\right\rangle\right|^2$ even though this means neglecting the phase information. We have found that the fit is more stable when fitting to the complex Fourier signal and the measurement-to-measurement fluctuations decrease. The explanation for this is straight forward when inspecting the Fourier data in Fig. 3.10. The two minor peaks are much more pronounced in the phase component than in the magnitude.

The comparison in Fig. 3.10 shows that the spectrum of the recorded data is incompatible with the thermal distribution model. The amplitude of the third peak is consequently underestimated. From here on we shall therefore use the "free" population model (eqs. 3.20) when determining atomic orientation.

Atomic orientation

It is common to give the macroscopic atomic spin orientation as a single parameter $p \leq 1$ which is the projection of $\hat{\vec{F}}$ onto the maximally polarized state with $\langle\hat{\sigma}_{4,4}\rangle = 1$. It is defined as

$$p = \frac{1}{F}\sum_{m_F=-F}^{F} m_F\,\langle\hat{\sigma}_{m_F,m_F}\rangle\ . \tag{3.21}$$

We typically achieve $p > 98\%$ with $\langle\hat{\sigma}_{3,3}\rangle$ as the dominating population after $\langle\hat{\sigma}_{4,4}\rangle$. Under this condition the population in $|3,3\rangle$ is approximately $\langle\hat{\sigma}_{3,3}\rangle \approx 4(1-p)$.

Ensemble excitation

The above analysis only concerns the individual atomic response whereas the Faraday interaction is enhanced by the number of atoms (optical depth). It is instructive also to consider

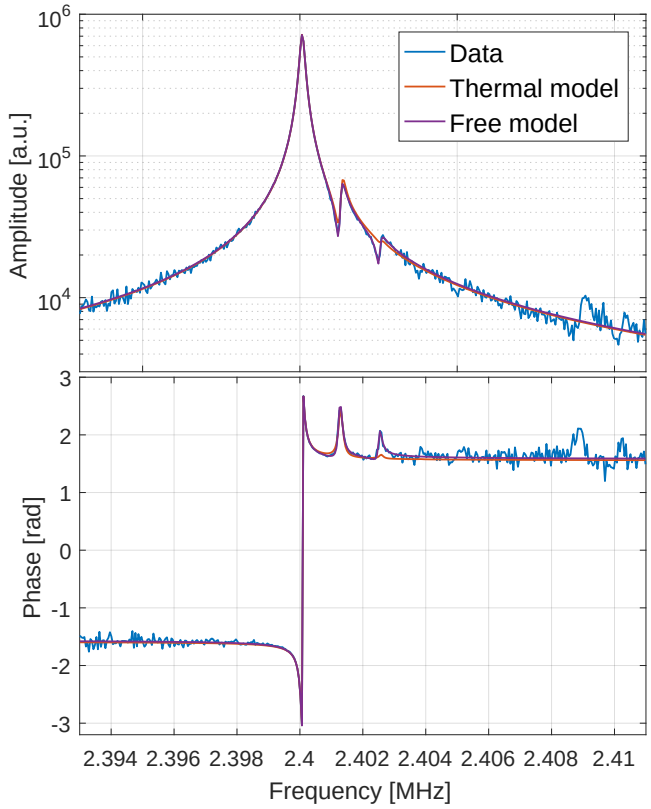

Figure 3.10: **Comparison of atomic population models.** Models of the form in eq. (3.18) are fitted to the pulsed MORS signal in the Fourier domain. The spectrum clearly contains interference dips between peaks because of the relative phase displayed in Fig. 3.9. The thermal model has one fit parameter to the population distribution as in eq. (3.19) and independent phases $e^{i\phi_{m_F}}$ for the first three peaks. The free model has three complex fit parameters according to eqs. (3.20). The signal out at $\approx 2.409\,\mathrm{MHz}$ comes from the weakly coupled $F = 3$ manifold. The thermal model yields orientation $p = 99.2\%$ but clearly underestimates the amplitude of the third peak from the left. The free model yields $p = 98.8\%$ and reproduces both amplitude and phase well including the destructive interference inbetween peaks. Peak width is $\Gamma = 2\pi \cdot 156\,\mathrm{Hz}$ (FWHM) which is the typical value and corresponds to $T_2 = 2.04\,\mathrm{ms}$.

how the Zeeman interaction affects the collective atomic modes. Since the RF coil is large compared to the cell, we assume the amplitude to be uniform. Furthermore, the wavelength of the RF field is orders of magnitude longer than the cell. Hence, we can neglect any spatial dependency of $B_{\mathrm{RF}}(t)$. This means that the RF field is only interacting with the symmetric atomic mode. We can expand the Zeeman Hamiltonian in eq. (3.13) to the ensemble

interaction by summing over all atoms. The RF term then becomes

$$\hat{H}'_Z = \frac{g_F \mu_B}{4} \sum_{m=1}^{N} \left(\hat{j}_-^{(m)} B_{\mathrm{RF}}(t) + \mathrm{h.c.} \right) = \frac{g_F \mu_B \sqrt{N}}{4} \left(\hat{a}^\dagger B_{\mathrm{RF}}(t) + \mathrm{h.c.} \right) \tag{3.22}$$

where we have used the definition of the symmetric mode in eq. (2.25). This Hamiltonian is the generator for the displacement operator, hence, the RF pulse generates a coherent state in the symmetric mode. We can utilize this interaction to make controlled excitation of the symmetric mode in order to characterize the beam-splitter interaction during the read pulse of the DLCZ scheme.

3.3.3 Pumping Optimization

Having established the pulsed MORS technique we can now apply it to characterize our pumping state and to optimize the pumping. Since the performance of our source/memory system strongly depends on atomic noise, a substantial amount of work was put into optimizing the optical pumping to reach the highest possible atomic orientation.

Beam size

One of the first parameters that we saw could make a substantial impact on the pumped state was the pumping spatial mode. Originally the pumping beam was prepared to illuminate the full side of the cell glass chip. We realized that by focussing down the vertical waist to fit the microchannel height, the pumped state improved. We measured an increase in p from 97.8% to 98.7%. An explanation for this sensitivity could be that when the vertical extension of the pump beam is too large, light will be scattered at the microchannel floor and ceiling. The polarization of the scattered light is not well defined and therefore disturbs the pumping.

Similarly, we tested the horizontal waist sensitivity. Varying beam radius from 3.7 mm to 5.9 mm and optimizing horizontal collimation only gave marginal improvement. However, when clipping the beam on a diaphragm with variable-size aperture, we do observe a drop in the atomic polarization for aperture diameter smaller than 8 mm. The dependency is depicted in Fig. 3.11. Since we operate at a saturating pumping power, the atomic polarization is insensitive to small variations in power. Hence, the drop in atomic polarization is not explained by the reduced power from clipping but must be from poor filling of the cell. The point at 3 mm in Fig. 3.11 corresponds to approx. 200 µW pump light at the cell which is still in the saturated region.

Pump polarization

We also verified that the pumping is sensitive to the polarization of the pump laser light. The pump polarization is optimised with a set of quarter-wave and half-wave plate. Turning the

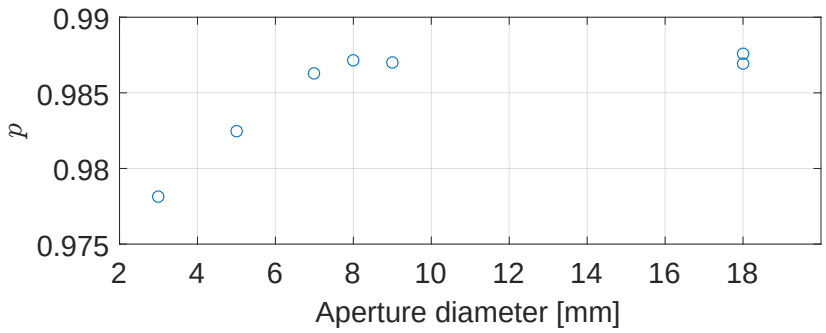

Figure 3.11: **Atomic orientation.** The pumping beam is clipped horizontally on a diaphragm with variable-size aperture.

waveplates by more than 4° away from the optimum angle reduces the atomic polarization by an amount that can be detected using the pulsed MORS method (approx. 0.1%).

Alignment of magnetic field and pumping light propagation

We also tested for the sensitivity to alignment of the pumping light propagation direction to the magnetic field direction. We can tilt the magnetic field by applying current in auxiliary coil sets on the coil frame. These coil sets produce a field along y and z, respectively. We can calibrate how much the bias field is tilted by monitoring the shift in Larmor frequency. We find that 1 A corresponds to 4.4°. This is the level of tilt where we start to see sensitivity. Thus, at our current level the atomic orientation is not extremely sensitive to this alignment.

Cell-to-cell variation

Since each cell is handmade and the whole process does not have a high degree of reproducibility, we test what level of atomic orientation can be reached in various cells. To that end we tested several cells. The variation can be found in Fig. 3.12. We see that there is some variation between the cells which could indicate that there is sensitivity to the production. In particular the cell J24 stands out with a noticeable higher atomic orientation. The design of this cell is also different from the rest in the sense that is does not have a encapsulating cylindrical cell. It consists of the glass chip with the microchannel to which small anti-reflection-coated windows have been laser bonded directly. The stem is directly attached to the chip via laser bonding, see Fig. 3.12. More details on this cell design can be found in Zugenmaier (2018). The advantage of the laser-bonded cell is that the microchannel can be accessed from the thin side of the chip without passing through encapsulating glass. This gives a cleaner interface for the pumping light and potentially a cleaner light polarization at the microchannel.

Unfortunately, the specific cell J24 has a broad linewidth which will limit the available storage time. Due to this we decided to use the cell G2. The short coherence time of J24

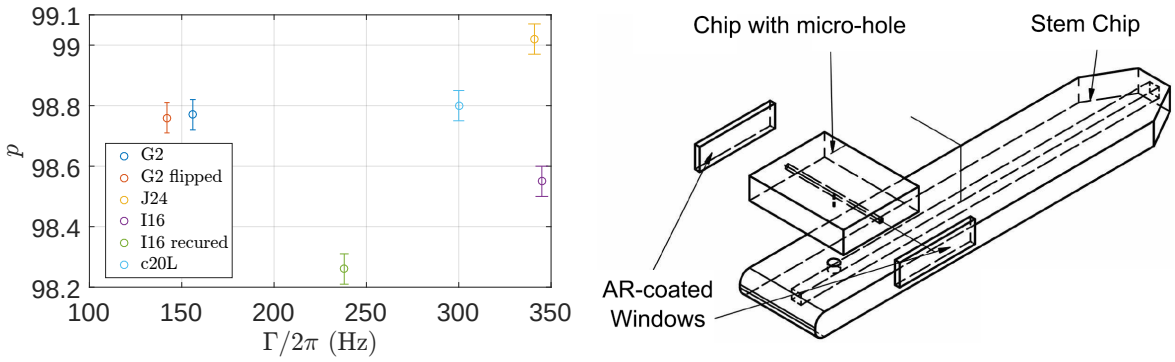

Figure 3.12: **Left: Maximally achieved atomic spin orientation for different cells vs. spin resonance linewidth.** The different cells are labelled according to internal catalogue. For the cell G2 we found a small variation when rotating 180 deg around the vertical. For the cell I16 both p and Γ reduced after a recuring cycle. Cells G2 and J24 are alkane coated while cells I16 and c20L are alkene coated. The different values of p were achieved without delayed pump laser turn-off. **Right: Laser-bonded cell design.** The glass chip with the microchannel is laser bonded to a 'stem' chip where glass blowing techniques for cell preparation can be performed without influencing the microchannel. Anti-reflection-coated windows are laser bonded to the micro chip to close off the the channel. Figure from Zugenmaier (2018).

is unlikely to be related to the cell design but rather originating from fabrication where we always see significant performance differences between cells of same design.

Delayed Pump turn-off

In the DLCZ scheme we are much more vulnerable to residual population in $|4,3\rangle$ than in the $F = 3$ manifold. This led us to try out what happens when the repump light is turned off before the pump light. The resulting atomic orientation can be found in Fig. 3.13. The data very clearly shows that p grows substantially until a pump turn-off delay of about 40 µs where it reaches a plateau at $p \approx 99.3\%$. Meanwhile, turning off the repump before the pump means that atoms will start populating the $F = 3$ manifold. This behaviour is apparent from the drop in the peak amplitude of the pulsed MORS signal. Also when comparing the raw pulsed MORS data of zero and 40 µs pump delay it is clear that the $F = 3$ signal at 2.41 MHz increases when the pump turn-off is delayed (Fig. 3.13). Based on this data we decide to conduct the DLCZ scheme using 40 µs delayed pump turn-off which also means that we sacrifice about 12 % of the optical depth.

Conclusion on pumping optimization

We observe that the spatial extent of the pumping beam has an influence on the atomic polarization and were able to improve by focusing the beam to minimize intensity on the

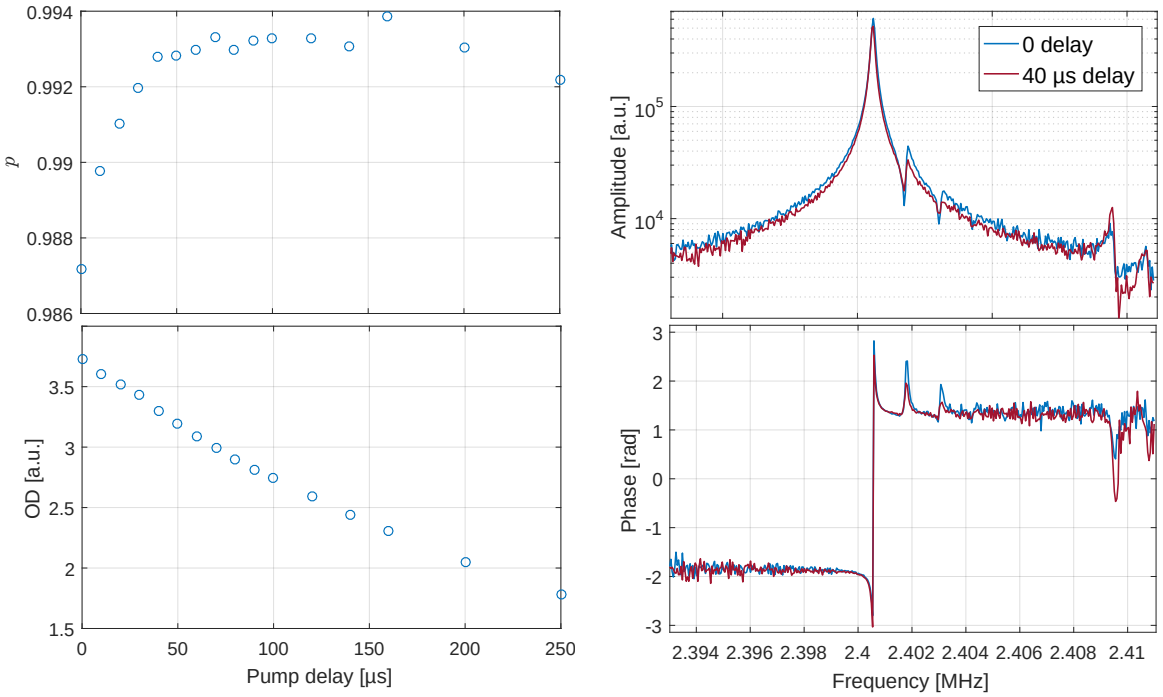

Figure 3.13: **Delayed Pump turn-off. Left:** Atomic orientation and optical depth vs. pump turn-off delay. The OD is proportional to the main MORS peak amplitude which is the value plotted. **Right:** Pulsed MORS spectrum for 0 and 40 µs pump turn-off delay. For the delayed turn-off the relative peak height of the second and third peaks decrease. Simultaneous the signal at ~ 2.41 MHz increases which demonstrates that atoms are transferred to the $F = 3$ manifold.

channel edges while still maintaining high beam filling of the cell.
In a comparison between different cells, we find that there is substantial variation. This indicates that fabrication influences the level of atomic polarization that can be obtained in the cell. The highest value was found from a miniaturized cell with good optical access.
Lastly, we find that a substantial improvement in the polarization of the $F = 4$ manifold can be obtained by keeping the pump laser on after the repump is turned off. Applying this technique the best orientation achieved is $p \approx 99.3\%$ immediately after the pumping stage.

3.3.4 Population decay in the dark

We can also use the pulsed MORS technique to track how the atomic population distribution evolves in the dark. This is done by increasing the time between the optical pumping stop and the RF kick. In Fig. 3.14 we plot the evolution of relative population of $|4,4\rangle$ and $|4,3\rangle$ while the ensemble decays in the dark. On the typical storage time scale of the DLCZ experiment we find that the decrease in $|4,4\rangle$ and the growth in $|4,3\rangle$ is approximately linear. Please note

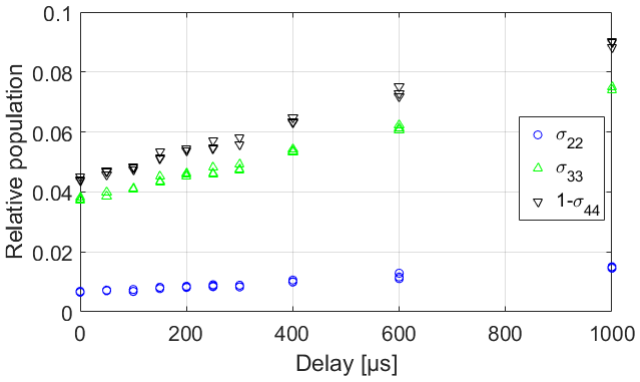

Figure 3.14: **Zeeman sublevel population vs. delay of the RF pulse.** The relative population is calculated from the free model. The pump turn-off is not delayed with respect to repump turn-off. First point corresponds to $p = 98.7\%$ from where the $|4,3\rangle$ population growth is approximately linear.

that in this measurement the pump and repump light turns off simultaneously.

A more detailed study of atomic population distribution evolution in the dark is presented by Zugenmaier (2018). Here also the $F = 3$ manifold is considered. Zugenmaier finds that the decay $|4,4\rangle$ to $|3,3\rangle$ is much more rapid than the decay to $|4,3\rangle$. The explanation for this decay branching is that the decay originates from two distinct processes: complete spin randomization and electron-spin randomization. The latter only weakly couples $|4,4\rangle$ to $|4,3\rangle$ because of the small overlap with the electron-spin-flipped state $\hat{O}_{\text{flip}}\,|F = 4, m_F = 4\rangle = |m_I = 7/2, m_J = -1/2\rangle$.

Both the aforementioned relaxation mechanisms are related to wall collision. Also atom-atom collisions exist in the vapour and give rise to spin-exchange relaxation. The main difference is that angular momentum is conserved under spin-exchange collision thus preserving the macroscopic spin orientation.

In fact under specific conditions Katz and Firstenberg (2018) demonstrated light storage where the spin-exchange relaxation of $\hat{\sigma}_{4,3}$ vanishes. This happens in the spin-exchange relaxation-free (SERF) regime where the Larmor frequency is much lower than the spin-exchange collision rate. Unfortunately, we are not able to operate the single-photon source in the SERF regime. In order to enable spectral filtering, the Larmor frequency has to be high to ensure sufficient spectral separation. According to Katz and Firstenberg (2018) the spin-exchange rate at our operating temperature is expected to be 160 Hz.

For this discussion it is also relevant to consider that the weakly excited coherence $\hat{\sigma}_{4,3}$ is insensitive to spin-exchange relaxation when the ensemble is highly polarised (Katz and Firstenberg, 2018). Indeed, if the transverse coherence time T_2 were to be limited by spin-exchange, we would expect to find that T_2 depends on the atomic orientation. We do not

observe such behaviour in the pulsed MORS experiments. Hence, the cell T_2 is not limited by spin-exchange relaxation but other mechanisms such as magnetic inhomogeneity and electron-spin randomization on the wall despite the anti-relaxation coating.

3.3.5 Cell Cavity

The cell cavity is a central feature of our DLCZ implementation. We shall therefore dedicate this current section to characterize the cavity that was used and discuss design choices.

Mode waist

The cavity spatial mode is a consequence of the cavity geometry, namely cavity length L_{cav} and mirror radii of curvature r_1, r_2. The choice for the cell cavity was to have $r_1 = r_2 = r = 110\,\text{mm}$. Due to the symmetry, the cavity mode has the waist at cavity centre. The waist size is given by (Kogelnik and Li, 1966)

$$w_0 = \sqrt{\frac{b\lambda}{2\pi}}\ , \tag{3.23}$$

$$b^2 = L_{\text{cav}}(2r - L_{\text{cav}})\ . \tag{3.24}$$

To make the waist sufficiently small to fit through the microchannel the cavity is set up in a near-concentric configuration ($L_{\text{cav}} \approx 2r$). This means that the cavity is close to the edge of the stability region (Kogelnik and Li, 1966). From eqs. (3.23) and (3.24) we see that one can maintain the waist size while moving farther into the stability region by decreasing the cavity length. However, in our case L_{cav} is limited by the magnetic shield because it is more practical to have the cavity mirrors mounted outside the shield.

Experimentally we verify the cavity waist size from the cavity length. A precise method for determining L_{cav} is from the cavity free-spectral range (FSR), $\nu_{\text{FSR}} = c/(2L_{\text{cav}}n)$ with n as the refractive index. We use a simple method for estimating the cavity FSR where we scan the cavity resonance by applying a ramping voltage on the cavity piezo. Simultaneously, the laser frequency is modulated by an electro-optic modulator (EOM) to produce strong first-order sidebands at $\pm\nu_{\text{EOM}}$. The cavity resonance scan now displays the resonance for both the laser carrier frequency and the sidebands. We then tune the EOM frequency until all three resonances overlap implicating that $\nu_{\text{EOM}} = \nu_{\text{FSR}}$.

The measurement is performed with the vapour cell in the cavity and the laser frequency is far detuned to avoid a shift in refractive index due to atomic transitions. However, because we are close to the concentric configuration where the waist size is highly sensitive to cavity length, we need to account for the thickness of the thin windows of the cell. The optical path

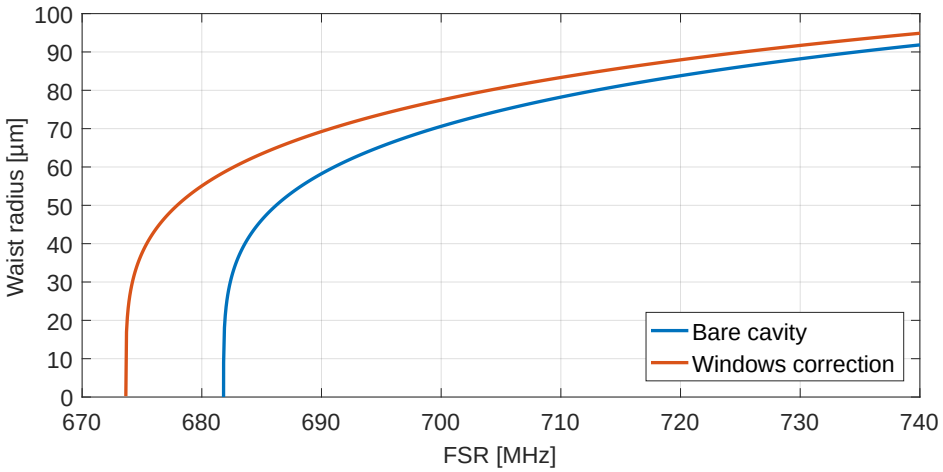

Figure 3.15: **Cell cavity waist for D_1 line.** Blue line shows the relation for an empty cavity. Red line shows the relation when correcting for two windows of thickness 1.6 mm and refractive index 1.5.

length than becomes

$$L_{\text{opt}} = L_{\text{cav}} + 2d(n_{\text{win}} - 1) \tag{3.25}$$

where $d = 1.6\,\text{mm}$ is the window thickness and $n_{\text{win}} \approx 1.5$ is the window refractive index. Evidently, the presence of windows decreases the FSR.

Meanwhile, the waist size changes because the Gaussian cavity mode is refracted on the window faces such that effective propagation length is shortened, i.e. $d \mapsto d/n_{\text{win}}$ (Kogelnik and Li, 1966). We can account for that by introducing an effective cavity propagation length

$$L'_{\text{cav}} = L_{\text{cav}} - 2d + \frac{2d}{n_{\text{win}}} = L_{\text{cav}} - 2d(1 - \frac{1}{n_{\text{win}}}) \ . \tag{3.26}$$

Inserting L'_{cav} in eq. (3.24) shows that the presence of windows make the waist smaller.

Figure 3.15 shows the waist size as a function of FSR of an empty cavity and when accounting for the cell windows. Because the write efficiency of the DLCZ scheme is sensitive to the filling factor of the cavity mode, we chose to trade higher filling factor for higher clipping losses on the cell. Starting from a mode waist of $w_0 \approx 70\,\mu\text{m}$ we see a single-pass transmission through the cell of $T_{\text{cell}} = 90.7\%$. We then decided to increase the mode waist to $w_0 \approx 90\,\mu\text{m}$ with $T_{\text{cell}} = 87.8\%$. This corresponds to a drop in finesse from 15 to 13.

Finesse

The cavity finesse is defined as the ratio of the FSR to the cavity FWHM linewidth, $\mathcal{F} = \nu_{\text{FSR}}/\Gamma$. To estimate the finesse we do a direct measurement of the FSR and linewidth. We send laser light to the cavity while scanning the cavity resonance frequency by applying a

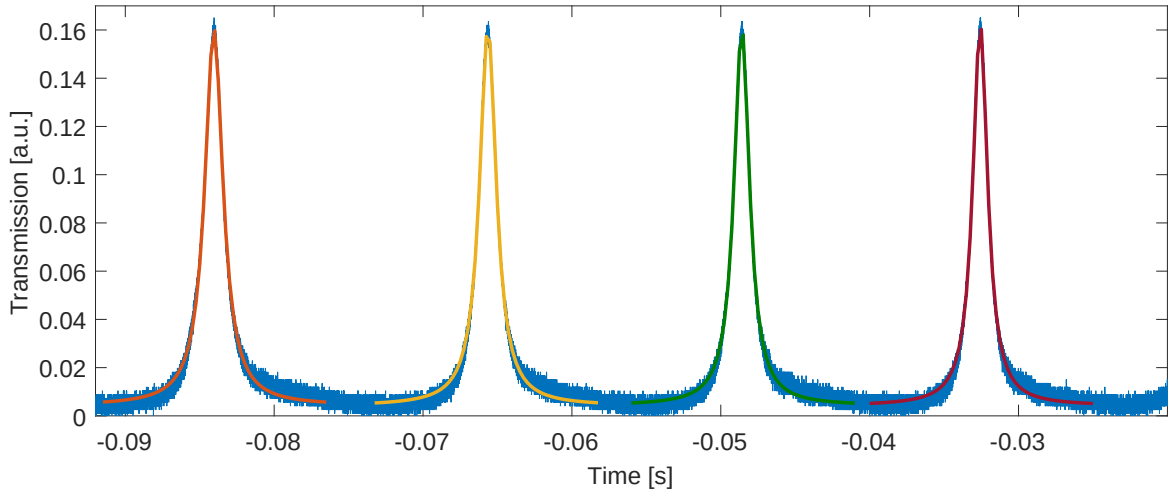

Figure 3.16: **Cell cavity finesse measurement.** The cavity transmission is recorded while ramping the cavity piezo. A Lorentzian lineshape is fitted to the vicinity of each of the four peaks independently.

ramping voltage on the cavity piezo. The recorded cavity transmission is displayed in Fig. 3.16. We fit a Lorentzian function

$$\mathcal{L}(t) = \frac{A}{(t - t_0)^2 + (\tilde{\Gamma}/2)^2} + B \tag{3.27}$$

to the individual peak vicinity. We mark Γ with a tilde because the measurement is performed in time. For each peak in the scan we get a finesse value from the ratio of the mean distance to neighbouring peaks to the FWHM ($\tilde{\Gamma}_i$). The piezo ramp is not completely linear and, hence, the finesse values vary with scan position. We estimate the cavity finesse as the mean over the finesse values from the individual peaks of the scan. From the data in Fig. 3.16 we estimate $\mathcal{F} = 13.0 \pm 0.2$. Together with an FSR of 725 MHz the cavity linewidth can be determined to be $\Gamma = 55.8$ MHz.

The cavity spectrum exhibits skewed shape on the right-hand side of each peak. This is caused by imperfect matching of the input light to the cavity fundamental mode. The higher order modes of the cavity have higher round-trip losses and therefore cannot be resolved. However, the imperfect mode matching does not significantly bias the finesse measurement.

Birefringence

For the empty cavity, the birefringence between linear input modes is much less than what can be resolved in the cavity spectrum. The same applies to the cavity with the cell inside when the atoms are unpumped. However, when we apply optical pumping to $|4, 4\rangle$, we observe a strong birefringence between horizontally polarized (π) and vertically polarized (σ) light. For a highly polarized ensemble we typically find that the two resonances are split by

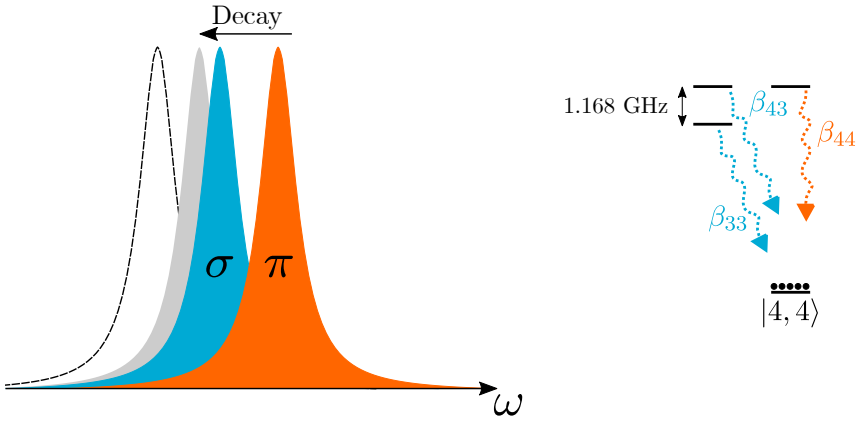

Figure 3.17: **Birefringence of the cell cavity. Left:** The atomic birefringence depends on the atomic population distribution. For the fully pumped ensemble the resonances for horizontally polarized (π) and vertically polarized (σ) light are strongly split. From here the two resonances shift to the same frequency for the ensemble at thermal equilibrium (grey). The dashed lineshape illustrates the empty-cavity resonance. **Right:** Atomic levels with non-vanishing dipole moments coupling to $|4,4\rangle$ and their respective Clebsch-Gordan coefficients.

$\Delta\nu_0 = \nu_0^\pi - \nu_0^\sigma = (32 \pm 1)\,\mathrm{MHz}$. The birefringent spectrum is illustrated in Fig. 3.17.

The cause of the birefringence is the dependency of the atomic susceptibility on the light polarization. When the atomic ensemble is fully polarized in the $|4,4\rangle$ state, the optical depth for the linear polarizations are strongly different. This is a manifestation of the hyperfine splitting of the excited states. On the D_1 line the excited state splitting is large compared to the D_2 line and hence the birefringence becomes stronger on D_1. We can calculate the optical depth d_σ for σ light similar to eq. (3.5). Along the atomic quantization axis the vertically-polarized light is a coherent superposition of the σ_+ and σ_- fields. Hence,

$$d_\sigma = \frac{1}{2}(d_{\sigma_-} + d_{\sigma_+}). \tag{3.28}$$

For the dark state $|4,4\rangle$ we have $d_{\sigma_+} = 0$. For d_{σ_-} we need to include both excited states

$$\frac{\tilde{d}_{\sigma_-}}{\Delta_{4'}} \propto \left(\frac{\beta_{43}}{\Delta_{4'}} + \frac{\beta_{33}}{\Delta_{3'}}\right) \tag{3.29}$$

where $\beta_{F'm'_F}$ is the Clebsch-Gordan coefficient for $|4,4\rangle \to |F', m'_F\rangle$. Because of the large hyperfine splitting of excited states, the excited state detuning will be different with $\Delta_{3'} = \Delta_{4'} + 1.168\,\mathrm{GHz}$ and $\tilde{d}_{\sigma_-}$ becomes detuning dependent, hence the 'tilde'. Since all factors except for Clebsch-Gordan coefficients are the same as in eq. (3.5), we can express $\tilde{d}_{\sigma_-}$ in terms of the OD for π-polarized light, d_π, as

$$\frac{\tilde{d}_{\sigma_-}}{\Delta_{4'}} = \frac{d_\pi}{\Delta_{4'}} \frac{\beta_{43}/\Delta_{4'} + \beta_{33}/\Delta_{3'}}{\beta_{44}/\Delta_{4'}} = \frac{d_\pi}{\Delta_{4'}} \left(\frac{1}{4} + \frac{7}{4}\frac{\Delta_{4'}}{\Delta_{3'}}\right). \tag{3.30}$$

Inserting the factor 1/2 from eq. (3.28), we find that the OD for vertically-polarized light is $\tilde{d}_\sigma \approx d_\pi/2$ for our operating detuning of $\Delta_{4'} = 0.92\,\mathrm{GHz}$. Please note that in the far-detuned regime ($\Delta_{3'} \approx \Delta_{4'}$) the OD for vertically-polarized light equals the OD for horizontally-polarized light.

For a detuning far outside the Doppler line, $\Delta \gg \Gamma_\mathrm{D}$, the refractive index (real part) is given in terms of OD as (Munns *et al.*, 2016)

$$n(\Delta) = 1 - \frac{c}{\omega_0 L_z}\frac{d\gamma}{2\Delta} \tag{3.31}$$

where we use the same convention for d as in eq. (3.5). γ is the natural linewidth (HWHM) and ω_0 is the atomic transition frequency (angular). This leads to an atomic phase shift per cavity round trip (two passes through the cell) of

$$\delta\phi = \frac{\omega}{c}(n-1)2L_z = -\frac{\omega}{\omega_0}\frac{d\gamma}{\Delta} \tag{3.32}$$

where ω is the light frequency. For Δ in the few GHz range we can take $\omega/\omega_0 \approx 1$. The resulting shift in the cell cavity resonance ($\Delta\nu$) is related to the cavity FSR by

$$\Delta\nu = \frac{\delta\phi}{2\pi}\nu_\mathrm{FSR}. \tag{3.33}$$

For an OD of $d_\pi = (0.32 \pm 0.03) \times 10^3$ (assuming fully polarized ensemble, see section 3.3.1), we should expect to observe a cavity resonance shift of $\Delta\nu_\pi = (91 \pm 9)\,\mathrm{MHz}$ for π-polarized light in a cavity with $\nu_\mathrm{FSR} = 725\,\mathrm{MHz}$ at the detuning $\Delta = 0.92\,\mathrm{GHz}$ (On D_1 line). This would give a resonance splitting $\Delta\nu_0 \approx \Delta\nu_\pi/2 = 46\,\mathrm{MHz}$ but we only observe approx. 2/3 of this.

The discrepancy between OD estimates from the absorption measurement in section 3.3.1 and from the cavity birefringence could be explained in two ways. Either the absorption measurement overestimates the OD or for the birefringence we observe there is still atoms residing in the $F = 3$ manifold due to imperfect pumping. The OD estimate from cavity birefringence is performed for the same optically pumped atomic state as during DLCZ experiments and should therefore resemble the experienced OD during measurements. Inserting experimental parameters in eqs. (3.32) and (3.33) we get $d_\pi = 224 \pm 7$ from cavity birefringence.

When the atoms decay to thermal equilibrium, the atomic polarization is isotropic with a fraction 9/16 atoms in $F = 4$. In this case, we can exploit the dipole operator symmetry (Steck, 2010) and obtain an OD scaling

$$\frac{\tilde{d}_\mathrm{therm}}{\Delta_{4'}} = \frac{9}{16}\frac{d_\pi}{\Delta_{4'}}\left(S_{44} + S_{43}\frac{\Delta_{4'}}{\Delta_{3'}}\right) \approx \frac{3}{8}\frac{d_\pi}{\Delta_{4'}} \tag{3.34}$$

where $S_{FF'}$ is the relative hyperfine transition strength factor (Steck, 2010). For the observed $\Delta\nu_0 = 32\,\mathrm{MHz}$ between linear polarizations in the pumped ensemble – which corresponds

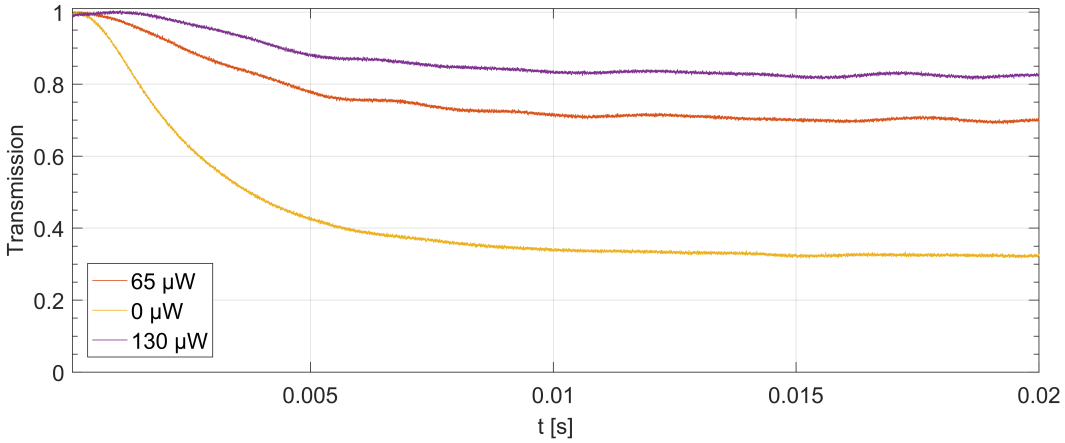

Figure 3.18: **Cell cavity transmission vs. decay time.** When starting at cavity resonance the transmission drops as the resonance shifts due to atomic rethermalization. The transmission decay is shown for four different repump powers applied during decay to compensate the resonance shift. Transmission is normalized to peak transmission. The 'wiggles' appearing on the traces are caused by a small amount of cavity disturbance.

to an OD difference of $d_\pi/2$ – the frequency difference between π in pumped and thermal ensemble should be $\Delta\nu_{\text{therm}} \approx \Delta\nu_\pi - 3/8\Delta\nu_\pi \approx 40\,\text{MHz}$.

The presence of a birefringent cavity spectrum means that we will have to correct for it during the experimental sequence to have both the write and read scattered light resonant during the respective pulse. One option would be to quickly step the cavity piezo to shift the resonance frequency between write and read pulses. However, it is unlikely that fast piezo steps would be sufficiently reproducible to allow for this compensation over tens of trials before relocking the cavity. What we chose instead was to have the write and read scattered light at separate frequencies. Since we use independent filtering setups this choice does not increase the complexity of the setup.

The cavity birefringence also means that the drive light will be off-resonant from the cavity by $\Delta\nu_{\text{Drive}} = \pm(\Delta\nu_0 + \nu_{\text{L}})$, for write and read respectively. Hence, more input drive light is required.

When the ensemble is left in the dark, the atomic distribution re-thermalizes and the cavity resonance returns to its unpumped position. This is a behaviour that we need to counteract when investigating the variable storage time of the DLCZ scheme. Fig. 3.18 shows how much the cavity transmission drops for a fixed input frequency starting at cavity resonance. The input light at $\Delta = 0.92\,\text{GHz}$ is sufficiently weak to avoid light-induced decay. After 2 ms, the cavity transmission has dropped to $\sim 70\%$, corresponding to a resonance shift of $\sim 18\,\text{MHz}$. This is the case for π-polarized light, i.e. the polarization of the read scattering mode. In the

long time limit the cavity transmission drops to $\sim 33\%$ which corresponds to 39 MHz. This matches well with the above theoretical prediction for resonance shift between pumped and thermal ensemble.

In the presence of this effect, the coupling of the spin wave to the cavity mode would decrease with storage time. Simultaneously, the cavity incoupling of drive light would decrease as well. One way of correcting for this would be to fix the storage time before the sequence and simply shift the drive frequency (and the filter resonance) such that it follows the cavity resonance. The downside of this method is that it does not allow for on-demand retrieval. The storage time would have to be set prior to executing the DLCZ sequence in order to lock the filter cavities at the correct frequency.

What we chose instead was to apply a weak repump pulse during the storage time to transfer the atoms decaying into the $F = 3$ manifold back to the $F = 4$ manifold. Mostly this will be transferring atoms from $|3, 3\rangle$ to $|4, 4\rangle$. Fig. 3.18 shows the cavity resonance shift for various repump powers. The cavity shift is compensated by the repump and the degree of compensation depends on the repump power. The repump has to be weak enough that the induced decoherence of σ_{43} from absorption in the $F = 4$ manifold is negligible. We confirmed by a pulsed MORS measurement with 130 µW repump light applied that only marginal decay was induced by the repump.

Escape Efficiency

The reason for working in a single-sided cell cavity is to have a high outcoupling efficiency to the mode going to the filtering and detection. Unfortunately, the transmission losses of the cell turned out to be comparable to the transmissivity of the outcoupling mirror. That means that a substantial amount of the intracavity light will be lost to imperfect cell transmission before escaping out of the cavity. Here we derive an expression for the escape efficiency, i.e. the probability of escaping out of the cavity.

We consider a cavity consisting of three components: incoupling mirror with reflectivity R_1, outcoupling mirror (R_2), and the cell with single-pass transmission T_c. The total round-trip loss will then be

$$\mathcal{L} = 1 - R_1 R_2 T_\mathrm{c}^2 \ . \tag{3.35}$$

In principle the escape efficiency depends on which side of the cell is taken as the reference point. But as we shall see, for high T_c the difference is negligible. We start out by considering right-propagating component with power P at position 1 in Fig. 3.19. The outcoupling is given by

$$\frac{P_\mathrm{out}^\mathrm{right}}{P} = (1 - R_2) \sum_{n=0}^{\infty} (R_1 R_2 T_\mathrm{c}^2)^n = \frac{1 - R_2}{\mathcal{L}} \ . \tag{3.36}$$

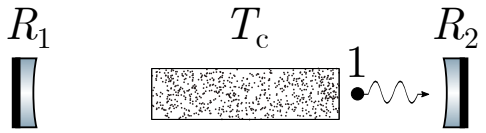

Figure 3.19: **Cell cavity illustration.** Cavity round trip losses are calculated from incoupling mirror reflectivity $R_1 \approx 1$, outcoupling mirror reflectivity R_2 and cell single-pass transmission T_c. Position 1 is used for the escape efficiency calculation.

Had we chosen the reference point on the other side of the cell there would have been and extra factor T_c in eq. (3.36).
Similar for the left-propagating component at position 1

$$\frac{P_{\text{out}}^{\text{left}}}{P} = (1-R_2)R_1T_c^2\sum_{n=0}^{\infty}(R_1R_2T_c^2)^n = \frac{(1-R_2)R_1T_c^2}{\mathcal{L}} \ . \tag{3.37}$$

Had we chosen the reference point on the other side of the cell there would have been and extra factor $1/T_c$ in eq. (3.37).
For a standing wave the power travelling left and right are equal so the escape efficiency for the cavity mode with respect to position 1 becomes the mean over the two directions

$$\frac{P_{\text{out}}^{(1)}}{P} = \frac{1}{2}\left(\frac{P_{\text{out}}^{\text{left}}}{P} + \frac{P_{\text{out}}^{\text{right}}}{P}\right) = \frac{(1-R_2)(1+R_1T_c^2)}{2\mathcal{L}} \ . \tag{3.38}$$

Had we chosen the reference point on the other side of the cell the numerator in eq. (3.38) would have been $T_c(1-R_2)(1+R_1)$.
In the limit $R_1 \to 1$ and for $1+T_c^2 \approx 2T_c$, the two reference points have the same outcoupling power and we find the approximate expression

$$\eta_{\text{esc}} \approx \frac{(1-R_2)T_c}{1-R_2T_c^2} \ . \tag{3.39}$$

The intuitive understanding of eq. (3.39) is that the escape efficiency should be the ratio of loss at the outcoupler to the total round-trip loss and multiplied by T_c because the light will on average have to pass through the cell once to reach the outcoupler.

For the D_1 line, the cavity parameters are $R_1 = 99.6\%$, $R_2 = 80.5\%$ and $T_c = 87.8\%$ (for the 90 µm waist). Inserting the parameter values into eq. (3.39) yields $\eta_{\text{esc}} \approx 45\%$. This is a very low value for something that is intrinsic to the scheme when thinking in terms of application. An important figure of merit for single-photon sources is the outcoupling efficiency from the system where the source material is located. However, for demonstrating the performance of the scheme it is not a show stopper since photon counting is immune to added vacuum noise due to losses (as opposed to homodyne detection).

The amount of cell transmission loss that we observe for the cell in the cavity cannot be explained from window losses alone. After the glass cell is fabricated we can typically achieve >97% transmission before coating and caesium filling. Particularly, applying the coating appears to degrade the cell transmission. For some cells we have seen >97% transmission even after coating and filling but typically cells with high transmissivity tend to have short atomic coherence time. However, we are convinced that the cell fabrication procedure can be optimized to yield cells that are better suited for cavity schemes.

At this point we can use the determined escape efficiency to calculate the reduction in filter requirement from the cavity enhancement, as was pointed out in section 2.5. We evaluate eq. (2.44) by using $T_{\text{out}} = 1 - R_2$ and find

$$\frac{\zeta_{\text{cav}}}{\zeta_{\text{fs}}} = \frac{2\mathcal{F}}{\pi}\eta_{\text{esc}}\left(\frac{2}{T_{\text{out}}} - 1\right) = 34. \tag{3.40}$$

Having established an expression for escape efficiency, we simplify eq. (2.44) by approximation. For low intracavity loss, $T_{\text{c}} \approx 1$, we have $\eta_{\text{esc}} \approx T_{\text{out}}/\mathcal{L} = T_{\text{out}}\mathcal{F}/(2\pi)$ such that we can write eq. (2.44) as

$$\frac{\zeta_{\text{cav}}}{\zeta_{\text{fs}}} \approx 2\frac{\mathcal{F}}{\pi}\left(\frac{\mathcal{F}}{\pi} - \eta_{\text{esc}}\right) \approx 2\left(\frac{\mathcal{F}}{\pi}\right)^2. \tag{3.41}$$

Thus, under the condition of low intracavity loss, the filter reduction from the cell cavity is given by the finesse alone.

While the cavity enhancement reduces the filtering requirement by more than an order of magnitude, it does fade in comparison to the 100 dB rejection from polarization and spectral filtering. Hence, the enhancement of the ratio of scattered photons to laser photons at the cavity output is not critical for the success of the scheme. However, the cavity still grants a critical enhancement of the readout efficiency as discussed in section 2.5.

Chapter 4

Four-Wave-Mixing-limited DLCZ scheme on the D_2 line

In this chapter we shall present and discuss the first attempt to herald and retrieve single excitations in the long-lived atomic mode using the DLCZ scheme. The attempt was done on the caesium D_2 line which was considered in the original motional-averaging proposal by Borregaard *et al.* (2016). The proposing authors considered hyperfine storage between $|4,4\rangle$ and $|3,3\rangle$. However, not long after commencing the experimental implementation of the scheme, we observed that coherences between hyperfine levels are significantly more short-lived than coherences between Zeeman levels. This observation is well-established (Robinson and Johnson, 1982; Budker *et al.*, 2005; Corsini *et al.*, 2013; Zugenmaier, 2018) and can be understood from fast decay to $|3,3\rangle$ from electron-spin randomization as discussed in section 3.3.4. Typical results show that the hyperfine decoherence is 10–100 times faster than Zeeman decoherence.

With this understanding we decided to employ Zeeman storage between $|4,4\rangle$ and $|4,3\rangle$ instead. This further had the advantage that the Zeeman splitting of a few MHz is much smaller than the hyperfine splitting $\nu_{\mathrm{HFS}} = 9.2\,\mathrm{GHz}$. For the Zeeman storage the excitation light addresses the same hyperfine manifold during write and read. Hence the frequency of the excitation light can be varied by tens of megahertz without significantly changing the excited-state detuning $\Delta \sim 1\,\mathrm{GHz}$. With this freedom, the frequency of the scattered light for write and read can be set to coincide such that both are resonant with the same narrowband filter cavity by proper choice of write and read drive frequencies. In contrast, the original idea for hyperfine storage was to have the 9.2 GHz separation of write and read scattered light matched to multiple FSRs of the filtering cavity. This would have posed a stronger technical requirement on the filtering cavity.

Unfortunately, as we shall describe in this chapter, the Zeeman storage scheme is much more prone to FWM than the hyperfine scheme. The FWM noise is detrimental to single-photon operation which is the reason we were unable to achieve single-photon statistics on

the D_2 line.

The work presented in this chapter is the outcome of a collaborative effort with Michael Zugenmaier and Boris Albrecht. The results of the experiment has been published in Communications Physics (Zugenmaier *et al.*, 2018) as well as in the PhD thesis of Zugenmaier (2018) and partly in Dideriksen (2017).

The results presented in this chapter originate from an earlier state of the experimental setup than described in the previous chapter. Therefore some characterization values differ from the previously stated in chapter 3. This is particularly T_2 which in the old setup was only 0.8 ms, an atomic polarization of only 98.5%, a cell cavity mode waist size of 55 µm, and escape efficiency of 62% due to the smaller cavity waist. Moreover, the cell cavity birefringence is much less significant because of the smaller excited-state splitting on the D_2 line.

4.1 Experimental realization

On the D_2 line, the Λ-scheme coupling $|4,4\rangle \rightarrow |4,3\rangle$ can be achieved via excited states of either $m'_F = 4$ or $m'_F = 3$. This enables the option to have the scattered light for both write and read in the π-polarisation and the excitation light in the σ-polarization for both processes. The level scheme is depicted in Fig. 4.1b and c. We chose to use vertical polarisation (σ) for excitation light. For the write pulse, $|4,3\rangle$ is ideally empty and the excitation light couples $|4,4\rangle$ to the three excited states with $m'_F = 3$ where spontaneous Raman scattering couples to $|4,3\rangle$. The light also incidentally excites on the cyclic transition $|4,4\rangle \rightarrow |5,5\rangle$. Because the transition is cyclic, the interaction does not couple to any spin-wave modes. The cyclic transition only leads to a phase shift for the drive light and negligible spin-wave dephasing due to absorption.

The excitation light simultaneously couples $|4,4\rangle \rightarrow |4,3\rangle$ via $m'_F = 3$ and $|4,3\rangle \rightarrow |4,4\rangle$ via $m'_F = 4$ as illustrated in Fig. 4.1c. This is particularly harmful for the read process as it enables FWM to build up readout noise that is not correlated with the write pulse.

We chose to vary the detuning Δ between write and read such that $\Delta_{\text{write}} = \Delta - \nu_{\text{L}}$ and $\Delta_{\text{read}} = \Delta + \nu_{\text{L}}$. Since the write (read) pulse scatters into the blue (red) Raman sideband, this choice of detuning means that the heralding photon and the readout photon coincide in frequency. Furthermore, by using σ-polarized light for both write and read excitation, the scattered quantum fields are both π polarized. Thus, the two fields will transmit through the same spectral filter and only one filtering setup is needed.

Fig. 4.1a shows a simplified overview of the experimental setup illustrating the propagation of light from cell to detection. The excitation light impinges on the high-reflector of the cell cavity and a small fraction is coupled into the cavity. At the cell, the light is scattered

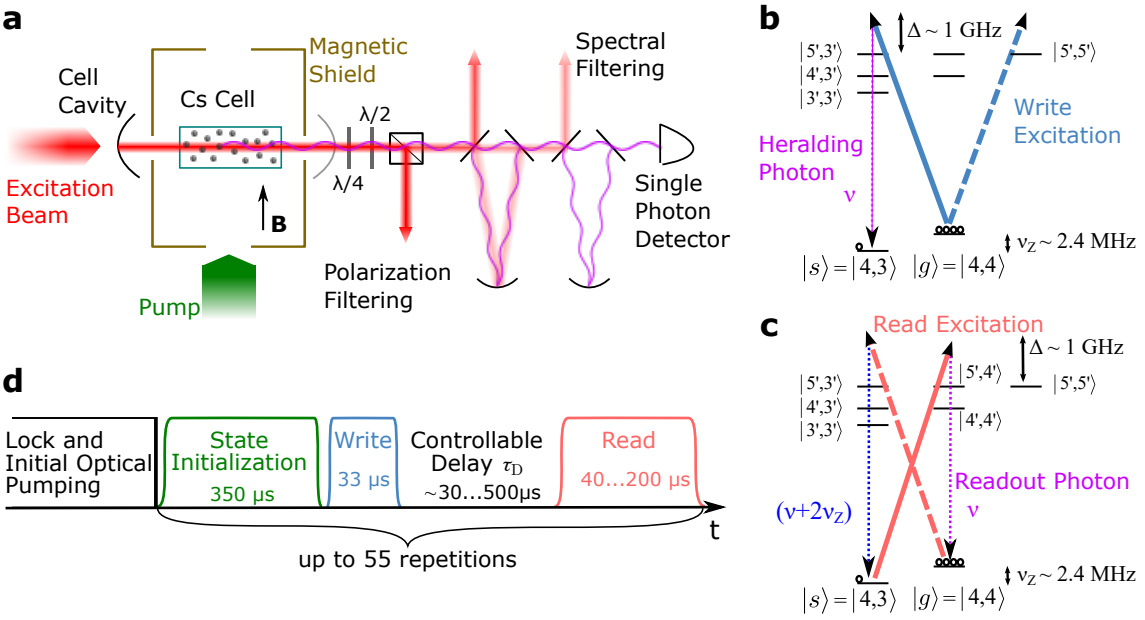

Figure 4.1: **DLCZ scheme on the D_2 line.** **a)** Conceptual sketch of the experimental setup. Elements are explained in the text. **b)** Λ configuration for $|g\rangle \rightarrow |s\rangle$ coupling during the write pulse. **c)** Λ configuration for $|s\rangle \rightarrow |g\rangle$ coupling during the read pulse. In b) and c) the dashed lines depict the unintentional coupling also caused by the excitation light. **d)** Pulse sequence. Figure from Zugenmaier *et al.* (2018).

into the orthogonal quantum mode of the cell cavity. Both excitation light and scattered light escapes the cavity through the partially-reflecting outcoupling mirror. A set of wave-plates optimises the rejection of the excitation light on a polarizer. The transmitted light, containing both the scattered light and a small fraction of excitation light, is spectrally filtered through two cascaded triangular cavities where the remaining excitation light is rejected.

An illustration of the pulse generation and cell cavity locking is presented in Fig. 4.2. The "control" AOM generates the write and read pulses impinging on the cell cavity. This light is vertically (σ) polarized by transmission through a Glan-Thompson polarizer. The control light is overlapped with "signal" light on a (non-polarising) beam splitter where the reflected light is recorded on a photo detector which serves as a input power reference. After the cell cavity a set of quarter-wave and half-wave plates optimises the control light rejection on a second Glan-Thompson polarizer.

Before the cell cavity, the control path is combined with the "locking" laser on a polarizing beam splitter. Through a small angle on the half-wave plate, a small amount of locking laser light is transmitted on the polarizer. This light is detuned by one cell cavity FSR from the scattered light frequency and used to lock the cell cavity resonance frequency.

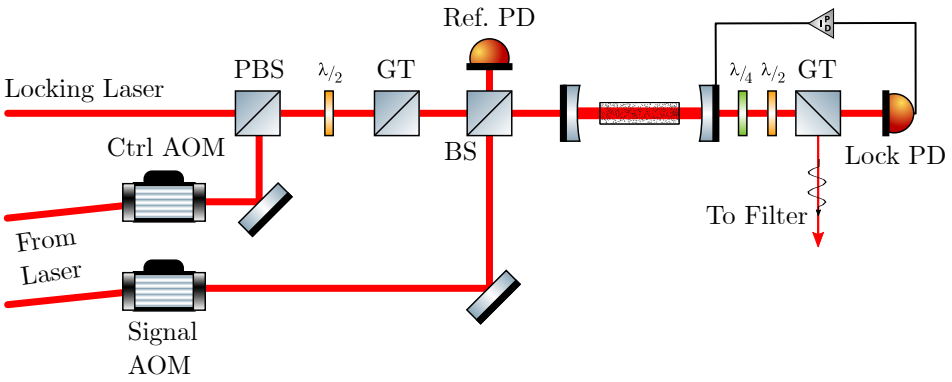

Figure 4.2: **Pulse generation and cell cavity locking.** Elements are explained in the text.

The signal AOM generates a beam at the scattering frequency. This light is used for locking the resonance frequency of the filter cavities (not shown). A pulse of signal light is input to the cell cavity at the end of the DLCZ sequence to serve as an *in situ* detection-efficiency measurement. The signal pulse travels through the whole setup as it is resonant with the filter cavities. By calibration of the input power and cell cavity transmission, the detection efficiency from cell cavity output to detector event can be determined.

A chopper wheel (not shown) blocks the locking light for the filter cavities during the DLCZ protocol to avoid locking light on the single-photon detector. The full experimental sequence is synchronized to the chopper wheel rotation.

Experimental sequence

The experimental sequence is comprised of the following stages as illustrated in Fig. 4.1d.

1. **Locking stage** (25 ms): All cavities are locked to the respective lock light. Chopper open.

2. **Initial pumping** (4.4 ms): All cavities are frozen. Atoms are being optically pumped. The duration of this stage is set to reach optimal atomic state. Chopper closed.

3. **DLCZ sequence** (Repeated up to 55 times):

   I **Write pulse** (33 µs)

   II **Variable delay** (τ_D): Up to 500 µs.

   III **Read pulse** (200 µs)

   IV **Intermediate pumping** (350 µs): Optical pumping with repump and pump before the next DLCZ sequence.

4. **Check pulse** (1000 µs, not shown in Fig. 4.1d): In-situ detection-efficiency measurement.

The total period of a experimental cycle is $\sim 65\,\text{ms}$ set by the chopper wheel period. For the shortest delay time $30\,\mu\text{s}$, the overall DLCZ repetition rate is then approx. $850\,\text{Hz}$.

4.2 Performance

We will now turn to the analysis of the single-photon source-memory performance. The histogram of recorded detection events is displayed in 4.3. The detection rate is clearly much higher during the read than during the write. This is a strong indication of the presence of excess readout noise. This noise will be discussed later in this chapter.

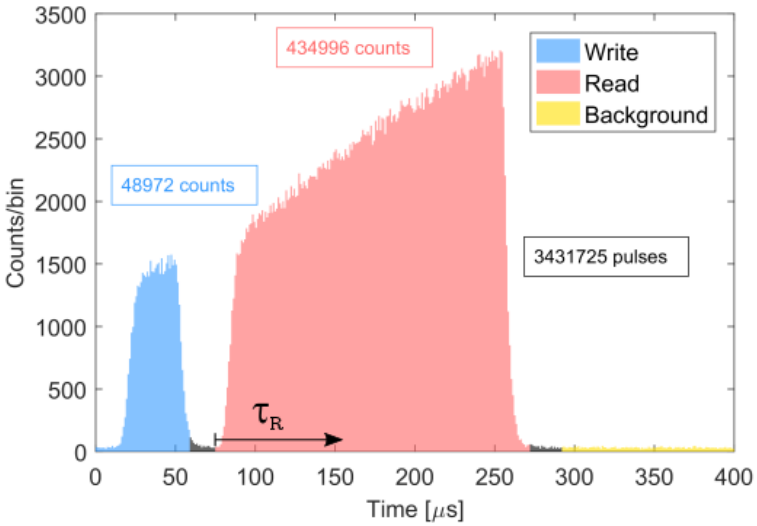

Figure 4.3: **Histogram of detection events for 3431725 repetitions.** Blue marks the definition of write detection window with a total 48972 events. Red marks the full read detection window with a total 434996 events, i.e. for $\tau_R = 200\,\mu\text{s}$. Yellow marks the window for background level estimation. Figure adapted from Dideriksen (2017).

Detection windows

From the temporal distribution of detection events, we can freely choose how to define the detection windows, i.e. the time windows in which a detection event is considered a write click or read click, respectively. We find the optimal settings for the detection windows in the data postprocessing. The aim is to find an optimum trade-off between SNR and sacrifice of signal. If we set the windows too narrow, the SNR is high but we also decrease the statistics by neglecting much of the recorded events. For too large windows, it is vice versa.

Since we are mostly concerned with the readout noise, the analysis is performed by varying the read detection window. We chose the procedure to fix the read window starting point and vary the duration. We introduce the analysis parameter τ_R which is the read detection

window duration (see Fig. 4.3). Varying τ_{R} corresponds to varying the read pulse length but is performed in the data post-processing. Fig. 4.4a shows the τ_{R} dependency of the Cauchy-Schwarz parameter R and retrieval efficiency η_{R}. Here we define η_{R} as the conditional readout with the unconditional readout subtracted, i.e.

$$\eta_{\mathrm{R}} = \left\langle n_{R|W=1} \right\rangle - \langle n_R \rangle \,. \tag{4.1}$$

Although $\langle n_R \rangle$ is not only the noise level but also contains the readout of unheralded excitations generated by the write pulse, this makes for a more experimentally practical quantity. As long as the excitation probability is fixed, the difference in generated excitations between heralded and unheralded states is constant with $\Delta\mu = \tilde{\mu} - \mu$ and η_{R} is proportional to $\Delta\mu$. In the ideal case, the generated number of excitations in the heralded state $\tilde{\mu}$ is exactly 1. However, the combination of write noise, multiple excitations and limited detection efficiency makes $\tilde{\mu}$ non-trivial. This will be discussed in more detail in chapter 5. Furthermore, as we show later, the unconditional readout is highly dominated by noise, hence $\langle n_R \rangle \approx \langle n_{\mathrm{noise}} \rangle$.

Fig. 4.4a shows the compromise between non-classicality and signal retrieval by cutting short the read pulse. We decided to use $\tau_{\mathrm{R}} = 40\,\mu\mathrm{s}$ for the remainder of the analysis. By doing so, we sacrifice the majority of the correlated readout but maintain an SNR that supports non-classical correlations.

Non-classical correlations

For this choice of read detection window we obtain the following correlation values:

$$\begin{aligned} \text{Cauchy-Schwarz parameter: } & R = 1.44 \pm 0.11, \\ \text{Cross-correlation: } & g^{(2)}_{WR} = 1.97 \pm 0.05, \\ \text{Write auto-correlation: } & g^{(2)}_{WW} = 1.86 \pm 0.07, \\ \text{Read auto-correlation: } & g^{(2)}_{RR} = 1.45 \pm 0.05. \end{aligned} \tag{4.2}$$

Note that $g^{(2)}_{\mathrm{WR}}$ is below the typical non-classical signature $g^{(2)}_{\mathrm{WR}} > 2$. However, because we are able to estimate the auto-correlations of the individual fields, we find that the correlations are non-classical from the criterion $R > 1$ with statistical significance. Unfortunately, with the present noise level, we were unable to observe single-photon readout. The conditional read field exhibits a weakly bunched photon statistics with $g^{(2)}_{\mathrm{RR|W=1}} = 1.3 \pm 0.2$.

Memory performance

Even though the correlations are not encouraging in terms of application, we can still have a look at the performance when the write-read delay, τ_{D}, is varied. The first measure to consider is the spin-wave lifetime. We can estimate this by analysing the retrieval efficiency decay as a function of τ_{D}. This quantity is inherently corrected for readout noise from definition and

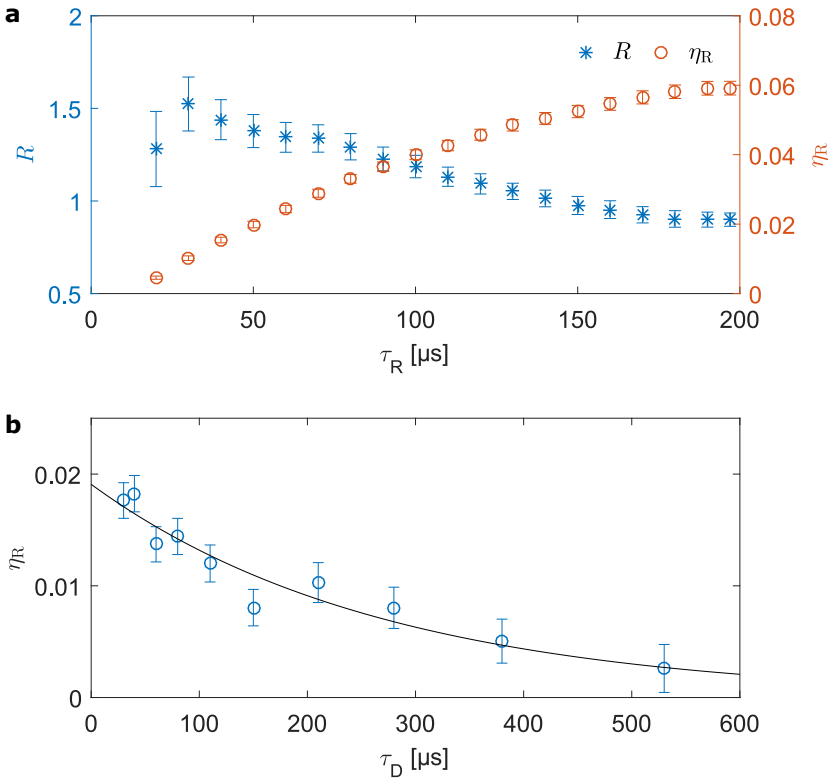

Figure 4.4: **Temporal dynamics of the readout.** **a**, Cauchy-Schwarz parameter (blue asterisks, left axis) and retrieval efficiency (red circles, right axis) versus read detection integration time for $\tau_D = 30\,\mu s$. We observe violation of the Cauchy-Schwarz inequality for $\tau_R < 140\,\mu s$ while the retrieval efficiency increases throughout the read pulse. To limit the influence of noise we choose $\tau_R = 40\,\mu s$ for our correlation analysis. **b**, Retrieval efficiency versus write-read delay, for $\tau_R = 40\,\mu s$. An exponential fit (line) yields a $1/e$ collective-excitation lifetime of $\tau = 0.27 \pm 0.04\,ms$. Figure and caption from Zugenmaier *et al.* (2018).

therefore a good measure for the lifetime of the coherent readout. The decay data is plotted in Fig. 4.4b together with an exponential fit. The best fit parameter for the $1/e$-lifetime of the collective excitation is $\tau_{CE} = 0.27 \pm 0.04\,ms$.

At the time when the D_2-line experiment was performed, the transverse-spin coherence time was measured to be $T_2 = 0.8\,ms$. We later realized that this was limited by magnetic inhomogeneity and improved T_2 (see chapter 5). As discussed in section 2.4, the limit on the collective-excitation lifetime is $\tau_{CE} \leq T_2/2$ which is in agreement with the estimated value for τ_{CE}. That τ_{CE} comes close to the limiting value shows that we are indeed heralding the excitation of the long-lived symmetric atomic mode. This was the first study to report non-classical correlations for single excitations in a mode that is long-lived at room-temperature. The lifetime is two orders of magnitude larger than previous results with non-classical correlations (Dou *et al.*, 2018; Bashkansky *et al.*, 2012).

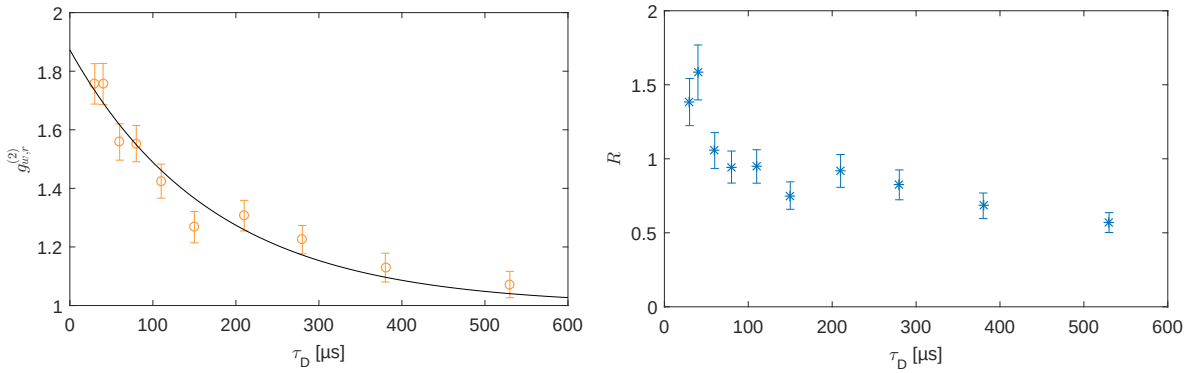

Figure 4.5: **Left:** Cross-correlation of write and read detection events versus write-read delay, for $\tau_R = 40\,\mu s$. A fit (line) to the function $g^{(2)}_{w,r}(t) = 1 + C\exp(-t/\tau_g)$ yields a characteristic decay time of $\tau_g = (0.17 \pm 0.02)\,ms$. **Right:** Cauchy-Schwarz parameter decay versus write-read delay, for $\tau_R = 40\,\mu s$. We observe non-classical correlations ($R > 1$) for $\tau_D < 80\,\mu s$. Both panels and captions from Zugenmaier *et al.* (2018).

Even though the birefringence on the D_2 line is small, the atomic phase shift changes the resonance frequency of the cavity for both polarizations. Since atoms decay into the $F = 3$ manifold, the cell cavity resonance shifts during storage. Thus, the readout field becomes detuned from the cavity mode for long τ_D. This causes a weaker coupling to the cavity mode and will make the readout rate slower and therefore introduce a faster decay of the retrieval efficiency. It is worth noting that for the experiments on the D_2 line, no repump light was applied during the storage window which we later found as a method to compensate cell cavity resonance shift (section 3.3.5).

Fig. 4.5 shows how the write-read correlation decays with τ_D. The correlations are sensitive to changes in the readout noise with increasing τ_D. Hence, correlations decay faster than the spin-wave lifetime. The exponential fit in Fig. 4.5 (left panel) yields a $1/e$ decay time of $\tau_g = 0.17 \pm 0.02\,ms$. From Fig. 4.5 (right panel) we see that non-classicality is conserved for data points for $\tau_D < 80\,\mu s$.

4.2.1 Noise sources

Having established that the correlation between write and read is non-classical but severely limited by readout noise, we now turn to investigate the sources of noise. The first relevant inspection is the Raman-sideband spectrum. We map out the optical spectrum by scanning the resonance frequency of the spectral filters in front of the single-photon detector. Hence, the output spectrum is a convolution of the light spectrum and the filter lineshape. The obtained spectra for write and read are shown in Fig. 4.6.

We see that both spectra have a distinct feature centered at the sideband frequency

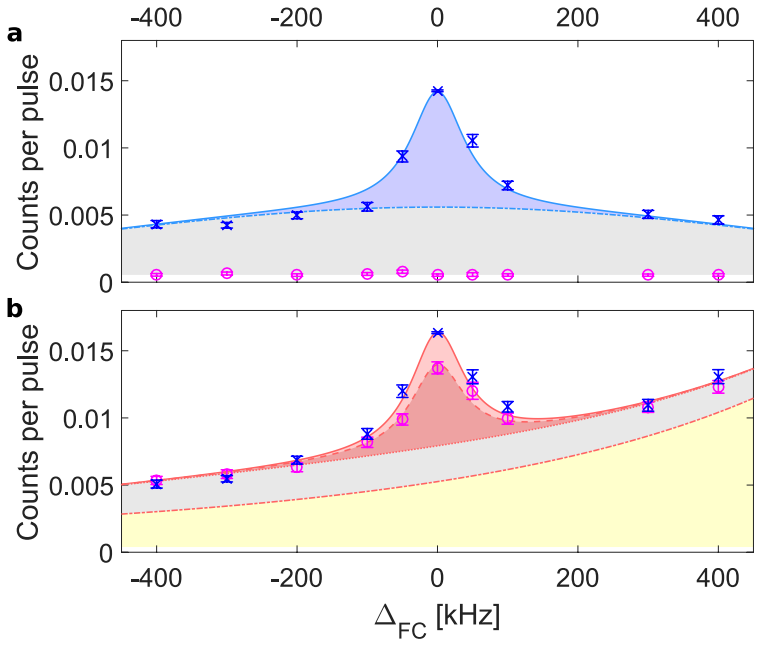

Figure 4.6: **Detected counts per pulse versus detuning of the filter resonance.** Zero detuning is one Zeeman splitting above (below) the write (read) excitation frequency. Each point represents around 1000 experiments with 55 repetitions each. The points on resonance with the write pulse include 60 times as many experiments. **a**, Heralding photon detection. **b**, Unconditional photon detection in the readout, considering only the first 40 µs. Blue crosses show data with write pulse present, magenta circles with write pulse off. The solid (dashed) lines show a fit with (without) write, containing scattered photons (blue, red), contribution from asymmetric excitations (grey), leakage (yellow) and background (unfilled). Figure and caption from Zugenmaier *et al.* (2018).

$\Delta_{\mathrm{FC}} = 0$ that corresponds to $+\nu_{\mathrm{L}}$ for write and $-\nu_{\mathrm{L}}$ for read where we expect to find the scattering signal. The plot shows two sets of data where the difference is whether the write pulse is blocked (magenta circles) or unblocked (blue crosses). In the write spectrum, the circles show the background noise level (dark counts) while the blocked-write dataset in the read spectrum shows the spectrum of the readout noise. Evidently, the readout noise also contains a distinct feature at $\Delta_{\mathrm{FC}} = 0$.

As argued in the section 2.6, we expect the spectrum to consist of a narrow response on top of a much broader pedestal – both centered at the Larmor frequency. Furthermore, the strong drive light will leak through to the detectors to some extent. This introduces asymmetry in the spectrum because the drive light appears at $\Delta_{\mathrm{FC}} = \pm\nu_{\mathrm{L}}$, minus for write and

plus for read. To extract the magnitude of the different spectral components we fit a model including the components described above. The model can be written

$$S_{\mathrm{WW}}(\Delta_{\mathrm{FC}}) = a_{\mathrm{NB}}\mathcal{L}_{\mathrm{FC}}(\Delta_{\mathrm{FC}}, 0) + a_{\mathrm{BB}}\mathcal{L}_{\mathrm{BB}}(\Delta_{\mathrm{FC}}, 0) + a_{\mathrm{lkg}}\mathcal{L}_{\mathrm{FC}}(\Delta_{\mathrm{FC}}, -\nu_{\mathrm{L}}) + a_{\mathrm{bg}} \tag{4.3}$$

where $\mathcal{L}_i(\Delta_{\mathrm{FC}}, \Delta_0)$ is the lineshape centered at Δ_0 with unity peak value. Subscript i indicates the relevant lineshape. The narrowband component, a_{NB}, as well as the leakage, a_{lkg} both originate from the laser linewidth. Hence, these spectral components are much narrower than the filter bandwidth (the resolution bandwidth for the output spectrum). The lineshape in the output spectrum thus follows the filter lineshape $\mathcal{L}_{\mathrm{FC}}(\Delta_{\mathrm{FC}}, \Delta_0) = \mathcal{L}_1(\Delta_{\mathrm{FC}}, \Delta_0)\mathcal{L}_2(\Delta_{\mathrm{FC}}, \Delta_0)$, given by the product of the transmission through the two cascaded filter cavities. The first cavity has an effective[1] FWHM linewidth of 92 kHz and the second 894 kHz. Both are modelled as Lorentzian lineshapes.

The broadband component is much broader than the filter. The expected FWHM is 1.5 MHz (section 2.6). Thus, the lineshape can be approximated without accounting for the finite resolution bandwidth. $\mathcal{L}_{\mathrm{BB}}(\Delta_{\mathrm{FC}}, 0)$ is therefore a Lorentzian of 1.5 MHz linewidth.

We fix the background level, a_{bg}, according to reference measurements with light pulses blocked. Then the parameters to fit are $a_{\mathrm{NB}}, a_{\mathrm{BB}}$, and a_{lkg}. The fitted model is depicted in Fig. 4.6a with three components: narrowband (blue shade), broadband (grey shade), and background (white). The leakage is negligible.

For the read spectra we fit the same model. A minor difference is that the model is fitted to two datasets simultaneously. The two measured spectra in Fig. 4.6 (circles and crosses) are acquired with and without a preceding write pulse, respectively. The model is restricted such that only the narrowband component b^i_{NB} differs in the two spectra. The model for the two spectra is

$$S^i_{\mathrm{RR}}(\Delta_{\mathrm{FC}}) = b^i_{\mathrm{NB}}\mathcal{L}_{\mathrm{FC}}(\Delta_{\mathrm{FC}}, 0) + b_{\mathrm{BB}}\mathcal{L}_{\mathrm{BB}}(\Delta_{\mathrm{FC}}, 0) + b_{\mathrm{lkg}}\mathcal{L}_{\mathrm{FC}}(\Delta_{\mathrm{FC}}, +\nu_{\mathrm{L}}) + b_{\mathrm{bg}}. \tag{4.4}$$

Superscript i refers to the two spectra: with preceding write pulse ("W") and without ("NW"). Here the filter lineshapes are the same as for write.

We fix the background level according to reference measurements with light pulses blocked. Then the fit parameters are $b^{\mathrm{W}}_{\mathrm{NB}}, b^{\mathrm{NW}}_{\mathrm{NB}}, b_{\mathrm{BB}}, b_{\mathrm{lkg}}$. The fitted model is depicted in Fig. 4.6b with five components: narrowband W (pale red shade), narrowband NW (dark red shade), broadband (grey shade), leakage (yellow shade) and background (white).

We use the output fit parameters to determine some characteristics of the noise present

[1] The cavity has a FWHM linewidth of 66 kHz but because the resonance frequency fluctuates (due to mechanical disturbance) during the freeze window, the effective linewidth over many repetitions increases by a factor 1.4.

in the DLCZ experiment. As discussed in section 2.6, the write spectrum attests how well the motional averaging works. We define the experimentally estimated write efficiency as $\eta_{\mathrm{W}} = a_{\mathrm{NB}}/(a_{\mathrm{NB}} + a_{\mathrm{BB}}) = (63 \pm 1\%)$. Here we neglect the leakage and background counts. In other words the write efficiency is the fraction of detection events originating from the narrowband feature when the filters are on resonance (in the absence of background counts). This number then defines the probability that the detected light is associated with excitation of the symmetric atomic mode.

The write count rate on filter resonance can be directly related to the average number of scattered photons, $n_{\mathrm{phot}} = S_{\mathrm{WW}}(\Delta_{\mathrm{FC}})/(\eta_{\mathrm{d}}\eta_{\mathrm{esc}})$, by correcting for detection efficiency, η_{d}, and cell cavity escape efficiency, η_{esc}. For $\eta_{\mathrm{d}} = 9.6\%$ and $\eta_{\mathrm{esc}} = 62\%$, we get $n_{\mathrm{phot}} = 0.23$ scattered photons per pulse. This leads to $\mu = \eta_{\mathrm{W}} n_{\mathrm{phot}} = 0.14$ excitations on average in the symmetric mode when accounting for write efficiency η_{W}.

The read spectrum tells us a few lessons. The first is that leakage of the excitation light constitutes almost 1/3 of the detection events at $\Delta_{\mathrm{FC}} = 0$. This should be considered a technical limitation only as the leakage can be mitigated by improving the setup (e.g. adding an extra cascaded filter cavity or improving polarization rejection).

The second lesson is that the rest of the readout noise has both substantial narrowband and broadband components. This noise originates from the atomic ensemble and will be discussed in more detail below. What is important to note here is that while the broadband component can be suppressed with a narrower spectral filter, the narrowband noise component is spectrally indistinguishable from the correlated readout. Hence, it cannot be suppressed without suppressing the correlated readout as well.

Temporal shape of readout

For a deeper investigation of the readout noise we consider the temporal shape of the detection event histogram. Fig. 4.8 displays the unconditional histogram (a) and the histogram for read pulses conditioned on a heralding write event (b). In both panels the readout noise histogram is included for reference. The shaded areas illustrate the contribution from leakage (yellow) and broadband (grey) components.

We see that the leakage noise rate grows over the duration of the pulse. This is likely due to the cell cavity resonance shifting during the read pulse. We also see that the narrowband noise increases over the pulse duration. This is an indication of a FWM process. If the readout was dominated by the intended retrieval process (beam-splitter interaction), we should expect to see an exponentially decaying narrowband readout as the symmetric atomic excitations are gradually read out, thus emptying the mode (see section 2.1). On the contrary, FWM would populate the atomic mode during the read pulse. This leads to an increasing narrowband FWM readout noise over time.

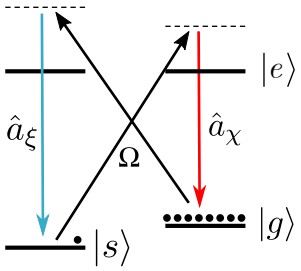

Figure 4.7: **Four-wave-mixing model.**

We adapt a FMW model described by Dąbrowski *et al.* (2014). Here the FWM Hamiltonian is given as

$$\hat{H}_{\mathrm{FWM}} = i\hbar\chi\hat{a}_\chi^\dagger\hat{b} + i\hbar\xi\hat{a}_\xi^\dagger\hat{b}^\dagger + \mathrm{h.c.} \tag{4.5}$$

The Hamiltonian in eq. (4.5) describes combination of a parametric-gain and beam-splitter interaction with strength parameter ξ and χ, respectively. Both interactions couple to the atomic mode described by $\hat{b}$ while the beam-splitter interaction couples to the optical flux mode $\hat{a}_\chi$ and the parametric gain to $\hat{a}_\xi$. This corresponds to simultaneous write and read processes where $\hat{a}_\chi$ ($\hat{a}_\xi$) describes the red (blue) Raman sideband, see Fig. 4.7.

Dąbrowski *et al.* find that the excitation of the optical field $\hat{a}_\chi$ (corresponding to the readout field in the DLCZ experiment) evolves as

$$\left\langle \hat{a}_\chi^\dagger(t)\hat{a}_\chi(t)\right\rangle = \chi^2 e^{t(\xi^2-\chi^2)}n_b + \frac{\chi^2\xi^2}{\xi^2-\chi^2}(e^{t(\xi^2-\chi^2)}-1). \tag{4.6}$$

Here $n_b = \left\langle \hat{b}^\dagger(0)\hat{b}(0)\right\rangle$ is the initial occupation of the spin-wave mode. In the absence of the parametric gain ($\xi = 0$), eq. (4.6) reduces to the intended readout $\left\langle \hat{a}_\chi^\dagger(t)\hat{a}_\chi(t)\right\rangle = \chi^2 e^{-\chi^2 t}n_b$. On the other hand, in the presence of weak parametric gain ($\xi^2 < \chi^2$), the readout of n_b decays slower leading to an increased readout gain. In this case the retrieval efficiency can exceed 100%. At the same time, the second term in eq. (4.6) describes the readout noise (i.e. $n_b = 0$). The readout noise will grow until reaching the equilibrium noise rate $\chi^2\xi^2/(\chi^2-\xi^2)$.

In Fig. 4.8a we plot the model prediction for $n_b = 0$ (cyan line) and $n_b = \mu^* = 0.13$ (green line). The latter is the $\mu = 0.14$ stated above corrected for FWM during write which removes $\sim 10\%$ of the excitations (see Zugenmaier, 2018). The coupling strength ξ is estimated from the scattering rate during write while the ratio $\chi/\xi = 1.36$ is calculated from the Clebsch-Gordan coefficients of the involved transitions. The latter also accounts for the difference in detuning from the cell cavity resonance frequency. More details on the parameter estimation can be found in Zugenmaier *et al.* (2018) and Zugenmaier (2018).

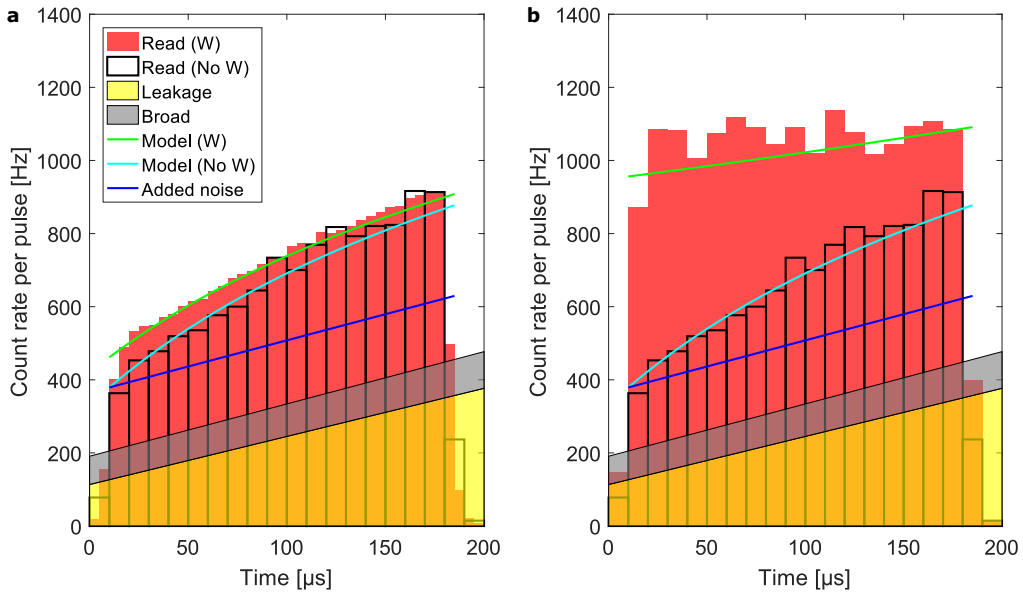

Figure 4.8: **Temporal shape of the detected readout photons. a**, Unconditional detection events. **b**, Heralded detection events. The red bar graphs represent the detection events after a preceding write pulse with a 5 µs (a), and 10 µs (b) binning. The black-framed bar graphs show the detection events without preceding write pulse in 10 µs binning. In both plots the leakage (yellow) and broad (grey) contributions have been extrapolated from fits to the spectrum obtained for segments of the detection window. The blue line represents an added constant offset. The green and cyan lines are the model predictions for readout and four-wave mixing noise contribution, respectively. The data presented correspond to the point at zero detuning in fig. 4.6. The origin of the horizontal axes is defined from the beginning of the detection window. Figure and caption from Zugenmaier *et al.* (2018).

In Fig. 4.8b the model is instead fitted to the conditional histogram with n_b as the only fit parameter. The fit optimum $n_b = 0.92$ for the conditional occupation is plotted as a green line.

To achieve good agreement between the model and the experimental histograms an extra constant noise term had to be added (blue line). The origin of this offset is unclear. We hypothesise that the main cause is imperfect initial atomic pumping. This would mean that $n_b > 0$ for the readout noise (black-framed bars). However, the magnitude of the added noise is not consistent with the estimated atomic orientation $p = 98.5\%$ which would mean approx. 6% of atoms in $|4, 3\rangle$.

4.2.2 Four-Wave-Mixing Suppression

Even though there is a substantial noise source which does not appear to be explained by FWM, we focus on the suppression of the latter. The reason for this is that in the work described above we realized that when running the DLCZ scheme on the caesium D_2 line we should expect to find a substantial amount of FWM noise. This noise will hamper the single-photon generation even if we manage to suppress the other noise sources. Thus, it does not seem feasible to use the caesium D_2 line for DLCZ with Zeeman storage.

FWM has been reported as the main noise limitation in several studies of quantum memories in warm atomic vapours, in particular for far-off resonance Raman schemes (e.g. Michelberger *et al.*, 2015). Here we give a short summary of the literature:

Following the first demonstration of single-photon generation and storage in warm vapour (Eisaman *et al.*, 2005), the same group realized that the memory readout was limited by noise from FWM (Walther *et al.*, 2007). The authors suggested to eliminate FWM by using a Λ-scheme where the write and read light have orthogonal circular polarization. The storage state would then be with $\Delta m_F = \pm 2$ with respect to the initial state. This would require the atoms to be pumped to a specific Zeeman level and not just into one hyperfine manifold.

Later, Vurgaftman and Bashkansky (2013) showed that the $\Delta m_F = \pm 2$ scheme has the disadvantage that the write process is weak because Raman transitions via the excited states interfere destructively (for all alkali atoms). The FWM-suppression in the $\Delta m_F = \pm 2$ scheme was demonstrated by Zhang *et al.* (2014) who also found a substantial suppression even in the case where atoms where pumped to one hyperfine manifold but not a specific Zeeman level.

A different strategy is to suppress the unwanted Raman transition that leads to FWM by means of a cavity. Saunders *et al.* (2016) used this technique and were able to achieve a suppression factor of 0.24 (i.e. $\xi/\chi \mapsto 0.24\xi/\chi$) as a result of a weaker cavity-mode coupling of the parametric-gain field (ξ) compared to the beam-splitter field (χ).

Alternatively, the unwanted ξ field can be suppressed through absorption. This was demonstrated by Prajapati *et al.* (2017) by introducing a pump beam which couples the ξ field to the D orbital via a Raman ladder scheme. In a far-off resonance scheme the authors reported a suppression of 85%. Similarly, Thomas *et al.* (2019) used built-in FWM suppression by selecting a pulse detuning such that the ξ photons produced from spontaneous FWM are resonant and therefore absorbed.

Ultimately, it was demonstrated (Finkelstein *et al.*, 2018; Kaczmarek *et al.*, 2018) that a quantum memory can be based on the coherence between orbital states S and D ($L = 2$) by using a Raman ladder scheme. This scheme is inherently FWM free. While the scheme shows a remarkable performance, particularly in Rb vapour, the memory time will be limited by the optical decay rate from the D state. Hence, the orbital storage can only be used for fast, short-lived storage.

Inspired by Vurgaftman and Bashkansky (2013) we investigate the Raman transition strengths in our $\Delta m_F = 1$ scheme. The rate of Raman scattering is calculated by summing over the dipole moments for each of the excited states that the transition can happen via. The problem therefore reduces to the calculation of Clebsch-Gordan coefficients.

The single-atom Raman-Rabi frequency for far-off resonance drive is given as (cf. eq. 2.30)

$$\Omega_R = \sum_i \frac{\Omega_i g_i}{2\Delta_i} \tag{4.7}$$

with i summing over the excited states. Dependent on which Λ-scheme is considered (via $m'_F = 3$ or $m'_F = 4$), Ω_R corresponds to χ or ξ. If we are only concerned with knowing the ratio χ/ξ, we can reduce eq. (4.7) to involved dipole moments without concern for the spatial modes of g and Ω. By summing over excited states with $m'_F = 4$ we have for the D_2 line

$$\chi \propto \frac{1}{\Delta_{4'}} \langle 4,4| e\hat{r}_\pi \left|4',4'\right\rangle \langle 4,3| e\hat{r}_{\sigma_+} \left|4',4'\right\rangle \tag{4.8}$$

$$+\frac{1}{\Delta_{5'}} \langle 4,4| e\hat{r}_\pi \left|5',4'\right\rangle \langle 4,3| e\hat{r}_{\sigma_+} \left|5',4'\right\rangle . \tag{4.9}$$

The expression for ξ is similar ($m'_F = 3$) but with the sum over three excited states $F' = 3, 4, 5$ and the relevant field polarizations. The dipole matrix elements can be either positive or negative as given by the Clebsch-Gordan coefficients. This means that the different excited-state pathways interfere destructively in the case of opposite signs and cancel the coupling at a specific detuning.

To account for the atomic line broadening including inhomogeneous broadening from Doppler shift, we multiply with the Faddeeva function $\mathrm{w}(z)$ (Borregaard *et al.*, 2016) such that

$$\Omega_R = \sum_i \frac{\Omega_i g_i}{2\Gamma_\mathrm{D}} \mathrm{w}\left(\frac{\Delta_i + i\gamma/2}{\Gamma_\mathrm{D}}\right). \tag{4.10}$$

In Fig. 4.9 $|\Omega_R|^2$ is plotted for the Raman coupling $|4,4\rangle \rightarrow |4,3\rangle$ for Λ-schemes with $m'_F = 3, 4$, respectively. We see that there is an appreciable suppression of the Raman transition via $m'_F = 4$ when slightly red-detuned. However, because of the small excited-state splitting for the D_2 line the elimination happens close to resonance. The optimal suppression is at $\sim 300\,\mathrm{MHz}$ red detuned from the $F = 4 \rightarrow F' = 3$ transition. Operating this close to resonance would mean a substantial amount of absorption and it is thus infeasible for the DLCZ protocol.

If we instead consider the D_1 line (Fig. 4.9, right), we see that the much larger excited state splitting leads to elimination of the Raman coupling via $m'_F = 3$ at a much larger detuning. The 'magic detuning' where the suppression is strongest is at 0.92 GHz blue detuned

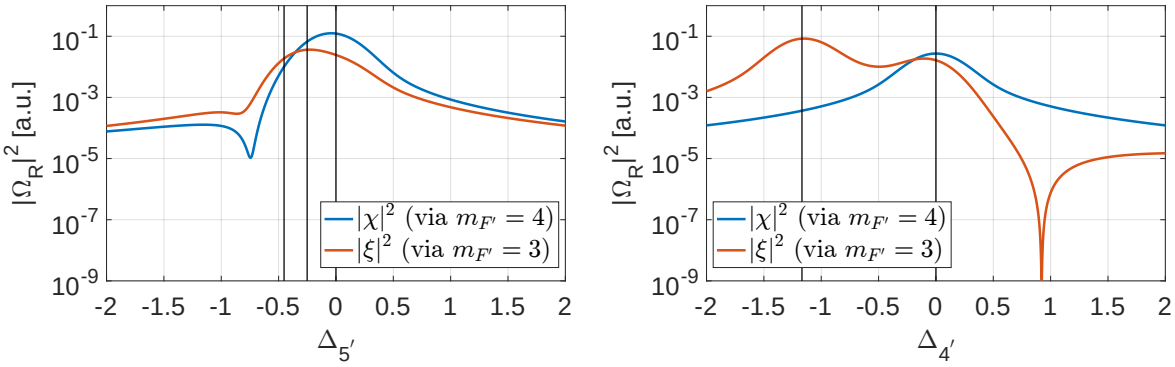

Figure 4.9: **Pathway strength comparison for D_2 line and D_1 line. Left:** D_2 line. Blue curve is coupling strength via $m'_F = 4$ and red curve is via $m'_F = 3$. Vertical lines indicate the transition frequency of (from the left) $F' = 3, 4, 5$. **Right:** D_1 line. Blue curve is coupling strength via $m'_F = 4$ and red curve is via $m'_F = 3$. Vertical lines indicate the transition frequency of (from the left) $F' = 3, 4$. At the magic detuning $\Delta_{4'} = 0.92\,\mathrm{GHz}$ the paths via $|4', 3'\rangle$ and $|3', 3'\rangle$ interfere destructively, thus suppressing FWM.

from the $F = 4 \to F' = 4$ transition. At this point the imaginary part of Ω_R crosses zero and only the weak real part contributes. We note that the Faddeeva function makes the magic detuning shift to larger detuning compared to the case of frozen atoms. The magic detuning value is therefore weakly dependent on the ensemble temperature. The stated magic detuning frequency is calculated for our typical operation temperature 42 °C where the Doppler broadening (HWHM) is $\Gamma_\mathrm{D} = 222\,\mathrm{MHz}$ (233 MHz) for D_1 (D_2).

Chapter 5

Single-photon source on the D_1 line

After realizing that FWM can be strongly suppressed on the caesium D_1 line, we set out to adapt the experimental setup to the relevant wavelength 894.6 nm and polarization scheme. The most significant change was the necessity for a second filtering and detection setup. The mechanism that allowed us to use just a single filtering and detection setup on the D_2 line is exactly the mechanism that enables FWM. Having both the heralding and retrieval field in the same mode, frequency and polarization, was possible because σ-polarized light can drive both the write and read processes on the D_2 line. For the D_1line, on the other hand, σ-polarized light can only drive the read process whereas π-polarized light drives the write process. The drive light polarization is thus the parameter selecting the type of interaction.

The work presented in this chapter is the outcome of a collaborative effort with Rebecca Schmieg and Michael Zugenmaier. The results of the experiment are reported in a manuscript currently under review (Dideriksen *et al.*, 2020) and preliminary results were reported in Schmieg (2019).

5.1 Experimental realization

On the D_1 line, the Λ-scheme coupling $|4,4\rangle \rightarrow |4,3\rangle$ via $m'_F = 3$-excited states (gray lines in Fig. 5.1b) is strongly suppressed. This is the mechanism that suppresses FWM. As a consequence, the Λ-scheme for both write and read processes have to couple via $|4',4'\rangle$. The relevant level scheme is illustrated in Fig. 5.1. A π-polarized write pulse couples $|4,4\rangle \rightarrow |4',4'\rangle$ and spontaneous Raman scattering into the σ-polarized $|4,3\rangle \rightarrow |4',4'\rangle$-transition heralds a collective excitation of the atomic ensemble. Afterwards and on demand, a horizontally-polarized (σ) read pulse couples $|4,3\rangle \rightarrow |4',4'\rangle$ and the collective excitation is retrieved on the π-polarized $|4,4\rangle \rightarrow |4',4'\rangle$-transition.

The excited-state detuning $\Delta_{4'}$ is close to the magic detuning 0.92 GHz discussed in chapter 4. Because of the cell cavity birefringence, the σ-polarized heralding photon and the

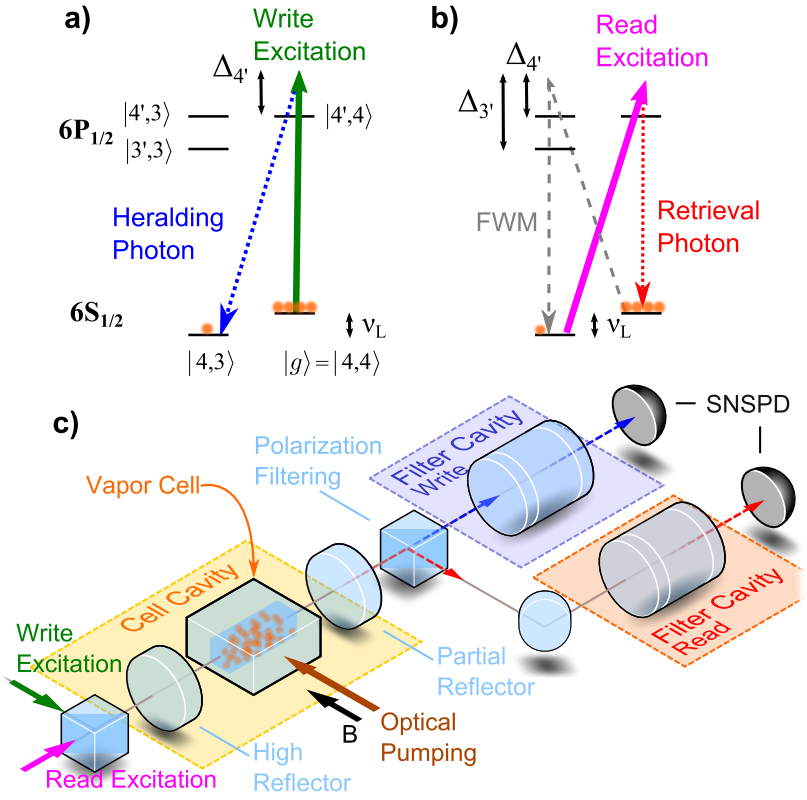

Figure 5.1: **a) and b): Atomic levels involved in the D_1 scheme.** a) Transitions involved in the write step. Excitation light in the π mode scatters light into the blue Raman sideband in the σ mode. b) Transitions involved in the read step. Excitation light in the σ mode retrieves light into the red Raman sideband in the π mode. **c) Conceptual sketch of the setup for the D_1 scheme.** The main difference to the setup for the D_2 scheme is orthogonally write and read excitation light as well as independent filtering and detection stages for write and read. Figure from Dideriksen *et al.* (2020).

π-polarized retrieval photon cannot simultaneously coincide in frequency and be resonant with the cell cavity. The birefringence shift of 32 MHz is, however, small compared to the magic detuning and within the region where FWM is strongly suppressed (see Fig. 4.9). Fig. 5.2 illustrates the optical frequencies involved in the experiment together with the cell cavity resonances. We note that the separation of resonance frequencies for horizontal and vertical polarization is more than double on the D_1 line compared to D_2. This is a consequence of the difference in excited-state hyperfine splitting.

The Larmor frequency was kept at the same value $\nu_L = 2.4$ MHz as for the D_2 line experiment.

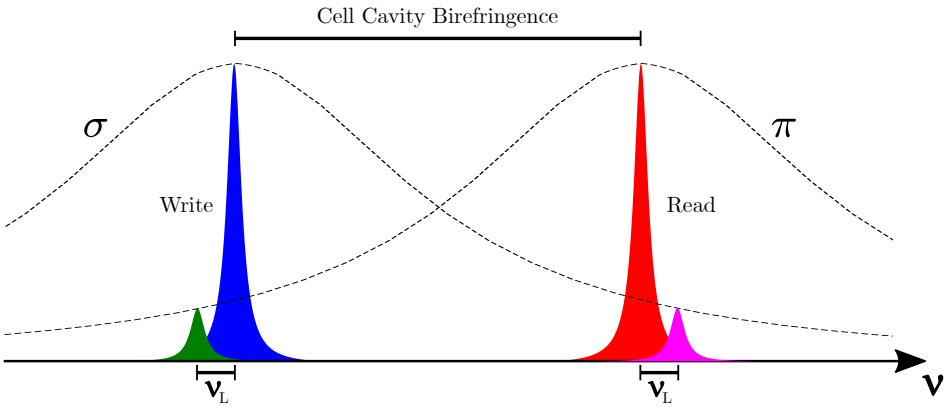

Figure 5.2: **Optical frequencies for the D_1 scheme.** Dashed lines illustrate the cell cavity resonance for σ and π polarizations. The excitation light frequency is set such that the relevant Raman sideband is resonant with the cavity. The peak heights illustrate the coupling to the cavity. Light colour codes are the same as in Fig. 5.1 with write excitation (green), heralding photon (blue), read excitation (pink), retrieval photon (red).

Fig. 5.3 displays all the essential optical components of the modified cell cavity setup. The main changes to the setup described in the previous chapter are the new read filter setup (see section 3.2.1) and the replacement of a single chopper wheel with seven mechanical blade shutters (not shown). The latter is due to an increased number of beam switches needed. We decided to reuse the two AOMs for pulse generation and since write and read drives are orthogonally polarized, we use one AOM for each. They are now designated "write" and "read" AOMs. The AOMs are also used for the lock light of the associated filter setup since the lock frequency is close. In this case routing all relevant beams through a central chopper wheel became impractical. The blade shutter design is based on that of Zhang *et al.* (2015).

For the D_1 line experiment, the avalanche detector for single-photon counting was replaced by two super-conducting detectors (SNSPD) – one for write and read, respectively. The advantage of the SNSPDs is primarily a significantly higher quantum efficiency (>90%). This reduces the run time of experiments for the same level of statistics. Secondly, the dark count rate of the SNSPDs is very low (<1 Hz instead of 10 Hz). Both advantages combined enables a substantial reduction in excitation probability before being dominated by dark counts.

We still use light near the D_2 line to lock the cell cavity. It is beneficial to have an auxiliary beam for this purpose to be able to set the cavity resonance frequency independent of other beam frequencies. For instance, the atomic state during the locking stage is not the same as the state before the write pulse. In particular because of the delayed pump laser turn-off (section 3.3.3). The advantage of using a separate colour for locking is that the cavity transmission can be filtered on a dichromatic mirror with only marginal loss of the quantum light.

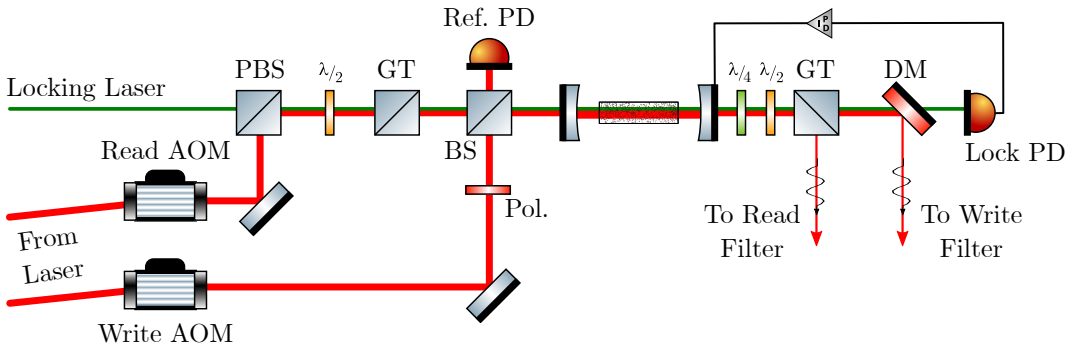

Figure 5.3: Pulse generation and cell cavity locking for the D_1 scheme. Main difference to the D_2 experiment is that the write and read pulses are orthogonally polarized and therefore generated by two independent AOMs. We reuse the D_2-line locking laser which can be separated from the quantum field on a dichroic mirror (DM).

Experimental sequence

The experimental sequence is almost identical to the one used in the D_2-line experiment. The main change to the experimental sequence is in the applied pulses. Contrary to the D_2 scheme, the write and read excitation pulses are much farther separated in frequency because of the much stronger cell cavity birefringence. Locking of the write and read filters happens simultaneously during the locking window of the sequence.

The experimental sequence consists of the following elements as illustrated in Fig. 5.4:

1. **Locking stage** (55 ms, not shown): All cavities are locked to the respective lock light.
2. **Initial pumping** (6.5 ms, not shown): All cavities are frozen. Atoms are being optically pumped. The duration of this stage is set by the actuation time of the mechanical shutters. The repump light turns off 40 µs before the pump light. Both have a smooth turn-off shape.
3. **DLCZ sequence** (Repeated up to 75 times):
   - I **Write pulse** (40 µs): Horizontally polarized. Smooth turn-on and turn-off shape.
   - II **Variable delay** (τ_D): Up to 1 ms. For delays longer than 100 µs weak repump light is applied to compensate cell cavity resonance shift due to atomic decay (section 3.3.5).
   - III **Read pulse** (200 µs): Vertically polarized. Smooth turn-on and turn-off shape.
   - IV **Intermediate pumping** (350 µs): Optical pumping with repump and pump before the next DLCZ sequence. The repump light turns off 40 µs before the pump light.

The total period of a experimental cycle is 120 ms and synchronized with the 50 Hz power line. For the shortest delay time 10 µs the overall DLCZ repetition rate is then 625 Hz.

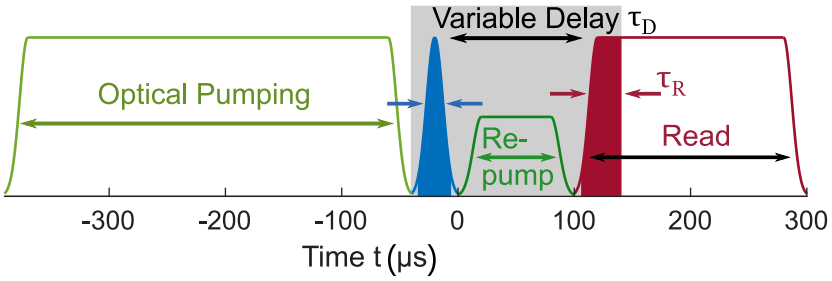

Figure 5.4: **Pulse sequence for the D_1 scheme.** A 350 µs optical pumping pulse initializes the atomic ensemble. Then a 40 µs write pulse (blue) probabilistically generates a single excitation. After a variable delay τ_D, the atomic state is retrieved by applying a read pulse (red). The filled areas illustrate the time windows used as write and read detection events. The duration of the read detection window (τ_R) is set in data post-processing. For large values of τ_D, a weak repump pulse compensates cell cavity frequency shift. Figure from Dideriksen *et al.* (2020).

5.1.1 Optimization of parameters

Read power

We optimize the read power by running the DLCZ scheme and analysing the readout noise and coherent readout as a function of read power. From eq. (2.45) it is expected that the readout rate is proportional to the read power. This matches well with the observed readout rates plotted in Fig. 5.5. The readout rates are extracted by fitting an exponential function to the read detection histograms. An example is given in Fig. 5.5. The initial rising part of the histogram is excluded in the model fit because it is related to the rising edge of the read pulse. The model does not include the weakly increasing noise level in the last half of the histogram but just a long-time offset noise level.Evidently, the readout time can be shortened by increasing the read power. It will likely be beneficial to increase the readout rate for most applications of the source-memory system.

Ultimately, the readout time will be limited by the motional averaging time since the interaction with the complete ensemble is necessary for efficient retrieval. Another practical limit is set by the filter cavities. The photon shape has to be long enough that the field can pass through the filter cavities with a high transmission. With the current spectral filter, the limiting timescale is a few microseconds. Unfortunately, we were unable to probe this limit because we are limited in read power. The reason for this is a combination of coupling through the high reflector of the cell cavity and limited output power of the narrow ECDL.

For the demonstration of single-photon generation our primary goal is to reduce the readout noise as much as possible to be able to observe strong antibunching. To this end, we consider the signal-to-noise ratio (SNR) of the readout. We define the retrieval efficiency as the

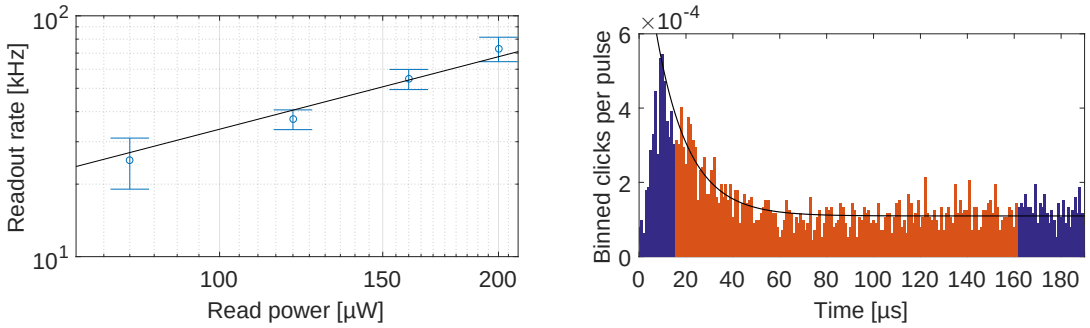

Figure 5.5: **Read power analysis I. Left:** Readout rate dependency on read power (cell cavity input). Black line is a fit to direct proportionality with ratio 0.34 kHz/µW. **Right:** Example of readout rate fitting with fitting region illustrated in orange. The data shown is for 200 µW read power.

difference between the unconditional mean readout with and without a preceding write pulse,

$$\eta_{\mathrm{R}}^{\mathrm{unc}} = \langle n_{\mathrm{R}} \rangle - \langle n_{\mathrm{noise}} \rangle \ . \tag{5.1}$$

Please note that the definition in eq. (5.1) is slightly different than the one used in chapter 4. The retrieval efficiency is plotted against the integration parameter τ_{R} in Fig. 5.6 for three different powers (for 80 µW the statistics are insufficient). We see that $\eta_{\mathrm{R}}^{\mathrm{unc}}$ rises as more of the readout pulse is included until plateauing when the full signal is read out. For the lowest read power the plateau level is slightly lower than for the others. This could be just due to small drifts in detection efficiency.

From the retrieval efficiency we define the SNR as

$$\alpha_{\mathrm{unc}} = \frac{\eta_{\mathrm{R}}^{\mathrm{unc}}}{\langle n_{\mathrm{noise}} \rangle} \ . \tag{5.2}$$

The corresponding SNR values are plotted in Fig. 5.6. Please note that the unconditional SNR is proportional to the excitation probability. The absolute number is therefore only relevant in comparison to the write power. We observe only very little variation in SNR between the read power values. This indicates that the achievable antibunching will only have a weak dependency on read power. Though it is worth noting that to optimize single-photon source performance, high retrieval efficiency is favourable. As we shall discuss below, we find that it is beneficial to truncate the read window before the readout is complete. For τ_{R} fixed at a value smaller than the full readout time, the retrieval efficiency will depend on the readout rate, as we see in 5.6 (left). Hence, high read power is favourable.

It would be interesting to investigate the readout power dependency at higher read power. Unfortunately, in the current setup we are unable to run the DLCZ scheme with higher read power. At some power the retrieval efficiency is expected to drop because of loss due to spontaneous emission (see Fig. 2.9). Such an investigation could then establish a bandwidth

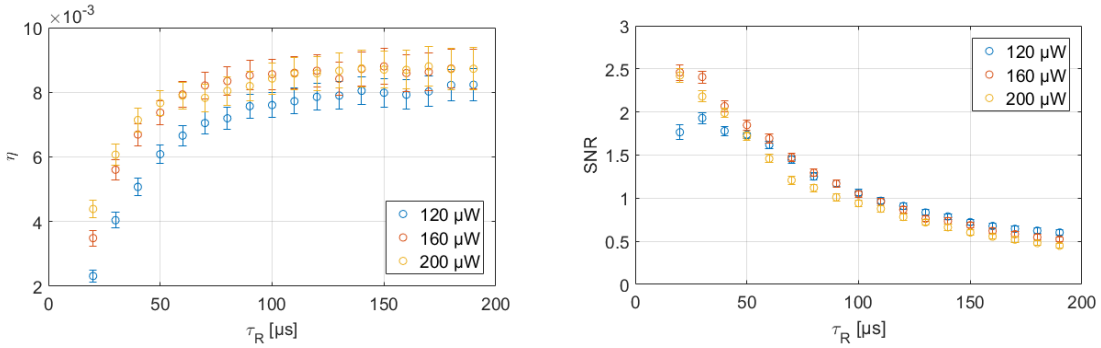

Figure 5.6: **Read power analysis II. Left:** Unconditional retrieval efficiency as defined in eq. (5.1) vs. integration parameter for various read powers. **Right:** Unconditional read SNR as defined in eq. (5.2) vs. integration parameter for various read powers. The data points for each power are derived from the same dataset and therefore not statistically independent.

limitation for readout. The bandwidth will be limited by the filter linewidth but for the read powers applied in this analysis, the readout is slower than the Fourier limit from the filter.

Pulse shapes

After investigating the dependency on read power an obvious related parameter to investigate is the temporal shape of the pulses involved. This would be pumping pulses, write pulse and read pulse. The concern is that an abrupt rise or fall of the applied pulses can generate atomic excitation because of the broadband spectral components associated with the fast shape. A similar sensitivity to abrupt pulse turn-off was claimed by Bao *et al.* (2020).

First we discuss the influence of the fall time of the optical pumping light, i.e. pump and repump together. The optical pumping intensity is quite high and the light is on atomic resonance. We test the difference between a fast fall time limited by AOM response ($\sim 100\,\mathrm{ns}$) and a $5\,\mu\mathrm{s}$ fall from slowly attenuating the AOM RF signal. As with the read power optimization, the most direct way of measuring the influence of the pulse shapes is by running the DLCZ scheme. In Fig. 5.7 we plot the readout noise from the two cases. We plot noise through the filter cavities when locked on the Raman sideband (readout resonance) where both narrowband and broadband noise contribute. As a reference we plot the noise with filters $200\,\mathrm{kHz}$ detuned where only broadband noise contributes. This enables us to distinguish between narrowband and broadband noise. We see that there is no influence from pumping fall time on the broadband noise while the narrowband noise drops slightly in the beginning of the pulse. When integrating over the count rate for the first $40\,\mu\mathrm{s}$, the abrupt pumping turn-off has 20% more noise. This indicates a small advantage from smooth turn-off. We confirm that this drop is not due to a general drop in retrieval efficiency. This is done by applying a weak RF magnetic pulse that generates atomic excitation at the few excitations

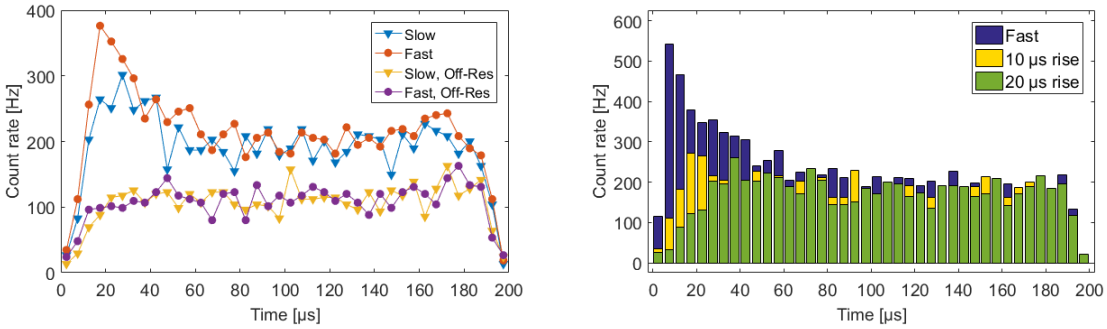

Figure 5.7: **Readout noise dependency on pulse shapes. Left:** Varying the turn-off shape of the preceding optical pumping pulse. With the filter cavity on resonance, the fast turn-off induces slightly more readout noise. For reference the filter cavity is shifted by 200 kHz where only broadband noise is recorded. Here there is no difference between the pulse shapes. Data was recorded with 10 µs read rise time. **Right:** Varying the rise time of the read pulse. When the read pulse rise time is fast, the readout noise increases.

level according to eq. (3.22). The atomic excitation can then be read out (not shown) as a retrieval signal much stronger than the unconditional DLCZ readout.

Similarly, we investigate the read pulse shape influence. In Fig. 5.7 we plot the readout noise histograms for different pulse rise times. The "fast" rise setting is again given by the AOM response ($\sim$ 100 ns). We test for smoother shapes with rise times of 10 µs and 20 µs respectively. The fast rise setting appears to cause a substantial amount of noise in the symmetric mode. This mode is read out in the beginning of the read pulse in a characteristic exponentially-decaying envelope. In comparison the noise level in the smoother pulses is significantly lower. Also here we perform reference measurements (not displayed) by applying an RF pulse to confirm the coherent readout for the different pulse settings. We see that the readout follows the slower rise of the pulse but the total readout is similar for all pulse settings. Thus, the smooth pulses yields better SNR because of the lower noise level. At $\tau_R = 40$ µs the SNR is $\sim$ 75% higher for the slow-rise pulses than for the fast-rise pulse.

This investigation demonstrates that sharp pulse shapes have an influence on the atomic state and that it appears to be stronger for the off-resonant read pulse than for the resonant pumping pulse. We attribute this excitation of atomic noise to stimulated Raman scattering. If the excitation light polarization is not purely vertical (i.e. σ-polarized), parasitic π-polarization can stimulate Raman scattering. When beams are switched fast, the broadband spectral components associated with the fast rise yields sidebands at the Larmor frequency. These then drive the stimulated Raman scattering.

Based on this analysis, we decide to conduct the DLCZ experiment by applying smooth

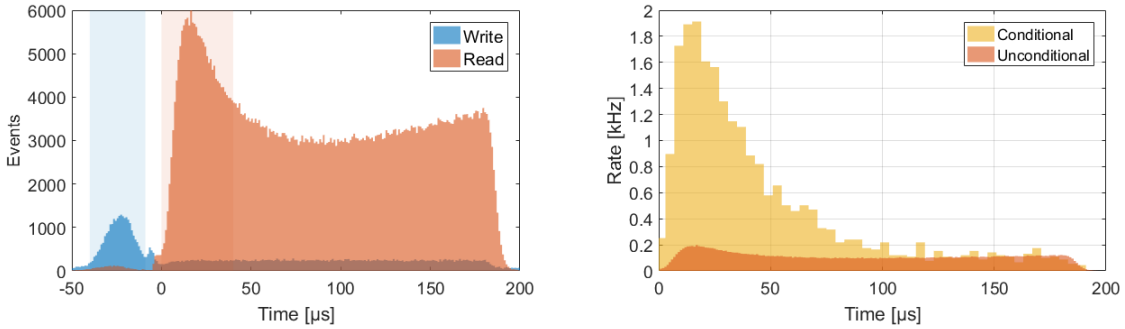

Figure 5.8: **Detection event histograms for D1 scheme. Left:** Unconditional histograms from the write and read detectors. The histograms are overlayed with transparency such that the both histograms can be seen for the full time window. Shaded bands mark the definition of respective detection windows for the correlation analysis. **Right:** Normalized unconditional read histogram (same data as in the left panel) overlayed with read histogram conditioned on a single write event. The bin width is higher for the conditional histogram because of lower statistics. The high conditional readout rate indicates strong correlation between write and read events.

pulse shapes with $\sim 10\,\mu s$ rise/fall time for all relevant pulses, i.e. pump/repump, write and read pulses.

5.2 Source-Memory Performance

We now turn to the actual performance characterization of the room-temperature single-photon source-memory protocol. This constitutes the main result of the thesis and demonstrates that the motional averaging technique can be employed to generate a single excitation in the long-lived atomic mode from where it can later be retrieved on demand as a single photon. Through noise analysis and suppression we have managed to reduce the readout noise to a level where the single-photon character of the retrieved field is not compromised.

Detection windows

Similar to the D_2-line analysis presented in chapter 4, we can freely choose how to define the detection windows, i.e. the time windows in which a detection event is considered a write click or read click, respectively. A histogram of the events is displayed in Fig. 5.8. We find the optimal settings for the detection windows in the data postprocessing. The aim is to find an optimum trade-off between SNR and sacrifice of signal. If we set the windows too narrow, the SNR is high but we also decrease the statistics by neglecting much of the recorded events. For too large windows, it is vice versa.

For the write process the temporal distribution of events follows the shape of the write pulse. Thus, the SNR during write does not vary much with time as long as the signal is sufficiently above the background level. We find that varying the window width and center position only has marginal influence on the correlations between write and read events. However, as can be seen from the histograms in Fig. 5.8 there is an intermediate region where both detectors see clicks. The reason for this is currently unknown, so we have chosen to exclude this region from the analysis.

The situation is very different for the read process. Here the coherent signal is retrieved in the beginning of the pulse while the end of the pulse only contains noise. That makes the outcome of the analysis much more sensitive to the chosen read detection window. In Fig. 5.8 (right), we plot the unconditional read histogram together with the conditional read histogram from read pulses with a single preceding write event. The histograms are normalized to the number of pulses and bin width such that they display the event probability per unit time. We clearly see that the conditional read is much more frequent than the unconditional. This indicates a strong correlation between write and read events. The histograms also show that the correlated readout happens in the beginning of the read pulse and after approx. 100 µs only (uncorrelated) noise is detected.

We consider *conditional* retrieval efficiency and SNR defined similar to eq. (5.1) and eq. (5.2) but from the conditional readout such that

$$\eta_{\mathrm{R}} = \left\langle n_{\mathrm{R|W=1}} \right\rangle - \left\langle n_{\mathrm{noise}} \right\rangle , \quad \alpha = \frac{\eta_{\mathrm{R}}}{\left\langle n_{\mathrm{noise}} \right\rangle} . \tag{5.3}$$

Both values will depend on the width of the read detection window, τ_{R}. The window start time is fixed so τ_{R} determines how much of the read pulse is integrated over. The outcome of the read detection window analysis is plotted in Fig. 5.9. The figures display the compromise between SNR and retrieval efficiency that can be freely chosen. For reasons that will be clearer when discussing correlation values, we have decided to use $\tau_{\mathrm{R}} = 40\,\mu\mathrm{s}$ for the characterization of the source-memory performance. Evidently, this involves sacrificing approx. 30% of the correlated readout. In the situation of an actual application of the source-memory system (e.g. photon interference), τ_{R} can be varied experimentally by choice of read pulse length. The optimal choice will depend on the application at hand and the sensitivity to readout noise. Please note that it is coincidental that the choice $\tau_{\mathrm{R}} = 40\,\mu\mathrm{s}$ is the same as for the D_2line.

5.2.1 Excitation probability influence

As discussed in chapter 2, limited detection efficiency demands a low excitation probability to achieve high fidelity of the heralded single atomic excitation. As a starting point for our single-photon source performance characterization we therefore investigate the influence of the excitation probability. Experimentally, this is simply done by varying the write pulse energy

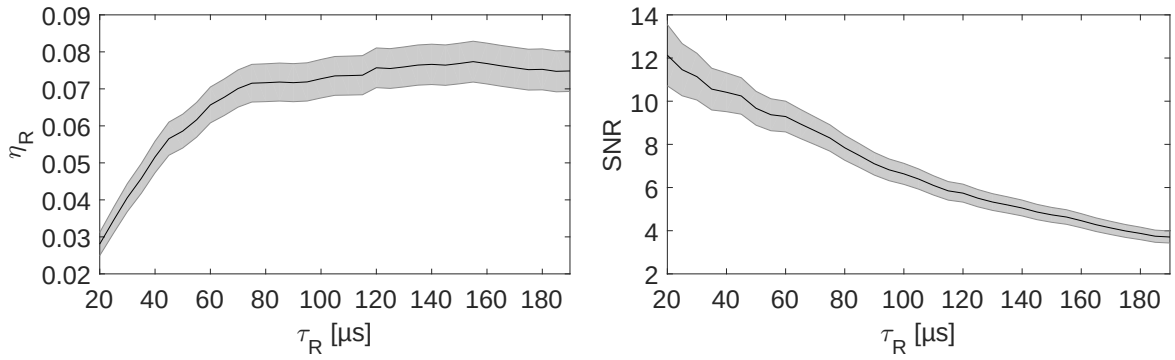

Figure 5.9: **Detection window influence. Left:** Conditional retrieval efficiency vs. integration time. **Right:** Conditional SNR vs. integration time. The two panels demonstrate the trade-off between retrieval efficiency and SNR when choosing the readout window width. We decided to use $\tau_R = 40\,\mu s$ in the remainder of the analysis. The data points are derived from the same dataset and therefore not statistically independent. The values in both plots are significantly higher than those in Fig. 5.6 because of conditioning on a write event.

while keeping all other parameters fixed. Furthermore, we also choose to fix the write pulse shape, which makes the write power the only variable parameter. The results discussed in this section are obtained for the shortest applied write-read delay $\tau_D = 10\,\mu s$, corresponding to the setting in Fig. 5.8.

The three main performance values are cross-correlation between write and read fields $g^{(2)}_{WR}$, retrieval efficiency η_R and conditional read field auto-correlation $g^{(2)}_{RR|W=1}$. The three quantities are plotted against the mean number of write events in Fig. 5.10. All plots in the figure contain a line depicting the fitted correlation model. This model will be discussed in section 5.2.4. The influence of excitation probability for all three quantities is in good agreement with the model.

Cross-correlation

For high excitation probability the heralded atomic state is contaminated with a non-vanishing double-excitation component. As discussed in section 2.7, multiple-excitation components decreases the cross-correlation even in the case of ideal number-resolving detection. The same behaviour is apparent in Fig. 5.10a. The cross-correlation peaks at $g^{(2)}_{WR} = 10 \pm 1$ for $\langle n_W \rangle \approx 0.5 \times 10^{-3}$. According to the fitted model this corresponds to an excitation probability $p_0 \approx 1.7\%$ when correcting for propagation losses and write efficiency. Evidently, the intensity correlation between the write and read fields is high for excitation probabilities of a few percent. In this regime, the correlation is deep into the non-classical region ($g^{(2)}_{WR} > 2$) and sufficient for entanglement generation and verification (see section 2.7).

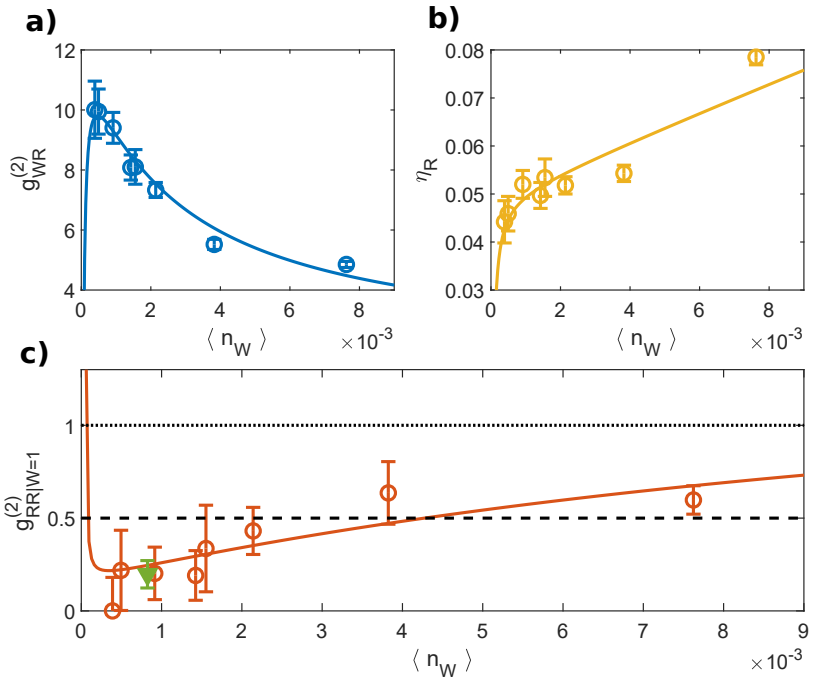

Figure 5.10: **Correlations vs. excitation probability. a)** Cross-correlation decreases for high excitation probability. **b)** Conditional retrieval efficiency increases for high excitation probability due to multiple atomic collective excitations. **c)** Conditional read auto-correlation. The model line exceeds 1 for low $\langle n_W \rangle$ because the readout noise is bunched. Figure from Dideriksen *et al.* (2020).

Retrieval efficiency

Opposite to the cross-correlation, the presence of double excitations in the heralded atomic state increases the retrieval efficiency. The mean number of excitations in the heralded atomic state grows with the excitation probability. Consequently, the retrieval efficiency increases with the mean write number as observed in Fig. 5.10b. In this sense, the retrieval efficiency versus mean write events becomes a measure for the mean number of conditional excitations $\tilde{\mu}$. Here we define the retrieval efficiency as the conditional readout with noise subtracted as in eq. (5.3). The advantage of this definition is that the subtracted level is independent of the excitation probability. Oppositely, in chapter 4, the unconditional readout was subtracted. This level is proportional to the excitation probability.

Due to imperfect write efficiency from incomplete motional averaging, the mean number of added excitations in the heralded atomic state reaches one for $\langle n_\mathrm{W} \rangle \approx 4 \times 10^{-3}$ ($p_0 \approx 14\%$) according to the fitted correlation model. Hence, the probability for a read event from a single atomic excitation in the symmetric mode is $\eta_Y = (6.0 \pm 0.2)\%$ (fit parameter of the model).

We can correct this number for known propagation losses to find the intrinsic retrieval

efficiency, i.e. the energy efficiency of converting the atomic state to the cell cavity light mode. The propagation losses can be separated into two components: the cell cavity escape efficiency and the propagation losses from the cell cavity output to detection including detector quantum efficiency. We refer to the latter as "detection efficiency". The escape efficiency is discussed in section 3.3.5. From a finesse measurement on the day of DLCZ experiments we find $\eta_{\mathrm{esc}} = (45 \pm 2)\%$.

We estimate the detection efficiency by transmitting a strongly attenuated light pulse and recording the detection event rate. For this, the pulse power after the cell cavity is calibrated using a power meter and strong attenuation is achieved by stacking calibrated neutral-density filters. We determine the detection efficiency $\eta_{\mathrm{d}} = (19 \pm 2)\%$ as an average over several measurements performed throughout the duration of the DLCZ experiments.

Applying the correction for propagation losses we determine the intrinsic retrieval efficiency

$$\eta_{\mathrm{R}}^{*} = \frac{\eta_Y}{\eta_{\mathrm{esc}}\eta_{\mathrm{d}}} = (70 \pm 8)\%. \tag{5.4}$$

This means that the retrieval process is highly efficient even though a substantial part of the retrieval is sacrificed to enhance the SNR. Unfortunately, more than half of the photons are lost inside the cell cavity which is intrinsic to the scheme. Improving the cell cavity escape efficiency will then be a critical task to enable scalable performance. Alternatively, a scheme without cell cavity can be envisioned (see chapter 6).

Conditional auto-correlation

Estimating the auto-correlation of the conditional read field requires substantially higher statistics than estimating $g^{(2)}_{\mathrm{WR}}$ and η_{R}. The reason for this is that while $g^{(2)}_{\mathrm{WR}}$ and η_{R} can be estimated from two-photon coincidences – single write, single read – $g^{(2)}_{\mathrm{RR|W=1}}$ relies on three-photon coincidences - single write, double read. Especially for low excitation probability it is cumbersome to generate large enough datasets while keeping the setup parameters stable. Despite the low statistics, $g^{(2)}_{\mathrm{RR|W=1}}$ also exhibits a trend which depends on excitation probability. Here the presence of multiple excitations in the heralded atomic state compromises the single-photon readout as multiple photons are retrieved. However, all values are in the non-classical region $g^{(2)}_{\mathrm{RR|W=1}} < 1$.

For low excitation probability, the estimated values of $g^{(2)}_{\mathrm{RR|W=1}}$ even fall below the two-photon limit $g^{(2)}_{\mathrm{RR|W=1}} < 0.5$. As a means of reducing the statistical uncertainty of the $g^{(2)}_{\mathrm{RR|W=1}}$ estimate, we combine datasets with $\langle n_{\mathrm{W}} \rangle < 2 \times 10^{-3}$ into a single estimate (green ∇ in Fig. 5.10). We justify this procedure by noting that, according to the correlation model, the correlations for the conditional read field is only expected to depend weakly on $\langle n_{\mathrm{W}} \rangle$ in this interval. The combined set yields $g^{(2)}_{\mathrm{RR|W=1}} = 0.20 \pm 0.07$. This result verifies the single-photon operation for low excitation probability with a margin of more than four standard

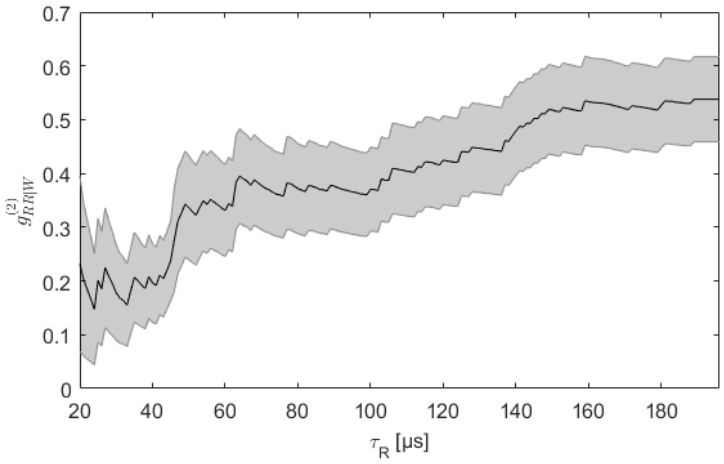

Figure 5.11: **Conditional auto-correlation vs. integration time.** When the read detection window is long, the SNR decreases and leads to increased conditional auto-correlation. All points are derived from the same dataset by varying the analysis parameter τ_R and hence are not statistically independent.

deviations to the two-photon level. In other words, the write process heralds the preparation of an atomic state close to the first Fock state while the read process transfers this state to the readout light field with sufficiently low added noise to conserve the strong antibunching statistics for the field intensity.

Please note that for very low excitation probability the write events will be dominated by uncorrelated background noise. Thus, the model lines show sharp changes when approaching this regime for $\langle n_\mathrm{W} \rangle \lesssim 0.2 \times 10^{-3}$.

The $g^{(2)}_{\mathrm{RR|W=1}}$ is the most important figure of merit for the single-photon source and we therefore also investigate how the value depends on the chosen readout window. Fig. 5.11 displays how $g^{(2)}_{\mathrm{RR|W=1}}$ grows with τ_R due to decreasing SNR. To ensure an antibunching well below the two-photon level, we choose $\tau_\mathrm{R} = 40\,\mu\mathrm{s}$ for the performance values discussed in this chapter.

5.2.2 Memory performance

Having verified the single-photon operation in the previous section, we turn to testing the performance of the memory part of the source-memory system. For this we focus on the non-classical correlation of the write and read field intensities. When increasing the write-read delay, τ_D, the experiment repetition drops which makes acquisition of data to estimate three-photon coincidence rates infeasible in the current setup. Hence, we are unable to get a good estimate of the conditional auto-correlation for variable τ_D.

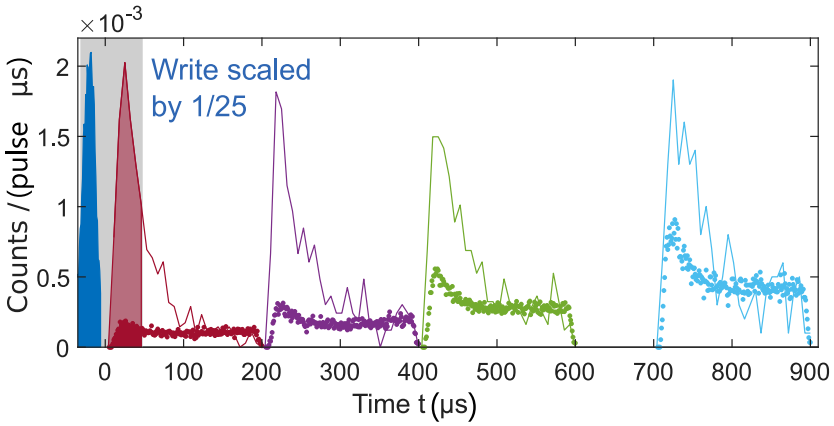

Figure 5.12: **b) Temporal shape of detection events:** Blue area - detected counts during heralding write pulses (31 µs, scaled 1/25). Solid curves - detected counts during read pulses (200 µs, delayed 10 to 710 µs) conditioned on the heralding write count (averaged over 7 µs bins). Dotted curves - the read noise level in the absence of write pulse (1 µs binning). Figure and caption from Dideriksen *et al.* (2020).

In Fig. 5.12 histograms of write and read events for different delays are plotted. We plot the conditional histograms (lines) on top of the noise histograms where the latter is obtained by blocking the write pulse. The figure shows two important characteristics of the memory scheme. 1) The noise level grows substantially with the delay time and 2) the coherent readout drops with delay time (this is the difference between conditional read and noise). The noise characteristics originate from atomic decay into $|4,3\rangle$ and will be discussed more in the next section. Fig. 5.13 shows the decay of the retrieval efficiency for $\tau_{\mathrm{R}} = 40\,\mu\mathrm{s}$, i.e. the difference between conditional readout and noise.

The decay of retrieval efficiency is a consequence of spin-wave dephasing. The observed characteristic decay time $\tau_{\eta_{\mathrm{R}}} = 0.89^{+0.49}_{-0.23}$ ms is close to the theoretical limit of $T_2/2$ for a transverse macroscopic spin decay $T_2 = 2.0\,\mathrm{ms}$ determined from pulsed MORS experiments. In comparison, we were only able to obtain a lifetime of $0.27 \pm 0.04\,\mathrm{ms}$ in the D_2-line experiment due to stronger magnetic inhomogeneities.

Both the spin-wave decay and the rise of atomic noise reduces the cross-correlation. Hence, the rate of cross-correlation decay is a consequence of both factors. If the readout noise was not rising, the decay of cross-correlation is expected to follow the spin-wave decay rate e^{-2t/T_2}.

The cross-correlation decay is plotted in Fig. 5.14 together with the Cauchy-Schwarz parameter R. The latter is a normalization to the auto-correlations of the write and read fields. When estimating auto-correlation values, we choose to combine datasets for all values of τ_{D} to reduce statistical uncertainty. The write auto-correlation is independent of τ_{D} and we see no significant influence of τ_{D} on the read auto-correlation .

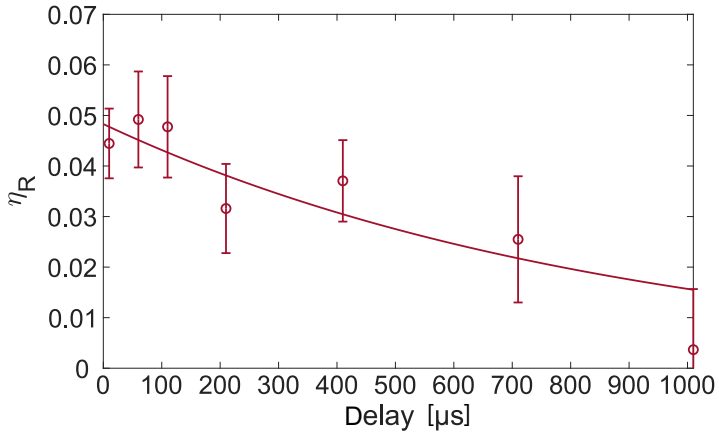

Figure 5.13: **Retrieval efficiency η_R vs. delay time τ_D:** Shown is the retrieval efficiency for various delay times and a fixed readout integration duration of $\tau_R = 40\,\mu s$. The uncertainty on the retrieval efficiency is calculated using Poissonian errors. An exponential function is fit to obtain the intrinsic memory time. Figure and caption from Dideriksen *et al.* (2020).

We fit an exponential decay

$$g^{(2)}_{WR}(\tau_D) = (g^{(2)}_{WR}(0) - 1)e^{-\tau_D/\tau_g} + 1 \tag{5.5}$$

to $g^{(2)}_{WR}(\tau_D)$ (red line) and normalize the fit result to write and read auto-correlations in order to plot the corresponding exponential decay of R (blue line). From the fit we can extract three important performance measures for the memory. The first measure is the characteristic decay time $\tau_g = 0.44 \pm 0.04\,ms$ which is half the decay of the spin wave, τ_{η_R}. This demonstrates the detrimental effect of the rising read noise.

The second measure is the crossing of $g^{(2)}_{WR} = 5.7$ [1]. The time until the crossing indicates the memory time available where the correlation is strong enough to enable Bell-inequality violation. This limit is discussed in section 2.7. The crossing happens for $\tau_{BI} = 0.15 \pm 0.03\,ms$.

The third measure is the crossing into the classical regime at $R \leq 1$. This happens at $\tau_{NC} = 0.68 \pm 0.08\,ms$. At this delay, quantum correlations are gone and therefore this quantity is often stated as the memory time for a single-photon memory (e.g. Dou *et al.*, 2018).

Please note that all three measures for the memory performance will depend of the choice of excitation power. The measurement displayed in Fig. 5.14 was carried out at $\langle n_W \rangle = 1.6 \times 10^{-3}$ to reach a heralding rate sufficient to generate enough statistics. For lower excitation probability where the cross-correlation is slightly higher, we should expect an impact on all three measures. τ_{BI} and τ_{NC} will increase because $g^{(2)}_{WR}$ starts out at a higher level, whereas τ_g will decrease because the rising noise pulls $g^{(2)}_{WR}$ to one faster.

[1] This threshold value deviates slightly from the $g^{(2)}_{WR} = 5.8$ from section 2.7. Here we state the value used in Dideriksen *et al.* (2020) which refers to the threshold used by Wallucks *et al.* (2020). The deviation likely comes from approximating $1/\sqrt{(2)} \approx 0.7$.

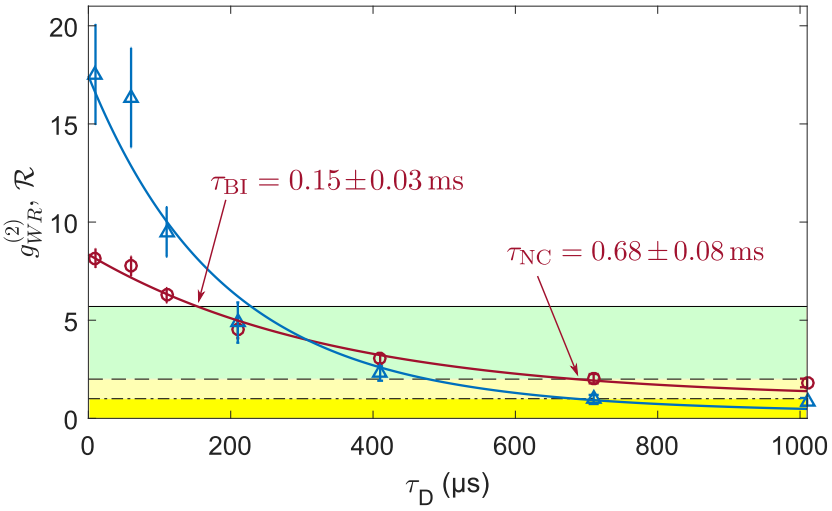

Figure 5.14: **Photon correlations for delayed readout:** Shown are $g^{(2)}_{\mathrm{WR}}$ (red) and the Cauchy-Schwarz parameter R (blue) versus various read pulse delays τ_{D} for an integrated read pulse duration of τ_{R} together with the fit to $g^{(2)}_{\mathrm{WR}}$ (red line) and the resulting R (blue line). The black line marks the Bell-inequality limit $g^{(2)}_{\mathrm{WR}} \geq 5.7$ and the dashed line marks the typical non-classicallity signature $g^{(2)}_{\mathrm{WR}} > 2$. The dash-dotted line is the formal non-classicallity criterion $R > 1$. Error bars represent one standard deviation. Figure and caption adapted from the Dideriksen *et al.* (2020).

If we take $\tau_{\mathrm{NC}} = 0.68 \pm 0.08\,\mathrm{ms}$ as the memory time, we can calculate the time-bandwidth product. A write pulse of 40 µs (where only 31 µs is used for the analysis) yields a time-bandwidth product of $B = 17 \pm 2$. Please note that this number does not account for any reinitialization of the source.

5.2.3 Noise Sources

Here we present an investigation of the noise of the write and read processes. First we map out the light spectrum near the Raman sidebands during write and read by scanning the resonance frequency of the filter cavities as described in section 4.2.1. The write and read spectra are plotted in Fig. 5.15. Both spectra show a distinct feature at the sideband frequency equal to $\pm\nu_{\mathrm{L}}$ where the filter resonance is locked during DLCZ experiments. In the figure this is referred to as $\Delta_{\mathrm{FC}} = 0$.

As argued in the section 2.6, we expect the spectrum to consist of a narrow response on top of a much broader pedestal – both centered at the Larmor frequency. Furthermore, the strong drive light will leak through to the detectors to some extent. This introduces asymmetry in the spectrum because the drive light appears at $\Delta_{\mathrm{FC}} = \pm\nu_{\mathrm{L}}$, minus for write and plus for read. In Fig. 5.15a we also plot the count rate when the write pulse is blocked. This

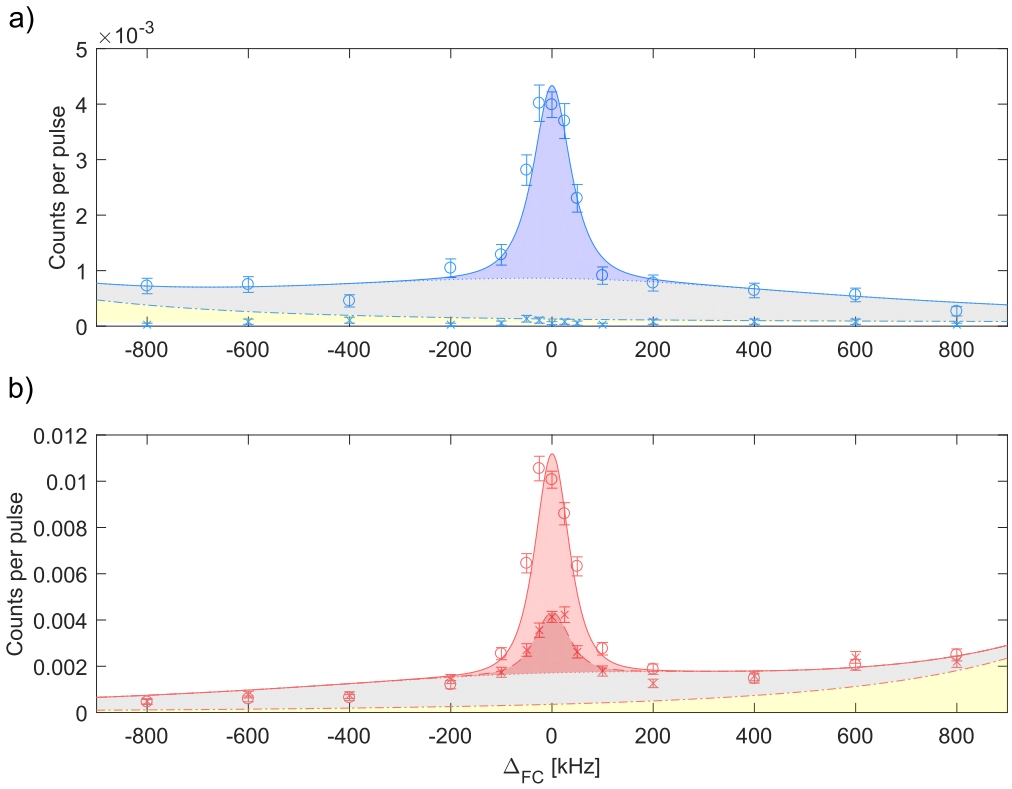

Figure 5.15: **a)** Mean number of noise counts per pulse measured during the write detection window (red circles) plotted versus the mean number of write counts with Poissonian standard deviation. Linear fit shown as yellow line. **b)** Mean number of counts per pulse measured during the read detection window (blue circles) plotted versus the mean number of write counts. Error bars are standard deviation assuming Poissonian distribution of $\langle n_R \rangle$. The fitted model is shown as the red line. Figure and caption from Dideriksen *et al.* (2020).

demonstrates that the background detection rate on the detector is negligible. The same holds for the read.

We extract the magnitude of the different spectral components using the same method described in section 4.2.1. The fit model is adapted to the filters of the D_1-line setup such that the write spectrum is

$$S_{\mathrm{WW}}(\Delta_{\mathrm{FC}}) = a_{\mathrm{NB}}\mathcal{L}_{\mathrm{W}}(\Delta_{\mathrm{FC}}, 0) + a_{\mathrm{BB}}\mathcal{L}_{\mathrm{BB}}(\Delta_{\mathrm{FC}}, 0) + a_{\mathrm{lkg}}\mathcal{L}_{\mathrm{W}}(\Delta_{\mathrm{FC}}, -\nu_{\mathrm{L}}) + a_{\mathrm{bg}} \tag{5.6}$$

with $\mathcal{L}_{\mathrm{W}}(\Delta_{\mathrm{FC}}, \Delta_0) = \mathcal{L}_1^{\mathrm{W}}(\Delta_{\mathrm{FC}}, \Delta_0)\mathcal{L}_2^{\mathrm{W}}(\Delta_{\mathrm{FC}}, \Delta_0)$ for the new write filter. The effective FWHM linewidth of the first write filter cavity is 98 kHz and the second 240 kHz.

Similarly, the read spectrum model is adapted to the new read filter such that

$$S^i_{\mathrm{RR}}(\Delta_{\mathrm{FC}}) = b^i_{\mathrm{NB}}\mathcal{L}_{\mathrm{R}}(\Delta_{\mathrm{FC}},0) + b_{\mathrm{BB}}\mathcal{L}_{\mathrm{BB}}(\Delta_{\mathrm{FC}},0) + b_{\mathrm{lkg}}\mathcal{L}_{\mathrm{R}}(\Delta_{\mathrm{FC}},+\nu_{\mathrm{L}}) + b_{\mathrm{bg}}. \tag{5.7}$$

Here the filter lineshape is again the product of the transmission through of two cascaded filter cavities $\mathcal{L}_{\mathrm{R}}(\Delta_{\mathrm{FC}},\Delta_0) = \mathcal{L}^{\mathrm{R}}_1(\Delta_{\mathrm{FC}},\Delta_0)\mathcal{L}^{\mathrm{R}}_2(\Delta_{\mathrm{FC}},\Delta_0)$. For the new read filter setup, the first cavity has a FWHM linewidth of 117 kHz and the second 128 kHz.

From the fit parameters we can estimate the SNR for the write process. We define the experimentally estimated write noise as $\langle n_{\mathrm{W,noise}}\rangle = S_{\mathrm{WW}}(\Delta_{\mathrm{FC}}=0) - a_{\mathrm{NB}}$. In Fig. 5.16 the write noise is plotted for different write powers. We find good agreement with a linear dependency on $S_{\mathrm{WW}}(0)$. This means that the ratio between narrowband and broadband is constant as we would also expect from the theoretical treatment in section 2.6. The small offset comes from a_{bg}. We can use the slope of the linear fit in Fig. 5.16 to estimate the write efficiency $\eta_{\mathrm{W}} = a_{\mathrm{NB}}/(a_{\mathrm{NB}} + a_{\mathrm{BB}}) = (82 \pm 1\%)$.

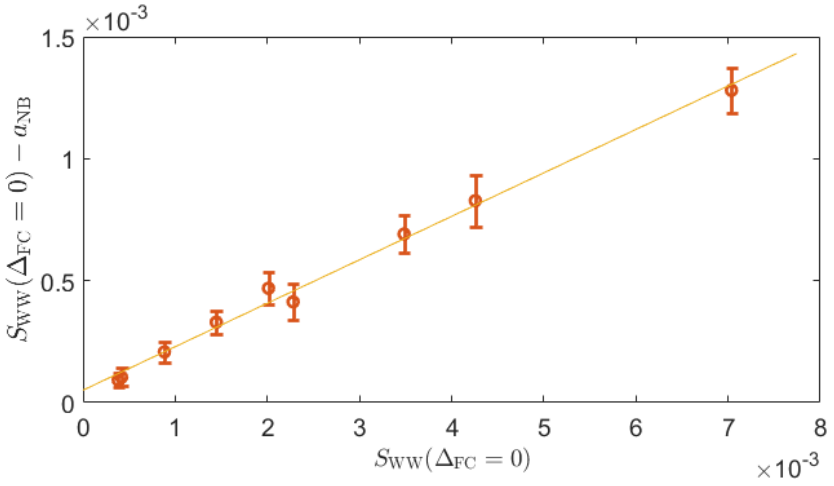

Figure 5.16: Mean number of noise counts per pulse measured during the write detection window (red circles) plotted versus the mean number of write counts with Poissonian standard deviation. Linear fit shown as yellow line. Figure and caption from Dideriksen *et al.* (2020).

Experimentally, the path to improving η_{W} is to increase the filling factor. This will increase the ratio of narrowband to broadband components in the light spectrum. Indeed, in the D_1-line experiment the write efficiency is considerably higher than what we found in the D_2-line experiment. This is a result of the increased waist size of the cavity mode (55 µm → 90 µm). Unfortunately, expanding further comes at the price of higher intracavity losses (see section 3.3.5).

Alternatively, η_{W} can be improved by implementing a narrower filter, thus transmitting less of the broadband noise. However, the transmission of the narrowband signal through a narrower filter will be more sensitive to frequency fluctuations. Increased SNR is only achieved

if the narrowband signal transmission remains high. Improving the spectral filtering should be considered a technological challenge rather than a fundamental issue.

We now proceed by analysing the read spectrum. Here the first conclusion is that there is no correlation between the broadband readout and the write pulse. The datasets for preceding write pulse and without preceding write pulse (circles and crosses, respectively, in Fig. 5.15) coincide outside of the narrowband signal.

For the remaining part of this noise analysis we only concern ourselves with the readout *noise* spectrum (crosses in Fig. 5.15). We can use the spectrum to understand where the readout noise originates. In particular we can get three valuable perspectives on the noise. First, we consider how the noise spectrum varies during the read pulse. Second, we observe how the spectrum changes when increasing the write-read delay. Third, we relate the readout noise to the residual population in $|4,3\rangle$ by varying the initial atomic state.

Spectro-temporal readout shape

The histograms in Fig. 5.7 (left panel) illustrate the temporal shape of the readout. On resonance, the temporal shape of the readout noise has a characteristic shape exhibiting a 'bump' in the beginning before flattening out and slowly rising. The same shape can also be seen in higher resolution in Fig. 5.8. Off resonance, there is no bump but a slowly increasing trend towards the end of the pulse. This shows that the bump is dominated by narrowband noise while the slowly rising base level is an almost even mix of narrowband and broadband noise. This supports a hypothesis that the narrowband readout noise stems from excitation of the symmetric mode due to residual population in $|4,3\rangle$. The symmetric mode is read out fast in the beginning which causes the bump. The narrowband noise appearing in the base level can be understood as continuous repopulation of $|4,3\rangle$ during the pulse which causes the symmetric mode to rethermalize. This is then constantly being read out.

As discussed in section 2.6, the broadband readout noise originates from incoherent scattering associated with asymmetric atomic modes. This process is analogues to the write process and we can get a rough estimate of the scattering probability by comparing to the write process. Whereas the write process scatters from $|4,4\rangle$, the incoherent scattering during read is from $|4,3\rangle$. The differences are that there are fewer atoms in $|4,3\rangle$ compared to $|4,4\rangle$ ($N_{(4,3)} \approx 0.03 N_{(4,4)}$) and that the read pulse is much more energetic (E_R) than the write pulse (E_W). The Λ-scheme for write and read involves the same optical transitions, so no correction for dipole moments is needed. We can write the expected broadband readout noise as

$$\left\langle n_R^{BB} \right\rangle (\tau_\mathrm{R}) = \frac{N_{(4,3)}}{N_{(4,4)}} \frac{\eta_d^R}{\eta_d^W} \frac{E_R(\tau_\mathrm{R})}{E_W} a_{BB} \tag{5.8}$$

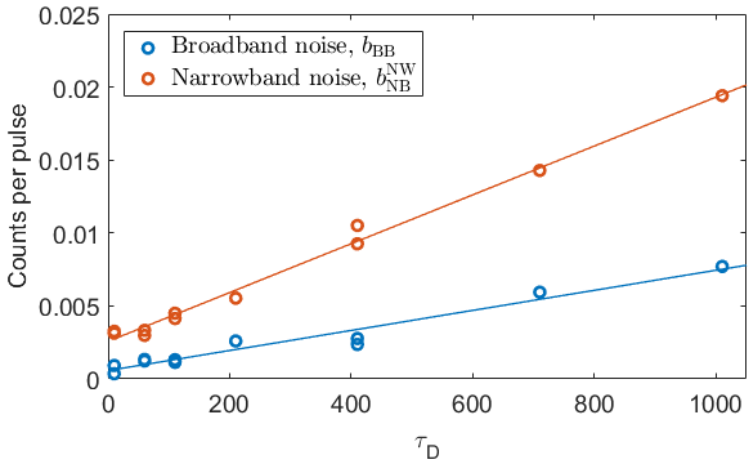

Figure 5.17: **Readout noise vs. storage time.** Broadband and narrowband components are determined from fits to spectra as shown in Fig. 5.15. Both components follow linear trends with best fits $b_{BB} = (0.57 + 6.9/\text{ms} \cdot \tau_D) \times 10^{-3}$ and $b_{NB}^{NW} = (2.57 + 17/\text{ms} \cdot \tau_D) \times 10^{-3}$.

where we also correct for the difference in detection efficiency, η_d, between the write and read setups. If we consider the first 40 µs of the read pulse, we get $\langle n_R^{BB} \rangle \approx 1.1 \times 10^{-3}$. This rough estimate fits surprisingly well with the observed broadband noise of $b_{BB} = 1.2 \pm 0.1 \times 10^{-3}$ from the fit in Fig. 5.15.

Readout noise vs. τ_D

Fig. 5.17 displays how the readout noise increases with write-read delay τ_D. Both the narrowband and broadband readout noise components follow a linear trend. This supports the claim that the two spectral components share the same origin. In the dark, we found in section 3.3.4 that the $|4,3\rangle$ population grows linearly with time due to wall collisions. This is then consistent with the readout noise being proportional to the $|4,3\rangle$ population. Furthermore, the observation that the noise scales linearly with τ_D can be fed to the correlation model. This will be discussed in the next section.

Atomic readout noise

We use the pulsed MORS technique to characterize the sensitivity of the readout noise to atomic population. As a parameter to control the $|4,3\rangle$ population, we consider the pump light power during the pumping stage. In Fig. 5.18 we show the $|4,3\rangle$ population dependency on pump power determined from pulsed MORS experiments. The data verifies that the pump power is a parameter that can be used to reproducibly control the residual atomic population in $|4,3\rangle$.

With the control of the $|4,3\rangle$ population we can test the influence on readout noise. We

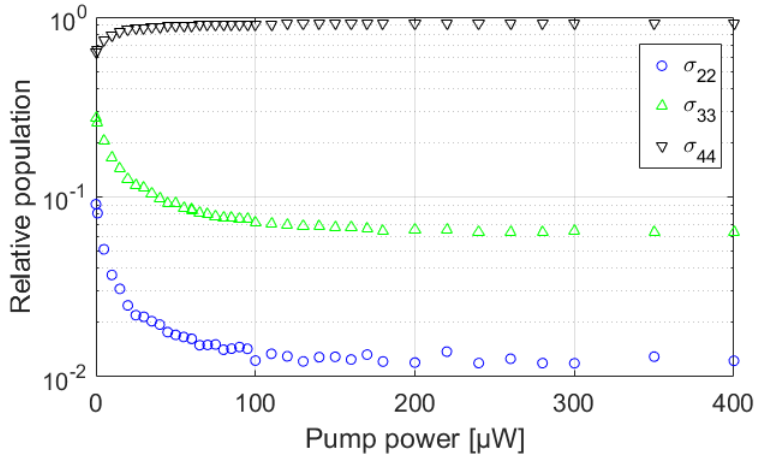

Figure 5.18: **Zeeman sublevel population vs. pump power.** The relative population is calculated from the free model. Pump turn-off not delayed with respect to repump.

run the DLCZ scheme without the write pulse to only see noise during the readout. In Fig. 5.19 the readout noise is plotted against the macroscopic spin orientation p and the residual population in $|4,3\rangle$. The data shows a clear dependency which appears to be close to linear in the fractional $|4,3\rangle$ population, i.e. $\langle\sigma_{3,3}\rangle$. If other sources of noise independent of atomic population would have had a significant contribution, we should see the noise curve flatten out for low $\langle\sigma_{3,3}\rangle$ (or equivalent high p). This is not what we observe. However, the noise data is not completely consistent with directly proportionality to $\langle\sigma_{3,3}\rangle$ since the data points at minimum and maximum $\langle\sigma_{3,3}\rangle$ deviate from the trend of the three middle points. There could be several explanations to this. One is that the calibration of $\langle\sigma_{3,3}\rangle$ could be off. The calibration comes from the data presented in Fig. 5.18 obtained on another day of measurements. Moreover, two independent measurements were performed at minimum $\langle\sigma_{3,3}\rangle$ and the outcomes differ by 50% – significantly more than the statistical uncertainty from number of counts. Thus, drifts in the experimental setup cause a substantial uncertainty on the exact noise values.

From Fig. 5.19 we see that both narrowband and broadband components depend on the residual $|4,3\rangle$ population in the same way. This is consistent with the behaviour observed in Fig. 5.17. The theoretical explanation for this atomic noise was discussed in chapter 2 where it was found that the occupation of symmetric and asymmetric modes scales with the fractional occupation of $|4,3\rangle$. In Fig. 5.19 we observe that the two components are approximately equal in amplitude. There is no fundamental reason for this similarity but it happens to be the case for the specific parameters (mainly filter linewidth and cavity waist size) of the present implementation.

In conclusion, the readout noise is by far dominated by atomic noise due to population in

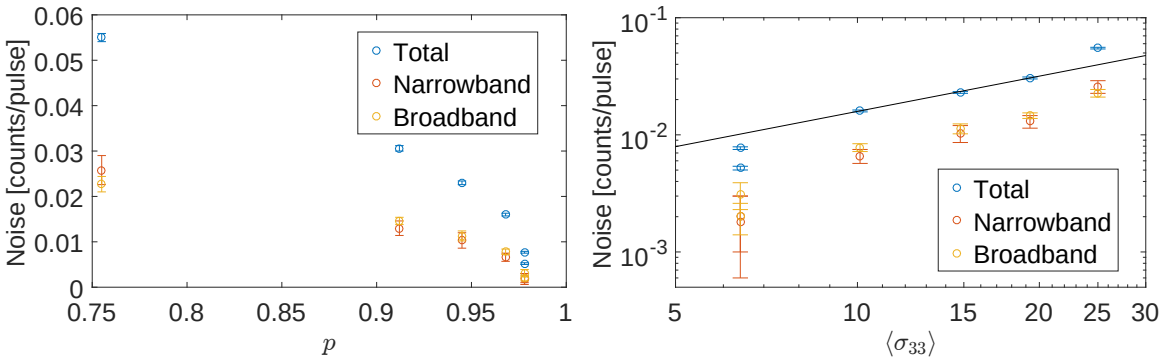

Figure 5.19: DLCZ readout noise vs. macroscopic spin orientation (left) and fractional population of $|4,3\rangle$ (right). A line of slope one is included in the right panel to guide the eye for direct proportionality. The population was controlled by pump power. Errorbars represent statistical uncertainty.

$|4,3\rangle$. Removing the detrimental $|4,3\rangle$ population is a matter of optimizing optical pumping. However, improved optical pumping only reduces atomic population noise for short storage times in the scheme. When the ensemble is left in the dark during storage, atomic population decay increases the $|4,3\rangle$ population and thereby also the readout noise. Even for perfect initial state preparation, the repopulation of $|4,3\rangle$ in the dark will hamper the lifetime of correlations.

Moreover, the narrowband readout noise is spectrally indifferent to the correlated readout. Hence, rejection cannot be achieved by filtering. On the other hand, the broadband readout noise can be suppressed by using a narrower filter. The same technical challenge applies for a narrower read filter as discussed for write efficiency above.

5.2.4 Modelling correlations in the presence of noise

To get a quantitative understanding of how the presence of noise during write and read influences the observed correlations, we establish analytic expressions for the correlations of the DLCZ experiment including noise. The expressions are based on a statistical model where the light pulse energy is assumed quantized and detected as quanta at the detectors. Both coherent and noise contributions to the write and read fields are quantized. Furthermore, phase relations between light Fock states are ignored since the detection is a measurement in the Fock basis. The derivation is performed in the framework of probability generating functions (PGFs). The full derivation can be found in appendix A.

We start out with the two-mode squeezed state of coherent write (X) and read (Y) contributions to the detection. The joint state is a thermal distribution of photon pairs with the

probability of n pairs as given in eq. (2.4)

$$p_n = (1-p_0)p_0^n \text{ with mean excitation } \mu = \frac{p_0}{1-p_0}. \tag{5.9}$$

We then add noise as independent processes such that the detection outcome is the sum of the outcomes for the two-mode squeezer and for noise. Please note that this would not be the case for noise originating from FWM as we shall discuss in the next chapter. For write we have $W = X + A$ and for read $R = Y + B$. The noise processes A and B have mean number λ_A and λ_B, respectively, at the detector.

Furthermore, we introduce finite detection efficiencies. For the write we have $\eta_X = \eta_{\text{esc}}\eta_{\text{det}}^{\text{W}}$ as the product of cell cavity escape efficiency and detection efficiency of light escaping through the cavity outcoupling mirror and propagating to the write detector. For read we also factor in a finite intrinsic retrieval efficiency for the conversion of atomic excitation to light in the cavity mode such that $\eta_Y = \eta_{\text{R}}^{*}\eta_{\text{esc}}\eta_{\text{det}}^{\text{R}}$.

Cross-correlation

The cross-correlation is independent of the auto-correlation of the noise processes. In the derivation we find that the cross-correlation can be expressed as (eq. A.21)

$$g_{WR}^{(2)} = 1 + \frac{\mu(1+\mu)}{(\mu + \lambda_A/\eta_X)(\mu + \lambda_B/\eta_Y)} \tag{5.10}$$

We see that when the noise level is comparable to the coherent detection ($\lambda_A \sim \eta_X\mu$ or $\lambda_B \sim \eta_Y\mu$), the correlation starts dropping because the uncorrelated noise dominates. Notice that eq. (A.21) is a function of $\mu, \lambda_A/\eta_X, \lambda_B/\eta_Y$ only. We note that $\lambda_A/\eta_X, \lambda_B/\eta_Y$ can be understood as the equivalent noise rates at the ensemble.

Auto-correlation

For the auto-correlation of the write and read fields, the noise auto-correlation plays a role. We use $g_{AA}^{(2)}$ ($g_{BB}^{(2)}$) to designate the write (read) *noise* auto-correlation function. The write and read functions then follow (eq. A.25)

$$\begin{aligned} g_{WW}^{(2)} &= \frac{\eta_X^2\mu^2 g_{XX}^{(2)} + \lambda_A^2 g_{AA}^{(2)} + 2\eta_X\mu\lambda_A}{\eta_X^2\mu^2 + \lambda_A^2 + 2\eta_X\mu\lambda_A}, \\ g_{RR}^{(2)} &= \frac{\eta_Y^2\mu^2 g_{YY}^{(2)} + \lambda_B^2 g_{BB}^{(2)} + 2\eta_Y\mu\lambda_B}{\eta_Y^2\mu^2 + \lambda_B^2 + 2\eta_Y\mu\lambda_B}. \end{aligned} \tag{5.11}$$

where $g_{XX}^{(2)} = g_{YY}^{(2)} = 2$ is the auto-correlation of the individual modes of the two-mode squeezer. This result can be understood as an average of the auto-correlation of the individual processes weighted according to the mean (detected) number squared – plus uncorrelated coincidences between the processes. The result in eq. (5.11) matches what was found by Michelberger *et al.* (2015).

Conditional auto-correlation

Finding an expression for the conditional auto-correlation is substantially more complex as it requires an expression for the probability distribution of atomic excitations given that the write detector clicked once. To find an exact expression in the presence of write noise, one needs knowledge of the write noise probability distribution and not just the auto-correlation. Here we assume the write noise to be Poissonian. This assumption is justified from the origin of the write noise. A small portion stems from detector dark counts while the remaining portion is from the scattering associated with asymmetric modes. Since these modes are many and short lived, the noise becomes Poissonian. This assumption fits well with the write auto-correlation that we observe in experiments.

With this assumption, the conditional auto-correlation of the *atomic mode* is given as (eq. A.39)

$$g^{(2)}_{YY|W=1} = \frac{2(1-\eta_X)(\lambda_A+\eta_X\mu+\lambda_A\eta_X\mu)(\lambda_A+2\eta_X-\lambda_A\eta_X+3\eta_X\mu-\eta_X^2\mu+\lambda_A\eta_X\mu-\lambda_A\eta_X^2\mu)}{(\lambda_A+\eta_X-\lambda_A\eta_X+2\eta_X\mu-\eta_X^2\mu+\lambda_A\eta_X\mu-\lambda_A\eta_X^2\mu)^2}. \tag{5.12}$$

Note that in absence of write noise ($\lambda_A = 0$), for small $p_0 \approx \mu \ll 1$ and low detection efficiency $\eta_X \ll 1$, the expression in eq. (5.12) approximates to $g^{(2)}_{YY|W=1} \approx 4p_0$ as in eq. (2.72). This demonstrates that for low η_X, the heralding advantage of number-resolved detection vanishes.

From the same PGF we find that the conditional mean excitation of the atomic mode is given by (eq. A.40)

$$\tilde{\mu} = \frac{\mu(\lambda_A+\eta_X-\lambda_A\eta_X+2\eta_X\mu-\eta_X^2\mu+\lambda_A\eta_X\mu-\lambda_A\eta_X^2\mu)}{(1+\eta_X\mu)(\lambda_A+\eta_X\mu+\lambda_A\eta_X\mu)}. \tag{5.13}$$

This result can be used to calculate the conditional retrieval efficiency by simply multiplying by the detection efficiency, i.e. $\eta_R = \eta_Y\tilde{\mu}$.

With the knowledge of the atomic mode conditional auto-correlation and conditional mean excitation $\tilde{\mu}$, we can write the read auto-correlation by including noise in analogy with eq. (5.11)

$$g^{(2)}_{RR|W=1} = \frac{\eta_Y^2\tilde{\mu}^2 g^{(2)}_{YY|W=1} + \lambda_B^2 g^{(2)}_{BB} + 2\eta_Y\tilde{\mu}\lambda_B}{\eta_Y^2\tilde{\mu}^2 + \lambda_B^2 + 2\eta_Y\tilde{\mu}\lambda_B}. \tag{5.14}$$

Fitting the model to data

In the above derivation we have introduced the parameters $\eta_X, \eta_Y, \lambda_A, \lambda_B, g^{(2)}_{BB}$ that the model takes as input to predict the outcomes for variable μ. We fix the values $\lambda_B = 4.3 \times 10^{-3}$ and $g^{(2)}_{BB} = 1.3$ which are measured independently by blocking the write pulse to only read out noise. We further assume write noise to be linear in μ as supported by the data in Fig. 5.16.

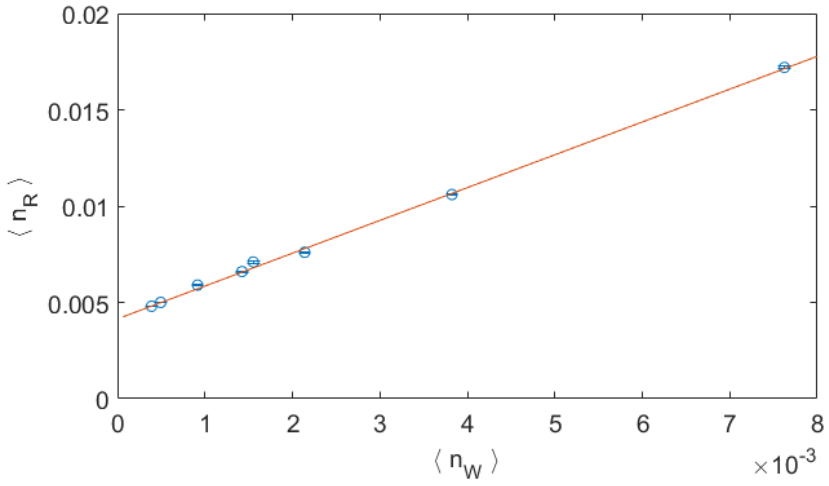

Figure 5.20: Mean number of counts per pulse measured during the read detection window (blue circles) plotted versus the mean number of write counts. Error bars are standard deviation assuming Poissonian distribution of $\langle n_R \rangle$. The fitted model is shown as the red line. Figure and caption from Dideriksen *et al.* (2020).

This is implemented as $\lambda_A(\mu) = (1/\eta_W - 1)\eta_X \mu + a_{bg}$ with $\eta_W = 0.822$ and $a_{bg} = 62 \times 10^{-6}$ corresponding to the linear fit in Fig. 5.16. We leave η_X and η_Y as free fit parameters.

The model is fitted simultaneously to three quantities derived from the same large data set. The first two quantities are $g^{(2)}_{WR}(\mu)$ and $\eta_R(\mu)$, which are displayed in Fig. 5.10. The third quantity is the mean read count rate $\langle n_R \rangle(\mu)$ displayed in Fig. 5.20. To relate the direct measurement value $\langle n_W \rangle$ to μ, we rescale with the fit parameter η_X such that $\langle n_W \rangle(\mu) = \eta_X \mu/\eta_W + a_{bg}$. Note that the relation obeys $\langle n_W \rangle(\mu) - \lambda_A(\mu) = \eta_X \mu$.

When fitting, the data points for the three quantities are weighted according to the inverse of the data point uncertainty. The model is in good agreement with the data for the optimal fit values $\eta_X = (2.9 \pm 0.1)\%$ and $\eta_Y = (6.0 \pm 0.2)\%$.

The fit value for η_X matches well with a separate detection efficiency measurement and the expected cell cavity escape efficiency (see section 3.3.5). Despite also containing the intrinsic retrieval efficiency, η_Y is more than double η_X. This is an expected outcome and is caused by a much lower detection efficiency in the write filter setup. The lower efficiency is partly because the narrow write filter cavity has a low on-resonance transmission, and partly because we were experiencing a low transmission in the fibre connecting the SNSPD. Due to lack of time – caused by delays related to the international COVID-19 crisis – we were unable to mitigate the low detection efficiency before performing the experiment. We emphasize that η_X does not alter the obtained performance results but only the data acquisition time.

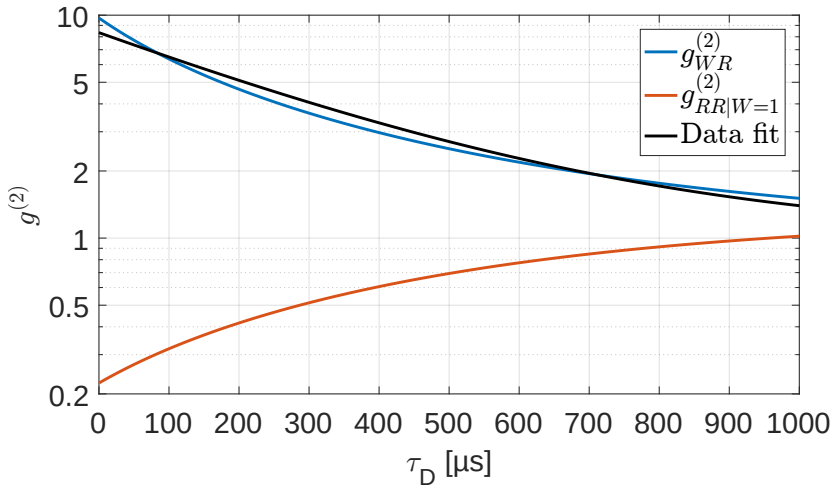

Figure 5.21: **Model prediction for correlation functions vs. memory time.** Feeding observed readout decay and readout noise dependency on memory time to the correlation model, we predict the behaviour of cross-correlation (blue) and conditional read auto-correlation (red). For comparison the exponential fit of Fig. 5.14 is reprinted (black).

Extrapolation to memory values

We can use the correlation model to predict how the correlations vary with the memory time τ_D. This is particularly interesting for the antibunching $g^{(2)}_{RR|W=1}(\tau_D)$ where reliable estimates are hard to obtain.

The write process is independent of τ_D and we also assume read noise auto-correlation $g^{(2)}_{BB}$ to be independent – as was done in Fig. 5.14. The read noise mean value $\lambda_B(\tau_D)$ is modelled to be linear in τ_D with parameters given by the fits in Fig. 5.17. The spin wave lifetime is incorporated into $\eta_Y(\tau_D)$ and modelled to follow an exponential decay as observed in Fig. 5.13. We introduce the τ_D dependency in the expressions for $g^{(2)}_{WR}$ (eq. 5.10) and for $g^{(2)}_{RR|W=1}$ (eq. 5.14) and keep μ fixed at the value that yields minimal $g^{(2)}_{RR|W=1}$. The output is displayed in Fig. 5.21.

We see that the model reproduces the behaviour of $g^{(2)}_{WR}$ with a high degree of quantitative agreement when comparing to measured values in Fig. 5.14. For $g^{(2)}_{RR|W=1}$, the model yields a slowly rising curve similar to the slowly decaying curve for $g^{(2)}_{WR}$. The model predicts that $g^{(2)}_{RR|W=1} < 0.5$ should be observed for $\tau_D < 290\,\mu s$. This value can be taken as the theoretical storage time for which the conditional output is below the single-photon threshold. As such, $\tau_{SP} = 290\,\mu s$ constitutes a fourth benchmark value for the memory performance. Similar to the other benchmark values τ_{SP} depends on the excitation probability. The relevant memory time scale depends on the exact application and particularly the sensitivity to readout noise.

Chapter 6

Discussion and future outlook

6.1 Limiting noise processes

The change in excitation scheme from D_2 line to D_1 line represents a substantial improvement in the source-memory performance. After realizing that the D_2-line scheme would inevitable be limited by FWM, further optimization of the readout noise in that scheme was in vain. This left a complete understanding of the readout noise open. Contrary, in the D_1 scheme we could assume the FWM process to be suppressed which motivated the detailed investigation of limiting noise processes. It became clear that a substantial amount of the noise is correlated with the atomic population in $|4,3\rangle$. After carefully optimizing the pumping scheme the fractional occupation of $|4,3\rangle$ was reduced by a factor two (see chapter 3). Despite much effort we are currently unable to improve further, likely being limited by optical access in the current cell design. The atomic noise is still the dominating noise source contributing far more than the excitation light leakage and detector dark counts.

As an instructive exercise we can estimate the influence of the initial occupation of $|4,3\rangle$. From the noise analysis in chapter 5, more specifically Fig. 5.17, we see that the initial readout noise level at $\tau_D = 10\,\mu s$ is doubled after approx. $180\,\mu s$. For the hypothetical case of perfect initialization with no occupation of $|4,3\rangle$, we would then reach the same readout noise level at $\tau_D = 180\,\mu s$ as we started out with in experiments. In this case, the memory time definitions that depend on a threshold value (like Bell-inequality violation or non-classicality) would therefore increase by approx. the same amount, not accounting for a correction from the decay of retrieval efficiency. I.e. after $180\,\mu s$ we are limited by noise from atomic decay and not atomic initialization.

This highlights an important lesson for what will be limiting the memory performance of schemes that store in the long-lived symmetric atomic mode in anti-relaxation-coated cells. While the spin coherence time is long and the retrieval-efficiency decay time equally long, there will be a substantial increase in the readout noise on this timescale. This is specific to coated cells. In buffer gas cells the memory time is limited mostly by atomic exchange and

not population decay. Coherent atoms diffuse out of the interaction region but the new atoms diffusing into the region are in the initial state. This dephases the spin wave as discussed in section 2.4 but does not introduce extra readout noise.

6.2 Verification of FWM suppression

The experimental verification that FWM is suppressed is not very explicit in chapter 5. We shall therefore discuss it here in more detail. The first observation is that from the theory presented in 4.2.2 we expect a large suppression at the magic detuning. The model by Dąbrowski *et al.* (2014) predicts that, if the ratio ξ/χ does not vanish, then for small initial spin-wave occupation n_b, the readout shape will increase with time. This is exactly the photon shape behaviour observed for D_2-line excitation in Fig. 4.8. We can use the model to put an upper limit on the ratio ξ/χ in the D_1-line scheme. The change in output photon flux is given by the time derivative of eq. 4.6

$$\frac{\partial}{\partial t}\left\langle \hat{a}_\chi^\dagger(t)\hat{a}_\chi(t)\right\rangle = -\chi^2(\chi^2-\xi^2)e^{-t(\chi^2-\xi^2)}n_b + \chi^2\xi^2 e^{-t(\chi^2-\xi^2)}. \tag{6.1}$$

From this we get a lower threshold for n_b at which the readout flux will grow with time due to FWM, i.e.

$$\frac{\partial}{\partial t}\left\langle \hat{a}_\chi^\dagger(t)\hat{a}_\chi(t)\right\rangle > 0 \iff \frac{\xi^2}{\chi^2} < \frac{n_b}{1+n_b}\,. \tag{6.2}$$

In the D_1-line experiment we observe that there is an exponentially decaying readout flux in both conditional, unconditional and blocked-write cases. Out of those, the blocked-write case has the lowest spin-wave occupation which is non-zero because of imperfect pumping. We estimate the occupation to be $n_b = 3\%$. The upper limit for FWM gain ratio is thus $\xi^2/\chi^2 < 3\%$. This is a substantial improvement compared to D_2 line where the estimate is $\xi^2/\chi^2 = 54\%$ (section 4.2.1).

The fact that we see the exponential readout shape in the pure noise readout where the preceding write pulse is blocked, also demonstrates that the performance of the scheme is not limited by readout noise from FWM but by readout noise from residual atomic population in $|4,3\rangle$ which populates the symmetric mode. In a sense, this is 'thermal' occupation of the mode after the cooling from optical pumping.

A more subtle effect is that FWM would alter the conditional readout photon statistics because the FWM is seeded by atomic excitations. In the case of non-vanishing FWM, the write-correlated readout cannot be modelled as the two-mode squeezed state as was done in the correlation model described in chapter 5. The parametric gain introduced by FWM during the readout process means that the readout field does not have the same auto-correlation as the atomic excitation. This was demonstrated in a work by Michelberger *et al.* (2015). Here the quantum memory readout was limited by FWM to a degree where the auto-correlation

was strongly altered. In that work they estimate the FWM strength to be $\xi/\chi = 62.5\%$ ($\xi^2/\chi^2 = 39\%$) and show that a ratio $\xi/\chi > 25\%$ ($\xi^2/\chi^2 > 6.3\%$) prevents readout with $g^{(2)}_{\mathrm{RR}} < 0.5$ – even for a perfect single-photon memory state. Contrary, in the present scheme the two-mode squeezed state model with independent readout noise yields good agreement with the observed conditional read auto-correlation. This is thus a strong indication that FWM is negligible.

6.3 Efficient motional averaging

It is evident that we are able to interact with the long-lived mode, because we observe write-read correlations on a time scale much longer than motional dephasing would allow. At the same time, we also confirm that the single-photon detection mode is motionally averaged. If the detection mode would not have had a large overlap with the symmetric mode, the conditional atomic state would have strong contribution from asymmetric modes. Since these quickly dephase, the retrieval efficiency would be low and hence also the conditional readout SNR. The outcome would be lower cross-correlation and higher $g^{(2)}_{\mathrm{RR|W=1}}$. The ability for the correlation model to reproduce experimental results with the input from characterization measurements, verifies the estimates obtained from characterization measurements. In particular, it confirms the spectral analysis of the write field as a useful tool to characterize effectiveness of motional averaging.

The motional averaging is mostly ensured by the spectral filter. If the spectral filter had not been there, we should expect to find an write efficiency which is given by the mode overlap between the cavity mode and symmetric atomic mode. This can be calculated as

$$\eta_W = \frac{\pi w^2}{4L^2} = 0.28 \tag{6.3}$$

(cf. eq. (2.59) for $\kappa_2 \to \infty$).

That we observe $\eta_W = 82\%$ can then be assigned to the spectral filter which successfully motionally averages the detection mode such that we project onto the symmetric mode with a high fidelity. We also note that the observed write efficiency is close to the theoretical prediction in eq. (2.59). For experimental parameters $w = 90\,\mu\mathrm{m}, L = 150\,\mu\mathrm{m}, \kappa_2 = 2\pi \cdot 98\,\mathrm{kHz}$ and expected $\Gamma = 2\pi \cdot 0.75\,\mathrm{MHz}$, the prediction from theory is $\eta_W^{\mathrm{th}} = 87\%$.

In Fig. 6.1 we assess the influence of the write and read noise. While the write efficiency matters for the total efficiency of the source, we see that the influence on correlation values is marginal at the current level. The correlation values are mainly limited by readout noise. From the figure, we see that a factor 5 in readout noise reduction would have a high im-

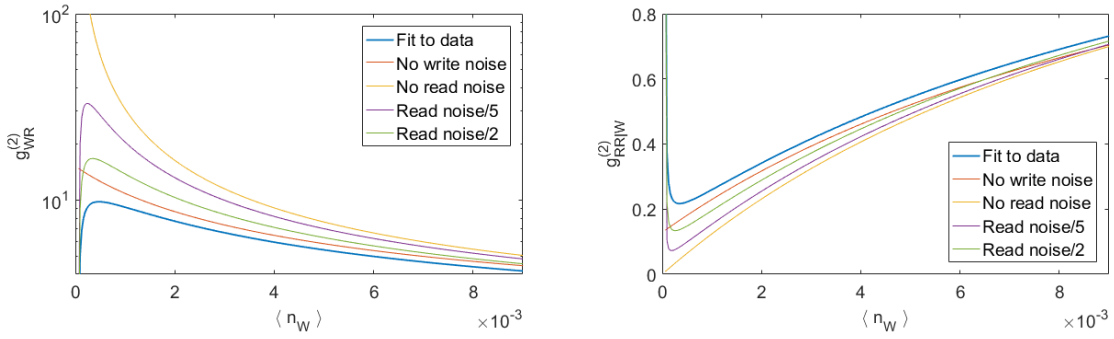

Figure 6.1: **Projected influence of noise. Left:** Cross-correlation. **Right:** Conditional auto-correlation. Curves are calculated from the model described in chapter 5. Blue line is the fit to the data in Fig. 5.10. Orange line uses fit parameters but with write noise $\lambda_A = 0$. Yellow line uses fit parameters but with read noise $\lambda_B = 0$. Purple and green lines are intermediate read noise with $\lambda_B/5, \lambda_B/2$, respectively.

pact on the correlation values. This corresponds to initializing the atoms with an orientation $p \approx 0.9986$.

6.4 Benchmarking

After having shown that the coated vapour cell can be used for single-photon generation, we shall now attempt to benchmark it against other systems. As a first comparison we can consider the single-photon generation from a single system, i.e. no multiplexing or synchronization. In our coated vapour cell scheme on D_1, the detected rate of conditional readout is only approx. 40 mHz during the overall running time, i.e. including the cavity relocking stage. Here we used the combined data point in 5.10 for low excitation probability. The corresponding purity is quantified by the anti-bunching $g^{(2)}_{\mathrm{RR|W=1}} = 0.2$. In comparison, the best cryogenic single-photon sources can reach above 10 MHz in detected rate with vanishing auto-correlation $g^{(2)}$ at a few percent or below (Uppu *et al.*, 2020). Similarly, room-temperature down-conversion sources can reach a few MHz in detected rate and also show $g^{(2)}$ at the few-percent level (Zhong *et al.*, 2018).

We can imagine straightforward modifications that would enhance the detection efficiency in our experiment. This includes improvement of the cell cavity escape efficiency by reducing the intracavity loss from low cell transmission. However, it is currently unknown how good the escape efficiency can get while still preserving cavity finesse and anti-relaxation coating. A realistic estimate would be that high-quality fabrication and optimized filter setup could lead to an overall detection efficiency of 50% for photons generated inside the cavity. This would enhance the write detection probability by a factor 17 and read a factor 6. In total the achievable single-photon detection rate could reach 4 Hz with such improvement.

Clearly the vapour cell source is inferior to the benchmark sources, even after optimized detection, mainly because the motional averaging demands slow operation. But this comparison also does not harness the advantage from the built-in memory. A better comparison would be to consider the rate for generating synchronized, multiple photons. We can use the expression discussed in section 1.2 for the coincidence probability of n parallel memory-enhanced sources

$$P = (p\eta_W\eta_R B)^n, \tag{6.4}$$

where for the present scheme we have

$$p = p_0\eta_d = 2.5\%, \tag{6.5}$$
$$\eta_W = 82\%, \tag{6.6}$$
$$\eta_R = \eta_d\eta_R^* = 50\% \cdot 70\% = 35\%, \tag{6.7}$$
$$B = 17, \tag{6.8}$$

in the case where losses have been optimized such that $\eta_d = 50\%$. The performance numbers are from the results of chapter 5. Here we neglect reinitialization time when heralding fails and we also assume that we can use the full non-classical storage time $\tau_{\mathrm{NC}} = 0.68\,\mathrm{ms}$ when calculating the time-bandwidth product. The expression in eq. (6.4) does not include effects of readout noise. In practise one would have to choose a fidelity threshold dependent on the requirement for the intended photonic network. For photon-pair sources, the fidelity of the heralded state can be approximated by

$$F = \left|\langle 1|\psi_{R|W=1}\rangle\right|^2 \approx 1 - p_2 \approx 1 - \frac{g^{(2)}_{\mathrm{RR|W=1}}}{2} \tag{6.9}$$

where the vacuum component is ignored.

The six-photon probability then becomes 3 ppm which corresponds to $\approx 0.08\,\mathrm{Hz} = 5\,\mathrm{min}^{-1}$ rate. Again, this assumes a repetition rate of $1/40\,\mu\mathrm{s}$ when reinitialization is ignored. We stress that this is an optimistic projection because we have not accounted for the readout noise. Without the assumed improvement in detection efficiency the six-photon probability is scaled by a factor $\approx 1/(6 \cdot 17)^6 = 4 \times 10^{-12}$.

In a comparison of absorptive memories Finkelstein *et al.* (2018) calculate the projected six-photon coincidence rate based on the model by Nunn *et al.* (2013) for several demonstrated quantum memories. Their comparison figure is displayed in Fig. 6.2. The comparison shows that six-photon coincidence rates approach one per minute in state-of-the-art demonstrations of absorptive memories. With the improvements discussed above, the DLCZ scheme in a coated cell could reach seemingly competitive rates. However, our noise-to-signal ratio is $\mu_1 = \lambda_A/\eta_Y = 0.072$ (cf. section 5.2.4) but cannot be separated from the photon source,

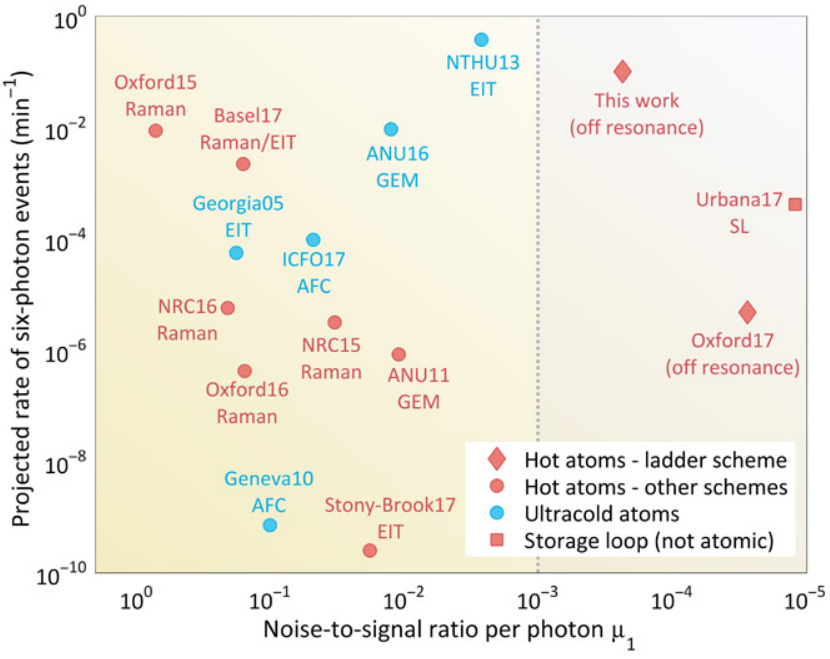

Figure 6.2: **Comparison of different memory protocols.** The six-photon rate is calculated from the numbers reported for the different protocols. All protocols considered are absorptive memories thus requiring an input from an external single-photon source. The calculation assumes an external source operated at excitation probability 0.001 at up to 50 GHz dependent on the memory protocol bandwidth. The vertical line marks the intrinsic noise of the assumed source. Figure from Finkelstein *et al.* (2018) and the label "this work" refers to the same paper. The references to the different protocols can be found in Finkelstein *et al.* (2018). Licensed under CC BY-NC.

since in the DLCZ protocol source and memory is the same system. The observed μ_1 is the reason we do not improve performance by reducing the excitation probability further.

In the memory comparison, to ensure high fidelity an external single-photon source for input to the memories was assumed to operate at $p = 0.1\%$ which is an order of magnitude less than our current demonstration. If instead the external source is operated at p of order few percent, the coincidence rate would increase by several orders of magnitude. Taking this into consideration, it is unlikely that the slow but long-lived source-memory system presented in this thesis will compete with the fast, short-lived memories for application to photon synchronization. However, interfacing with a single-photon source – as well as sufficiently fast feed-forward to operate the memory together with a 50 GHz source – remains to be demonstrated for many of the considered memory protocols.

We shall here also relate our results to a similar DLCZ experiment in caesium vapour by Dou *et al.* (2018). The main difference is that Dou *et al.* use a buffer-gas cell without anti-

relaxation coating. In their scheme, the authors claim the memory time is limited by a combination of atomic diffusion out of the interaction region and wall collisions (*ibid.*). The experiment employs a hyperfine storage scheme where atoms are initially pumped to the $F = 3$ manifold while the $F = 4$ manifold is used for storage. In the buffer-gas cell experiment there is no advantage of motional averaging. Hence, the buffer gas scheme can be used with very fast pulses. Dou *et al.* apply 2 ns write and read pulses. By operating at a "sweet spot" detuning at 4 GHz where noise from collisions with the buffer gas is minimal, they are able to achieve a low readout noise level – not limited by initial optical pumping. They achieve a cross-correlation between write and read of up to $g^{(2)}_{\mathrm{WR}} = 28$ (for an excitation probability $p_0 \approx 3\%$). The correlations remain non-classical ($g^{(2)}_{\mathrm{WR}} > 2$) for 6 µs. The $1/e$ decay time is 1.4 µs which yields a time-bandwidth product $B = 700$ when neglecting reinitialization time. The necessary initialization time is not reported. Dou *et al.* do also not report the conditional read auto-correlation but from the reported cross-correlation it is supposedly below 0.5. However, the retrieval efficiency is limited to 10% and a practical concern is that the scheme needs high-intensity pulses.

With the reported performance, the scheme of Dou *et al.* (2018) is better suited for scalable photon-synchronization application than the scheme presented in this thesis. The advantage of the present scheme is the long lifetime of the atomic excitation which becomes important if the operation bandwidth is not set by the pulse length, e.g. long-distance quantum communication.

Quantum-repeater application

An actual benchmarking of the quantum-repeater performance in a DLCZ protocol is very involved – particularly if one aims to include both finite memory time and readout noise. For the scheme of this thesis, Borregaard *et al.* (2016) calculated an average rate of Bell-state distribution over 80 km of 0.2 Hz for 80% state fidelity – without accounting for finite memory time. The calculation assumes lower noise levels (0.5% residual population in the storage state) and higher detection efficiency ($\sim 80\%$) than we have been able to achieve but also longer duration of write and read pulses. They used the lowest level of repeater architecture with a single repeater station in between the end nodes such that only a single entanglement swap operation is necessary. In order to verify the end-node entanglement Borregaard *et al.* consider two parallel quantum-repeater channels and include a final post-selection by reading out the end nodes. Although the calculation is not performed for the experimentally obtained parameters, it provides a sense for the order of magnitude of the achievable entanglement-distribution rate.

The average distribution time and memory time requirement can be substantially reduced through spatial multiplexing. In particular if the multiplexed channel is not simply parallel

repeater lines but includes real-time reconfiguration of nodes. Collins *et al.* (2007) have shown that for such a 10-fold multiplexed channel, a memory time of $10L_0/c$, where L_0/c is the time-of-flight in the elementary links, almost mitigates the limitation from finite memory time. For an 80 km channel with two 40 km links this would correspond to 1.3 ms memory time for free-space links. Collins *et al.* estimate that 100-fold multiplexed channels with tens of millisecond storage in the nodes would enable quantum communication over 1000 km. We emphasize that the numbers should be considered with reservations since the analysis of Collins *et al.* does not include noise beyond the intrinsic multi-pair noise from an ideal two-mode squeezer.

Whereas the prospects of multiplexing have sparked ideas of multimode storage in a single system, the approach to spatial multiplexing in a coated vapour cell would be different. The memory protocol is intrinsically single mode since only the symmetric atomic mode benefit from the spin-protecting coating. However, the vapour cell is in itself a very simple system which should enable mass production and hence many cells can be operated in parallel without extreme deployment costs. One could even imagine a fibre-coupled cell where the cell cavity is comprised of a tunable fibre cavity (e.g. the design of Saavedra *et al.*, 2021). Another advantage of the present protocol is the low optical power requirement. At current the cavity input power for the read pulse is less than 200 µW and pumping pulses require only a few milliwatt. The optical power consumption for operating tens of cells in parallel is thus within the power output of standard laser systems (e.g. Titanium-Sapphire lasers). The most concerning equipment in terms of multiplexing would be the spectral filters. Narrowband optical filters are not yet commercial off-the-shelf equipment. However, clever engineering could make such optical cavity filters mass-producible, as has been seen with laser systems. Furthermore, in a multiplexing scheme with active routing, it is in principle not necessary to have independent filter and detection setups for each cell during entanglement swapping (the read process).

With improvements to readout noise (from better optical pumping), propagation losses and memory time, the coated vapour cell could become relevant for quantum repeater application. A factor 1/5 in readout noise would bring us to $g^{(2)}_{\mathrm{RR}|\mathrm{W}=1} = 0.1$ (cf. Fig. 6.1) and to the noise level assumed by Borregaard *et al.* A high overall detection efficiency is required to reach scalable performance and 50% could be set as a first target. Furthermore, a factor 10 increase in the memory time would take the scheme into the few millisecond regime which is the onset of multiplexed quantum repeaters. To show that these improvements are within experimental reach will require substantial work on particularly the vapour cell design.

The state of the art performance for DLCZ repeater nodes is achieved with ultracold atoms. In the work of Yang *et al.* (2016) the authors demonstrated a scheme using rubidium atoms trapped in a 3D lattice inside a ring cavity. The scheme employs storage on the magnetic-field insensitive "clock" transition and exhibits a $1/e$ storage time of 0.22 s. The intrinsic retrieval

efficiency at minimal storage time is 76% (18% external efficiency) and after 100 ms storage the conditional autocorrelation is 0.28. The same scheme has later been used to demonstrate heralded entanglement generation over 50 km (Yu *et al.*, 2020).

Clearly, the performance of our room-temperature scheme is inferior to the cold-atoms scheme but the necessary requirements for comparable performance have been demonstrated in separate room-temperature experiments. While the long-time storage of light in vapour cells was demonstrated recently (Katz and Firstenberg, 2018), the result presented in this thesis provides a scheme for efficient single-photon generation and retrieval in the long-lived atomic mode of coated vapour cells. Bringing the two properties together in the same cell setup would comprise a milestone for room-temperature quantum repeaters.

Other advantages

A more subtle advantage of the presented scheme is that the generated single photons are extremely narrowband. From the filters, an upper limit on the bandwidth is ~ 100 kHz while in reality it is likely limited by the laser linewidth < 30 kHz. Narrowband photons have the advantage that the signal can be easily filtered and separated from incoherent noise sources. In particular for free-space communication this enables rejection of ambient light in real-life situations.
Another advantage is in photon-photon interference (Hong-Ou-Mandel) where narrowband photons are insensitive to path length difference. Photon indistinguishability can remain high at path difference at the 100 metres scale (Rambach *et al.*, 2018).
It has also been suggested (Rambach, 2018) that narrowband photons can be used for fundamental quantum mechanics tests of causal non-separability (Branciard, 2016). An example of this is the "quantum switch" (Procopio *et al.*, 2015) where quantum computing is performed with a quantum superposition of gates. This is in contrast to the typical quantum computer where the input can be in a quantum superposition but where the gates are arranged in a fixed circuit.

Moreover, a narrow bandwidth makes the generated photons compatible with many other memory platforms, e.g. opto-mechanical systems. Since the scheme presented in this thesis can efficiently herald the generation of a single atomic excitation, the scheme could be used in combination with heralded single-*phonon* excitation (Riedinger *et al.*, 2016) to generate hybrid single-excitation entanglement. This would be a complimentary result to the hybrid continuous-variable entanglement already demonstrated in our group (Thomas *et al.*, 2021).

In this thesis we have shown by single-photon detection the heralded addition of a single atomic excitation to an initial state close to the ground state. We have also shown beam-splitter interaction with suppressed FWM noise which together with single-photon counting

can be used for heralded single-excitation *subtraction*. Both addition and subtraction happens in the long-lived symmetric mode because of motional averaging.

Heralded addition/subtraction of bosons can be used to generate exotic quantum states (Bellini and Zavatta, 2010; Milburn *et al.*, 2016). In particular, it can be used to create a superposition of coherent states – so-called Schrödinger-cat states – when performed on squeezed vacuum (e.g. the work of Neergaard-Nielsen *et al.*, 2006). Our group has previously demonstrated spin squeezing in the microcell-in-cavity system by stroboscopic quantum non-demolition measurement (Vasilakis *et al.*, 2015). Hence, we now posses the tools to create cat states in the collective spin mode. If this idea were to be pursued, it would be a new demonstration of the macroscopic quantum properties of room-temperature atomic vapours.

6.5 Possible improvements

Besides the improvement of the total detection efficiency discussed above, we also find it realistic that other improvements are within experimental reach. First, further investigation is required to determine the limit of optical pumping efficiency. We have already discussed how limited optical access from the side in the current microcell design appears to limit the purity of the initial atomic state. Improvement of the cell design could be a viable route to better pumping. Alternatively, one could consider schemes beyond standard optical pumping for removing $|4,3\rangle$ population. Such schemes could involve driving $|4,3\rangle$ population into the other hyperfine manifold via optical Raman transitions or microwave pulses. Microwave-assisted pumping in a continuous pumping scheme has been implemented in our group with limited success (Thomas, 2020) where it was found that microwave power requirements are quite high. To remedy that the magnetic shield could be designed to form a microwave cavity at the relevant wavelength.

In the presented experiment we used a cell with paraffin coating which shows a transverse-spin coherence time $T_2 = 2.0\,\mathrm{ms}$. However, alkene coatings show better performance and champion alkene-coated microcells have shown $T_2 = 10\,\mathrm{ms}$, like the one used by Vasilakis *et al.* (2015). The main reason that the same cell could not be used in the DLCZ experiment, relies on the fact that the higher magnetic field strength heated the shield compartment to a temperature above the alkene melting point. This can be readily remedied by changing the current design. Then it can be explored if the optical depth of an alkene-coated cell at 30 °C is sufficient for the single-photon generation. The lower optical depth requires higher write and read power but rejection of the excitation beam is currently not a limitation.

Even with better protection from the wall coating, the limiting factor for the coherence time is the time between wall collisions which is set by the dimensions of the cell. An obvious route is therefore to perform the experiment in a cell with larger cross section. This will increase

both the coherence time but also the motional averaging time because the atomic transit time increases. In the spectral domain, this corresponds to the broadband noise becoming narrower since $\Gamma \propto 1/w$ (section 2.6), hence the spectral filter will have to be narrower to achieve similar write efficiency. Because of this relation the cell cross section alone cannot be used as a parameter to increase the time-bandwidth product.

An idea that we are currently exploring is to convert the Gaussian-profile excitation beam to a top-hat profile. This way the excitation laser mode will be overlapping with the symmetric mode. A bigger challenge is to tailor the detection mode to have the top-hat spatial profile because the mode will have to couple to the filter cavities. If we imagine the case of top-hat (uniform) excitation beam, we have the situation described by the Hamiltonian in eq. 2.32 where the detection mode, $\hat{a}_m$, couples to the corresponding transverse atomic mode, $\hat{b}_m$. Even if the detection mode remains Gaussian in profile, there is still a considerable benefit of the top-hat drive. This can be seen from eq. 2.53. In this case there is no spatial dependency for Ω (hence also no temporal dependency). When both g and Ω are Gaussian, the product is

$$g(x,y)\Omega(x,y) \propto \left(e^{-\frac{x^2+y^2}{w^2}}\right)^2 = e^{-2\frac{x^2+y^2}{w^2}}. \tag{6.10}$$

But when $\Omega(x,y)$ is uniform, we get an effective increase in the waist size from replacing $w \to \sqrt{2}w$. This means a factor 2 increase in effective filling factor, cf. eq. 6.3.

If we would then aim for a cell cross section 3 mm x 3 mm, i.e. $L \to 10L$, we should expect to gain a factor 10 in coherence time. We can estimate the filter linewidth requirement from eq. (2.59) with the effective waist increase from a top-hat beam. The dependency is given in Fig. 6.3. We see that $\eta_W > 80\%$ is obtainable for $\kappa_2 < 2\pi \cdot 70\,\mathrm{kHz}$. Here we have used $\Gamma \to \Gamma/10$ to include the longer temporal correlations in a larger cell. The top-hat excitation beam thus means that we should be able to increase the memory time by a factor 10 while only increasing the averaging time by about a factor 2. This would mean an increase in time-bandwidth product of a factor five and possibly more if the write pulse length is pushed to the Fourier limit of the filter.

Meanwhile, three circumstances speaks in favour of realizing a DLCZ scheme without a cell cavity: 1) The overall efficiency of the current scheme is limited by a low cell cavity escape efficiency. 2) The cell cavity birefringence prohibits coinciding frequencies of write and read photons, hence adding complexity to the filtering setups. 3) The top-hat beam configuration is hard to achieve in a cavity. It is therefore likely that we will explore the scheme in a larger cell without a cavity.

However, a scheme without cell cavity will require substantially more excitation rejection from the filters because we no longer benefit from cavity enhancement. On top of that, for the suggested 100-fold larger cross-section area, we will need 100 times more excitation laser

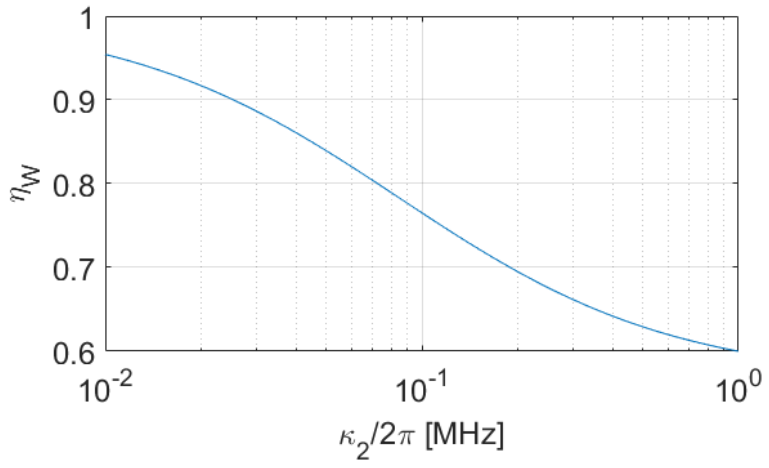

Figure 6.3: **Projection of write efficiency vs. filter cavity linewidth.** Calculated for 3 mm x 3 mm cell cross section and excitation beam assumed uniform over the cross section. The ratio $w/L = 0.6$ for the detection mode is the same as used in the microcell experiment.

power at the atoms to achieve the same mean intensity. To some degree the higher rejection requirements can be compensated by employing a longer cell to increase the optical depth. Moreover, a double-pass configuration – like the one of Thomas *et al.* (2021) – will yield an extra factor two in OD. However, the amount of compensation is limited to a factor 10-20 for a realistic cell length. We also note that the way to achieve higher laser extinction would be to cascade several cavities to avoid having one very narrow filter where only very slow pulses can transmit.

Chapter 7

Conclusion

The work presented in this thesis represents the first demonstration of single-photon generation in the long-lived mode of an atomic vapour cell with anti-relaxation coating. Moreover, the presented experiments are the first demonstration of discrete-variable interaction with the long-lived mode. This was achieved by successful implementation of the novel technique of motionally-averaged photon counting. The technique yields a scheme for generating single excitations in the long-lived atomic mode and retrieve them on demand within the near-millisecond memory time of the mode. In order to attain high-fidelity readout, the atomic four-wave-mixing process has to be strongly suppressed. We show how this can be achieved by operating at the magic detuning in caesium where the type of light-matter interaction – parametric gain or beam splitter – is selected by the linear polarization of the driving laser pulse. The strong four-wave-mixing suppression scheme is only allowed for the D_1 line and not available on the D_2 line.

We show that the readout fidelity is limited by atomic state preparation for short storage time and atomic repopulation (re-thermalization) of the storage state for long storage times. By optimization of the optical pumping process employed for state preparation we are able to limit the initial occupation of the storage state to 3%.

By bringing these building blocks together, we demonstrate single-photon generation and retrieval in an atomic ensemble at room temperature. For immediate readout the cross-correlation between heralding light and retrieved light reaches $g^{(2)}_{\mathrm{WR}} = 10 \pm 1$ which is strongly non-classical and above the threshold that allows for Bell-inequality violation by entangling two identical atomic ensembles. The readout fidelity is quantified by the auto-correlation of the retrieved field conditioned on a heralding detection event. For immediate readout we obtain an auto-correlation of $g^{(2)}_{\mathrm{RR|W=1}} = 0.20 \pm 0.07$ which verifies the anti-bunched nature of retrieved photons.

When characterizing the memory performance, we see that the correlation above the Bell-inequality threshold is maintained for $\tau_{\mathrm{BI}} = 0.15 \pm 0.03\,\mathrm{ms}$ of storage. In contrast, non-classical correlation is maintained for $\tau_{\mathrm{NC}} = 0.68 \pm 0.08\,\mathrm{ms}$. The observed τ_{NC} is two orders

of magnitude longer than previous demonstrations in room-temperature atomic ensembles. As a figure of merit for photon synchronization application we find that the memory time-bandwidth product is 17 ± 2 and limited by the long pulses required for motional averaging.

The scheme is performed inside a cell cavity which enhances the effective optical depth of the atomic ensemble. While we find that the retrieval process is efficient with an intrinsic efficiency of $(70 \pm 8)\%$, limited by the chosen read truncation time, the external efficiency is restricted because more than half of the retrieved light is lost due to intracavity losses.

We assess that the scheme does not show competitive performance for short-distance photon synchronization but that it could find application within long-distance quantum communication at room temperature and identify three main parameters that require improvement for successful employment.

1) The external efficiency must increase significantly. This concerns technical improvements of the transmission through the filter cavities as well as cavity escape efficiency. To remedy the latter we suggest to explore the scheme without the use of a cell cavity.

2) The memory time needs to increase by at least an order of magnitude. The memory time is currently limited by the small cell cross section and can be increased by using a larger cell. We suggest to investigate the scheme in a larger cell and find that it will require more filtering. Moreover, the memory time should be increased without the need to prolong the duration of the light pulses. To conserve the motional averaging we suggest that a scheme involving a top-hat beam profile is explored.

3) The atomic noise should be further suppressed to enable higher single-photon readout fidelity. This will require further work on the optical pumping process with the possible implementation of microwave assistance as well as further investigation into the limitation from cell fabrication.

In the context of academic interest we find that the successful implementation of the scheme opens a path towards new experiments such as hybrid spin-mechanical entanglement in discrete variables and generation of collective-spin Schrödinger-cat states.

As a final remark, it will constitute a breakthrough in room-temperature quantum memory if this first demonstration of motionally-averaged photon counting in warm atomic vapour were to be followed up by an identification of a viable path to combine the scheme with storage in the spin-exchange-relaxation-free regime which offers second-scale memory time.

Appendices

Appendix A

Correlation model

Here we present a detailed derivation of the correlation model introduced in chapter 5. The derivation is performed in the framework of probability generating functions (PGFs). The PGF $G_X(s)$ of a certain process X with outcomes $\{x\}$ is defined as (Riley and Hobson, 2011)

$$G_X(s) = \mathbb{E}(s^x) = \sum_{x=0}^{\infty} \mathbb{P}(X = x)s^x \tag{A.1}$$

and has the following basic properties.

$$\text{Probabilities: } \mathbb{P}(X = x) = \left(\frac{1}{x!}\right) \frac{d^x}{ds^x} G_X(s)\bigg|_{s=0} \tag{A.2}$$

$$\text{Factorial moments: } \mathbb{E}\{X(X-1)...(X-k+1)\} = \frac{d^k}{ds^k} G_X(s)\bigg|_{s=1} \tag{A.3}$$

$$\text{Sums: } G_{X+Y}(s) = G_X(s)G_Y(s) \text{ for } X, Y \text{ independent} \tag{A.4}$$

$$\text{Joint PGF: } G_{X,Y}(s,t) = \mathbb{E}(s^x t^y) = \sum_{x=0}^{\infty}\sum_{y=0}^{\infty} \mathbb{P}(X = x, Y = y)s^x t^y. \tag{A.5}$$

In the DLCZ experiment we mainly deal with two distributions: the Poisson distribution models the uncorrelated noise and the geometric distribution describing the thermal fields of the two-mode squeezed state. The PGFs for the two distributions are given as

$$\text{Poisson: } G_X^{\text{Poiss}}(s) = e^{\lambda(s-1)} \tag{A.6}$$

$$\text{Geometric: } G_X^{\text{Geo}}(s) = \frac{1}{1+\mu(1-s)} \tag{A.7}$$

where λ and μ are the respective mean numbers. Another relevant distribution is the binomial distribution which we shall use for introducing finite detection efficiency. The binomial PGF is

$$\text{Binomial: } G_X^{\text{Binom}}(s) = (ps+q)^n = \sum_{x=0}^{\infty} \binom{n}{x} p^x q^{n-x} s^x \tag{A.8}$$

where n is the number of trials and $p = 1 - q$ is the success probability.

If we introduce a finite detection efficiency η, this will change our original PGF $G_X(s) = \sum_{n=0}^{\infty} p_n s^n$ by modifying the the detection outcome (success/fail) according to a binomial distribution. We can write this as

$$G_X^{(\eta)}(s) = \sum_{x=0}^{\infty} \tilde{p}_x s^x = \sum_{n=0}^{\infty} p_n \sum_{x=0}^{\infty} \binom{n}{x} \eta^x q^{n-x} s^x \tag{A.9}$$

$$= \sum_{n=0}^{\infty} p_n (\eta s + q)^n = G_X(\eta s + q). \tag{A.10}$$

where we recognize the last sum in the first line as $G_X^{\text{Binom}}(s)$. Thus, we can introduce finite detection efficiency by making the substitution

$$s \mapsto \eta s + 1 - \eta = 1 + \eta(s - 1). \tag{A.11}$$

DLCZ model

We start out with the two-mode squeezed state of coherent write (X) and read (Y) contributions to the detection. Since the joint state is a thermal distribution of photon pairs, the joint PGF can be written

$$G_{X,Y}(s,t) = \frac{1}{1 + \mu(1 - st)}. \tag{A.12}$$

We then add noise as independent processes for write ($W = X + A$) and read ($R = Y + B$) by multiplying the joint PGF to get

$$G_{W,R}(s,t) = G_{X,Y}(s,t) G_A(s) G_B(t). \tag{A.13}$$

This is the joint PGF for write and read detection events where X, Y are the underlying coherent excitations and A, B the noise processes.

Cross-correlation

First we consider noise-free case where we have complete correlation in X and Y. We calculate the (unnormalized) cross-correlation according to eq. (A.3).

$$\mathbb{E}(XY) = \frac{d^2}{dsdt} G_{X,Y}(s,t)\bigg|_{s=1,t=1} = 2\mu^2 + \mu \tag{A.14}$$

From this we calculate the normalized cross-correlation

$$g_{XY}^{(2)} = \frac{\mathbb{E}(XY)}{\mathbb{E}(X)\mathbb{E}(Y)} = \frac{2\mu^2 + \mu}{\mu^2} = 2 + \frac{1}{\mu} = 1 + \frac{1}{p_0}. \tag{A.15}$$

Here $p_0 = \mu/(1 + \mu)$ is the excitation probability, i.e. $p_0 = \mathbb{P}(X \geq 1)$ is the probability for one or more excitations in the thermal distribution.

Since the noise is an independent process, we can include it by adding the accidental coincidences. We then have

$$\mathbb{E}(WR) = \mathbb{E}\left[(X+A)(Y+B)\right] \tag{A.16}$$
$$= \mathbb{E}(XY) + \mathbb{E}(X)\mathbb{E}(B) + \mathbb{E}(Y)\mathbb{E}(A) + \mathbb{E}(A)\mathbb{E}(B) \tag{A.17}$$
$$= 2\mu^2 + \mu + \mu(\lambda_A + \lambda_B) + \lambda_A\lambda_B. \tag{A.18}$$

Notice that the correction from noise is independent of the probability distribution of the noise. Only the mean noise numbers λ_A and λ_B enters. The cross-correlation then becomes

$$g^{(2)}_{WR} = \frac{2\mu^2 + \mu + \mu(\lambda_A + \lambda_B) + \lambda_A\lambda_B}{\mu^2 + \mu(\lambda_A + \lambda_B) + \lambda_A\lambda_B} = 1 + \frac{\mu(1+\mu)}{(\mu+\lambda_A)(\mu+\lambda_B)}\ . \tag{A.19}$$

We now introduce the detection efficiency. The joint PGF in eq. (A.12) describes the pair-wise generation of heralding photon and atomic excitation (in the symmetric mode). Thus, detection efficiencies should include all losses from generated quanta to detection event. I.e. $\eta_X = \eta_{\mathrm{esc}}\eta^{\mathrm{W}}_{\mathrm{det}}$ and $\eta_Y = \eta^{*}_{\mathrm{R}}\eta_{\mathrm{esc}}\eta^{\mathrm{R}}_{\mathrm{det}}$. We use the substitution in eq. (A.11) and perform the same step as above:

$$\mathbb{E}(XY) = \frac{d^2}{dsdt}G^{\eta_X,\eta_Y}_{X,Y}(s,t)\bigg|_{s=1,t=1} = \eta_X\eta_Y(2\mu^2+\mu). \tag{A.20}$$

In the absence of noise the cross-correlation is unchanged because also $\mathbb{E}(X)\mathbb{E}(Y) = \eta_X\eta_Y\mu^2$ is scaled with the detection efficiencies.

We can adapt the noise result in eq. (A.19) to the result above by scaling with the detection efficiencies:

$$\begin{aligned} g^{(2)}_{WR} &= \frac{\eta_X\eta_Y(2\mu^2+\mu) + \mu(\eta_Y\lambda_A + \eta_X\lambda_B) + \lambda_A\lambda_B}{\eta_X\eta_Y\mu^2 + \mu(\eta_Y\lambda_A + \eta_X\lambda_B) + \lambda_A\lambda_B} \\ &= 1 + \frac{\eta_X\eta_Y(\mu^2+\mu)}{\eta_X\eta_Y\mu^2 + \mu(\eta_Y\lambda_A + \eta_X\lambda_B) + \lambda_A\lambda_B} \\ &= 1 + \frac{(\mu^2+\mu)}{\mu^2 + \mu(\lambda_A/\eta_X + \lambda_B/\eta_Y) + \lambda_A\lambda_B/(\eta_X\eta_Y)} \end{aligned} \tag{A.21}$$

We take λ_A and λ_B to be *detected* noise levels. Hence, we do not scale these values with detection efficiencies.

Auto-correlation

Similarly, we can get an analytic expression for auto-correlation in presence of noise. E.g. the first factorial moment of the write auto-correlation is

$$\mathbb{E}(W(W-1)) = \mathbb{E}((X+A)(X+A-1)) \tag{A.22}$$
$$= \mathbb{E}(X(X-1)) + \mathbb{E}(A(A-1)) + 2\mathbb{E}(X)\mathbb{E}(A) \tag{A.23}$$
$$= \mu^2 g^{(2)}_{XX} + \lambda^2_A g^{(2)}_{AA} + 2\mu\lambda_A. \tag{A.24}$$

From this we calculate the normalized auto-correlation function

$$g^{(2)}_{WW} = \frac{\mu^2 g^{(2)}_{XX} + \lambda_A^2 g^{(2)}_{AA} + 2\mu\lambda_A}{\mu^2 + \lambda_A^2 + 2\mu\lambda_A}. \tag{A.25}$$

Since this expression depends only on the mean and individual process auto-correlation, we can include detection efficiency by the simple transformation $\mu \mapsto \eta_X \mu$ and the expression becomes:

$$g^{(2)}_{WW} = \frac{\eta_X^2\mu^2 g^{(2)}_{XX} + \lambda_A^2 g^{(2)}_{AA} + 2\eta_X\mu\lambda_A}{\eta_X^2\mu^2 + \lambda_A^2 + 2\eta_X\mu\lambda_A}. \tag{A.26}$$

Conditional auto-correlation

We now turn to the more complex problem of deriving an expression for the auto-correlation conditioned on a single heralding write event. Conditional probabilities can be generated from the PGF through the following operation:

$$G_{Y|X=1}(t) = \frac{\frac{d}{ds}G_{X,Y}(s,t)\big|_{s=0}}{\frac{d}{ds}G_{X,Y}(s,t)\big|_{s=0,t=1}} \tag{A.27}$$

where the numerator contains all terms for $X = 1$ (cf. eq. (A.2)) and the denominator is normalization by the probability of having exactly one write event (cf. eq. (A.3) with $k = 0$).

If we consider the noise-free DLCZ with perfect write detection, we get by definition $g^{(2)}_{RR|W} = 0$. Introducing non-perfect write detection efficiency η_X will increase the conditional mean excitation number because multiple excitations can be perceived as single excitation. We calculate the numerator and denominator in eq. (A.27) as follows:

$$\frac{d}{ds}G^{\eta_X,\eta_Y}_{X,Y}(s,t)\bigg|_{s=0} = \frac{\mu\eta_X(1+\eta_Y(t-1))}{((1-\mu[-\eta_X+\eta_Y(t-1)-\eta_X\eta_Y(t-1)])^2}\ , \tag{A.28}$$

$$\frac{d}{ds}G^{\eta_X,\eta_Y}_{X,Y}(s,t)\bigg|_{s=0,t=1} = \frac{\mu\eta_X}{(1+\mu\eta_X)^2}. \tag{A.29}$$

Inserting eqs. (A.28) and (A.29) in eq. (A.27) yields

$$G^{\eta_X,\eta_Y}_{Y|X=1}(t) = \frac{(1+\eta_Y(t-1))(1+\mu\eta_X)^2}{(1-\mu(-1+(1-\eta_X)[1+\eta_Y(t-1)])^2}. \tag{A.30}$$

Here we recognize the substitution for detection efficiency in read. If we transform back ($\eta_Y = 1$), the expression reads

$$G^{\eta_X}_{Y|X=1}(t) = \frac{t(1+\mu\eta_X)^2}{(1-\mu(-1+(1-\eta_X)t)^2}. \tag{A.31}$$

For perfect heralding $\eta_X = 1$, then $G^{\eta_X}_{Y|X=1}(t) = t$ which is the generator for $\mathbb{P}(Y = 1) = 1$. This reproduces the ideal two-mode squeezer correlation.

From the conditional PGF in eq. (A.31) we can calculate the auto-correlation as was done above:

$$\mathbb{E}(Y|X=1) = \frac{d}{dt}G^{\eta_X}_{Y|X=1}(t)\Big|_{t=1} = 1 + \frac{2\mu(1-\eta_X)}{1+\mu\eta_X} \tag{A.32}$$

$$\mathbb{E}\left[Y(Y-1)|X=1\right] = \frac{d^2}{dt^2}G^{\eta_X}_{Y|X=1}(t)\Big|_{t=1} = \frac{(4+\sqrt{6})\mu(1-\eta_X)}{1+\mu\eta_X} \tag{A.33}$$

$$\frac{\mathbb{E}\left[Y(Y-1)|X=1\right]}{\mathbb{E}(Y|X=1)^2} = g^{(2)}_{YY|X=1} = \frac{(4+\sqrt{6})\mu(1-\eta_X)(1+\mu\eta_X)}{(1-\mu\eta_X+2\mu)^2} \tag{A.34}$$

The result in eq. (A.34) demonstrates that the conditional auto-correlation for imperfect detection efficiency is non-trivial. The next step is to introduce false heralds from write noise A. We again have to construct the conditional PGF as

$$G^{\eta_X}_{Y|W=1}(t) = \frac{\frac{d}{ds}G^{\eta_X}_{W,Y}(s,t)\Big|_{s=0}}{\frac{d}{ds}G^{\eta_X}_{W,Y}(s,t)\Big|_{s=0,t=1}} \tag{A.35}$$

with the joint PGF given by

$$G^{\eta_X}_{W,Y}(s,t) = G^{\eta_X}_{X,Y}(s,t)G_A(s) = \frac{e^{\lambda_A(s-1)}}{1+\mu(1-[1+\eta_X(s-1)]t)}. \tag{A.36}$$

Note that we assume the write noise to be Poissonian.

The numerator and denominator of eq. (A.35) can be written as

$$\frac{d}{ds}G^{\eta_X}_{W,Y}(s,t)\Big|_{s=0} = \frac{\mu\eta_X t e^{-\lambda_A}}{(1+\mu(1-[1-\eta_X]t))^2} + \frac{\lambda_A e^{-\lambda_A}}{1+\mu(1-[1-\eta_X]t)} \tag{A.37}$$

and

$$\frac{d}{ds}G^{\eta_X}_{W,Y}(s,t)\Big|_{s=0,t=1} = \frac{\mu\eta_X e^{-\lambda_A}}{(1+\mu\eta_X)^2} + \frac{\lambda_A e^{-\lambda_A}}{1+\mu\eta_X} = Z. \tag{A.38}$$

Then we calculate the autocorrelation in the same way as above:

$$g^{(2)}_{YY|W=1} = \frac{\mathbb{E}(Y(Y-1)|W=1)}{\mathbb{E}(Y|W=1)^2} = \frac{Z\,\frac{d^2}{dt^2}\left(\frac{d}{ds}G^{\eta_X}_{W,Y}(s,t)\Big|_{s=0}\right)\Big|_{t=1}}{\left(\frac{d}{dt}\left(\frac{d}{ds}G^{\eta_X}_{W,Y}(s,t)\Big|_{s=0}\right)\Big|_{t=1}\right)^2} =$$
$$\frac{2(1-\eta_X)(\lambda_A+\eta_X\mu+\lambda_A\eta_X\mu)(\lambda_A+2\eta_X-\lambda_A\eta_X+3\eta_X\mu-\eta_X^2\mu+\lambda_A\eta_X\mu-\lambda_A\eta_X^2\mu)}{(\lambda_A+\eta_X-\lambda_A\eta_X+2\eta_X\mu-\eta_X^2\mu+\lambda_A\eta_X\mu-\lambda_A\eta_X^2\mu)^2}. \tag{A.39}$$

And the conditional mean occupation of the atomic mode

$$\tilde{\mu} = \mathbb{E}(Y|W=1) = \frac{\mu(\lambda_A+\eta_X-\lambda_A\eta_X+2\eta_X\mu-\eta_X^2\mu+\lambda_A\eta_X\mu-\lambda_A\eta_X^2\mu)}{(1+\eta_X\mu)(\lambda_A+\eta_X\mu+\lambda_A\eta_X\mu)}. \tag{A.40}$$

As I final step we add read noise following the result in eq. (A.27) and substitute with the conditional mean $\mu \mapsto \tilde{\mu}$:

$$g^{(2)}_{RR|W=1} = \frac{\eta_Y^2 \tilde{\mu}^2 g^{(2)}_{YY|W=1} + \lambda_B^2 g^{(2)}_{BB} + 2\eta_Y \tilde{\mu} \lambda_B}{\eta_Y^2 \tilde{\mu}^2 + \lambda_B^2 + 2\eta_Y \tilde{\mu} \lambda_B}. \tag{A.41}$$

Bibliography

Azuma, K., Tamaki, K., and Lo, H.K. (2015). All-photonic quantum repeaters. *Nature Communications*, **6**:6787.

Balabas, M.V., Karaulanov, T., Ledbetter, M.P., and Budker, D. (2010). Polarized Alkali-Metal Vapor with Minute-Long Transverse Spin-Relaxation Time. *Physical Review Letters*, **105**(7):070801.

Bao, H., Duan, J., Jin, S., Lu, X., Li, P., Qu, W., Wang, M., Novikova, I., Mikhailov, E.E., Zhao, K.F., Mølmer, K., Shen, H., and Xiao, Y. (2020). Spin squeezing of 1011 atoms by prediction and retrodiction measurements. *Nature*, **581**(7807):159–163.

Bao, X.H., Reingruber, A., Dietrich, P., Rui, J., Dück, A., Strassel, T., Li, L., Liu, N.L., Zhao, B., and Pan, J.W. (2012). Efficient and long-lived quantum memory with cold atoms inside a ring cavity. *Nature Physics*, **8**(7):517–521.

Bashkansky, M., Fatemi, F.K., and Vurgaftman, I. (2012). Quantum memory in warm rubidium vapor with buffer gas. *Optics Letters*, **37**(2):142–144.

Bellini, M. and Zavatta, A. (2010). Manipulating Light States by Single-Photon Addition and Subtraction. In E. Wolf (editor), *Progress in Optics*, volume 55, pages 41–83. Elsevier Masson SAS.

Bennett, C.H. and Brassard, G. (1984). Quantum Cryptography: Public Key Distribution, and Coin-Tossing. In *Proc. 1984 IEEE International Conference on Computers, Systems, and Signal Processing*, pages 175–179.

Bennett, C.H., Brassard, G., Crépeau, C., Jozsa, R., Peres, A., and Wootters, W.K. (1993). Teleporting an unknown quantum state via dual classical and Einstein-Podolsky-Rosen channels. *Physical Review Letters*, **70**(13):1895–1899.

Borregaard, J., Zugenmaier, M., Petersen, J.M., Shen, H., Vasilakis, G., Jensen, K., Polzik, E.S., and Sørensen, A.S. (2016). Scalable photonic network architecture based on motional averaging in room temperature gas. *Nature Communications*, **7**:11356.

Boto, E., Holmes, N., Leggett, J., Roberts, G., Shah, V., Meyer, S.S., Muñoz, L.D., Mullinger, K.J., Tierney, T.M., Bestmann, S., Barnes, G.R., Bowtell, R., and Brookes, M.J. (2018). Moving magnetoencephalography towards real-world applications with a wearable system. *Nature*, **555**(7698):657–661.

Bouillard, M., Boucher, G., Ferrer Ortas, J., Pointard, B., and Tualle-Brouri, R. (2019). Quantum Storage of Single-Photon and Two-Photon Fock States with an All-Optical Quantum Memory. *Physical Review Letters*, **122**(21):210501.

Branciard, C. (2016). Witnesses of causal nonseparability: an introduction and a few case studies. *Scientific Reports*, **6**(1):26018.

Budker, D., Hollberg, L., Kimball, D.F., Kitching, J., Pustelny, S., and Yashchuk, V.V. (2005). Microwave transitions and nonlinear magneto-optical rotation in anti-relaxation-coated cells. *Physical Review A*, **71**(1):012903.

Carolan, J., Harrold, C., Sparrow, C., Martin-Lopez, E., Russell, N.J., Silverstone, J.W., Shadbolt, P.J., Matsuda, N., Oguma, M., Itoh, M., Marshall, G.D., Thompson, M.G., Matthews, J.C.F., Hashimoto, T., O'Brien, J.L., and Laing, A. (2015). Universal linear optics. *Science*, **349**(6249):711–716.

Chalupczak, W., Godun, R.M., and Pustelny, S. (2018). Radio-Frequency Spectroscopy as a Tool for Studying Coherent Spin Dynamics and for Application to Radio-Frequency Magnetometry. In E. Arimondo, L.F. DiMauro, and S.F. Yelin (editors), *Advances in Atomic, Molecular and Optical Physics*, volume 67, chapter 5, pages 297–336. Academic Press, Cambridge, USA.

Chi, H., Quan, W., Zhang, J., Zhao, L., and Fang, J. (2020). Advances in anti-relaxation coatings of alkali-metal vapor cells. *Applied Surface Science*, **501**:143897.

Chou, C.W., Polyakov, S.V., Kuzmich, A., and Kimble, H.J. (2004). Single-Photon Generation from Stored Excitation in an Atomic Ensemble. *Physical Review Letters*, **92**(21):213601.

Clauser, J.F. (1974). Experimental distinction between the quantum and classical field-theoretic predictions for the photoelectric effect. *Physical Review D*, **9**(4):853–860.

Clauser, J.F., Horne, M.A., Shimony, A., and Holt, R.A. (1969). Proposed Experiment to Test Local Hidden-Variable Theories. *Physical Review Letters*, **23**(15):880–884.

Clauser, J.F. and Shimony, A. (1978). Bell's theorem. Experimental tests and implications. *Reports on Progress in Physics*, **41**(12):1881–1927.

Collins, O.A., Jenkins, S.D., Kuzmich, A., and Kennedy, T.A.B. (2007). Multiplexed Memory-Insensitive Quantum Repeaters. *Physical Review Letters*, **98**(6):060502.

Corsini, E.P., Karaulanov, T., Balabas, M., and Budker, D. (2013). Hyperfine frequency shift and Zeeman relaxation in alkali-metal-vapor cells with antirelaxation alkene coating. *Physical Review A*, **87**(2):022901.

Dąbrowski, M., Chrapkiewicz, R., and Wasilewski, W. (2014). Hamiltonian design in readout from room-temperature Raman atomic memory. *Optics Express*, **22**(21):26076.

de Riedmatten, H., Laurat, J., Chou, C.W., Schomburg, E.W., Felinto, D., and Kimble, H.J. (2006). Direct Measurement of Decoherence for Entanglement between a Photon and Stored Atomic Excitation. *Physical Review Letters*, **97**(11):113603.

Dideriksen, K.B. (2014a). *A Laser System for a Deterministic Single Photon Source*. Bachelor's thesis, University of Copenhagen.

Dideriksen, K.B. (2014b). *Linewidth Measurement of Near-Infrared Laser Systems*. Report (unpublished), University of Copenhagen.

Dideriksen, K.B. (2017). *Development of a Single-Photon Source with Room-Temperature Atomic Ensembles*. Master's thesis, University of Copenhagen.

Dideriksen, K.B., Schmieg, R., Zugenmaier, M., and Polzik, E.S. (2020). *Room-temperature single-photon source with near-millisecond built-in memory*. Preprint, arxiv:2010.06875.

Dou, J.P., Yang, A.L., Du, M.Y., Lao, D., Gao, J., Qiao, L.F., Li, H., Pang, X.L., Feng, Z., Tang, H., and Jin, X.M. (2018). A broadband DLCZ quantum memory in room-temperature atoms. *Communications Physics*, **1**(1):55.

Duan, L.M., Lukin, M.D., Cirac, J.I., and Zoller, P. (2001). Long-distance quantum communication with atomic ensembles and linear optics. *Nature*, **414**(6862):413–418.

Eisaman, M.D., André, A., Massou, F., Fleischhauer, M., Zibrov, A.S., and Lukin, M.D. (2005). Electromagnetically induced transparency with tunable single-photon pulses. *Nature*, **438**(7069):837–841.

Ekert, A.K. (1991). Quantum cryptography based on Bell's theorem. *Physical Review Letters*, **67**(6):661–663.

Enault-Dautheribes, M. (2017). *Optically Narrowed Laser Towards the Implementation of a Single-Photon Source on the D1 Line of Caesium*. Master's thesis, University of Copenhagen.

England, D.G., Fisher, K.A.G., MacLean, J.P.W., Bustard, P.J., Lausten, R., Resch, K.J., and Sussman, B.J. (2015). Storage and Retrieval of THz-Bandwidth Single Photons Using a Room-Temperature Diamond Quantum Memory. *Physical Review Letters*, **114**(5):053602.

Fabricant, A. (2014). *Quantum-limited optical magnetometry with cesium microcells*. Master's thesis, University of Copenhagen.

Fang, J. and Qin, J. (2012). Advances in Atomic Gyroscopes: A View from Inertial Navigation Applications. *Sensors*, **12**(5):6331–6346.

Finkelstein, R., Poem, E., Michel, O., Lahad, O., and Firstenberg, O. (2018). Fast, noise-free memory for photon synchronization at room temperature. *Science Advances*, **4**(1):eaap8598.

Foot, C.J. (2005). *Atomic Physics*. Oxford University Press, Oxford.

Galinskiy, I., Tsaturyan, Y., Parniak, M., and Polzik, E.S. (2020). Phonon counting thermometry of an ultracoherent membrane resonator near its motional ground state. *Optica*, **7**(6):718.

Gerry, C. and Knight, P. (2004). *Introductory Quantum Optics*. Cambridge University Press, Cambridge.

Gorshkov, A.V., André, A., Lukin, M.D., and Sørensen, A.S. (2007a). Photon storage in Λ-type optically dense atomic media. I. Cavity model. *Physical Review A*, **76**(3):033804.

Gorshkov, A.V., André, A., Lukin, M.D., and Sørensen, A.S. (2007b). Photon storage in Λ-type optically dense atomic media. II. Free-space model. *Physical Review A*, **76**(3):033805.

Gorshkov, A.V., André, A., Lukin, M.D., and Sørensen, A.S. (2007c). Photon storage in Λ-type optically dense atomic media. III. Effects of inhomogeneous broadening. *Physical Review A*, **76**(3):033806.

Greenberger, D.M., Horne, M.A., and Zeilinger, A. (1989). Going Beyond Bell's Theorem. In M. Kafatos (editor), *Bell's Theorem, Quantum Theory and Conceptions of the Universe*, pages 69–72. Springer, Dordrecht.

Hacker, B., Welte, S., Rempe, G., and Ritter, S. (2016). A photon–photon quantum gate based on a single atom in an optical resonator. *Nature*, **536**(7615):193–196.

Hammerer, K., Sørensen, A.S., and Polzik, E.S. (2010). Quantum interface between light and atomic ensembles. *Reviews of Modern Physics*, **82**(2):1041–1093.

Hänsch, T. and Couillaud, B. (1980). Laser frequency stabilization by polarization spectroscopy of a reflecting reference cavity. *Optics Communications*, **35**(3):441–444.

Hayasaka, K. (2011). Modulation-free optical locking of an external-cavity diode laser to a filter cavity. *Optics letters*, **36**(12):2188–2190.

Hong, C.K., Ou, Z.Y., and Mandel, L. (1987). Measurement of subpicosecond time intervals between two photons by interference. *Physical Review Letters*, **59**(18):2044–2046.

Hosseini, M., Campbell, G., Sparkes, B.M., Lam, P.K., and Buchler, B.C. (2011). Unconditional room-temperature quantum memory. *Nature Physics*, **7**(10):794–798.

Jensen, K., Skarsfeldt, M.A., Stærkind, H., Arnbak, J., Balabas, M.V., Olesen, S.P., Bentzen, B.H., and Polzik, E.S. (2018). Magnetocardiography on an isolated animal heart with a room-temperature optically pumped magnetometer. *Scientific Reports*, **8**(1):16218.

Jensen, K., Wasilewski, W., Krauter, H., Fernholz, T., Nielsen, B.M., Owari, M., Plenio, M.B., Serafini, A., Wolf, M.M., and Polzik, E.S. (2011). Quantum memory for entangled continuous-variable states. *Nature Physics*, **7**(1):13–16.

Jeong, T., Lee, Y.S., Park, J., Kim, H., and Moon, H.S. (2017). Quantum interference between autonomous single-photon sources from Doppler-broadened atomic ensembles. *Optica*, **4**(10):1167.

Julsgaard, B. (2003). *Entanglement and Quantum Interactions with Macroscopic Gas Samples*. Ph.D. thesis, University of Aarhus.

Julsgaard, B., Kozhekin, A., and Polzik, E.S. (2001). Experimental long-lived entanglement of two macroscopic objects. *Nature*, **413**(6854):400–403.

Julsgaard, B., Sherson, J., Cirac, J.I., Fiurášek, J., and Polzik, E.S. (2004a). Experimental demonstration of quantum memory for light. *Nature*, **432**(7016):482–486.

Julsgaard, B., Sherson, J., Sørensen, J.L., and Polzik, E.S. (2004b). Characterizing the spin state of an atomic ensemble using the magneto-optical resonance method. *Journal of Optics B: Quantum and Semiclassical Optics*, **6**(1):5–14.

Kaczmarek, K.T., Ledingham, P.M., Brecht, B., Thomas, S.E., Thekkadath, G.S., Lazo-Arjona, O., Munns, J.H.D., Poem, E., Feizpour, A., Saunders, D.J., Nunn, J., and Walmsley, I.A. (2018). High-speed noise-free optical quantum memory. *Physical Review A*, **97**(4):042316.

Kalb, N., Reiserer, A.A., Humphreys, P.C., Bakermans, J.J.W., Kamerling, S.J., Nickerson, N.H., Benjamin, S.C., Twitchen, D.J., Markham, M., and Hanson, R. (2017). Entanglement distillation between solid-state quantum network nodes. *Science*, **356**(6341):928–932.

Kaneda, F. and Kwiat, P.G. (2019). High-efficiency single-photon generation via large-scale active time multiplexing. *Science Advances*, **5**(10):eaaw8586.

Katz, O. and Firstenberg, O. (2018). Light storage for one second in room-temperature alkali vapor. *Nature Communications*, **9**(1):2074.

Knapkiewicz, P. (2018). Technological Assessment of MEMS Alkali Vapor Cells for Atomic References. *Micromachines*, **10**(1):25.

Knill, E., Laflamme, R., and Milburn, G.J. (2001). A scheme for efficient quantum computation with linear optics. *Nature*, **409**(6816):46–52.

Kogelnik, H. and Li, T. (1966). Laser beams and resonators. *Proceedings of the IEEE*, **54**(10):1312–1329.

Krauter, H., Muschik, C.A., Jensen, K., Wasilewski, W., Petersen, J.M., Cirac, J.I., and Polzik, E.S. (2011). Entanglement Generated by Dissipation and Steady State Entanglement of Two Macroscopic Objects. *Physical Review Letters*, **107**(8):080503.

Krauter, H., Salart, D., Muschik, C.A., Petersen, J.M., Shen, H., Fernholz, T., and Polzik, E.S. (2013). Deterministic quantum teleportation between distant atomic objects. *Nature Physics*, **9**(7):400–404.

Kübler, H., Shaffer, J.P., Baluktsian, T., Löw, R., and Pfau, T. (2010). Coherent excitation of Rydberg atoms in micrometre-sized atomic vapour cells. *Nature Photonics*, **4**(2):112–116.

Kutluer, K., Mazzera, M., and de Riedmatten, H. (2017). Solid-State Source of Nonclassical Photon Pairs with Embedded Multimode Quantum Memory. *Physical Review Letters*, **118**(21):210502.

Laplane, C., Jobez, P., Etesse, J., Gisin, N., and Afzelius, M. (2017). Multimode and Long-Lived Quantum Correlations Between Photons and Spins in a Crystal. *Physical Review Letters*, **118**(21):210501.

Laurat, J., Choi, K.S., Deng, H., Chou, C.W., and Kimble, H.J. (2007). Heralded Entanglement between Atomic Ensembles: Preparation, Decoherence, and Scaling. *Physical Review Letters*, **99**(18):180504.

Li, H., Dou, J.P., Pang, X.L., Yang, T.H., Zhang, C.N., Chen, Y., Li, J.M., Walmsley, I.A., and Jin, X.M. (2020). *Heralding Quantum Entanglement between Two Room-Temperature Atomic Ensembles*. Preprint, arxiv:2007.10948.

Li, L., Dudin, Y.O., and Kuzmich, A. (2013). Entanglement between light and an optical atomic excitation. *Nature*, **498**(7455):466–469.

Makino, K., Hashimoto, Y., Yoshikawa, J.i., Ohdan, H., Toyama, T., van Loock, P., and Furusawa, A. (2016). Synchronization of optical photons for quantum information processing. *Science Advances*, **2**(5):e1501772.

Marcikic, I., de Riedmatten, H., Tittel, W., Zbinden, H., Legré, M., and Gisin, N. (2004). Distribution of Time-Bin Entangled Qubits over 50 km of Optical Fiber. *Physical Review Letters*, **93**(18):180502.

Matekole, E.S., Lee, H., and Dowling, J.P. (2018). Limits to atom-vapor-based room-temperature photon-number-resolving detection. *Physical Review A*, **98**(3):1–6.

Matsukevich, D.N., Chanelière, T., Bhattacharya, M., Lan, S.Y., Jenkins, S.D., Kennedy, T.A.B., and Kuzmich, A. (2005). Entanglement of a Photon and a Collective Atomic Excitation. *Physical Review Letters*, **95**(4):040405.

Mewes, C. and Fleischhauer, M. (2005). Decoherence in collective quantum memories for photons. *Physical Review A*, **72**(2):022327.

Meyer-Scott, E., Silberhorn, C., and Migdall, A. (2020). Single-photon sources: Approaching the ideal through multiplexing. *Review of Scientific Instruments*, **91**(4):041101.

Michelberger, P.S., Champion, T.F.M., Sprague, M.R., Kaczmarek, K.T., Barbieri, M., Jin, X.M., England, D.G., Kolthammer, W.S., Saunders, D.J., Nunn, J., and Walmsley, I.A. (2015). Interfacing GHz-bandwidth heralded single photons with a warm vapour Raman memory. *New Journal of Physics*, **17**(4):043006.

Mika, J. and Slodička, L. (2020). High nonclassical correlations of large-bandwidth photon pairs generated in warm atomic vapor. *Journal of Physics B: Atomic, Molecular and Optical Physics*, **53**(14):145501.

Milburn, T.J., Kim, M.S., and Vanner, M.R. (2016). Nonclassical-state generation in macroscopic systems via hybrid discrete-continuous quantum measurements. *Physical Review A*, **93**(5).

Munns, J.H.D., Qiu, C., Ledingham, P.M., Walmsley, I.A., Nunn, J., and Saunders, D.J. (2016). In situ characterization of an optically thick atom-filled cavity. *Physical Review A*, **93**(1):013858.

Namazi, M., Kupchak, C., Jordaan, B., Shahrokhshahi, R., and Figueroa, E. (2017). Ultralow-Noise Room-Temperature Quantum Memory for Polarization Qubits. *Physical Review Applied*, **8**(3):034023.

Neergaard-Nielsen, J.S., Nielsen, B.M., Hettich, C., Mølmer, K., and Polzik, E.S. (2006). Generation of a superposition of odd photon number states for quantum information networks. *Physical Review Letters*, **97**(8):083604.

Neuhaus, L. and Deléglise, S. (2017). *PyRPL*. [computer software], Available at pyrpl.readthedocs.io.

Nunn, J. (2019). 22. Linear optical quantum computing. In Minzioni, P. et al., Roadmap on all-optical processing, volume 21 of *J. Opt.*, 063001.

Nunn, J., Langford, N.K., Kolthammer, W.S., Champion, T.F.M., Sprague, M.R., Michelberger, P.S., Jin, X.M., England, D.G., and Walmsley, I.A. (2013). Enhancing Multiphoton Rates with Quantum Memories. *Physical Review Letters*, **110**(13):133601.

Pang, X.L., Yang, A.L., Dou, J.P., Li, H., Zhang, C.N., Poem, E., Saunders, D.J., Tang, H., Nunn, J., Walmsley, I.A., and Jin, X.M. (2020). A hybrid quantum memory–enabled network at room temperature. *Science Advances*, **6**(6):eaax1425.

Prajapati, N., Romanov, G., and Novikova, I. (2017). Suppression of four-wave mixing in hot rubidium vapor using ladder scheme Raman absorption. *Journal of the Optical Society of America B*, **34**(9):1994.

Procopio, L.M., Moqanaki, A., Araújo, M., Costa, F., Alonso Calafell, I., Dowd, E.G., Hamel, D.R., Rozema, L.A., Brukner, Č., and Walther, P. (2015). Experimental superposition of orders of quantum gates. *Nature Communications*, **6**(1):7913.

Radnaev, A.G., Dudin, Y.O., Zhao, R., Jen, H.H., Jenkins, S.D., Kuzmich, A., and Kennedy, T.A.B. (2010). A quantum memory with telecom-wavelength conversion. *Nature Physics*, **6**(11):894–899.

Rambach, M. (2018). *Narrowband Single Photons for Light-Matter Interfaces*. Springer Theses. Springer International Publishing, Cham.

Rambach, M., Lau, W.Y., Laibacher, S., Tamma, V., White, A.G., and Weinhold, T.J. (2018). Hectometer Revivals of Quantum Interference. *Physical Review Letters*, **121**(9):93603.

Reim, K.F., Michelberger, P., Lee, K.C., Nunn, J., Langford, N.K., and Walmsley, I.A. (2011). Single-Photon-Level Quantum Memory at Room Temperature. *Physical Review Letters*, **107**(5):053603.

Riedinger, R., Hong, S., Norte, R.A., Slater, J.A., Shang, J., Krause, A.G., Anant, V., Aspelmeyer, M., and Gröblacher, S. (2016). Non-classical correlations between single photons and phonons from a mechanical oscillator. *Nature*, **530**:313–316.

Riley, K.F. and Hobson, M.P. (2011). *Essential mathematical methods for the physical sciences*. Cambridge University Press, Cambridge, UK.

Ripka, F., Chen, Y.H., Löw, R., and Pfau, T. (2016). Rydberg polaritons in a thermal vapor. *Physical Review A*, **93**(5):053429.

Ripka, F., Kübler, H., Löw, R., and Pfau, T. (2018). A room-temperature single-photon source based on strongly interacting Rydberg atoms. *Science*, **362**(6413):446–449.

Robinson, H.G. and Johnson, C.E. (1982). Narrow 87Rb hyperfine-structure resonances in an evacuated wall-coated cell. *Applied Physics Letters*, **40**(9):771–773.

Saavedra, C., Pandey, D., Alt, W., Pfeifer, H., and Meschede, D. (2021). Tunable fiber Fabry-Perot cavities with high passive stability. *Optics Express*, **29**(2):974.

Saglamyurek, E., Sinclair, N., Jin, J., Slater, J.A., Oblak, D., Bussières, F., George, M., Ricken, R., Sohler, W., and Tittel, W. (2011). Broadband waveguide quantum memory for entangled photons. *Nature*, **469**(7331):512–515.

Sangouard, N., Simon, C., De Riedmatten, H., and Gisin, N. (2011). Quantum repeaters based on atomic ensembles and linear optics. *Reviews of Modern Physics*, **83**(1):33–80.

Saunders, D.J., Munns, J.H.D., Champion, T.F.M., Qiu, C., Kaczmarek, K.T., Poem, E., Ledingham, P.M., Walmsley, I.A., and Nunn, J. (2016). Cavity-Enhanced Room-Temperature Broadband Raman Memory. *Physical Review Letters*, **116**(9):090501.

Schmieg, R. (2018). *Coherent dynamics of atomic vapors.* Project report (unpublished), University of Copenhagen.

Schmieg, R. (2019). *Observation of non-classical photon pairs from room-temperature atomic ensembles through suppression of four-wave mixing and classical noise sources.* Master's thesis, University of Copenhagen.

Schünemann, U., Engler, H., Grimm, R., Weidemüller, M., and Zielonkowski, M. (1999). Simple scheme for tunable frequency offset locking of two lasers. *Review of Scientific Instruments*, **70**(1):242–243.

Sedlacek, J.A., Schwettmann, A., Kübler, H., Löw, R., Pfau, T., and Shaffer, J.P. (2012). Microwave electrometry with Rydberg atoms in a vapour cell using bright atomic resonances. *Nature Physics*, **8**(11):819–824.

Sekatski, P., Sangouard, N., Bussières, F., Clausen, C., Gisin, N., and Zbinden, H. (2012). Detector imperfections in photon-pair source characterization. *Journal of Physics B: Atomic, Molecular and Optical Physics*, **45**(12):124016.

Shaham, R., Katz, O., and Firstenberg, O. (2020). Quantum dynamics of collective spin states in a thermal gas. *Physical Review A*, **102**(1):012822.

Sherson, J.F., Krauter, H., Olsson, R.K., Julsgaard, B., Hammerer, K., Cirac, I., and Polzik, E.S. (2006). Quantum teleportation between light and matter. *Nature*, **443**(7111):557–560.

Simon, C. (2017). Towards a global quantum network. *Nature Photonics*, **11**(11):678–680.

Specht, H.P., Nölleke, C., Reiserer, A., Uphoff, M., Figueroa, E., Ritter, S., and Rempe, G. (2011). A single-atom quantum memory. *Nature*, **473**(7346):190–193.

Steck, D.A. (2010). *Cesium D Line Data*. Revision 2.1.4. Available online at http://steck.us/alkalidata.

Tanji-Suzuki, H., Leroux, I.D., Schleier-Smith, M.H., Cetina, M., Grier, A.T., Simon, J., and Vuletić, V. (2011). Interaction between Atomic Ensembles and Optical Resonators. In E. Arimondo, P. Berman, and C. Lin (editors), *Advances in Atomic, Molecular and Optical Physics*, volume 60, chapter 4, pages 201–237. Academic Press, Cambridge, USA.

Thomas, R.A. (2020). *Optical spin-mechanics quantum interface: entanglement and back-action evasion*. Ph.D. thesis, University of Copenhagen.

Thomas, R.A., Parniak, M., Østfeldt, C., Møller, C.B., Bærentsen, C., Tsaturyan, Y., Schliesser, A., Appel, J., Zeuthen, E., and Polzik, E.S. (2021). Entanglement between distant macroscopic mechanical and spin systems. *Nature Physics*, **17**(2):228–233.

Thomas, S.E., Hird, T.M., Munns, J.H.D., Brecht, B., Saunders, D.J., Nunn, J., Walmsley, I.A., and Ledingham, P.M. (2019). Raman quantum memory with built-in suppression of four-wave-mixing noise. *Physical Review A*, **100**(3):033801.

Tiarks, D., Schmidt-Eberle, S., Stolz, T., Rempe, G., and Dürr, S. (2019). A photon–photon quantum gate based on Rydberg interactions. *Nature Physics*, **15**(2):124–126.

Uppu, R., Pedersen, F.T., Wang, Y., Olesen, C.T., Papon, C., Zhou, X., Midolo, L., Scholz, S., Wieck, A.D., Ludwig, A., and Lodahl, P. (2020). Scalable integrated single-photon source. *Science Advances*, **6**(50):eabc8268.

van der Wal, C.H., Eisaman, M.D., André, A., Walsworth, R.L., Phillips, D.F., Zibrov, A.S., and Lukin, M.D. (2003). Atomic memory for correlated photon states. *Science*, **301**(5630):196–200.

Vasilakis, G., Shen, H., Jensen, K., Balabas, M., Salart, D., Chen, B., and Polzik, E.S. (2015). Generation of a squeezed state of an oscillator by stroboscopic back-action-evading measurement. *Nature Physics*, **11**(5):389–392.

Vurgaftman, I. and Bashkansky, M. (2013). Suppressing four-wave mixing in warm-atomic-vapor quantum memory. *Physical Review A*, **87**(6):063836.

Wallucks, A., Marinković, I., Hensen, B., Stockill, R., and Gröblacher, S. (2020). A quantum memory at telecom wavelengths. *Nature Physics*, **16**(7):772–777.

Walther, P., Eisaman, M.D., André, A., Massou, F., Fleischhauer, M., Zibrov, A.S., and Lukin, M.D. (2007). Generation of Narrow-Bandwidth Single Photons Using Electromagnetically Induced Transparency in Atomic Ensembles. *International Journal of Quantum Information*, **5**:51–62.

Wang, Y., Um, M., Zhang, J., An, S., Lyu, M., Zhang, J.N., Duan, L.m., Yum, D., and Kim, K. (2017). Single-qubit quantum memory exceeding ten-minute coherence time. *Nature Photonics*, **11**(10):646–650.

Wasilewski, W., Fernholz, T., Jensen, K., Madsen, L.S., Krauter, H., Muschik, C., and Polzik, E.S. (2009). Generation of two-mode squeezed and entangled light in a single temporal and spatial mode. *Optics Express*, **17**(16):14444.

Wehner, S., Elkouss, D., and Hanson, R. (2018). Quantum internet: A vision for the road ahead. *Science*, **362**(6412):eaam9288.

Yang, S.J., Wang, X.J., Bao, X.H., and Pan, J.W. (2016). An efficient quantum light–matter interface with sub-second lifetime. *Nature Photonics*, **10**(6):381–384.

Yin, J., Cao, Y., Li, Y.H., Liao, S.K., Zhang, L., Ren, J.G., Cai, W.Q., Liu, W.Y., Li, B., Dai, H., Li, G.B., Lu, Q.M., Gong, Y.H., Xu, Y., Li, S.L., Li, F.Z., Yin, Y.Y., Jiang, Z.Q., Li, M., Jia, J.J., Ren, G., He, D., Zhou, Y.L., Zhang, X.X., Wang, N., Chang, X., Zhu, Z.C., Liu, N.L., Chen, Y.A., Lu, C.Y., Shu, R., Peng, C.Z., Wang, J.Y., and Pan, J.W. (2017). Satellite-based entanglement distribution over 1200 kilometers. *Science*, **356**(6343):1140–1144.

Yu, Y., Ma, F., Luo, X.Y., Jing, B., Sun, P.F., Fang, R.Z., Yang, C.W., Liu, H., Zheng, M.Y., Xie, X.P., Zhang, W.J., You, L.X., Wang, Z., Chen, T.Y., Zhang, Q., Bao, X.H., and Pan, J.W. (2020). Entanglement of two quantum memories via fibres over dozens of kilometres. *Nature*, **578**(7794):240–245.

Zhang, G.H., Braverman, B., Kawasaki, A., and Vuletić, V. (2015). Note: Fast compact laser shutter using a direct current motor and three-dimensional printing. *Review of Scientific Instruments*, **86**(12):126105.

Zhang, K., Guo, J., Chen, L.Q., Yuan, C., Ou, Z.Y., and Zhang, W. (2014). Suppression of the four-wave-mixing background noise in a quantum memory retrieval process by channel blocking. *Physical Review A*, **90**(3):033823.

Zhao, B., Chen, Y.A., Bao, X.H., Strassel, T., Chuu, C.S., Jin, X.M., Schmiedmayer, J., Yuan, Z.S., Chen, S., and Pan, J.W. (2009). A millisecond quantum memory for scalable quantum networks. *Nature Physics*, **5**(2):95–99.

Zhong, H.S., Li, Y., Li, W., Peng, L.C., Su, Z.E., Hu, Y., He, Y.M., Ding, X., Zhang, W., Li, H., Zhang, L., Wang, Z., You, L., Wang, X.L., Jiang, X., Li, L., Chen, Y.A., Liu, N.L., Lu, C.Y., and Pan, J.W. (2018). 12-Photon Entanglement and Scalable Scattershot Boson Sampling with Optimal Entangled-Photon Pairs from Parametric Down-Conversion. *Physical Review Letters*, **121**(25):250505.

Zhong, H.S., Wang, H., Deng, Y.H., Chen, M.C., Peng, L.C., Luo, Y.H., Qin, J., Wu, D., Ding, X., Hu, Y., Hu, P., Yang, X.Y., Zhang, W.J., Li, H., Li, Y., Jiang, X., Gan, L., Yang, G., You, L., Wang, Z., Li, L., Liu, N.L., Lu, C.Y., and Pan, J.W. (2020). Quantum computational advantage using photons. *Science*, **370**(6523):1460–1463.

Zhong, T., Kindem, J.M., Bartholomew, J.G., Rochman, J., Craiciu, I., Miyazono, E., Bettinelli, M., Cavalli, E., Verma, V., Nam, S.W., Marsili, F., Shaw, M.D., Beyer, A.D., and Faraon, A. (2017). Nanophotonic rare-earth quantum memory with optically controlled retrieval. *Science*, **357**(6358):1392–1395.

Zugenmaier, M. (2018). *Towards a room temperature single photon source based on atomic vapour*. Ph.D. thesis, University of Copenhagen.

Zugenmaier, M., Dideriksen, K.B., Sørensen, A.S., Albrecht, B., and Polzik, E.S. (2018). Long-lived non-classical correlations towards quantum communication at room temperature. *Communications Physics*, **1**(1):76.